

AD-A272 518



## INTELLIGENT PROCESSING OF FERROELECTRIC THIN FILMS

### Annual Report

Period: May 2, 1992 to July 1, 1993

### OFFICE OF NAVAL RESEARCH

Contract No. N0014-91-J-1508

Principal Investigator: Gene Haertling  
Co-Investigator: Eric Skaar

Supporting Investigators: Feiling Wang  
Joyti Guha  
David Dausch  
James Barrett  
Youngwoo Moon

DTIC  
FEB 1994  
NOV 04 1993  
E D

September 3, 1993

93-26693

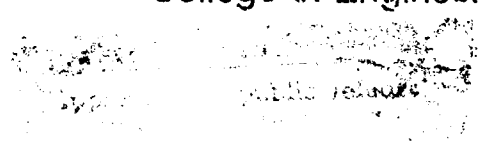
2



CLEMSON  
UNIVERSITY

The Gilbert C. Robinson  
Department of Ceramic Engineering

College of Engineering



**Best  
Available  
Copy**

# **INTELLIGENT PROCESSING OF FERROELECTRIC THIN FILMS**

## **Annual Report**

Period: May 2, 1992 to July 1, 1993

## **OFFICE OF NAVAL RESEARCH**

Contract No. N0014-91-J-1508

Principal Investigator: Gene Haertling  
Co-Investigator: Eric Skaar

Supporting Investigators: Feiling Wang  
Joyti Guha  
David Dausch  
James Barrett  
Youngwoo Moon

Accession For	
NTIS	CR&I
DTRC	TAB
University	U.S.
JSC	per DTR
By	
Date	
Funding Source	
Date	Approved by
A-1	

September 3, 1993



**The Gilbert C. Robinson  
Department of Ceramic Engineering  
College of Engineering**

**Table of Contents**

- Part I. .... Introduction
- Part II. .... Intelligent Processing Implementation and Automation
- Part III. .... Powder Processing and Characterization of Bulk Ceramics
- Part IV. .... Spin Coated Thin Films and Bulk Ceramics
- Part V. .... Sputtered Thin Films and Electrooptics
- Part VI. .... Publications

## SUMMARY

This report details work that was performed in the Ceramic Engineering Department of Clemson University over the period from May 2, 1992 to July 1, 1993 under ONR contract No. N0014-91-J-1508. The work described in this report covers the second year of a three-year program involving intelligent processing of ferroelectric thin films and bulk materials. It is presented in seven parts dealing with automation, powder processing, bulk materials characterization, thin film fabrication and evaluation, electrooptic behavior of thin films and published work.

In regard to process automation and intelligence, the two-conductor ac resistance probe was tested for reading stability and response time. Both requirements were easily met, and simulated batching experiments were carried out. The fluid flow pattern for the batching system has required special attention and optimization. Programming of the device drivers which are needed to link the computer and its neural network has now been completed, thus paving the way for making the system totally operational.

During this period, additional processing studies were carried out on various methods of producing an optimum ferroelectric powder with the acetate precursors. The results from these experiments involving coprecipitation, hydrothermal, spray pyrolysis and freeze drying have shown that with the present facilities, coprecipitation and subsequent calcining is the best method. A processing and characterization study of PMN-based materials has yielded material with excellent properties.

An automatic spin coat reactor/analyizer was used to produce PLZT thin films from acetate precursors on Pt-coated Si wafers. The spin coater is computer controlled and fully automated for hands-off processing, thus providing a cleaner environment and more flexibility in processing parameters. The spin coating process is fully integrated with rapid thermal processing, atmosphere control and in-situ ellipsometry in one chamber. It is believed that this unit is the first of its type to promise optimum fabrication of ferroelectric thin films for IC devices. Thin films produced by the automatic spin coater were found to be more uniform and of superior electrical properties than those produced manually.

The magnetron sputtering of acetate-derived PLZT powder has produced high quality thin films in terms of dielectric and electrooptic properties. A systematic investigation of these properties have yielded some significant results. A phenomenon of birefringent bistability has been observed in ferroelectric films which are electrode with a metal and a semiconductor layer. A non-volatile electrooptic switching is realized by applying bipolar electric pulses the MFS structure. With a newly developed reflection-

mode differential ellipsometry technique, a digital electrooptic response was observed to

mode differential ellipsometry technique, a digital electrooptic response was observed to exist in lead zirconate thin films for the first time. The modeling of the differential ellipsometry by taking into account multiple reflections has resulted in a more sophisticated and reliable measuring method. It is shown by the model that this measuring technique may be utilized to separate the extraordinary optical index from the ordinary index. A prototype optical phase modulator has been fabricated from a PLZT material derived from acetate precursors. By choosing different values of dc bias, the modulator may be operated in either the linear or the quadratic region. Thus, the modulating frequency is either equal to or double the driving signal.

During this year, seven papers were published from this work with several more in various stages of pre-publication.

**Part I.**

**Introduction**

## Introduction

The continuing drive toward greater integration and miniaturization of present-day discrete (bulk) electronic components has led to the development of thin film materials for many applications, and among these are the thin film ferroelectrics. New chemical methods of fabricating thin films via sol-gel, metallo-organic decomposition and chemical vapor deposition are now complementing the traditional vacuum technology approach to thin films. These films offer a wide range of applications such as capacitors, buffer layer dielectrics, piezoelectric filters, pyroelectric detectors, optical modulators, displays and integrated optics as well as the newer applications of ferroelectric memories and "smart" sensors.

The drive behind all of the research and development of ferroelectric (FE) thin films stems from a number of advantages which accrue for thin films in comparison to bulk material. The include:

1. lower voltage/thinner structures
2. higher speed/less power
3. greater integration/smaller size/lighter weight
4. unique structures/multilayer composites
5. multifunction applications
6. lower costs/fewer processing steps/lower temperatures.

In addition, FE thin films for random access memories are of special interest because they are:

1. non-volatile
2. radiation hard
3. high dielectric constant dielectrics
4. amenable to standard photolithographic processes
5. integratable with silicon logic circuitry.

While it is true that FE thin films can now be prepared by several techniques, the best method or methods are still to be determined. Ultimately, their long term future depends heavily on their ability to be fabricated by a method which is compatible with present-day silicon or gallium arsenide technology while maintaining a high level of quality and reproducibility over fairly large areas ( $>100\text{ cm}^2$ ). In addition, it is vital to their successful application to have a clear understanding of (1) the basic nature of the films, (2) the mechanisms which govern their behavior (e.g., polarization development, switching, internal strain, ageing, etc.) and (3) the agreement or differences which exist in extrapolating bulk phenomena and properties to thin films.

With this in mind, it has become increasingly apparent that investigations involving both bulk and thin films simultaneously are beneficial to achieving the overall goals of preparing, characterizing and understanding these complex materials. There are good reasons to believe that the gap between bulk materials and thin films will eventually be filled with materials appropriately fabricated and suitably applied. Indeed, the present difficulty in fabricating ceramic structures in this range of thicknesses; i.e., 125 um to 1 um, is the primary reason for their notable absence in present-day devices. Recognizing that this thickness range is a problem in regard to materials preparation, it, nevertheless, still holds promise as a fruitful area of research since it is generally recognized that certain phenomena such as electromechanical (piezoelectric) and electrooptic effects could be profitably applied to devices within this range.

This report describes work associated with the utilization and optimization of a water-soluble acetate precursor system which is amenable both to the fabrication of chemically-derived ferroelectric thin films and to the production of chemically-derived ferroelectric pyrolyzed ultrafine powders for bulk materials. While the emphasis of the work is on the processing and application of thin films by this technique, the fact that both materials are derived from the identically same precursors makes it possible to quantify direct comparisons of properties and phenomena of the macro (bulk) and micro (thin film) materials.

In order to achieve maximum film and powder quality, the concept of "intelligent processing of materials" (IPM) is being initiated in this program but has been employed to only a limited extent, thus far. The IPM concept is a computer interactive, smart processing technique for producing thin films and powders in a hands-off environment. For multiple-layer thin films, the implementation of this concept involves specifically designed and custom built dipping and spinning equipment. This equipment was acquired under separate funds, and during this reporting period was used for the first time to fabricate thin films.

**Part II.**

**Intelligent Processing Implementation and Automation**

# **INTELLIGENT PROCESSING OF FERROELECTRIC THIN FILMS**

## **Annual Report**

### **Part II.**

#### **Intelligent Processing Implementation and Automation**

Submitted by: James Barrett  
Eri. Skaar

**The Gilbert C. Robinson Department of Ceramic Engineering  
Clemson University**

## **SYNOPSIS**

This report describes current efforts involved in the implementation of Intelligent Processing of Materials (IPM) for the production of PLZT acetate thin films and powders. It summarizes progress made during the second year of the program on Intelligent Processing of Ferroelectric Thin Films sponsored by the Office of Naval Research.

## **OBJECTIVES**

The objectives of this portion of the program are to develop software and hardware to implement IPM for powder production from acetate solutions:

1. Develop software to implement IPM.
2. Develop sensors for controlling solution composition and properties.
3. Design and purchase equipment for automated solution processes.

## **INTRODUCTION**

### **Intelligent Processing of Materials (IPM) for PLZT Acetate Powders:**

The purpose of IPM is to reduce the lead time between materials development and the production of those materials while at the same time increasing the quality of the product. The quality that is achieved through the IPM process is built-in during the production and not the result of post-manufactured inspection. IPM is desirable because it can improve the quality, reliability, and yield of processed materials. Quality is achieved in the IPM process by "building" it into production, and is not the result of inspection after manufacture.

IPM combines the expertise of the process engineer and the knowledge of the materials scientist through the use of an expert system. The expert system is an application of artificial intelligence that utilizes efficient and effective data handling and retrieval to analyze and predict processing events so that corrections and/or compensations can instantaneously be made in the process to achieve a high quality product. This system monitors all processing steps from raw material characteristics to the final product during manufacturing so that changes can be made in each step and in future steps to attain the highest quality product. Process models and real-time sensors are heavily relied upon in the IPM strategy so that higher levels of control and awareness can be attained than in conventional processing. In-situ sensors can monitor complex characteristics such as microstructures in real time and combine this data with conventionally sensed data, such as temperature or viscosity and the resulting combination is used by the expert system to make process judgements to compensate for

process and raw material variability.

To implement IPM in the production of powders from PLZT acetate solutions, a production process that is compatible with the requirements of an automated process is needed. The process must be completely defined. The entire process for this system includes: the making of PLZT acetate solutions, the precipitation of a solid, the separation of the solid from the liquid, and the processing of the solid into a powder. As the process is defined, process variables are defined and assessed. These variables must be isolated and treated in a manner that is consistent with the IPM process. It is also important that the equipment that makes up the system be compatible so that it can be linked efficiently and effectively. The hardware, such as mixing equipment, valves, and sensors must be linked to the software (computer) that runs the system. The hardware and software are the two major components of any IPM system, and each has its own purpose.

The majority of the hardware needed to initiate and implement IPM to the batching component of manufacturing PLZT acetate powders has been purchased or fabricated from existing parts and adapted to perform specific tasks. A computer has been purchased and is currently in use in controlling the batching equipment. The software that has been acquired is conducive to self-learning processing algorithms and capable of correcting errors in manufacture. Other software has been written to enable the communication between the computer and the process equipment, as well as enabling the use of the purchased software in this system. The unique requirements of IPM make it necessary that the software be developed for the specific tasks and functions at hand.

Sensors are the link between the process and the computer that drives the process. In order to select or design sensors, it is necessary to establish the parameters that affect the product properties that are important. One type of sensor, for fluid level control, has been installed in the batching system. Another type of sensor has been designed and tested for the PLZT fluid system to measure the fluid resistivity under alternating current. All process variables and their limits must be assessed, then the methods and conditions under which they are monitored must be considered.

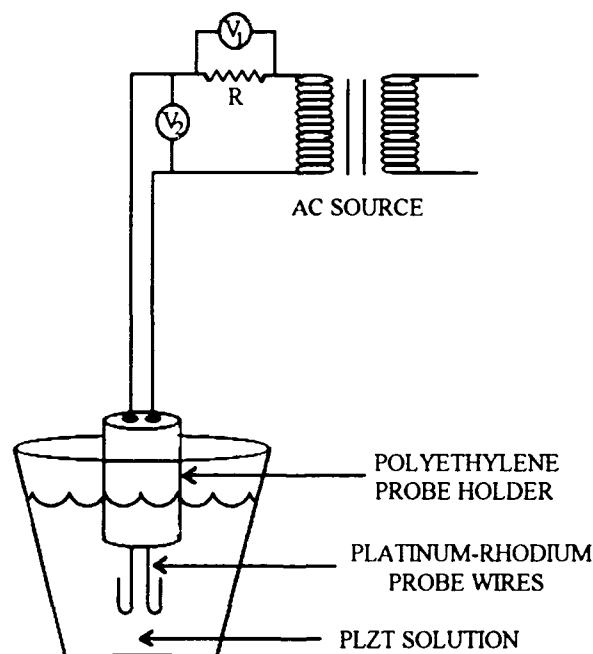
Traditional programming is not designed to apply experience to control. An alternative software scheme is neural networking software. Another requirement for software is that it be compatible with the computers that are available at present, in this case, an MS-DOS™ machine. A software package called NeuroWindows™ has been purchased to partially fulfill these requirements. The software is not geared specifically for control, so it was necessary to write device drivers that will work concurrently with NeuroWindows™ to complete the software needs in linking the computer to the other hardware. To implement IPM in the production of powders from PLZT acetate solutions, a production process that is

compatible with the requirements of an automated process is needed. The production process must be completely defined. The entire process includes the making of solutions, the precipitation of a solid, and the separation of the solid from the liquid. The major variables need to be isolated and treated in a manner that is amenable and consistent with the IPM process. In addition, the hardware, software, and sensors must be set up as a system.

## EXPERIMENTAL

### I. Hardware:

As stated, sensing is the key component in linking hardware and software in an IPM process. The sensors for fluid levels in the batching system have been built from stainless steel rods and installed in the batch reservoirs. Included in each reservoir are a low-level sensor and a high-level sensor. The electronics linking the sensors and the input board for the computer are currently being installed. The AC resistivity sensor that was described in the last annual report can be used in conjunction with the level sensor to assess raw material properties within the reservoirs using the same hardware, but separate electronic hookups. A schematic of the AC resistivity sensor used can be found in Figure 1.



$$R_{\text{fluid}} = \frac{V_2}{I}$$

Figure 1. Method of measuring resistance of PLZT solutions using alternating current.

The materials chosen for the batch system and sensors have been evaluated for corrosion. The stainless steel rods used for level sensing were checked by immersion and storage in a container of each batch constituent, at an ordinary concentration. The samples were examined on an approximately daily basis for six weeks. No apparent signs of any corrosion were present. The same test was applied to the thread tape that was used to seal the valves and reservoir connections, with similar results. The compatibility of the polyethylene reservoirs with the batch constituents has already been established.

The entire automated process for the production of PLZT acetate powders that is being developed has many parts that need to be both optimized and automated. The section of the process that received the greatest attention initially in the development of the total process is the batching system itself. The automated process hardware for the batching of PLZT acetate solutions has been assembled and the equipment has been constructed, tested, and is operating properly. The system utilizes manually filled reservoirs containing the liquefied constituents of the PLZT acetate system that supply smaller, computer-controlled reservoirs that are used to dispense batch amounts. Solenoid valves have been installed beneath each reservoir, to permit control of dispensation. Polyethylene containers, which are used as reservoirs, and tubing connecting the valves and reservoirs has been set up on a custom built chemical rack. The level sensors mentioned previously are a part of a switch system that is used to control the filling of the computer-controlled reservoirs from the manually-controlled reservoirs, as well as being a low-liquid-level alarm. When the valve for the manually controlled reservoirs is opened, the fluid will flow until the liquid completes the circuit between the common rod and the high-level rod. The computer will detect the signal through an input board that links the valve to the computer. Then, the computer can send a signal to the output board that links the valves and the computer, and the valve can be closed to stop fluid flow. The low-level sensor is useful in determining when the valves from the manually-filled reservoirs need to be opened to replenish the computer-controlled reservoirs, or to signal the need to refill the manually-filled reservoirs. An IBM 433DX/S has been joined to the batch system through the I/O relay boards that are connected to the solenoid valves and level sensors. Again, the stainless steel level sensors are in place in the solution reservoirs and are being connected to the input relay board for automatic switching. The computer currently controls and times the switching of valves on and off, through the output board and the device drivers that were written. In addition, all ten valves can be operated manually via a switch panel, and indicator lights for each open valve operate whether the system is under automatic or manual control. A main power switch separates computer control and manual control, such that manual control can be used to override the computer control, if necessary. A diagram of the equipment setup is shown in Figure 2.

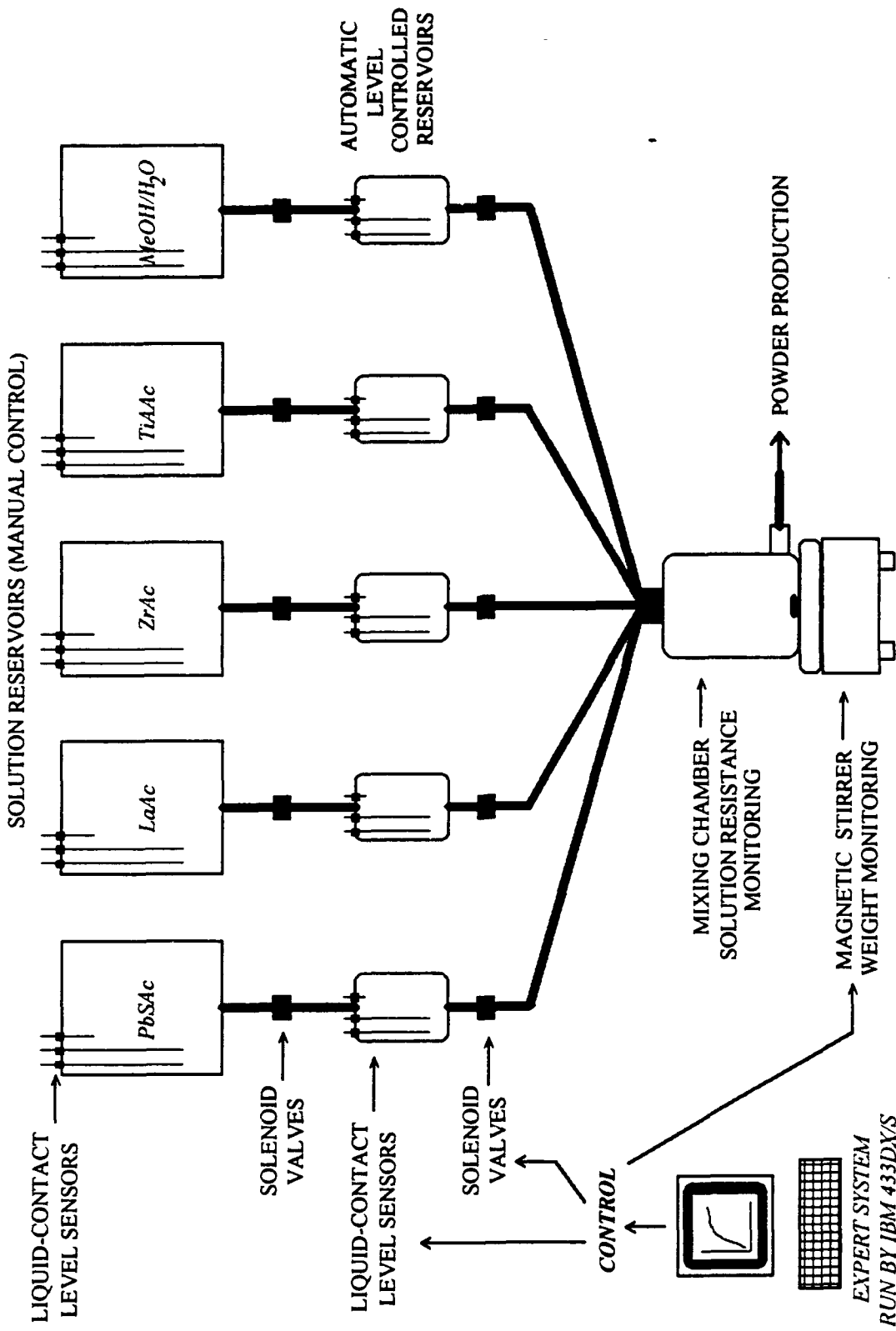


Figure 2. Automated solution batching system controlled by IBM PC.

The input and output boards used to interface the computer and batch equipment are Advantech PCL-812 electronic cards. They are high speed, multi-function data acquisition cards and are compatible with many types of software and hardware. The key applications include: process control, automatic testing, data acquisition, and process automation. A schematic of the features and layout of the boards is shown in Figure 3.

## II. Software and Programming of Batch System Elements:

The device drivers needed to link the computer and its neural network, NeuroWindows,<sup>TM</sup> with the batch system hardware were designed for the MS-DOS platform. The drivers permit the use of the input and output boards to control communication and execution between the computer and batch equipment. The software operates under the Microsoft Windows system, which greatly enhances its compatibility with any other software packages that may be necessary.

The control algorithm for the automated batching process is a two part algorithm. The first part is a normal weighing or batching algorithm. It contains a database of recipes for the solutions required to make powders of various compositions. As long as the process does not vary, and all the settings remain constant, the process is capable of running with this section of the algorithm alone. The second part of the algorithm (currently under development) is designed to sense problems and makes corrections to the process.

This second section is an artificially intelligent program based on a neural network. It is designed to sense "out of control" conditions and make appropriate corrections to the weighing or batching algorithm.

Neural networks excel at pattern recognition, diagnosis, and decision making. The idea behind this section of the algorithm is to recognize an assignable problem as it develops, and compensate. In a sense, the computer is programmed to utilize statistical process control.

For example, suppose the metering mechanism for one of the constituents became partially clogged. The result would be a variance from normal with respect to the weight and the resistance measurements for the batch. The pattern of these measurements would change. The neural network would be taught to recognize this pattern, and effect the appropriate compensation. Other types of assignable problems would also present their unique patterns that the neural network would be taught to recognize.

The unique beauty of using neural network technology for this application is that the teaching of the network is not a function of programming, but rather simulation. For the network to function, it has to be taught the patterns that specific problems create. This task is accomplished by actually simulating the problem in the process. The network is programmed to learn and recognize the resulting sensor patterns. Once the network recognizes the pattern, it is programmed to compensate for the deficiency. A properly designed network, therefore,

PCL-812 BLOCK DIAGRAM

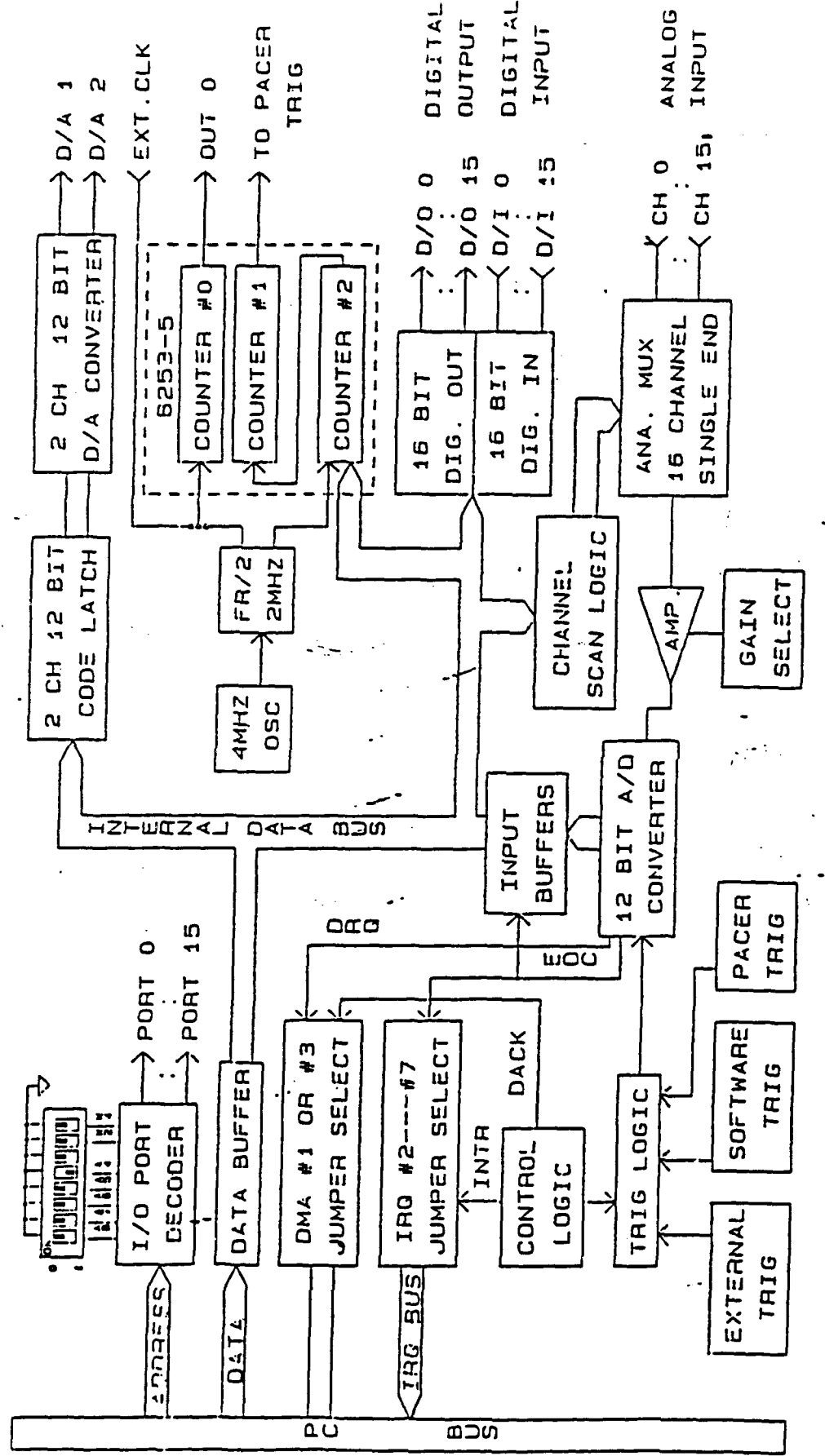


Figure 3. Schematic of the Advantech PCL-812 PC-LabCard™ used for input and output.

does not depend upon an exhaustive database of every problem. Rather, as experience is gained with a process, the problems and solutions can be taught to the network. The algorithm improves with operating experience and thus the process can proceed toward optimization.

## RESULTS

### I. Hardware:

The two-conductor AC resistance probe that was constructed has been tested for reading stability and response time. Both requirements for this resistivity measurement tool were easily met by the probe, as the response time for a change in resistance was two to five seconds and the resulting readings were stable for days. No probe maintenance occurred during these tests, as it was used continuously, as required by the IPM process. The main application of the AC resistivity sensor will be in the mixing vessel of the batch system. Again, a schematic of the probe can be seen in Figure 1.

The AC resistance probe has also been tested in a simulated batching experiment. The batch constituents for a 9/65/35 PLZT acetate solution were added, one at a time, and the changes in resistance of the total solution were tabulated and plotted, as can be seen in Figure 4. An order of addition of constituents was chosen to best suit the homogeneity of the batch. Generally, the resistance of the total batch increased as each constituent was added. This result shows that this tool is amenable for use in an IPM process. The constituent that shows a possible exception for the upward trend is lead subacetate, for which the resistance decreased after a point. However, the neural network that runs the system can be "trained" to compensate for this result. The probe can be used to help the expert system "learn" the characteristics and properties of the batching process, from one constituent to the next. The process model for the batching procedure must be available to the network, and it can be referenced by the process algorithm as a guide and a check. The neural network should be able to take the resulting "batch pattern" and use it to develop a process model to assist in the preparation of solutions through the automated batch system.

The fluid-flow pattern for the batch system is being assessed at this time. The preliminary data shows that the gravity-flow of solutions through the system should be sufficient for batching into a central mixing vessel. A sample time of three seconds was used to check the flow volumes through each valve. The computer controlled and timed the valve openings automatically for these tests. The fluid from the open valve was collected and measured, through eleven trials per lower valve (one valve per solution constituent). The fluid used for the preliminary tests was water, one of the batch constituents. The flow data can be

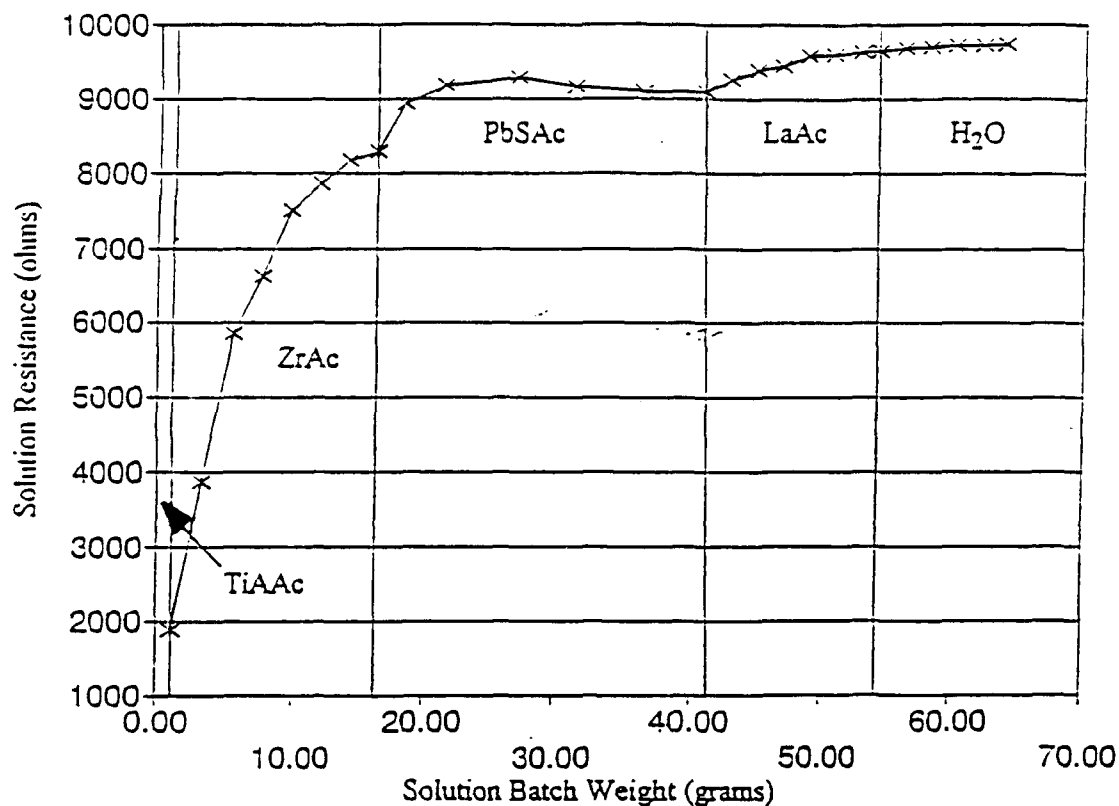


**Figure 4.** Solution resistance (AC measurement) for the total PLZT acetate batch as constituents were added.

seen in Figure 5. The results indicate that there is a need to prime the batching lines before attempting to batch. The results were much more consistent after the first run, as can be seen in Figure 5. Also, the length of the tubing from each valve to the central mixing area seemed to affect the results. Valve numbers 2 and 10 have the same length batch lines, as well as 4 and 8. The line for valve 6 is the shortest, and also showed the most variability. The stability of the dispensed volume appears to be inversely proportional to the length of the line. These results, as well as the relatively high volume dispensed in three seconds, show that there is sufficient back pressure to drive the fluid delivery without additional equipment. In addition, it is recognized that reducing nozzles inserted in the tubing can reduce the need for priming the lines and slow the flow of fluid into the mixing vessel. Different sized nozzles will be needed based on differing viscosities and required volumes per batch. It is believed that this step will heighten the ability to control the batching process, and make it more consistent.

## II. Software and Programming of Batch System Elements:

The programming uses the modular design. Using this approach code can be written and "debugged" in segments, rather than developed and debugged as a complete program. This minimizes development time, and greatly facilitates software maintenance.

# Flow Volumes for Open Valves

(Time Valve Open = 3 sec)

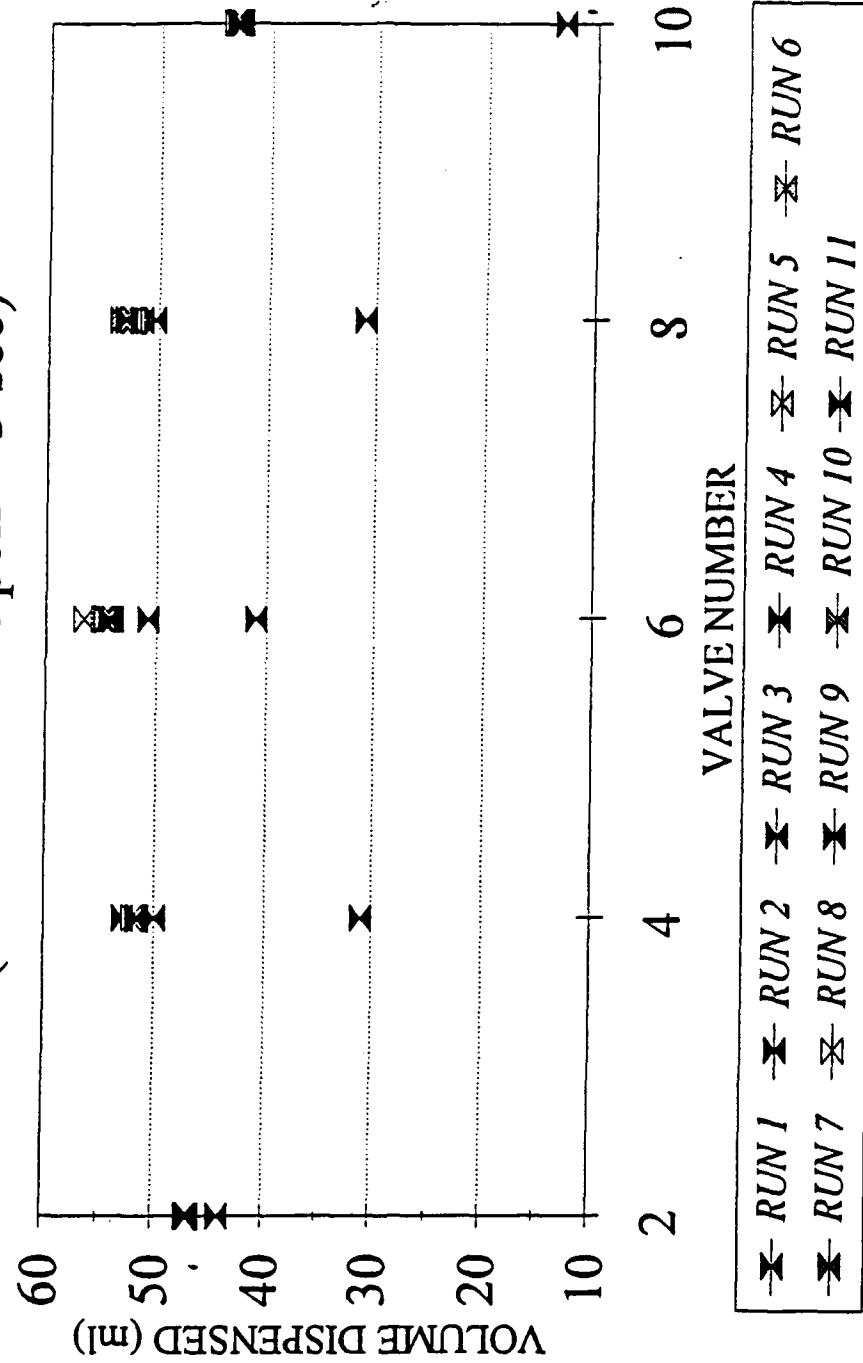
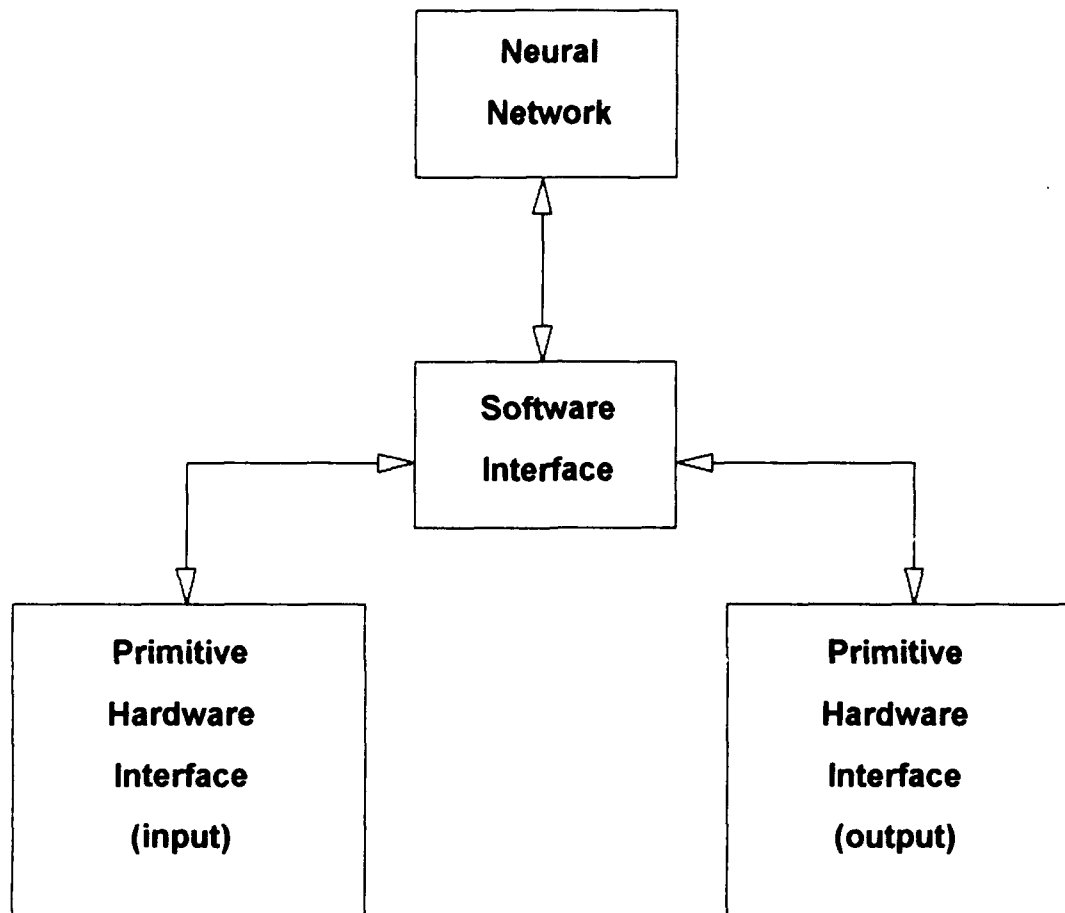


Figure 5. Flow data for valve opening time of three seconds each run (unrestricted flow).

Basically, the program consists of 4 main segments, as shown in Figure 6. They are the neural network, the software interface, the primitive hardware interface output, and the primitive hardware interface input.



**Figure 6.** Elements of the Batch System Program.

The two primitive hardware interfaces control the hardware directly by writing and reading from memory mapped addresses. These primitives were designed as device drivers, because this provided the most flexibility in the other segments.

The software interface is the "spinal column" of the program. This segment of the program contains three main sections, according to Figure 7. These are the human interface, neural network interface, and the primitive software interface.

The human interface section of the program reports progress, accepts input, and selects program functions. This section allows the operator to teach the neural network new sensor patterns. This section allows the operator to use manual control where applicable. This

section allows the use of automatic control. In each case the human interface section displays the progress of the process. This section also allows the operator to select various recipes to make under automatic control.

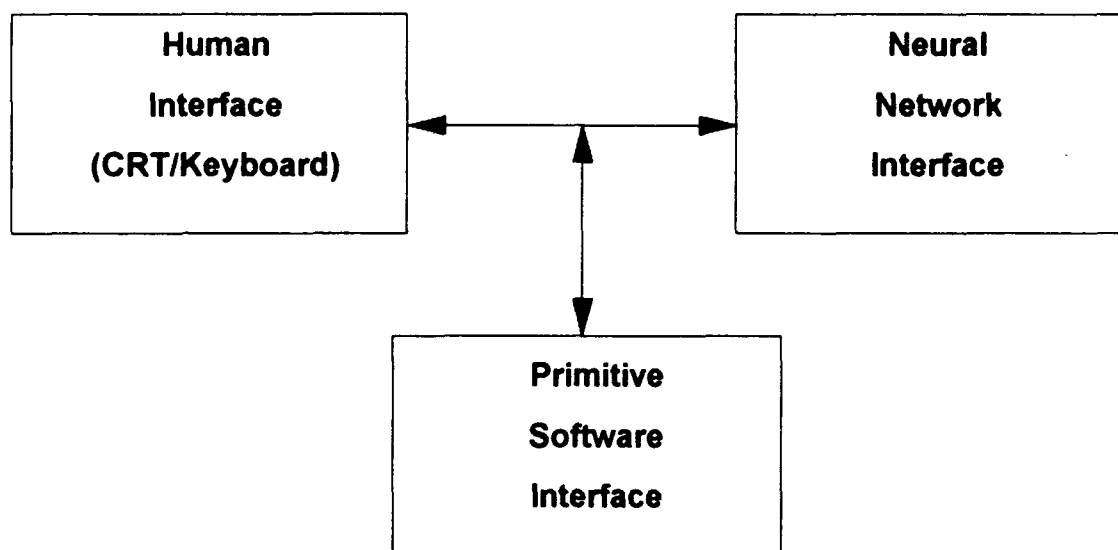


**Figure 7.** Schematic of the Control System.

The neural network interface section is the section of the program which takes the primitive data and massages it to input to the neural network. For example the raw data coming off the resistivity sensor is in arbitrary data units. For measurement of the AC resistance of the solution, two raw data measurements have to be combined and fed to the network. This section of the program accomplishes that task. This section of the program also translates the output from the neural network into commands suitable for the other sections of the program to utilize to control the hardware.

The final section of the software interface segment is the primitive software section. Basically, this section interfaces with the two primitive hardware interfaces. This section contains the filling algorithms and input algorithms to pass along the primitive input data to the rest of the program.

The last main segment is the neural network. This is the "brains of the program." This segment, developed with NeuroWindows,<sup>TM</sup> can recognize patterns which it is taught. This segment will store data patterns for all materials taught, for both well functioning and faulty runs. This segment will be able to diagnose problems, and develop a corrective action.

The primitive hardware interface segments have to be written in assembly language.

The other two segments can be written in a higher level language. The preferred software that has been chosen for the software interface segment is Visual Basic™ because it has facilities to design a sophisticated human interface, and interfaces with NeuroWindows™. The initial human interface that has been constructed using Visual Basic™ is shown in Figure 8, and will

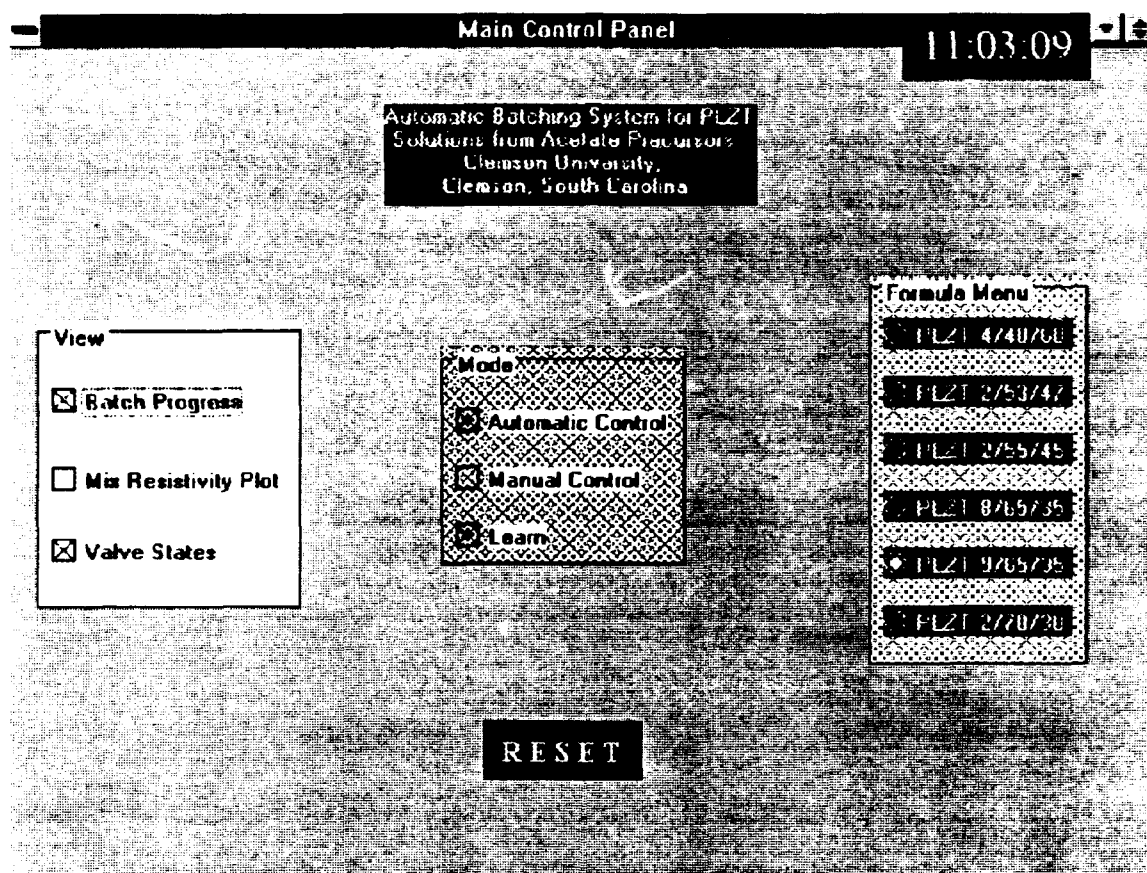


**Figure 8.** Main Control Panel for automated batch system, the human interface.

serve as the main user control panel. It includes a "Mode" section for the selection of automatic or manual operating states, as well as the option to initiate a "learning session" through either automatic or manual operation. Also, a list of formulations is included. Of course, each formulation will have to be evaluated and formatted for the computer before it can be placed on an activation menu. There is a "View" section that provides the operator with different options to track the process, such as the opening and closing of valves. The final element of the Main Control Panel is a "RESET" button to automatically stop the process and switch all control to manual at one time, in the event that the process needs to be stopped.

The following is the listing of the primitive output segment:

```
.MODEL    tiny
.286
cseg      segment public 'code'
org      0h
assume cs:cseg, ds:cseg, es:cseg
exdrv proc far
        dd 0fffffffh
        dw 8000h
        dw dev_strategy
        dw dev_interrupt
        db 'DIGOUT '
dev_strategy:
        mov cs:keep_es, es
        mov cs:keep_bx, bx
        ret
keep_es   dw ?
keep_bx   dw ?
mssg     db 0ah,0dh,'Binary Output Driver is installed.',0ah,0dh,'$'
swtchs   db 0h,1h,2h,4h,8h,10h,20h,40h,80h
ps1      db 0h
ps2      db 0h
dev_interrupt:
        push es
        push ds
        push ax
        push bx
        push cx
        push dx
        push si
        push di
        push bp
        mov ax, cs:keep_es
        mov es, ax
        mov bx, cs:keep_bx
        mov al, es:[bx] + 2
```

```
shl    al, 1  
sub    ah, ah  
lea    di, functions  
add    di, ax  
jmp    word ptr [di]
```

functions label word

```
dw    initialize  
dw    check_media  
dw    make_bpb  
dw    ioctl_in  
dw    input_data  
dw    nondestruct_in  
dw    input_status  
dw    clear_input  
dw    output_data  
dw    output_verify  
dw    output_status  
dw    clear_output  
dw    ioctl_out
```

check\_media:

make\_bpb:

ioctl\_in:

input\_data:

nondestruct\_in:

input\_status:

clear\_input:

output\_verify:

output\_status:

clear\_output:

ioctl\_out:

```
or     es:word ptr[bx]+3, 8103h  
jmp    quit
```

```
initialize:
    lea    ax, e_o_p
    mov    es:word ptr[bx]+14, ax
    mov    es:word ptr[bx]+16, cs
; Device initialization code goes here.
    mov    ah, 09h
    lea    dx, mssg
    int    21h
    jmp    quit

output_data:
    mov    cx, es:[bx]+18 ;get character count from table
    mov    ax, es:[bx]+16 ;get data buffer address
    mov    ds, ax
    mov    dx, es:[bx]+14 ;and put in DS:DX
; The business starts here.
    cmp   cx, l
    jg    tooman
    pushf
    pusha
    xor   ax,ax
    mov   bx,dx
    mov   al,ds:[bx]
    mov   si,OFFSET swtchs
    cmp   al,0h
    jg    lastmin
    xor   ax,ax
    mov   dx,23dh
    out   dx,al
    mov   dx,23eh
    out   dx,al
    mov   cs:ps1,0h
    mov   cs:ps2,0h
    jmp   zappit
lastmin: cmp   al,8h
        jle   fstjmp
```

```
    cmp al,10h
    jle sndjmp
    cmp al,18h
    jle trdjmp
    cmp al,20h
    jle ftjmp
zappit: popa
        popf
tooman: jmp quit
fstjmp: mov dx,23dh
        mov bx,ax
        xor ax,ax
        mov al,cs:[si+bx]
        or al,cs:ps1
        mov cs:ps1,al
        jmp frtjmp
sndjmp: sub al,8h
        mov dx,23eh
        mov bx,ax
        xor ax,ax
        mov al,cs:[si+bx]
        or al,cs:ps2
        mov cs:ps2,al
        jmp frtjmp
trdjmp: sub al,10h
        mov dx,23dh
        mov bx,ax
        xor ax,ax
        mov al,cs:[si+bx]
        not al
        and al,cs:ps1
        mov cs:ps1,al
        jmp frtjmp
ftjmp: sub al,18h
        mov dx,23eh
        xor bx,bx
```

```
xor bx,bx
mov bx,ax
xor ax,ax
mov al,cs:[si+bx]
not al
and al,cs:ps2
mov cs:ps2,0h
mov cs:ps2,al
frtjmp: ;out dx,al
        mov ah,0eh
        mov bh,0
        int 10h
        jmp zappit
; The business ends here.

quit:
        or es:word ptr[bx]+3, 100h
        pop bp
        pop di
        pop si
        pop dx
        pop cx
        pop bx
        pop ax
        pop ds
        pop es
        ret

e_o_p:
exdrvrv endp
cseg      ends
end exdrvrv
```

The following is the listing of the primitive input segment:

```
.MODEL    tiny
cseg      segment public 'code'
          org    0h
```

```
assume cs:cseg, ds:cseg, es:cseg
exdrv proc far
    dd 0fffffffh
    dw 8000h
    dw dev_strategy
    dw dev_interrupt
    db 'DIGIN '
dev_strategy:
    mov cs:keep_es, es
    mov cs:keep_bx, bx
    ret
keep_es    dw ?
keep_bx    dw ?
mssg      db 'Driver is installed.',0ah,0dh,'$'
dev_interrupt:
    push es
    push ds
    push ax
    push bx
    push cx
    push dx
    push si
    push di
    push bp
    mov ax, cs:keep_es
    mov es, ax
    mov bx, cs:keep_bx
    mov al, es:[bx] + 2
    shl al, 1
    sub ah, ah
    lea di, functions
    add di, ax
    jmp word ptr [di]
functions label word
    dw initialize
    dw check_media
```

```
        dw    make_bpb
        dw    ioctl_in
        dw    input_data
        dw    nondestruct_in
        dw    input_status
        dw    clear_input
        dw    output_data
        dw    output_verify
        dw    output_status
        dw    clear_output
        dw    ioctl_out

check_media:
make_bpb:
ioctl_in:
nondestruct_in:
input_status:
clear_input:
output_verify:
output_status:
clear_output:
ioctl_out:
output_data:
        or     es:word ptr[bx]+3, 8103h
        jmp   quit

initialize:
        lea    ax, e_o_p
        mov    es:word ptr[bx]+14, ax
        mov    es:word ptr[bx]+16, cs
;
;      Device initialization code goes here.
        mov    ah, 09h
        lea    dx, mssg
        int    21h
        jmp   quit
```

input\_data:

```
    mov al, es:[bx]+18  
    cbw  
    mov cx, ax  
    mov ax, es:[bx]+16  
    mov ds, ax  
    mov dx, es:[bx]+14
```

; the input routine goes here

```
    push ax  
    push bx  
    cmp cx, 1h  
    jne finis  
    xor ax, ax  
    mov bx, dx  
    push dx  
    mov dx, 27h  
    in al, dx  
    pop dx  
    mov ds:[bx], al  
    pop bx  
    xor ax, ax  
    mov ax, 01h  
    mov ds:[bx]+18, ax  
    pop ax  
    jmp quit
```

finis: pop bx

```
    pop ax  
    jmp quit
```

quit:

```
    or es:word ptr[bx]+3, 100h  
    pop bp  
    pop di  
    pop si  
    pop dx  
    pop cx
```

```
pop    bx
pop    ax
pop    ds
pop    es
ret
```

```
e_o_p:
```

```
exdrvr endp
```

```
cseg      ends
```

```
end      exdrvr
```

**Part III.**

**Powder Processing and Characterization of Bulk Ceramics**

# **INTELLIGENT PROCESSING OF FERROELECTRIC THIN FILMS**

## **Annual Report**

### **Part III.**

#### **PLZT Powder Preparation and Characterization**

**Submitted by: Youngwoo Moon  
Gene Haertling**

**The Gilbert C. Robinson Department of Ceramic Engineering  
Clemson University**

## **1. Introduction**

Powder characteristics before firing have been recognized to be an important factor affecting material properties. It is critical to employ appropriate powder processing methods to produce advanced ceramic materials. Recently, great efforts have been made to develop better powders to enhance material properties and to reduce manufacturing costs. In this study, several non-conventional processing techniques were performed to produce PLZT powders. They include:

- A. Freeze Drying after coprecipitation (FD)
- B. Vacuum Drying after coprecipitation (VD)
- C. Spray Pyrolysis (SP)
- D. Hydrothermal Processing (HP)

The powder produced by each process was characterized by X-ray diffraction (XRD) and scanning electron microscope (SEM). The powders thus obtained were sintered and their microstructures and electrical properties were investigated. The results were compared with those prepared by the mixed oxide method. The research is still ongoing and current results are reported.

## **2. Experimental Procedure**

### **A. Freeze Drying after coprecipitation**

Freeze drying technique was employed to the precipitant gel prepared by a coprecipitation method. A mixture of acetate precursor solution of PLZT was precipitated in an ammonia solution mixed with distilled water (1:3 volume ratio). The pH values required for precipitation were investigated for each precursor. In order to prevent dissolving the precipitant gel, the pH value was controlled. The precipitant gel thus obtained was washed to remove excess ions and then freeze dried. For the characterization of the powders thus obtained, SEM and XRD were used. To investigate the material properties, the powders were calcined at 550 °C for 4 hrs and sintered at several temperatures between 1100 °C and 1250 °C for 4 hrs. Also, the specimens prepared by mixed oxide method were sintered at the same conditions to compare the microstructure and properties. The mixed oxide powders were calcined at 900 °C for 2 hrs. In this report, the compositions 7/70/30 and 8/65/35 are reported.

### **B. Vacuum Drying after coprecipitation**

The compositions 2/55/45, 9/65/35, 8.6/65/35, 5.5/56/44 and 5.5/58/42 were prepared by a vacuum drying method. The same acetate precursors were used as described above. Instead of ammonia solution, an oxalic acid solution was used as the precipitating agent. The precipitants were dried in a vacuum oven without filtering. The

powders thus obtained were calcined at 550 °C for 4 hrs. and sintered at 1250 °C for 2 hrs. The density of the specimens and their electrical properties were measured.

### C. Spray Pyrolysis

The equipment used for spray pyrolysis is shown in Fig. 1. The precursor materials used were the same as described above. A mist was generated which was allowed to react in the hot-zone of the furnace. The material was decomposed and calcined at about 700°C, and the resulting powder was collected at the bottom.

### D. Hydrothermal Process

Lead-, lanthanum-, zirconium- and titanium-hydroxides were precipitated from the respective acetate precursor solutions. An ammonia solution was used as the precipitating agent. Hydrothermal processing was performed on each precipitated gel. The reaction temperature and pressure were 130 °C and 35 psi, respectively.

## 3. Results and discussion

### A. Freeze Drying

To prevent agglomeration, the freeze drying method was applied to the coprecipitated gel. Each precursor has a different critical point of pH value for precipitation in an ammonia solution. The critical pH values are shown in Table 1.

Table 1. The critical pH values for precipitation in ammonia solution for different precursors.

<u>Precursor</u>	<u>Critical pH value</u>
Lead subacetate solution	10.1
Zirconium acetate	5.6
Titanium acetate	7.1
Lanthanum acetate	8.3

Washing of the gel was performed for easy freezing. However, vigorous washing resulted in a loss of the lead component due to a high critical pH value. The morphology of the freeze dried powder is shown in Fig. 2. As was observed before calcination, the powder was weakly agglomerated. The particle size was about 0.1 μm. The powder was ball milled after calcination and then used for sintering.

Fig. 3 (a) and (b) show the final state of the freeze dried powder and mixed oxide powder, respectively. The crystallinity was investigated using a X-ray diffractometer for both the freeze dried and mixed oxide powders as shown in Fig. 4. In case of the freeze dried powder, the X-ray pattern indicates that the calcination was not completed and

required a higher temperature and/or longer time. Fig. 4 (b) shows well-developed crystallinity of the mixed oxide powder.

The specimens were sintered at several temperatures to investigate the densification characteristics. Fig. 5 (a) and (b) show the microstructure of fractured surfaces of a specimen sintered at 1100 °C and 1250 °C for 4 hrs. By comparing these microstructures, it was recognized that a lower sintering temperature can be employed in the freeze drying process. Well developed microstructures as compared in Fig. 5 (b) and Fig. 6 (b) represent the morphology of the sintered specimens prepared from the freeze dried and the mixed oxide powders, respectively. The freeze dried specimen shows small grain size and a narrow grain size distribution. On the other hand, this specimen shows larger shrinkage than the mixed oxide specimen. The shrinkage were 21% and 18%, respectively. The density increased when the sintering temperature was increased. However, a liquid phase was formed when the specimen was sintered for a prolonged time at temperature above 1250 °C. The densities of the specimens prepared at different sintering temperature are given in Table 2. The measured electrical properties and hysteresis loops are given in Fig. 7.

Table 2. The density of PLZT ceramics prepared by freeze drying method as a function of sintering temperature (g/cm<sup>3</sup>).

<u>Composition</u>	<u>1100°C</u>	<u>1150°C</u>	<u>1250°C</u>
7/70/30 (CP)	7.39	7.69	7.68
7/70/30 (MO)	7.59	7.62	7.64
8/65/35 (CP)	7.43	7.60	7.57
8/65/35 (MO)	-	7.62	-

### B. Vacuum Drying

Lead subacetate solution does not precipitate in oxalic acid. Therefore, it is required that the precipitant gel must be dried without filtering. As shown in Fig. 8, the powder was strongly agglomerated after drying. Table 3 shows the densities of PLZT ceramics prepared by the vacuum drying method.

Table 3. The density of PLZT ceramics prepared by vacuum drying method.

<u>Composition</u>	<u>Density (g/cm<sup>3</sup>)</u>
2/55/45	7.40
9/65/35	7.40
8.6/65/35	7.34
5.5/56/44	7.00
5.5/58/42	7.31

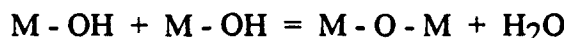
The measured electrical properties which are given in Fig. 9. show typical values reported in an earlier study. Vacuum drying after coprecipitation has advantages of easy processing and a high homogeneity. However, because of the strong agglomeration, it is hard to control the particle size and the distribution.

### C. Spray Pyrolysis

The powders produced by spray pyrolysis were found to be spherical. The size distribution of the powder ranges from about 3  $\mu\text{m}$  through 20  $\mu\text{m}$ , as shown in Fig. 8. An advantage of the spray pyrolysis technique is that the desired powder can be produced without calcination. In the hot zone of the furnace, the liquid droplet was readily decomposed. An important aspect of this process was to obtain a narrow distribution of the liquid droplet. It is also important to allow an adequate reaction time for completing the decomposition and subsequent calcination processes. In the present study, some of the liquid droplets hit the furnace wall before decomposition. Further study is in progress to examine these aspects of the spray pyrolysis technique.

### D. Hydrothermal Process

The hydrothermal process was originally applied to liquid solutions in order to grow crystallites from a liquid solution. However, the hydrothermal process is also applied to precipitating gels which contain metal hydroxide or oxyhydroxide phases. The principal purpose of the hydrothermal process is to transform the gels to metal oxide powders. The hydrothermal process consists of two steps. Firstly, a metal hydroxide is precipitated from the liquid precursor solution. The precipitated gel thus obtained is in the form of fine particles distributed in the liquid phase. Secondly, the metal hydroxide gel is transformed to the oxide by the following reaction.



In general, the applied temperature and pressure varied between 100°C and 300°C and 1 and 100 Mpa, respectively. The advantages of this process are as follows :

- A. Powder synthesis can be performed at a low temperature.
- B. The powder thus produced is very fine ( nano/micron scale ) with a narrow size distribution.
- C. The powder is chemically homogeneous.
- D. No additional calcination is required.

However, it is difficult to employ the hydrothermal process to a multicomponent system, such as the PLZT system, due to the different reaction conditions and different reaction affinities between the precursors. The concentration and structure of the precursor gel, reaction temperature, pressure and catalyst are considered to be the critical factors. In the present study for the hydrothermal synthesis of PLZT powder, efforts will be made to :

- A. synthesize  $TiO_2$  and  $ZrO_2$  powders. Also, the condition for synthesis of  $PbO$  and  $La_2O_3$  will be investigated.
- B. On the basis of (A), the synthesis of  $PbTiO_3$ ,  $PbZrO_3$  and PZT will be performed.
- C. Finally, lanthanum doping to PZT system will be studied.

The powder thus obtained will be characterized at different stages of processing. Research efforts will be focused on controlling the critical factors mentioned above.

#### 4. Summary

The non conventional processes for obtaining PLZT powders as examined in the present study show their individual characteristics. It was observed that careful handling was required for freeze drying process of coprecipitant gel. A longer processing time was required to obtain the desired products. The pH value should be kept to an appropriate range to prevent any changes during processing. An advantage of this process is that the powders thus prepared were fine and highly reactive. Vacuum drying process of precipitant gel was easy to handle so that a homogeneous powder can be obtained. However, it is difficult to avoid some degree of agglomeration which reduces the reactivity of the powder. The powder prepared by the spray pyrolysis process has good geometrical shapes. The critical point of this process is how to make fine liquid droplets and to bring them to the reaction zone without any appreciable physical changes. In the hydrothermal process, oxide powders can be produced directly at a low temperature. Under the hydrothermal conditions, there are several problems associated with the reaction of the precursors under a given temperature and pressure which prevent the formation of the PLZT powders. These problems will be solved by optimizing the processing conditions.

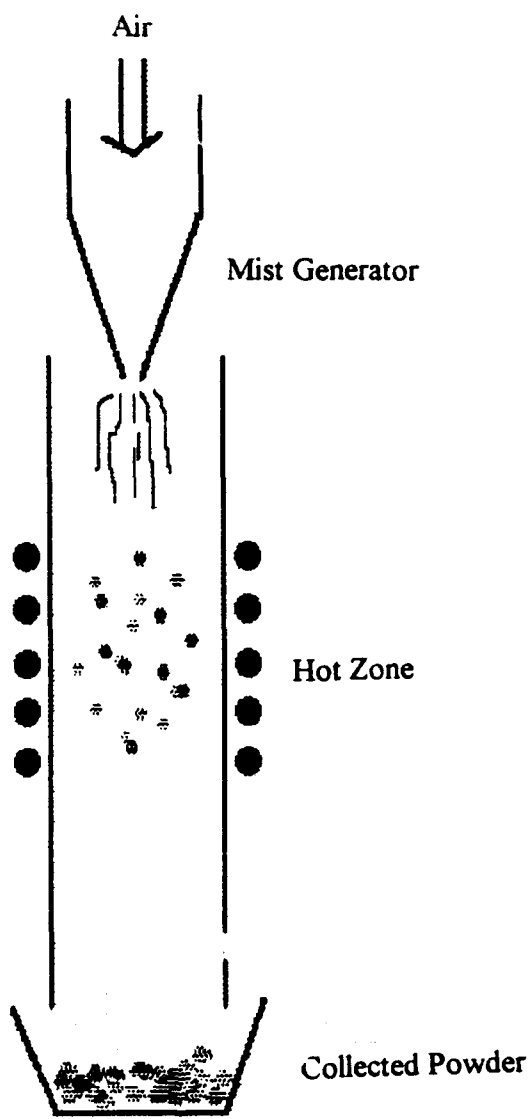


Fig. 1 Apparatus for spray pyrolysis.

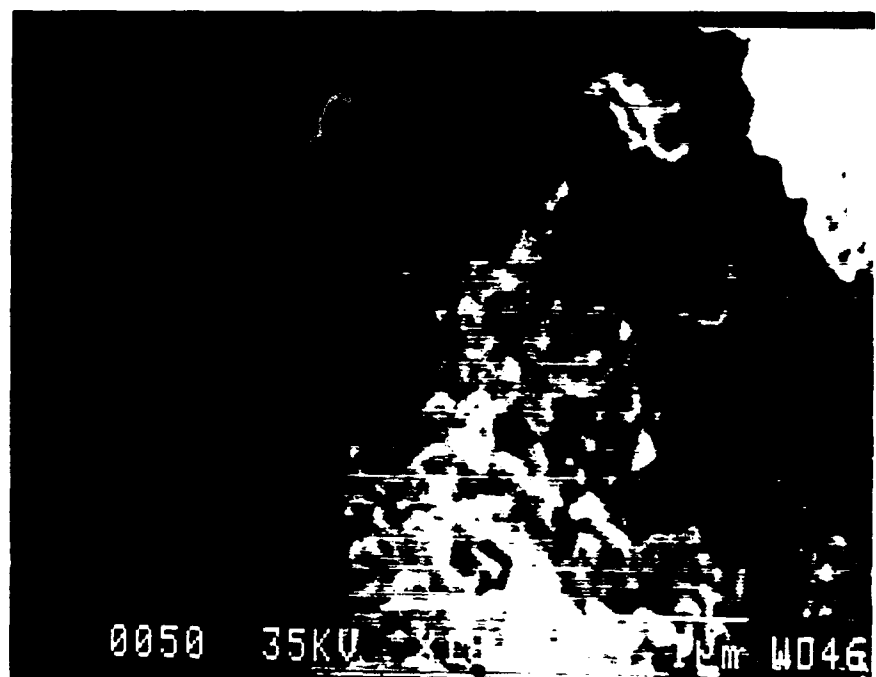
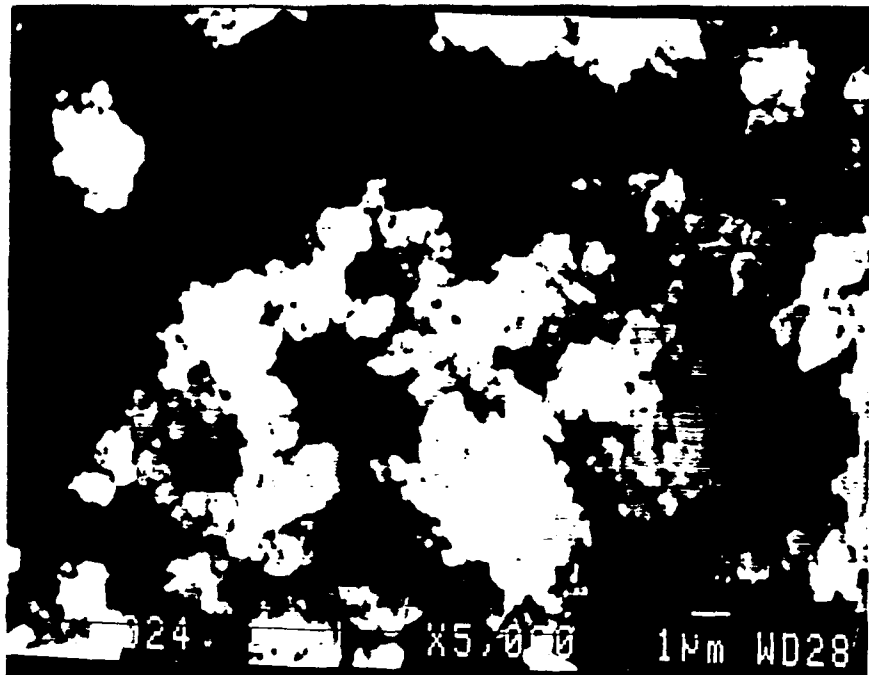
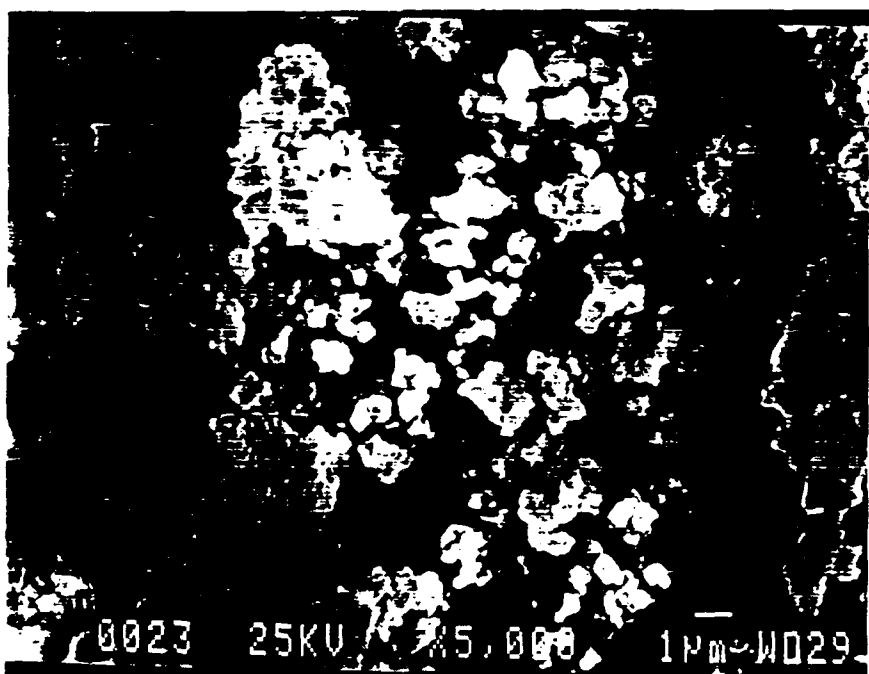


Fig. 2 Scanning electron micrograph of freeze dried powder (x18,000 ).



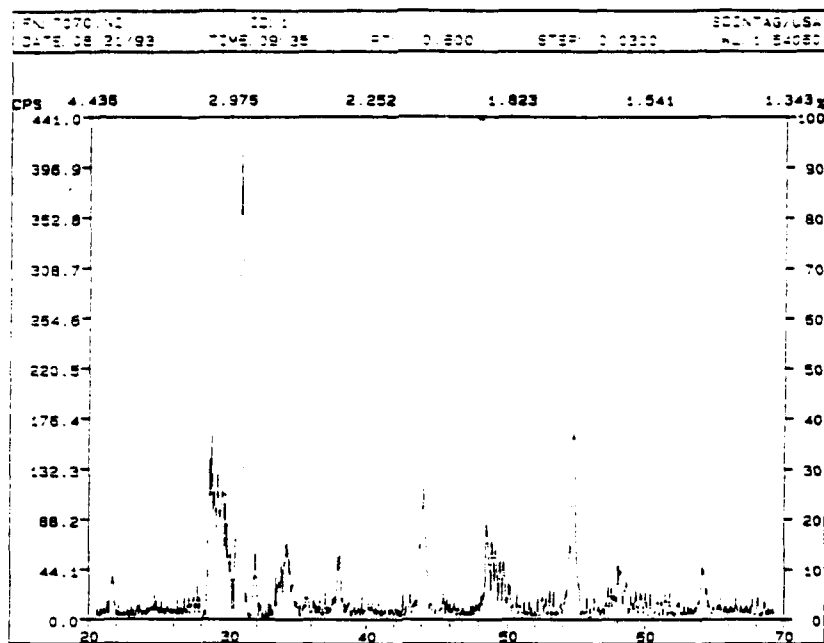
( a )



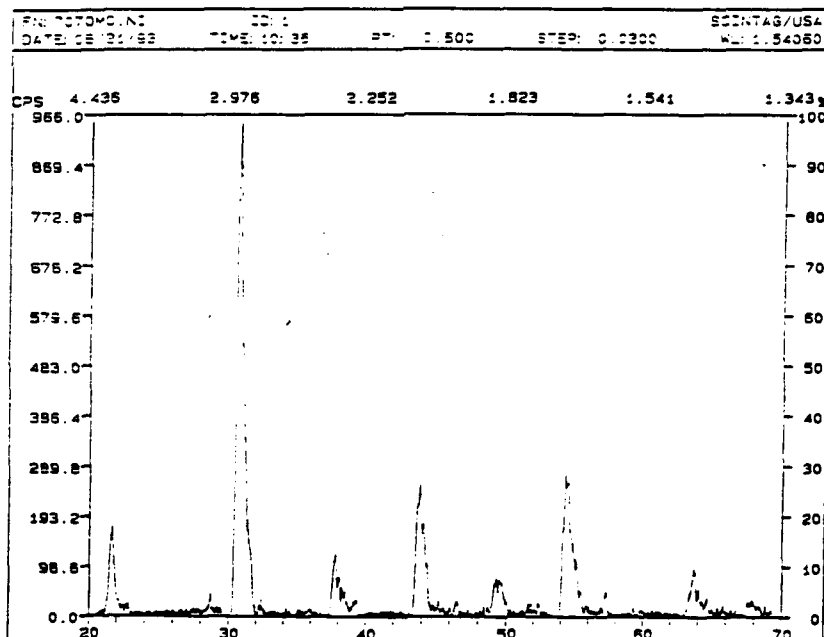
( b )

Fig. 3 Scanning Electron Micrograph of PLZT powder.

- (a) Freeze dried powder after calcination at  $550\text{ }^{\circ}\text{C}$ , 4hrs
- (b) Mixed oxide powder after calcination at  $900\text{ }^{\circ}\text{C}$ , 2hrs



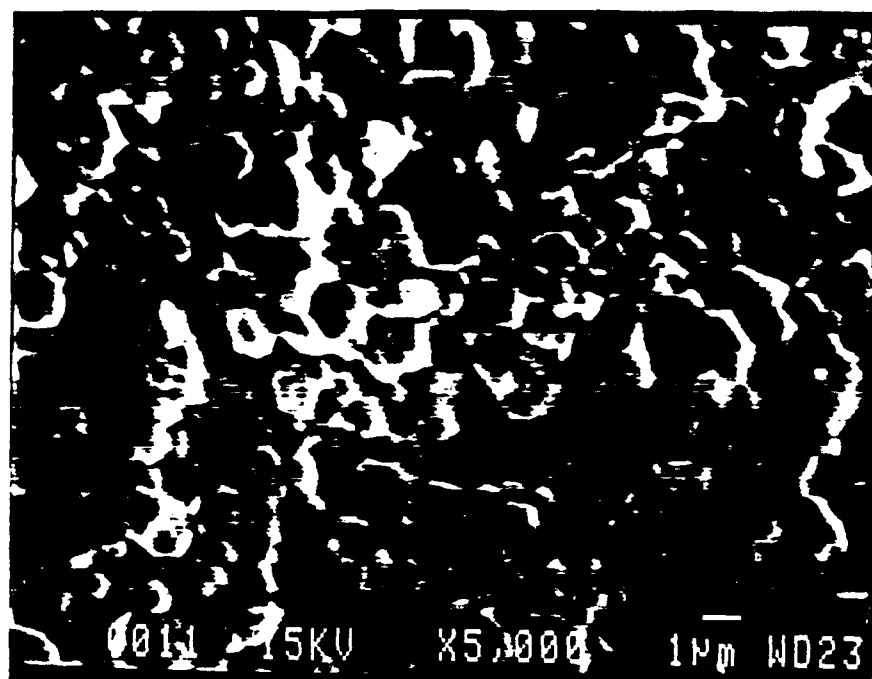
(a)



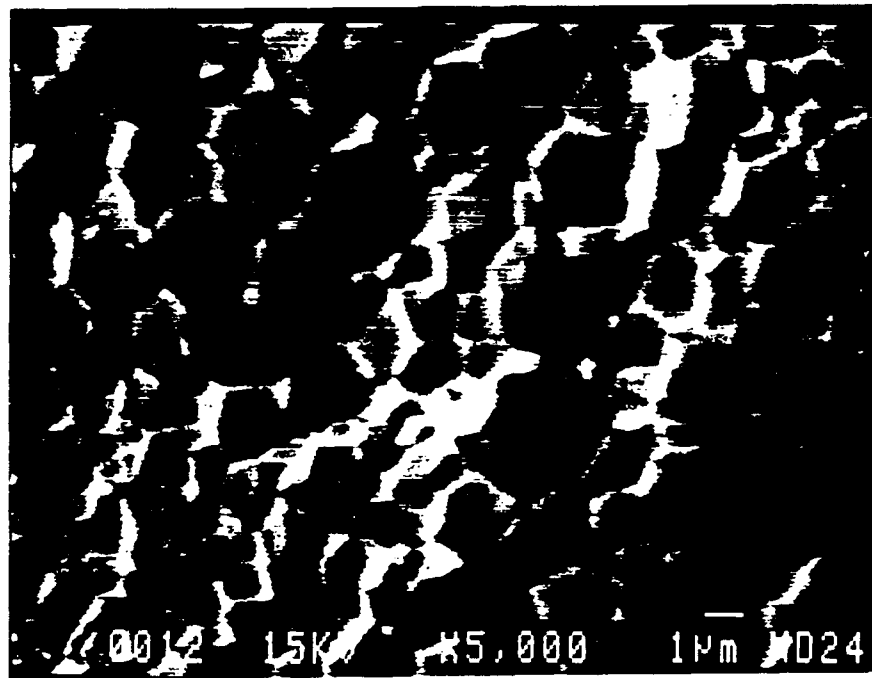
(b)

Fig. 4 X - ray diffraction pattern of PLZT powder.

- (a) Freeze dried powder after calcination at 550 °C, 4hrs
- (b) Mixed oxide powder after calcination at 900 °C, 2hrs

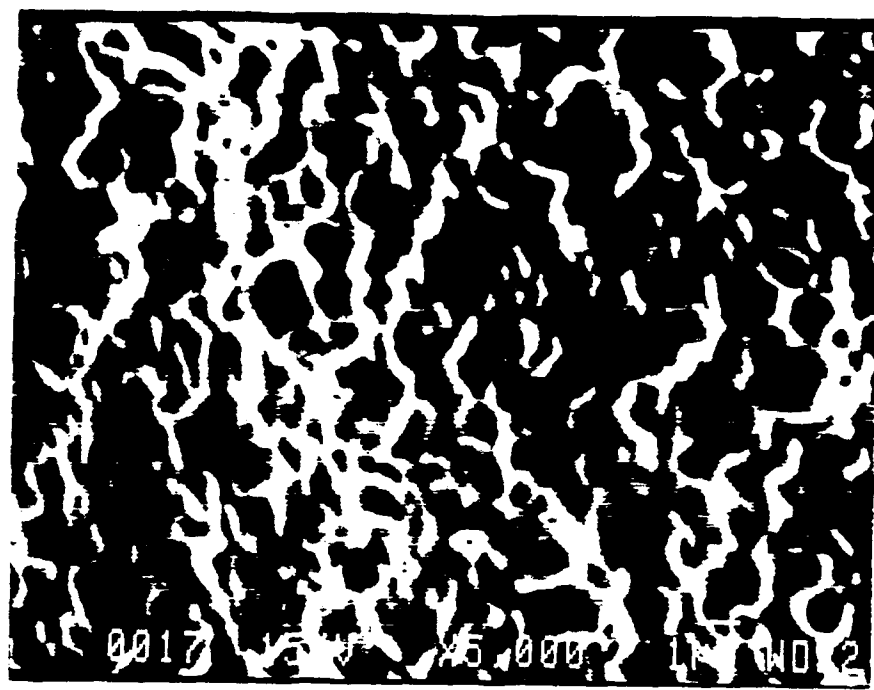


( a )

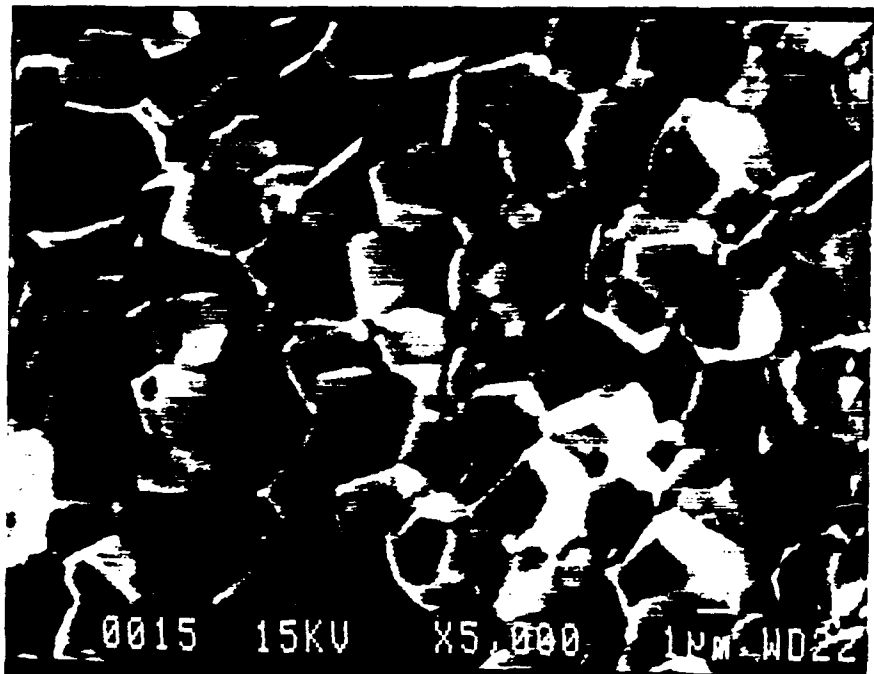


( b )

Fig. 5 Fracture surface of PLZT ceramics prepared by freeze drying method.  
(a) sintered at 1100 °C, 4hrs  
(b) sintered at 1250 °C, 4hrs



( a )



( b )

Fig. 6 Fracture surface of PLZT ceramics prepared by mixed oxide method  
(a) sintered at  $1100^{\circ}\text{C}$ , 4hrs  
(b) sintered at  $1250^{\circ}\text{C}$ , 4hrs

1100 °C, 4 hours

<u>Composition</u>	<u>K</u>	<u>tan d</u>	<u>E<sub>c</sub> ( kv/cm )</u>	<u>P<sub>R</sub> ( <math>\mu</math>C/cm<sup>2</sup> )</u>
7/70/30 (CP)	1147	0.036	7.2	29
7/70/30 (MO)	4179	0.030	4.6	23
8/65/35 (CP)	3056	0.039	7.6	6
8/65/35 (MO)	2972	0.027	5.3	11

1250 °C, 4 hours

<u>Composition</u>	<u>K</u>	<u>tan d</u>	<u>E<sub>c</sub> ( kv/cm )</u>	<u>P<sub>R</sub> ( <math>\mu</math>C/cm<sup>2</sup> )</u>
7/70/30 (CP)	1361	0.074	6.1	28
7/70/30 (MO)	4446	0.048	4.6	28
8/65/35 (CP)	4442	0.059	-	-
8/65/35 (MO)	2311	0.076	4.6	28

1100 °C, 4 hours

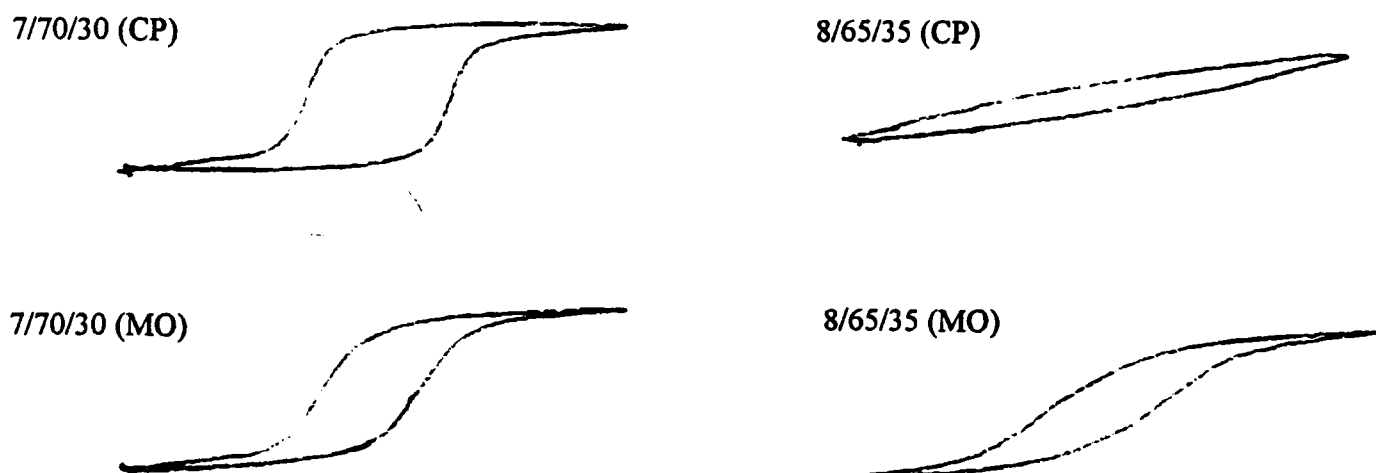


Fig. 7 Electrical properties and hysteresis loops of PLZT ceramics produced by freeze drying process.

1250 °C, 4 hours

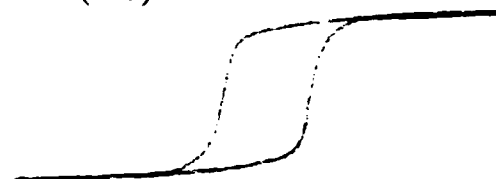
7/70/30 (CP)



8/65/35 (CP)



7/70/30 (MO)



8/65/35 (MO)

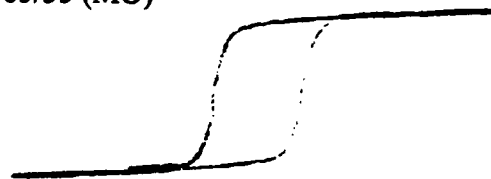


Fig. 7 (continued )

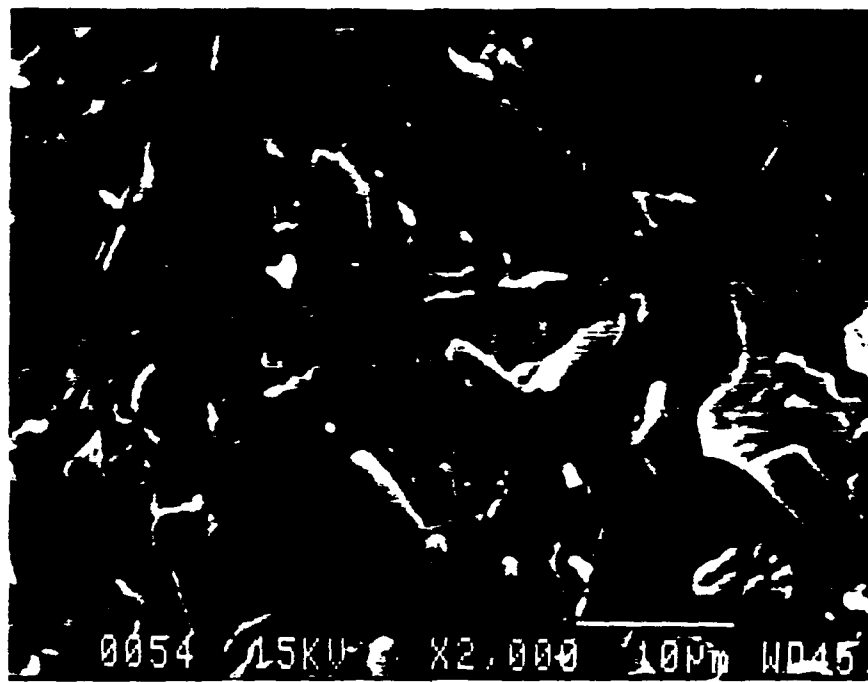


Fig. 8 Scanning electron micrograph of vacuum dried powder.

<u>Composition</u>	<u>K</u>	<u>tan d</u>	<u>E<sub>c</sub> ( kv/cm )</u>	<u>P<sub>R</sub> ( <math>\mu</math>C/cm<sup>2</sup> )</u>
2/55/45	958	0.037	6.7	41.2
9/65/35	5686	.200	1.2	7.4
8.6/65/35	6810	0.062	2.9	17.7
5.5/56/44	2726	0.020	10.2	27.7
5.5/58/42	3533	0.023	9.1	32.1

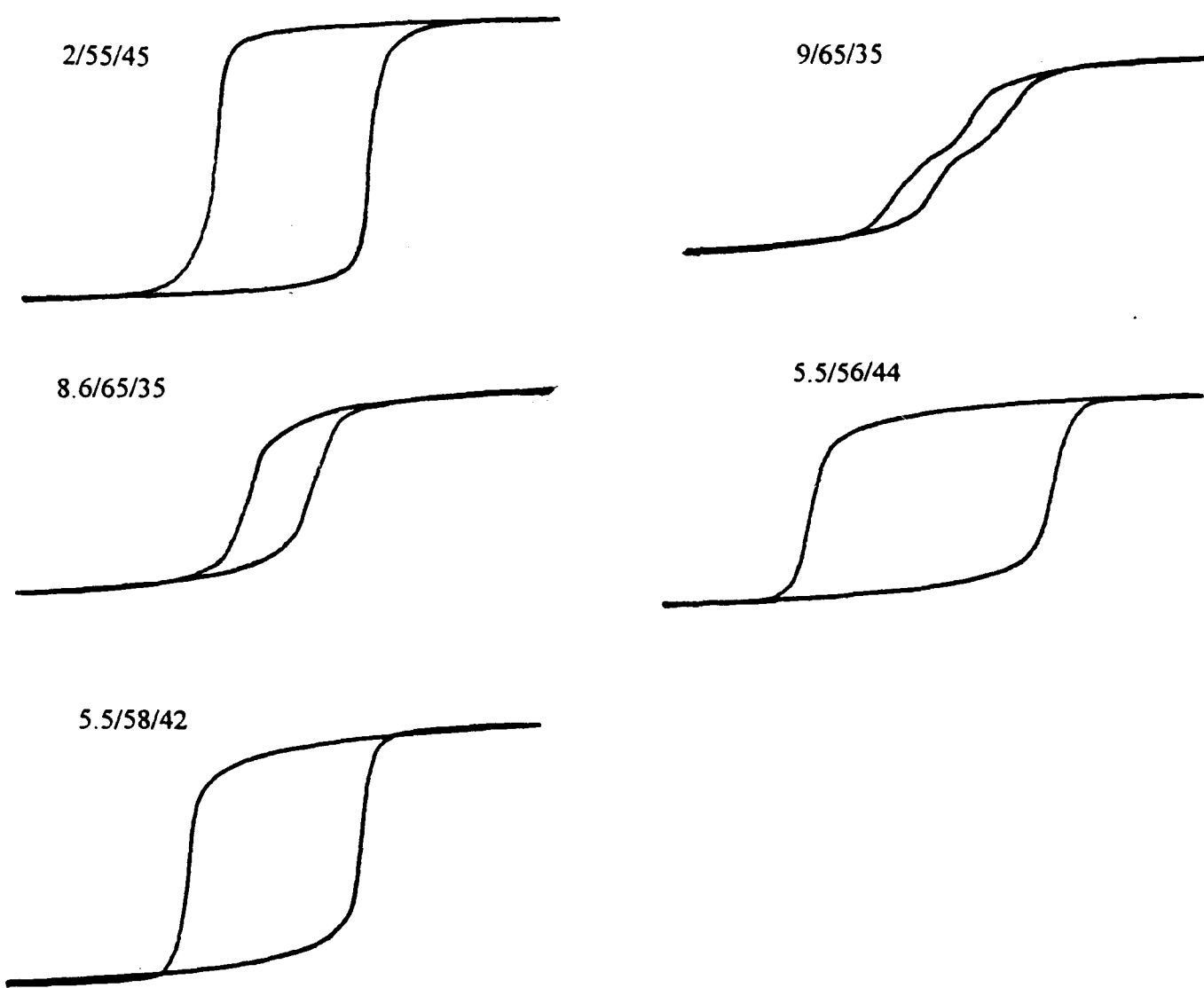


Fig. 9 Electrical properties and hysteresis loops PLZT ceramics produced by vacuum drying process.

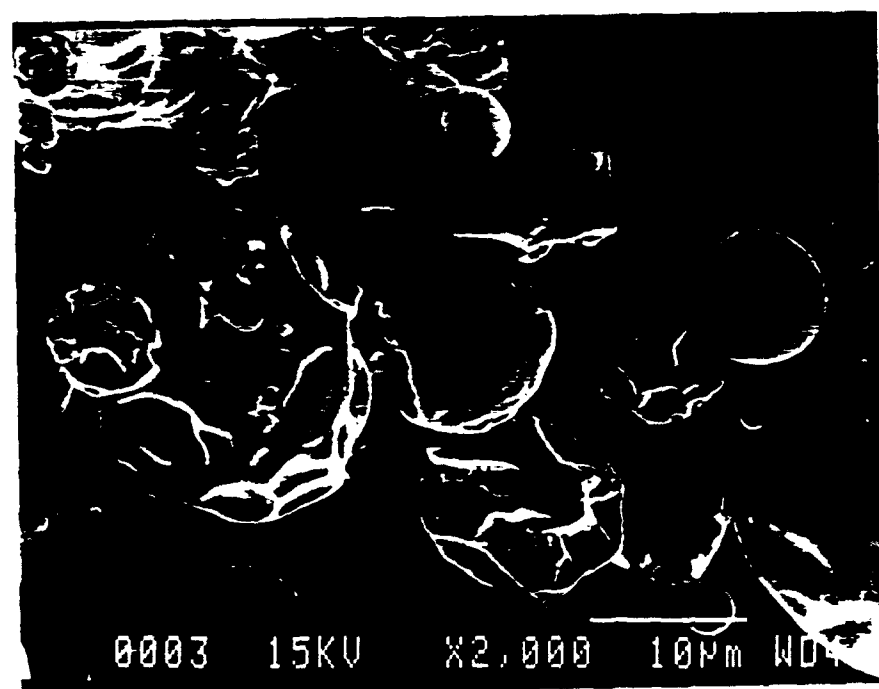


Fig. 10 Scanning electron micrograph of PLZT powder prepared by spray pyrolysis.

# **INTELLIGENT PROCESSING OF FERROELECTRIC THIN FILMS**

## **Annual Report**

### **Part III.**

#### **Processing and Characterization of PMN-Based Materials**

Submitted by: Joyti Guha  
Guang Li  
Gene Haertling

**The Gilbert C. Robinson Department of Ceramic Engineering  
Clemson University**

## INTRODUCTION

Perovskite solid solutions based on Pb-based relaxor compounds exhibit excellent dielectric and piezoelectric properties and are of current interest as materials for electronic applications. Among the several known materials, the most widely studied is the perovskite compound  $\text{Pb}(\text{Mg}_{1/3}\text{Nb}_{2/3})\text{O}_3$  which exhibits a high dielectric constant and, consequently, has been used as materials for multilayer capacitors. In addition to the excellent dielectric properties,  $\text{Pb}(\text{Mg}_{1/3}\text{Nb}_{2/3})\text{O}_3$ -based solid solutions exhibit high strains with minimal hysteresis. However, the induced strain exhibited by these materials depends, to a large extent, on the composition and processing parameters. As often is the case, an unwanted pyrochlore phase frequently appears during processing of the compound and its solid solutions with other oxides. The presence of this pyrochlore phase in the end product, even in minute quantities, has been associated with inferior dielectric and piezoelectric properties. Additionally, the grain size of the processed materials affect the induced strain as well as the hysteresis, probably due to the low permittivity pyrochlore phase.

One of the major limitations in the utilization of these solid solutions for various electronic applications is the lack of a simple and reproducible fabrication technique by which a single-phase material can be readily obtained. Numerous studies reported in the literature have revealed that the ferroelectric perovskite phase is extremely difficult to obtain without the formation of an undesirable pyrochlore phase. In the case of the solid solutions based on the  $\text{Pb}(\text{Mg}_{1/3}\text{Nb}_{2/3})\text{O}_3$ - $\text{PbTiO}_3$  system, several modifications of the processing technique have been proposed to obtain a single-phase perovskite material. Among these, the use of prefabricated  $\text{MgNb}_2\text{O}_6$  or  $\text{Pb}_3\text{Nb}_2\text{O}_8$  as the starting materials, additions of excess  $\text{MgO}$  and/or  $\text{PbO}$  to the stoichiometric solid solution composition, and repeated calcinations for prolonged periods at elevated temperatures have been found to be useful for the elimination of the pyrochlore phase. However, additions of excess  $\text{MgO}$  or  $\text{PbO}$ , and variations of the fabrication technique have some adverse effects on the sintering behavior and related microstructure development. This, in turn,

affects the relevant properties of the final product. Furthermore, the stoichiometric  $\text{Pb}(\text{Mg}_{1/3}\text{Nb}_{2/3})\text{O}_3$ - $\text{PbTiO}_3$  solid solution is difficult to sinter to high densities at temperatures below 1250°C at which an excessive PbO loss due to volatilization from the specimens leads to inferior properties. However, a slight compositional variation from the stoichiometry, particularly, a shift towards the PbO-rich region allows the formation of a low-melting liquid phase which greatly enhances the sintering process and promotes grain growth. Additionally, minor additions of several oxides to the solid solutions promote liquid formation at a considerably low temperature, thereby allowing rapid densification to occur during sintering. Unfortunately, a lowering of the sintering temperature through the addition of a low-melting liquid phase does not necessarily ensure superior properties of the resulting ceramics. Nevertheless, development of an appropriate composition in a given system with required phase content and then sintering the composition to the desired property specifications seem to be the most logical step for obtaining well-characterized materials with improved properties.

In the present investigation, attention was focused on the processing of high permittivity solid solution compositions in the system  $\text{Pb}(\text{Mg}_{1/3}\text{Nb}_{2/3})\text{O}_3$ - $\text{PbTiO}_3$  with suitable additions of secondary phases to shift the Curie temperatures to near room temperature. The primary objective of this study was to develop phase-pure perovskite solid solution compositions through a basic understanding of the reaction chemistry involved in this relaxor system. The phase-pure compositions, once obtained, can be subsequently used for obtaining thin films for dielectric, piezoelectric and electrooptic measurements. It is envisaged that the various data emerged from this study will serve as guidelines for optimizing the processing conditions and to obtain a wide variety of well-characterized materials exhibiting superior electronic properties.

## **BACKGROUND**

### **(a) Relaxor Characteristics**

Lead oxide-based ternary compounds, hereafter referred to as relaxors, are a class of ferroelectric materials originally synthesized by a group of Russian workers.<sup>1-6</sup> These

compounds have been known to possess a perovskite crystal structure and exhibit excellent dielectric and piezoelectric properties and, therefore, are of considerable interest as materials for various electronic devices. Lead-based relaxors have the general formula  $A(B'B'')O_3$ , where  $B'$  is typically a low valence cation, e.g.  $Mg^{+2}$ ,  $Zn^{+2}$ ,  $Ni^{+2}$ ,  $Co^{+3}$ ,  $Fe^{+3}$ ,  $Sc^{+3}$  etc., and  $B''$  a penta- or hexavalent cation, e.g.  $Nb^{5+}$ ,  $Ta^{5+}$ ,  $W^{6+}$  etc. The temperature characteristics of the permittivity peaks of the relaxors show a greater dependency on frequency than many normal ferroelectric materials. Furthermore, these materials exhibit a broadening of the permittivity peak, often referred to as a ferroelectric diffuse phase transition, which is used to distinguish them from the other classes of ferroelectric materials. The reason for the diffuse phase transition in relaxors is not yet clearly understood. However, it is believed that a certain concentration fluctuation develops in these materials due mainly to the absence of ordering in the sublattice of the ions occupying the octahedral positions in the perovskite structure. The absence of ordering allows the formation of very finely divided domains which, under the influence of an applied electric field, join together into larger ones and allows numerous microregions to develop in the crystals. The phase transitions caused by the spontaneous polarization in the different microregions become independent of one another which gives rise to different Curie points. The distribution of Curie points of the individual microregions in a crystal allows the phase transition to spread over a broad temperature range which causes the broadening of the permittivity peak in these materials.

It is known that the degree of ordering in several relaxor compounds increases appreciably by suitable annealing treatment, thereby allowing the permittivity peak to sharpen with a slight reduction of the permittivity values.<sup>7-10</sup> Nevertheless, for the majority of the relaxors, ordering can not be easily accomplished by thermal annealing alone. For these compounds, varying degrees of ordering are achieved by forming solid solutions with isostructural substitutions.<sup>11,12</sup> A list of known relaxor compounds with physical and dielectric properties are given in Table I.

**Table I. Physical and Dielectric Properties of Known Relaxor Compounds.**

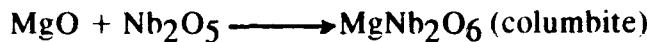
Compound	Lattice Const.(A)	Density (gm/cm <sup>3</sup> )	Curie point (°C)	Dielectric Const.( $\epsilon$ )
<b><math>A^{2+}(B_{1/3}^{'}B_{2/3}^{\prime\prime})O_3</math></b>				
Pb(Mg <sub>1/3</sub> Nb <sub>2/3</sub> )O <sub>3</sub>	4.04	8.18	-15	15,000
Pb(Ni <sub>1/3</sub> Nb <sub>2/3</sub> )O <sub>3</sub>	4.02	8.57	-120	4,000
Pb(Co <sub>1/3</sub> Nb <sub>2/3</sub> )O <sub>3</sub>	4.04	8.48	-70	6,000
Pb(Zn <sub>1/3</sub> Nb <sub>2/3</sub> )O <sub>3</sub>	4.04	8.43	140	2,000
<b><math>A^{2+}(B_{1/2}^{'}B_{1/2}^{\prime\prime})O_3</math></b>				
Pb(Fe <sub>1/2</sub> Nb <sub>1/2</sub> )O <sub>3</sub>	4.01	8.54	114	12,000
Pb(Sc <sub>1/2</sub> Nb <sub>1/2</sub> )O <sub>3</sub>	4.07	7.98	90	2,400
<b><math>A^{2+}(B_{2/3}^{'}B_{1/3}^{\prime\prime})O_3</math></b>				
Pb(Fe <sub>2/3</sub> W <sub>1/3</sub> )O <sub>3</sub>	3.97	9.38	-95	9,000

**(b) Pb(Mg<sub>1/3</sub>Nb<sub>2/3</sub>)O<sub>3</sub>-PbTiO<sub>3</sub> Based Solid Solutions**

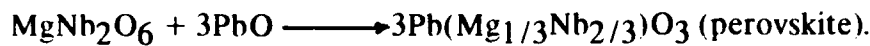
The dielectric and piezoelectric properties of perovskite solid solutions based on the compound Pb(Mg<sub>1/3</sub>Nb<sub>2/3</sub>)O<sub>3</sub> have been investigated by several workers<sup>13-18</sup>. In addition to many published studies, the patent literature in this system is extensive. In the studies reported so far, it has been recognized that the processes which reduce the volatility of PbO, such as low sintering temperature and short sintering time, closed crucible firing etc. lead to the formation of an increased amount of the desirable perovskite phase. Conversely, processes that cause an excessive PbO loss during firing increase the amount of the undesirable pyrochlore phase which is detrimental to the dielectric and piezoelectric properties of the ceramics.

In the synthesis of the perovskite compound  $Pb(Mg_{1/3}Nb_{2/3})O_3$  by the conventional solid state reaction techniques, a number of lead niobate-based pyrochlore phases are formed which coexist with the perovskite phase<sup>19-21</sup>. These pyrochlore phases, once formed, remain stable at high temperatures and cause deterioration of the dielectric properties. However, subsequent studies<sup>22-24</sup> have revealed that the pyrochlore phase is a ternary lead magnesium niobate which apparently forms at the initial stages of the reaction process and then reacts with an excess of PbO and MgO to yield the perovskite phase. Several workers<sup>21,25</sup> have suggested certain modifications of the processing techniques for the elimination of the pyrochlore phase. In one of these processing techniques,<sup>21</sup> MgO was first reacted with  $Nb_2O_5$  to form the columbite  $MgNb_2O_6$ . The  $MgNb_2O_5$  thus formed was further reacted with an appropriate amount of PbO to yield the perovskite  $Pb(Mg_{1/3}Nb_{2/3})O_3$ . The reaction sequences reported in this study are given as follows:

1000°C



700°C

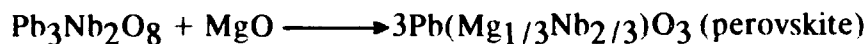


An alternative method<sup>25</sup> for obtaining perovskite  $Pb(Mg_{1/3}Nb_{2/3})O_3$  in which PbO was first reacted with an appropriate amount of  $Nb_2O_5$  to form  $Pb_3Nb_2O_8$  which was then reacted with the required amount of MgO to yield  $Pb(Mg_{1/3}Nb_{2/3})O_3$ . In this method, the reaction sequences have been described as follows:

800°C



1000°C



In both the methods described above, the addition of an excess MgO to the stoichiometric  $Pb(Mg_{1/3}Nb_{2/3})O_3$  composition was found to cause a significant improvement of the reaction process with the formation of a near single-phase cubic perovskite end product.

The sintering characteristics of  $\text{Pb}(\text{Mg}_{1/3}\text{Nb}_{2/3})\text{O}_3$ - $\text{PbTiO}_3$  based solid solutions with additions of various sintering aids have been examined by several workers<sup>26-28</sup>. In these studies, it has been observed that a small addition of excess  $\text{PbO}$  to the solid solution enhances the sintering process via the formation of a liquid phase. However, too high a sintering temperature, especially, above  $1290^\circ\text{C}$  leads to the development of inhomogeneous microstructure consisting of a  $\text{PbO}$ -rich liquid near the surface with a porous interior<sup>29</sup>. In another study<sup>30</sup> which was primarily concerned with the reaction chemistry in the system  $\text{PbO}-\text{MgO}-\text{Nb}_2\text{O}_5-\text{TiO}_2$ , it has been reported that a ternary pyrochlore phase with a chemical composition  $\text{Pb}_{1.71}(\text{Mg}_{.29}\text{Nb}_{1.71})\text{O}_{6.23}$  is formed at a low temperature. The perovskite compound  $\text{Pb}(\text{Mg}_{1/3}\text{Nb}_{2/3})\text{O}_3$  is formed when the pyrochlore phase reacts with  $\text{MgO}$  and  $\text{PbO}$ . The pyrochlore phase, once formed, remains stable with the perovskite  $\text{Pb}(\text{Mg}_{1/3}\text{Nb}_{2/3})\text{O}_3$  at elevated temperatures. The perovskite  $\text{Pb}(\text{Mg}_{1/3}\text{Nb}_{2/3})\text{O}_3$  is compatible with both  $\text{PbO}$  and  $\text{MgO}$ , and forms binary eutectics with one other. On the other hand, the compound  $\text{Pb}(\text{Mg}_{1/3}\text{Nb}_{2/3})\text{O}_3$  is not compatible with  $\text{Nb}_2\text{O}_5$ . These two phases react with one another at temperature below  $1000^\circ\text{C}$  to form the pyrochlore compound.

## EXPERIMENTAL

The experimental method used in this study was primarily concerned with reacting presynthesized precursors at temperatures below the melting point of  $\text{PbO}$  ( $890^\circ\text{C}$ ). This technique was combined with a number of analytical methods capable of providing chemical, structural and microstructural details critical to the property evaluation.

### (i) Reaction Chemistry and Phase Formation :

Starting materials in the form of high-purity powders having controlled particle size, surface area and impurity content were used. Appropriate proportions of the powdered materials were mixed and pressed to pellets using a polyvinyl alcohol-water solution as a binder. The pressed pellets were heat-treated at temperatures below the melting point of  $\text{PbO}$  to prevent an excessive volatilization of  $\text{PbO}$ . For compositions requiring higher reaction temperatures, weight-loss experiments were performed and necessary

adjustment were made to the final compositions. In general, the PbO losses were kept to less than 0.5 % by controlling the firing cycle and loading the sample in a tightly-fitted crucible containing coarse-grained PbZrO<sub>3</sub> powder. The powdered mixtures were pressed into pellets and calcined in an alumina crucible at 800°C for various periods of time. On cooling to room temperature, the pellets were examined for weight-loss and then ground to fine powders which were then subjected to x-ray diffraction analysis (XRD) to identify the crystalline phases present.

**(ii) Phase Identification :**

The crystalline phases present in the heat-treated specimens were identified by the conventional x-ray powder diffraction technique. A Ni-filtered CuK<sub>α</sub> radiation was employed for all specimens. The XRD patterns thus obtained were compared with those listed in the JCPDS Card Index. For microstructural analysis, specimens from the sintered pellets were prepared by standard techniques which include mounting of the specimens followed by grinding and polishing to obtain surfaces ready for etching with a diluted HCl-water solution containing a few drops of HF. The polished and etched sections were examined by an optical microscope using reflected-light. Fracture surfaces of the sintered samples were analyzed by a scanning electron microscope (SEM) using both secondary emission and backscatter modes. Semiquantitative phase analysis of the selected samples were performed using an energy dispersive x-ray analyzer (EDX) in conjunction with the SEM. The amount of pyrochlore phase formed was determined from the characteristic (222) reflection of the final products.

**(iii) Sintering Characteristics :**

The initial efforts was to determine the parametric relationships among final density, shrinkage and microstructural uniformity as functions of several variables such as green density, time-temperature conditions and the type of atmosphere employed during sintering of the samples in addition to the heat-treatment in air. Once the optimum conditions required for densification of the base compositions were evolved, sintering of various compositions were performed under controlled conditions. The bulk densities of the sintered samples were determined by the liquid displacement method using xylene as

the medium. The grain size was measured from the polished section micrographs using representative areas with uniform grain size distribution.

**(iv) Property Measurements :**

Specimens in the form of discs were coated with an Ni-based electrode material. It should be noted that Ag and Ag-Pd based materials which are commonly used as electrodes are known to interact with PbO-based materials, and hence, the choice of the Ni-based electrode material. Prior to electroding, the parallel faces of the discs were ground and cleaned, and their geometric dimensions (diameter and thickness) were determined. The values for capacitance (C) and dissipation factor ( $\tan\delta$ ) were measured by an automatic capacitance bridge at 1 kHz over the temperature range of -10 to 100°C. At least four specimens from each composition were used for these measurements, the final values used being the average of three consistent readings. The resistivities were measured as a function of temperature by a picoampmeter using an appropriate test voltage applied across the specimens. The P-E hysteresis loops of the sintered specimens were measured at room temperature with a Sawyer-Tower circuit at 1 kHz. The electric-field induced strain was studied by a Magneto-resistive detector under an electric field at 0.05 Hz.

## **Results and Discussion**

In examining the key issues relevant to the development of well-characterized single-phase compositions in the solid solution system  $Pb(Mg_{1/3}Nb_{2/3})O_3$ - $PbTiO_3$ , the first and foremost concern was to obtain an understanding of the effect of compositional variations on the phase formation and to prepare a phase-pure perovskite composition. The processing of the solid solution composition, once successfully completed, was then extended to the determination of the relevant properties.

**(a) Processing and Characterization of  $Pb(Mg_{1/3}Nb_{2/3})O_3$ -based Solid Solutions**

In the solid solution system  $Pb(Mg_{1/3}Nb_{2/3})O_3$  -  $PbTiO_3$ , it is known that additions of  $PbTiO_3$  to the perovskite  $Pb(Mg_{1/3}Nb_{2/3})O_3$  allow a shift of the Curie point from -150°C to higher temperatures. Apparently, the B-site of the perovskite solid solutions

$\text{Pb}[(\text{Mg}_{1/3}\text{Nb}_{2/3})_{1-x}\text{Ti}_x]\text{O}_3$  is occupied by  $\text{Ti}^{4+}$ -ion, thereby causing a shift of the Curie point to higher temperatures. The shift of the Curie temperature of  $\text{Pb}(\text{Mg}_{1/3}\text{Nb}_{2/3})\text{O}_3$  as a function of  $\text{PbTiO}_3$  content is shown in Fig. 1. Seemingly, the permittivity maximum of the solid solutions also increases with increasing additions of  $\text{PbTiO}_3$  until the morphotropic phase boundary which occurs at 30 mol % Ti is reached.

In the present investigation, solid solution compositions represented by the general formula  $\text{Pb}[(\text{Mg}_{1/3}\text{Nb}_{2/3})_{1-x}\text{Ti}_x]\text{O}_3$ , where  $x$  varies between 0.06 and 0.12 were prepared. In this particular solid solution series, the  $\text{Pb}^{2+}$ -site was partially substituted by  $\text{Ba}^{2+}$  with a view to shift the Curie point further to lower temperatures. This was accomplished by the solid state reaction between appropriate proportions of  $\text{PbO}$ ,  $\text{BaCO}_3$ , prefabricated  $\text{MgNb}_2\text{O}_6$  and  $\text{PbTiO}_3$ . The shift of the Curie temperatures of various solid solutions effected by means of  $\text{Ba}^{2+}$  substitution are shown in Fig. 2. As can be seen, the solid solution of a composition  $[\text{Pb}_{.99}\text{Ba}_{.01}][(\text{Mg}_{1/3}\text{Nb}_{2/3})_{.9}\text{Ti}_{.1}]\text{O}_3$  has a Curie temperature between  $26^\circ$  and  $28^\circ\text{C}$ . The x-ray diffraction pattern of this mixture prepared at  $800^\circ\text{C}$  is shown in Fig. 3 which revealed that a near single-phase perovskite solid solution was formed at this reaction temperature. However, when the same composition was fired at  $850^\circ\text{C}$  for 3 h, a small amount of the unwanted pyrochlore phase was formed as can be seen in the XRD pattern shown in Fig. 4. This was probably due to a slight  $\text{PbO}$ -loss from the specimen which caused a shift of the composition from its stoichiometry to a phase-field area within which the pyrochlore phase coexists with the perovskite phase.

#### **(b) Property Evaluation of the Solid Solution :**

The phase-pure  $[\text{Pb}_{.99}\text{Ba}_{.01}][(\text{Mg}_{1/3}\text{Nb}_{2/3})_{.9}\text{Ti}_{.1}]\text{O}_3$  solid solution composition was sintered to a high density on firing at  $1250^\circ\text{C}$  in air. As observed in this study, a final density near 90 % of the theoretical density was achieved by sintering the perovskite solid solution without the addition of any sintering aid. However, in presence of an excess  $\text{MgO}$ , the density value increased significantly. Thus, an addition of 1 wt % excess  $\text{MgO}$ , allowed the density to increase from 90 % to near 95 % of the theoretical density value. The SEM microstructure of the sintered specimens revealed a homogeneous

grain morphology with very little porosity present. Seemingly, a few pores present in the specimens were located predominantly at the grain boundaries. The overall grain size of the sintered specimen as observed by SEM was found to vary within 5 to 12  $\mu$ m.

The temperature characteristics of the dielectric constant of the perovskite solid solution  $[Pb_{0.99}Ba_{0.01}][(Mg_{1/3}Nb_{2/3})_{0.9}Ti_{1.1}]O_3$  at 1 kHz are shown in Fig. 5. As evident from this figure, the main feature of the dielectric properties of the solid solution is its broad permittivity maximum which occurred near 26°C. This is typical of the relaxor ferroelectric materials which exhibit a diffuse phase transition causing the permittivity peak to broaden at the Curie temperature. The dissipation factors, not shown herein, varied between 2 to 4 % above the Curie temperature. The resistivity value of the specimen at room temperature was found to be about  $10^{11} \Omega\text{-cm}$ .

The hysteresis loop exhibited by the perovskite solid solution at 25°C is shown in Fig. 6. The characteristic nature of the hysteresis loop was due mainly to a shift of the Curie point to near room temperature. As described earlier, this was achieved through the A-site substitution of the perovskite lattice of the  $Pb[(Mg_{1/3}Nb_{2/3})_{1-x}Ti_x]O_3$  solid solution. The electrostrictive properties of the solid solution obtained at 25°C is shown in Fig. 7. This is typical of a relaxor material which exhibits a diffuse phase transition at the Curie temperature. The electrostrictive co-efficient,  $Q_{12}$  as determined from the data depicted in Fig. 7 is  $8 \times 10^{-4} C^2/m^4$ . It should be noted that the data on hysteresis and electrostriction as reported at this time are only preliminary. Further studies are currently in progress to evaluate these properties by characterizing the solid solutions in terms of the nature and distribution of the additive oxides, namely, excess MgO and PbO which were used as sintering aids. Furthermore, the effect of the pyrochlore phase on the dielectric and electrostrictive properties of the  $Pb(Mg_{1/3}Nb_{2/3})O_3$ -based relaxor materials will be investigated.

## SUMMARY

Perovskite solid solutions based on the compounds  $Pb(Mg_{1/3}Nb_{2/3})O_3$  and  $PbTiO_3$  are known to exhibit excellent dielectric and piezoelectric properties and are of current

interest as materials for electronic applications. In this study, phase-pure solid solutions with a general composition  $Pb[(Mg_{1/3}Nb_{2/3})_{1-x}Ti_x]O_3$  were prepared by the solid state reaction technique at a temperature below 850°C in air. The A-site ( $Pb^{2+}$ ) of the perovskite solid solution lattice was partially substituted by an alkaline-earth cation ( $Ba^{2+}$ ) to shift the Curie point to near room temperature. The phase-pure materials thus obtained were further doped with 1 wt % of excess MgO with a view to achieve a high sintered density. The dielectric constant of the material was over 22,000 at a Curie temperature of 26°C with a  $\tan\delta$  loss of less than 4 %. Some preliminary data on the hysteresis characteristics and electrostrictive co-efficient of the solid solution were also presented. It is envisaged that the various data obtained in this study can be used as guidelines for the optimization of the processing parameters and for obtaining ferroelectric thin films for dielectric, piezoelectric and electrooptic applications.

## REFERENCES

1. G.A. Smolenski and A.I. Agranovskaya, Sov. Phys.-Tech. Phys. (English Transl.) 3 [7] 1380 (1958).
2. G.A. Smolenski, V.A. Isupov and A.I. Agranovskaya, Sov. Phys. Solid State (English Transl.) 1 [1] 150 (1959).
3. G.A. Smolenski, A.I. Agranovskaya and S.N. Popov, Sov. Phys. Solid State (English Transl.) 1 [1] 147 (1959).
4. G.A. Smolenski and A.I. Agranovskaya, Sov. Phys.-Solid State (English Transl.) 1 [10] 1429 (1960).
5. V.A. Bokov and I.E. Mylnikova, Sov. Phys.-Solid State (English Transl.) 3 [3] 613 (1961).
6. G.A. Smolenski, A.I. Agranovskaya, S.N. Popov and V.A. Isupov, Sov. Phys. Tech. Phys., 3 [10] 1981 (1958).
7. C.G.F. Stenger, F.L. Scholten and A.J. Burggraf, Solid State Comm., 32, 898 (1979).
8. N. Setter and L.E. Cross, J. Appl. Phys., 51 [8] 4356 (1980).

9. N. Setter and L.E. Cross, *J. Mater. Sci.*, 15, 2428 (1980).
10. L.E. Cross, in *High Permittivity Relaxation Dielectrics*, Int. Conf. Mater. & Electronic Eng. I.E.E., London, 1961.
11. F.S. Galasso in *Structure, Properties and Preparation of Perovskite Type Compounds*, Pergamon Press, N.Y. 1969.
12. Landolt-Bornstein in *Ferroelectrics and Related Substances*, New Series, Vol. 16, Springer-Verlag Berlin, N.Y. 1981.
13. K. Furukawa, S. Fujiwara and T. Ogasawara, Proc. of Japan-US Study Seminar on Dielectric and Piezoelectric Ceramics, p.T-4 (1982).
14. M. Lejeune and J.P. Boilot, *Ceram. Int.* 9 [4] 119 (1983).
15. S.L. Swartz, T.R. Shrout, W.A. Schulze and L.E. Cross, *J. Amer. Ceram. Soc.*, 67 [5] 311 (1984).
16. J.P. Guha, *J. Amer. Ceram. Soc.*, 68 [3] C-86 (1985).
17. M.F. Yan, H.C. Ling and W.W. Rhodes, *J. Mater. Res.*, 4 [4] 930 (1989).
18. M.F. Yan, H.C. Ling and W.W. Rhodes, *J. Mater. Res.*, 4 [4] 945 (1989).
19. M. Inada, Japanese Natl. Tech. Report, 23 [1] 95 (1977).
20. M. Lejeune and J.P. Boilot, *Ceram. Int.*, 8 [3] 99 (1982).
21. T.R. Shrout and S.L. Swartz, *Met. Res. Bull.*, 18, 663 (1983).
22. E. Goo, *J. Am. Ceram. Soc.*, 69 [8] C-188 (1986).
23. J. Chen, A. Gorton, H.M. Chan and M.P. Harmer, *J. Am. Ceram. Soc.*, 69 [12] C-303 (1986).
24. S.L. Swartz and T.R. Shrout, *Mat. Res. Bull.*, 17, 1245 (1982).
25. J.P. Guha and H.U. Anderson, *J. Amer. Ceram. Soc.*, 69 [11] C-287 (1986).
26. M. Lejeune and J.P. Boilot, *Mat. Res. Bull.*, 20, 493 (1985).
27. M. Lejeune and J.P. Boilot, *Am. Ceram. Soc. Bull.*, 64 [4] 679 (1986).
28. J.P. Guha, D.J. Hong and H.U. Anderson, *J. Am. Ceram. Soc.*, 71 [3] C-152 (1988).
29. J.P. Guha and H.U. Anderson, *J. Amer. Ceram. Soc.*, 70 [3] C-39 (1987).
30. J.P. Guha and H.U. Anderson, *Ceramic Transactions*, Vol. 1, Part B, Ceramic Powder Science, p 1123 (1988).

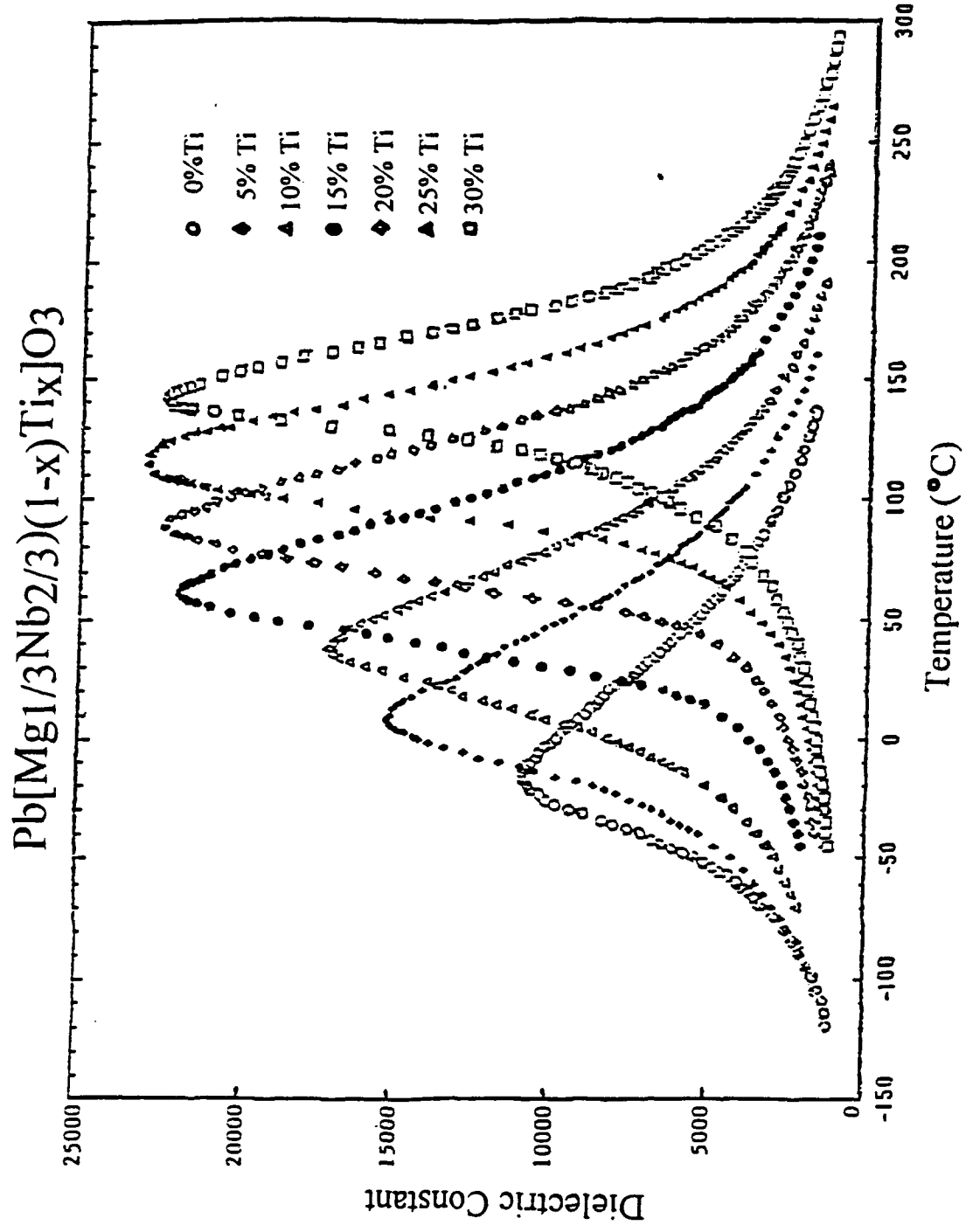


Fig. 1. Temperature Characteristics of the Dielectric Constant for  $\text{Pb}(\text{Mg}_{1/3}\text{Nb}_{2/3})\text{O}_3$ -Based Solid Solutions with Various Additions of  $\text{PbTiO}_3$ .

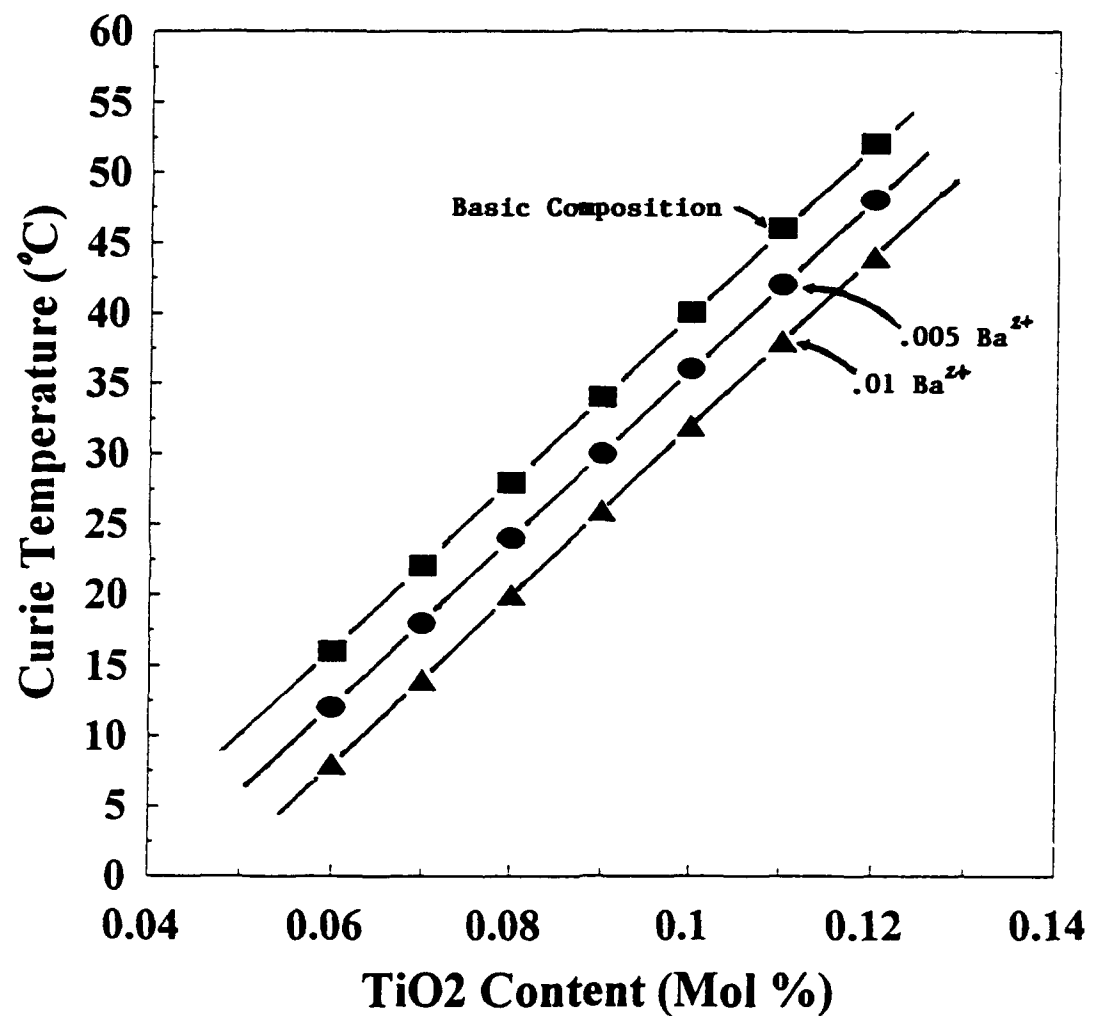


Fig. 2. Change in the Curie Temperatures ( $T_c$ ) of  $\text{Pb}(\text{Mg}_{1/3}\text{Nb}_{2/3})\text{O}_3\text{-PbTiO}_3$  Solid Solutions with Different  $\text{BaO}$  Substitutions.

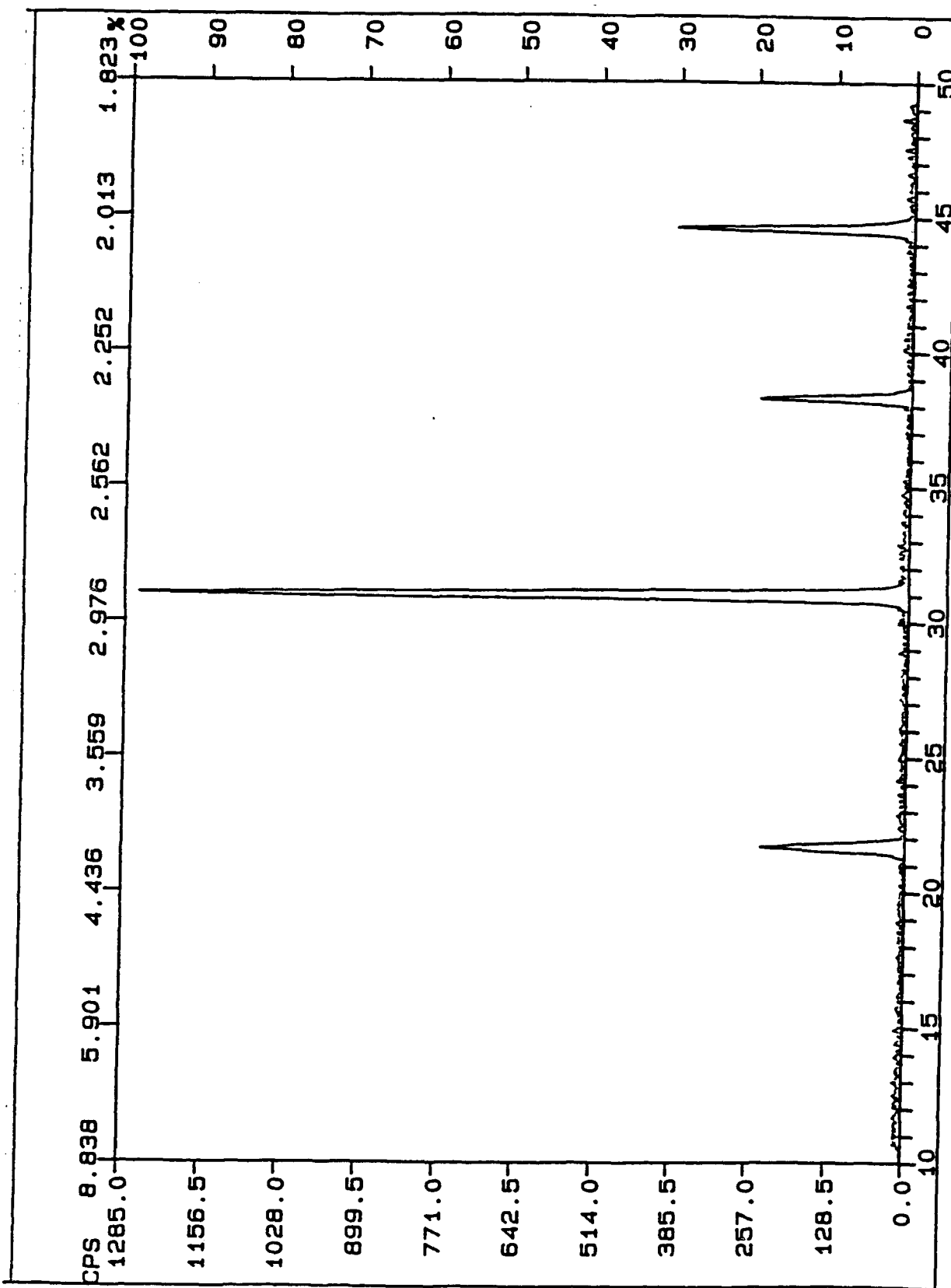
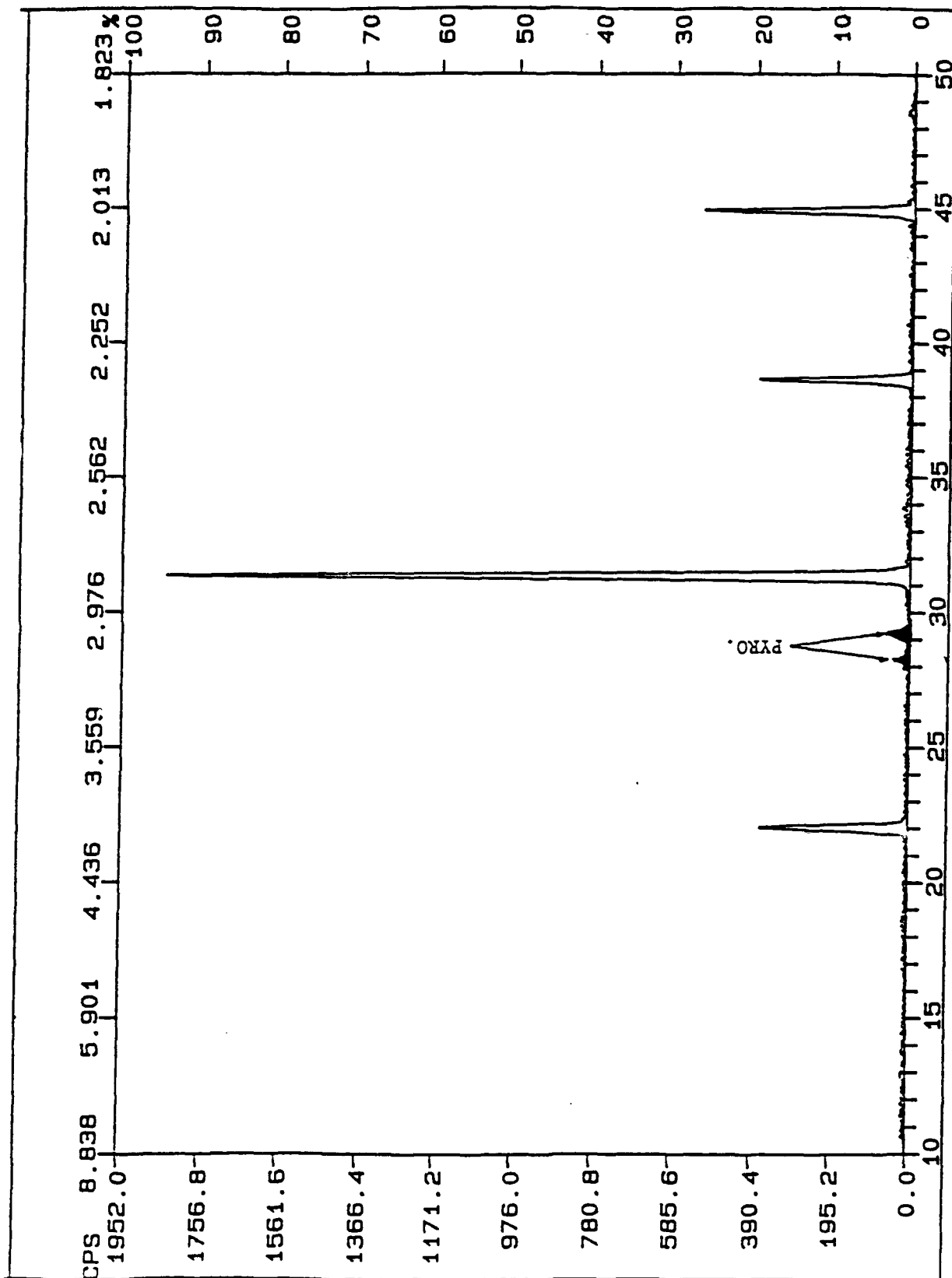


Fig. 3. X-ray Powder Diffraction Pattern of a  $[Pb_{0.99}Ba_{0.01}][Mg_{1/3}Nb_{2/3}]_9Ti_{11}O_3$  Solid Solution Prepared at 800°C Showing Single-Phase Perovskite Phase.



**Fig. 4.** X-ray Powder Diffraction Pattern of a  $[Pb_{0.99}Ba_{0.01}][(Mg_{1/3}Nb_{2/3})_9Ti_{11}O_3$  Solid Solution Fired at 850°C Showing the Formation of a Pyrochlore Phase.

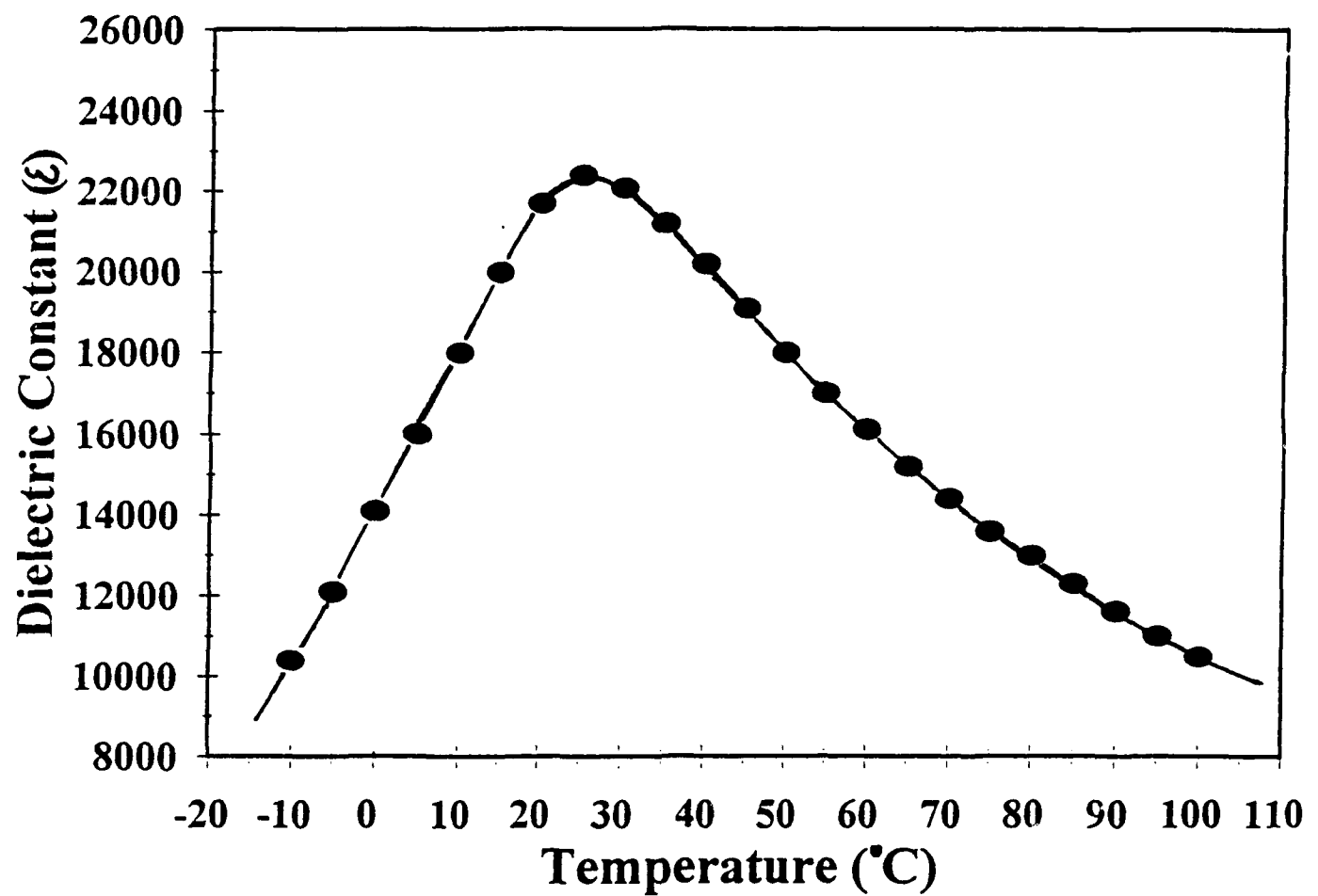


Fig. 5. Temperature Characteristics of the Dielectric Constant of a  $[\text{Pb}_{0.99}\text{Ba}_{0.01}][(\text{Mg}_{1/3}\text{Nb}_{2/3})_{0.9}\text{Ti}_{1.1}]\text{O}_3$  Solid Solution Composed Sintered at  $1250^{\circ}\text{C}$  for 3h.

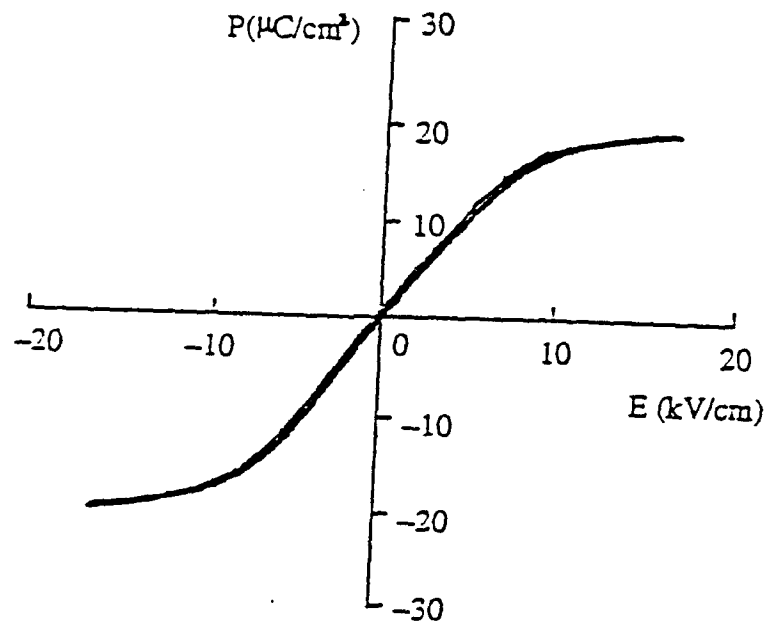


Fig. 6. Ferroelectric Hysteresis Loop for a  $[\text{Pb}_{0.99}\text{Ba}_{0.01}][(\text{Mg}_{1/3}\text{Nb}_{2/3})_{0.9}\text{Ti}_{1}] \text{O}_3$  Solid Solution at  $25^\circ\text{C}$ .

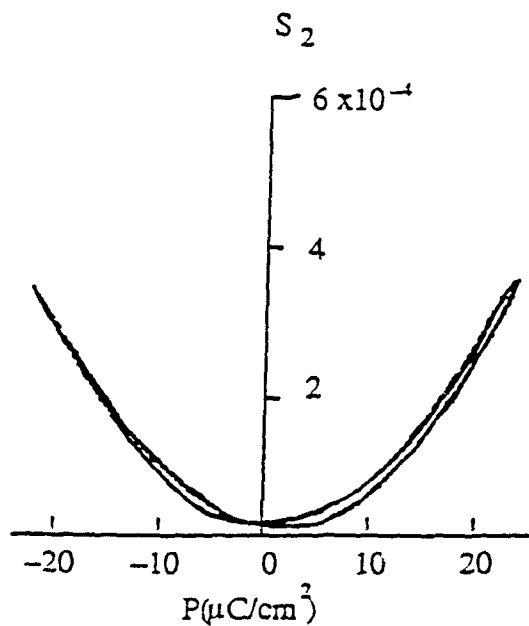


Fig. 7. Electrostriction Curve for a  $[\text{Pb}_{0.99}\text{Ba}_{0.01}][(\text{Mg}_{1/3}\text{Nb}_{2/3})_{0.9}\text{Ti}_{1}] \text{O}_3$  Solid Solution at  $25^\circ\text{C}$ .

**Part IV.**

**Spin Coated Thin Films and Bulk Ceramics**

# **INTELLIGENT PROCESSING OF FERROELECTRIC THIN FILMS**

## **Annual Report**

### **Part IV.**

#### **Spin Coated Thin Films and Bulk Ceramics**

Submitted by: David Dausch  
Gene Haertling

**The Gilbert C. Robinson Department of Ceramic Engineering  
Clemson University**

## **I. INTRODUCTION**

Ferroelectric materials have traditionally been fabricated by a variety of processes including thin film physical (i.e. sputtering, evaporation, laser ablation) and chemical (CVD, sol-gel, MOD) deposition processes as well as bulk ceramic processing techniques (i.e. cold press, tape cast, sintering, hot press); however, the properties of these materials can vary widely due to sample geometry, size and type of deposition process. A goal of "Intelligent Processing of Ferroelectric Thin Films" is to investigate these processes and discover the similarities and differences in material properties produced by these various processes. For this portion of the project, PLZT hot pressed bulk ceramics and spin coated thin films were evaluated in the following topics:

1. Comparison of Thin Films and Bulk Ceramics
2. Rapid Thermally Processed Thin Films

The initial topic includes a study of PLZT bulk ceramics and thin films produced from the same batch solutions, and the subsequent subject describes rapid thermally processed films produced with an automatic spin coat reactor/analyizer and compared to conventional furnace pyrolyzed thin films. These topics are presented independently in the following report.

## **II. COMPARISON OF THIN FILMS AND BULK CERAMICS**

### **II.1. Introduction**

Ferroelectric thin films have been the subject of years of ongoing research in the study and optimization of their processing and properties. The importance of ferroelectric thin films is evident in their many applications ranging from nonvolatile memories to electrooptic devices.<sup>1</sup> These thin film applications stem from the many ferroelectric bulk ceramic components successfully developed over the years. In some instances, however, thin films possess advantages over bulk ceramics which make them more desirable for many devices and broaden the range of applications for ferroelectric materials. Lower operating voltage, higher speed, easier integration with silicon technology and lower cost are among the advantages favoring thin film ferroelectrics.

In order to more fully understand and optimize thin film ferroelectric behavior, a comparison is necessary to bulk ferroelectric phenomena. Direct correlation between the bulk and thin film materials is difficult since the precursors and processing techniques of each are typically so dissimilar; however, a study is presented here that diminishes this disparity. This research focuses on the fabrication and characterization of PLZT bulk ceramics and thin films produced from the same acetate precursor solutions. It is believed that this process allows for a close comparison of PLZT bulk and thin film ferroelectrics by minimizing or eliminating differences in the processing of these materials induced by batching variations, precursor impurities and differences in mixing, reactivity and chemical composition of the precursor materials. A study of several PLZT compositions is presented to explore similarities and differences in the behavior of hot pressed bulk ceramics produced from chemically coprecipitated powders and spin coated thin films produced by a metallorganic decomposition (MOD) process.

## **II.2. Experimental Procedure**

### **II.2.1. Processing**

PLZT hot pressed ceramics and spin coated thin films were fabricated using a process similar to previously reported processes using a water soluble acetate precursor system.<sup>2</sup> The acetate precursors were chosen primarily for their chemical stability, insensitivity to moisture and low cost. The starting precursors included lead subacetate (PbAc) powder, lanthanum acetate (LaAc), zirconium acetate (ZrAc) and titanium acetyl acetonate (TiAAC) solutions. For processing simplicity and accuracy, PbAc was mixed into solution by the addition of acetic acid and methanol so that all of the acetate precursors were in liquid form. This ensured that the beginning acetate formulation was readily and completely mixed into solution. This step becomes important since only a small portion of the total acetate formulation is used for spin coating. Incomplete mixing would produce compositional fluctuations between bulk and thin film solutions. It should be noted that all of the precursors were assayed before experimentation, and the same stock solution of each precursor was used throughout these experiments. These precautions were taken to reduce the possibility of batching variations between bulk and thin film materials so that similarities and differences in their properties were not a result of these variations.

After initial acetate formulation, the solution was separated into bulk and thin film portions. The bulk portion was coprecipitated in a high speed blender with oxalic acid and

methanol and then vacuum dried at 70°C to produce a solid, friable cake. The cake was crushed, calcined at 500°C for 8 hours and milled in trichloroethylene for 6 hours to produce a PLZT oxide powder. Typically, 100g of powder was produced for hot pressing. Hot pressing conditions were 1200°C for 4 hours at 14 MPa. To prepare samples for electrical measurement, the hot pressed parts were sliced on a diamond saw and lapped to 0.5 mm (20 mil) thickness. Electroless nickel electrodes were plated onto the samples.

For thin film production, a small portion (usually 5g) of the acetate solution was decanted and diluted with methanol at a 2:1 ratio by weight. The solution was spun onto silver foil substrates using a photoresist spinner at 2000 rpm for 15 seconds, allowed to dry for 15 seconds and pyrolyzed at 700°C for 4 minutes. Repeating this process for 10 layers produced a PLZT thin film approximately 0.9 µm thick. For measurement of electrical properties, copper electrodes were applied to the surface of the films via vacuum evaporation. This process allowed for the fabrication of both bulk and thin film materials from the same batch solution.

### II.2.2. Measurements

Bulk and thin film samples were analyzed using several electrical and physical measurement techniques. The dielectric properties (virgin and poled capacitance and dissipation factor) were measured on bulk and thin film samples using a Leader LCR meter at a measuring frequency of 1 kHz. Polarization (P) vs. electric field (E) hysteresis loops were also measured for both materials. The bulk samples were measured using a Sawyer-Tower circuit with a dc applied voltage of  $\pm 1400$  V. The hysteresis loops were plotted with a Goerz Metrawatt X-Y plotter. Hysteresis loops of the thin film samples were customarily measured at 1 kHz using a Sawyer-Tower circuit and an oscilloscope readout; however, in order to more accurately compare measurement of bulk and film hysteresis loops, the thin films were also measured using a low voltage ( $\pm 30$ -50 V) dc looper.

The Curie temperature of bulk samples was determined for several PLZT compositions. Bulk samples were placed in a stirred oil bath and heated while taking capacitance and loss tangent measurements at 5°C increments. The Curie temperature was indicated by a maximum in the measured capacitance. X-ray diffraction analysis was also performed on bulk and thin film samples using a Scintag XDS 2000 diffractometer with Cu K $\alpha$  radiation.

## **II.3. Results and Discussion**

Several compositions were chosen for study near phase boundaries in the PLZT system. The morphotropic phase boundary compositions consisted of 2/55/45, 2/53/47 and 2/51/49 which regularly exhibit ferroelectric memory behavior. Compositions approaching and entering the paraelectric phase region with 65/35 Zr/Ti ratios included those with 6, 7, 8, 9, 9.5 and 10% La. These materials typically are memory materials at 6% La and range toward slim-loop ferroelectric materials in the 9 to 10% La range. Hot pressed bulk ceramics and spin coated thin films on Ag foil substrates were fabricated, and a comparison of properties was established.

### **II.3.1. Dielectric Properties**

Dielectric and ferroelectric properties are listed for bulk and thin film samples in Table II.1 including virgin and poled dielectric constants and dissipation factors for each. As expected, thin film dielectric constants were generally lower than their bulk counterparts. These effects have previously been reported to be due to several effects caused by the obvious differences between bulk and thin film configurations including small grain size of the thin films, mechanical clamping effects and voltage sensitivity of the dielectric measurement due to the high electric field applied to a  $<1\text{ }\mu\text{m}$  thin film.<sup>2</sup> The difference in dielectric properties found in the present results, however, was not as significant as that reported earlier.

In comparing bulk 2% La samples to thin films, some similarities and differences were noted. Unsurprisingly, both bulk and thin film data showed maxima in  $K_{vir}$  and  $K_{pol}$  at the 2/53/47 composition indicating the existence of the morphotropic phase boundary near this composition, although the position of the boundary for the thin films seemed to be slightly different than that of the bulk samples.  $K_{pol}$  and  $K_{vir}$  for 2/51/49 thin films was essentially equal to that of 2/55/45 films, while bulk 2/51/49 had a much greater poled dielectric constant than bulk 2/55/45. This result suggested that thin films and bulk ceramics did not behave equivalently near the morphotropic phase boundary since the dielectric constant was expected to peak at this boundary. A comparable result occurred for  $x/65/35$  compositions when the paraelectric phase boundary was encountered. The dielectric constant was expected to reach a maximum at this phase boundary which was previously reported at the 9/65/35 composition for mixed oxide processes.<sup>3</sup> Though both bulk and thin film samples seemed to have maximum dielectric constants at the 9.5/65/35

compositions, the 9/65/35 thin films were closer to 9.5/65/35 than the bulk. Note the occurrence of the high  $K_{pol}$  for the 8/65/35 bulk sample despite the lower  $K_{vir}$  shown by this sample. The bulk ceramics demonstrated a larger difference in dielectric constants between the 9 and 9.5/65/35 compositions. Additionally, the thin film 6/65/35 composition revealed a higher dielectric constant than the bulk 6/65/35. These results would suggest that bulk and thin film samples showed dissimilar behavior also near the paraelectric phase boundary.

As mentioned above, the expected maximum dielectric constant for  $x/65/35$  bulk ceramics produced via mixed oxide processes was 9/65/35; however, the results in Table II.1 for the chemical process generally indicate a maximum at the 9.5/65/35 composition. Furthermore, the dielectric constants for all of these compositions were higher than values reported for mixed oxide processes.<sup>3</sup> These results could possibly be explained by realizing the type of process used in this study for fabricating bulk ceramics and thin films; i.e., thoroughly mixed acetate precursor solutions to produce chemically derived powders and thin films. This process may provide improved mixing of components which could slightly alter stoichiometry in the bulk and thin film samples-- especially Zr/Ti ratio and dispersion of the La dopant in PLZT. This could have produced higher dielectric constants and shifted the maximum in dielectric constants of these materials to 9.5% La. In order to explore this supposition, Curie temperatures of bulk  $x/65/35$  samples were measured and are shown in Table II.2 and Figure II.1. The Curie temperatures measured were consistently 10°C lower than previously reported for bulk samples produced by a mixed oxide process.<sup>3</sup> This result further emphasizes the possibility that the stoichiometries of the chemically prepared materials presented here were slightly different than the mixed oxide materials.

### II.3.2. Crystallinity

X-ray diffraction patterns of thin film 8/65/35 and bulk 8/65/35 samples are shown in Figures II.2a and II.2b, respectively, and the d-spacings and diffraction angles are tabulated for the PLZT peaks in Table II.3. Due to their greater intensities, the three Ag substrate peaks labeled on the thin film pattern masked three PLZT film peaks expected at the same angles. The thin film sample produced lower intensity PLZT peaks than the corresponding bulk sample. This could be a result of the thin film having either a lower degree of crystallinity than the bulk sample or simply a smaller quantity of material being analyzed by the diffractometer. In analyzing the lattice spacings of the materials, it was found that the thin film d-spacings were slightly larger than in the bulk material. Watanabe

et al.<sup>4</sup> proposed that mechanical stress present in PZT thin films caused by lattice or thermal expansion mismatch between the film and the substrate can cause differences in lattice constant between bulk and thin film materials. This may be the cause of the difference in d-spacing observed here. The increase in d-spacing for the thin films is quite small-- approximately 0.6 to 1% between the bulk and thin film samples. An absence of larger differences in d-spacings could be attributed to the ductility of the Ag substrates which may have allowed the films to be relatively stress free compared to films fabricated on more rigid substrates (i.e. Si, sapphire, MgO).

### II.3.3. Ferroelectric Properties

The ferroelectric properties calculated in Table II.1 were taken from the  $P$  vs.  $E$  hysteresis loops shown in Figure II.3. As stated above in the discussion of dielectric properties, both bulk and thin film materials indicated a transition across the morphotropic phase boundary. This transition was also evident in the hysteresis loops of the materials. In the bulk materials, the transition was obvious with a widening of the hysteresis loop signaling the emergence of the tetragonal phase in the 2/51/49 material. This phenomenon, however, did not occur in the thin film samples. The tetragonal phase was evident in the dc hysteresis loops of the thin films by a slightly more square hysteresis loop for 2/51/49 than for the rhombohedral 2/55/45 film. The phase transition was apparent in both ac and dc hysteresis loops of the films by a rise in remanent polarization in the 2/53/47 film. Previous work mentioned that thin films have a lower  $P_R$  and higher  $E_C$  than bulk materials for reasons similar to differences in dielectric properties mentioned above (grain size, clamping, voltage sensitivity).<sup>2</sup> Although the thin films presented here with 2% La had a higher  $E_C$ , the  $P_R$  of these films was not necessarily lower than for bulk materials. In fact, 2/53/47 and 2/51/49 films had a higher  $P_R$  than bulk samples of the same composition. Again, as with dielectric properties, the ferroelectric properties of the thin films seemed to be different across the phase boundary than the bulk ceramics. This was also the case for x/65/35 materials.

In PLZT bulk x/65/35 samples, the hysteresis loops obtained were similar to those expected for these compositions. The remanent polarizations and coercive fields calculated were lower than reported mixed oxide values,<sup>3</sup> and this can possibly be attributed to the difference in processing between the coprecipitation and mixed oxide processes as discussed above. As anticipated, the 6, 7 and 8% La materials were memory materials, and the 9, 9.5 and 10% La materials were slim-loop materials. For the memory materials,  $E_C$  was higher and  $P_R$  was lower for thin films than for bulk materials which

was similar to previously reported results.<sup>2</sup> Although both bulk and thin film memory materials experienced narrowing of their hysteresis loops with increasing %La, the bulk materials transformed to slim-loop materials at 9% La, while the thin films maintained ferroelectric memory hysteresis loops beyond 9% La. Research by Gu et al.<sup>5</sup> on quenched PLZT 9.5/65/35 ceramics showed that internal stresses induced in quenched samples can enhance polar region ordering and produce a more ferroelectric-like response. This produced higher remanent polarizations in quenched samples than in annealed samples. These findings could explain the memory behavior observed in the 9, 9.5 and 10/65/35 thin films in this study. Residual stresses in the thin films which could have produced the differences in d-spacings discussed above may have caused these films to retain ferroelectric memory hysteresis loops that were not observed in the bulk materials of the same compositions. Nevertheless, thin film behavior again differed from bulk ceramic behavior near the paraelectric phase boundary.

#### II.4. Summary

PLZT bulk ceramics and thin films were fabricated from the same acetate precursor solutions in order to minimize batching variations and accurately compare properties between bulk and thin film samples of the same compositions. It was found that materials near the morphotropic phase boundary with 2% La differed in behavior. Maximum dielectric constants were found at 2/53/47 for both materials; however, the bulk 2/51/49 had a proportionally higher dielectric constant than the thin film when compared to their respective 2/55/45 samples. The hysteresis loops of the bulk samples indicated a transition to a tetragonal phase with a widening of hysteresis loops (increased  $E_C$ , decreased  $P_R$ ). Thin films also indicated a transition but with a maximum in  $P_R$  for the 2/53/47 composition.

Bulk x/65/35 materials behaved as expected with the exception of slightly lower Curie temperatures, coercive fields and remanent polarizations and slightly higher dielectric constants than previously reported. The 6, 7 and 8/65/35 materials produced memory hysteresis loops, and the 9, 9.5 and 10/65/35 materials produced slim hysteresis loops. The thin film memory loops were somewhat thinner than the bulk memory loops, and continual narrowing of the loops occurred toward the paraelectric phase boundary; however, slim-loop ferroelectrics were never completely achieved in the thin film materials. X-ray diffraction analysis showed that thin film lattice spacings were only

slightly greater than the corresponding bulk spacings as indicated by diffraction peaks slightly shifted in diffraction angle between the two materials.

This comparison of bulk and thin film ferroelectrics is believed to be an accurate comparison of properties caused only by the inherent differences in configuration between bulk ceramics and thin films. It is believed that the current process used to fabricate these materials is one in which complete mixing of precursors and accurate batching of materials provided a minimization of batching differences that could cause serious variations in composition and properties of bulk and thin film PLZT ferroelectrics. Hence, this process provided a valid comparison between these materials.

## II.5. References

- [1] L. M. Sheppard, *Am. Cer. Soc. Bull.*, **71**, 85 (1992).
- [2] G. H. Haertling, *Proc. IEEE 7th International Symposium on Applications of Ferroelectrics*, 292 (1990).
- [3] G. H. Haertling, Engineered Materials Handbook, vol. 4 (Ceramics and Glasses), ASM International, 1124 (1991).
- [4] H. Watanabe, T. Mihara and C. A. Paz De Araujo, *Proc. 3rd International Symposium on Integrated Ferroelectrics*, 139 (1991).
- [5] W. Y. Gu, E. Furman, A. Bhalla and L. E. Cross, *Ferroelectrics*, **89**, 221 (1989).

## III. RAPID THERMALLY PROCESSED THIN FILMS

### III.1. Introduction

Rapid thermal processing (RTP) has become an increasingly more popular technique for the fabrication of ferroelectric thin films. The growing interest in utilizing these films as integrated circuit devices<sup>1</sup> has led to the search for a processing technique which is

compatible with semiconductor integrated circuits. RTP has been used for many applications in semiconductor IC processing, and this technique possesses advantages over conventional furnace pyrolysis (CFP) that have justified its use for the processing of ferroelectric thin films.<sup>2-5</sup> Such advantages include reduction in the thermal budget or decrease in the temperature and time required to produce the same results, increased heating rate which promotes the formation of the desired crystalline phase and reduced annealing time which minimizes film/substrate reaction, evaporation and electrode degradation.

The properties of PZT and PLZT metallorganic decomposition processed thin films fabricated by spin coating have been widely studied.<sup>5-11</sup> These processes typically include a heat treatment and/or post-anneal performed in a conventional box furnace for removal of residual organics and crystallization. CFP, however, is not ideal for the production of actual ferroelectric thin film devices, especially IC devices. Since IC device applications require shorter annealing times and lower annealing temperatures, RTP has been investigated of late as a candidate not only for increasing process compatibility with Si IC technology, but also for improving the properties of PZT and PLZT thin films.<sup>2,4-6,11-13</sup>

Typically, RTP is performed in a separate reaction chamber; however, the ideal situation for IC processing is a single multi-process reactor utilizing RTP.<sup>3</sup> This multi-process reactor would decrease cost and increase flexibility in IC fabrication by incorporating several processes into one automated system. In addition, a cleaner environment would more easily be controlled in a single chamber since many processing steps could be completed without exposure of the wafer to contamination sources outside of the chamber. Because of the characteristics of RTP which include faster heating rate, shorter annealing times and lower temperatures, RTP enhances the properties of ferroelectric thin films typically produced by CFP.<sup>5,6,11,12,14</sup> The increased heating rate of RTP inhibits the sluggish formation of the undesirable pyrochlore phase and favors the development of the ferroelectric perovskite phase which leads to improved crystallinity. Other improvements include higher dielectric constants, higher remanent polarizations ( $P_R$ ), lower coercive fields ( $E_C$ ), reduced Pb loss due to shorter annealing times and smoother surfaces due to smaller grain size.

In this study, a computer controlled multi-process reactor has been utilized for spin coating and rapid thermal processing of thin films from liquid precursors. This automatic spin coat reactor/analyizer was used to produce PLZT thin films by spinning an acetate precursor solution onto Pt-coated Si substrates and crystallizing the films by RTP. Computer control provides hands-off fabrication and flexibility in processing of the films, while laser ellipsometry, used to perform film thickness analysis within the reaction

chamber, provides in-situ analysis of the films. PLZT thin films were produced on 3" diameter and 5/8" square Si substrates with the automatic spin coater. The larger sample was fabricated for study of the thickness uniformity yielded by the spin coating process, and the smaller samples were measured for electrical properties. Additionally, the physical and electrical properties of rapid thermally processed films were compared to conventional furnace pyrolyzed films. Properties examined were crystallinity, P vs. E hysteresis loop, dielectric constant, dissipation factor and resistivity.

### **III.2. Experimental Procedure**

#### **III.2.1. Automatic Spin Coater Design**

The automatic spin coat reactor/analyzer, produced by Digital Controls, Inc. in Rolla, MO, utilizes the four basic systems diagrammed in Figures III.1-III.4: fluid dispense system, rapid thermal processing unit, atmosphere control system and in-situ laser ellipsometer. The systems are controlled by an IBM compatible, 80386DX computer with software to operate the ellipsometer and set parameters for deposition, spinning, atmospheric gas control, heating and cooling. Multiple layers can be deposited onto one film with different parameters for each layer, if desired. Samples may be prepared and analyzed without exposure to the external environment. Although described here, the atmosphere control system was not used for this study.

The fluid dispense system has the capability of depositing one of three precursor solutions onto 1/2" to 4" diameter substrates. The fluid, stored in one of the three fluid reservoirs, is pumped by diaphragm-operated resist pumps through a dispense arm onto the substrate. A vacuum pump in conjunction with the resist pumps provides a "suck-back" feature which prevents the fluid from dripping onto the substrate while the sample is spinning. A nitrogen dusting step can also be inserted through the dispense arm before fluid deposition. Located on the left side of the chamber, the dispense arm is moved over the sample chuck for deposition and is returned after spinning. Spinning is executed with an ac brushless servo motor and controller with programmable time, speed and acceleration.

Six water-cooled parabolic strip heaters with infrared quartz lamps containing tungsten filaments comprise the rapid thermal processing unit. Positioned in the rear of the chamber during deposition, the heater assembly is moved forward over the sample stage for heating. The temperature is controlled by a thermocouple placed directly above the

sample surface and was calibrated by observing the temperature recorded from a thermocouple located under the sample. This RTP unit allows the sample to be heated to 700°C within 5 to 10 seconds by direct radiation from the parabolic strip heaters.

Variable atmospheric gases (N<sub>2</sub>, O<sub>2</sub>, Ar) and low pressures as well as vacuum capability are possible in the atmosphere control system. The gas or vacuum pressure is displayed by the computer during atmosphere control before deposition. Oxygen content in the atmospheric gas is monitored by a ZrO<sub>2</sub> oxygen probe and is also displayed.

In-situ thickness measurements are taken before and after heating by a Gaertner Scientific laser ellipsometer ( $\lambda = 6328$  angstroms). The ellipsometer is moved across the surface of the wafer in order to obtain thickness measurements for various locations on the film. An ellipsometer software program calculates the thickness of the film. The laser is passed through the reactor chamber via optic ports at an angle of incidence of 70° from the sample surface normal.

### **III.2.2. Thin Film Preparation**

PLZT thin films of composition 2/55/45 (La/Zr/Ti) were produced with the automatic spin coater on 3" diameter and 5/8" square Pt-coated Si wafers. Deposited solution was derived from liquid acetate precursors consisting of lead subacetate (mixed into solution form with methanol and acetic acid), lanthanum acetate, zirconium acetate and titanium acetyl acetonate with methanol and water.<sup>15</sup> The film deposition cycle was repeated for 5 layers yielding a final thickness of 4000 to 5000 angstroms. Films were spun automatically at 2000 rpm for 30 seconds, dried for 3 minutes before RTP, heated at 700°C and cooled to room temperature for 20-30 minutes between layers. The 3" sample was heated for 1 minute per layer, and the smaller samples used for measurement of electrical properties were heated at 700°C for a total of 15 minutes which was divided into the firing schedules listed in Table III.1. A rapid thermal post-anneal was used for these films. The temperature controlling thermocouple, which reached 700°C in 2 to 3 seconds, was positioned directly above the sample surface. Actual sample temperature and heating rate, however, were calibrated by contacting an additional measuring thermocouple to the reverse side of the sample. It was found that the back of the substrate reached 700°C in 10 seconds; consequently, the film on the surface of the sample presumably heated at a rate greater than 70°C per second.

Manually spun films were also produced for comparison with the automatically spun films. This process involved depositing the precursor solution for 5 layers onto 5/8" Pt-coated Si substrates and spinning at 2000 rpm for 15 seconds per layer with a photoresist

spinner. Conventional furnace pyrolysis was performed at 700°C in a Thermolyne furnace using firing schedules 1-3 in Table III.1 with conventional furnace post-anneals. The last two firing schedules did not produce electrically stable films with CFP. A thermocouple placed above the sample indicated that the furnace reached 700°C in approximately 20 seconds. This implied that the CFP samples heated to the firing temperature at a rate no more than 35°C per second. Hence, the heating rate for RTP thin films is at least if not more than twice that for the CFP samples.

### III.2.3. Measurement

A 3" diameter thin film sample was measured for thickness uniformity with the laser ellipsometer after RTP. The index of refraction for the film was fixed at 2.45 (PLZT for red light), and the index of refraction of the substrate used was 2.33 for Pt. A 775 angstrom standard SiO<sub>2</sub> film on Si was used to calibrate the ellipsometer. Measurements were taken starting from the center of the film and again at 1/4" intervals to the edge of the wafer. Another series of measurements was taken after a 90° rotation of the sample. After completing four of these series of measurements, the data was grouped in order to display two sequences across perpendicular diameters of the wafer. These measurements produce two thickness profiles of the film. Ellipsometry was also used to determine the thickness of the 5/8" samples.

Evaporated Cu was applied as the top electrode on the films for measurement of electrical properties. Poled and virgin dielectric constants ( $K_{pol}$  and  $K_{vir}$ ) and dissipation factors ( $\tan \delta$ ) were measured on a Leader LCR meter at 1 kHz. A Sawyer-Tower circuit and oscilloscope readout yielded ac hysteresis loops at a frequency of 1 kHz. Resistivity was measured using a Keithley electrometer. X-ray diffraction patterns, produced using a Scintag XDS 2000 diffractometer with Cu K $\alpha$  radiation, and SEM micrographs, obtained by a Jeol JSM-IC 848 microscope, were also observed.

## III.3. Results and Discussion

### III.3.1. Thickness Uniformity

An important property when considering IC device manufacture and reliability is thickness uniformity of the ferroelectric film across the surface of the Si wafer substrate. Variation in thickness could mean variation in properties and performance; hence, uniform

thickness is a critical factor in producing a wafer with the maximum possible yield of consistent devices. A PLZT film on a 3" diameter Si wafer produced by the automatic spin coat reactor/analyizer was analyzed using the laser ellipsometer. Figure III.5 displays the thickness profiles obtained for this film. The thickness of the film was determined to be  $4291 \pm 151$  angstroms for the first profile and  $4293 \pm 120$  angstroms for the second profile revealing a maximum thickness variation of only 7%. Upon closer examination, however, it appears that most of this variation occurs on the outer portion of the film. This could be due to greater stresses on the outer portion of the film causing larger thickness variation, or the variation could be a result of the nature of the spinning process which builds up more solution on outward regions of the wafer. In addition, the film seems to have some discolored areas on its outer section corresponding to cavities in the sample chuck. The thickness variation corresponds to these areas which may have cooled more quickly or been at a slightly lower temperature than the rest of the film. When neglecting the outer two measurements on each side of the profiles or, in other words, when only considering the inner 1.5" diameter of the wafer, the thickness is even more uniform. The maximum variation in this case is less than 3% with an average thickness of 4307 angstroms. Considering these results, the automatic spin coater appears to produce uniform films with most of the variation in thickness occurring on the outer portion of the 3" coated wafer.

### III.3.2. Physical Properties

As discussed earlier, previous research has shown that because of much higher heating rates, the perovskite phase forms more readily with RTP than with CFP.<sup>12,15</sup> In addition, sharper, more intense x-ray peaks have been observed in rapid thermally processed films.<sup>5</sup> X-ray diffraction patterns of the rapid thermally processed thin films for this study are displayed in Figure III.6. The films seemed to show some preferential orientation in the [110] and [111] directions. Upon comparison of these films to the conventional furnace pyrolyzed films in Figure III.7, the CFP films were generally oriented in the [100] direction. The (110), (111) and (211) peaks of the RTP films were more intense than the corresponding peaks in the CFP films. Similarly, the (100) and (200) peaks of the CFP films were more intense than those of the RTP films. It is interesting to note that the 2/55/45 composition is a rhombohedral phase, and rhombohedral distortion from the cubic unit cell is along the [111] direction; furthermore, the polarization direction of the rhombohedral unit cell is the [111] direction. Consequently, it can be inferred that a [111]

or [110] orientation would be more beneficial for this composition than [100] since the dipoles will more easily align in the polarization direction.

Another general observation from the diffraction patterns of the entire group of films was in relation to the firing schedule. For both processes, the crystallinity improved as the firing time per layer decreased and the post-anneal time increased. In addition, more peak splitting was observed in the (111) and (211) peaks of the films fired longer per layer with less post-anneal for both types of films. All of the films in this study were found to be perovskite phase with no pyrochlore detectable by x-ray diffraction. The 3" PLZT film rapid thermally processed at 700°C for 1 minute per layer was also evaluated by x-ray diffraction and found to have the perovskite structure with no detectable pyrochlore. X-ray diffraction patterns of this film as well as the 5/8" film with RTP for 1 minute per layer and a rapid thermal post-anneal of 10 minutes are displayed in Figure III.8. The larger sample was observed to be more preferentially oriented in the [100] direction, while the smaller sample was more oriented toward the [111] direction. The only difference between these samples, except for size, was the rapid thermal post-anneal for 10 minutes of the small sample.

SEM micrographs of rapid thermally processed and conventional furnace pyrolyzed thin films are shown in Figures III.9 and III.10, respectively. As expected, the grain sizes of the RTP films were smaller than for the CFP films. The finer microstructures are particularly apparent in Figures III.9a and III.10a which display films from the two different processes with equivalent firing schedules. Previous investigators have observed smaller grain size for RTP films due to faster heating rate which reduces the time for grain growth kinetics.<sup>5</sup>

Another more drastic difference in morphology is observed with changes in firing schedule. In both Figures III.9 and III.10, the grain size for the films fired for less time per layer with longer post-anneal is much finer than the films fired 3 minutes per layer. Perhaps this shorter firing time per layer has again limited the time for grain growth resulting in smaller grain size.

### III.3.3. Electrical Properties

The dielectric and ferroelectric properties of the 5/8" automatically spun and manually spun films are shown in Tables III.2 and III.3, respectively. With respect to firing schedule, it was observed that the properties improved as the firing time per layer decreased and the post-anneal time increased. Dielectric constants increased, coercive fields decreased and remanent polarizations showed some increase with shorter firing time

per layer and longer post-anneal; however, the dissipation factor also increased with these parameters which may have indicated some conduction. The resistivity of all of the films was on the order of  $10^{11} \Omega\text{-cm}$ .

Automatically spun films with RTP also exhibited improved properties compared to the manually spun films with CFP. Dielectric constants were higher and coercive fields were lower for RTP thin films. Remanent polarizations, however, did not seem to increase with RTP. One possible reason for this improvement in properties was the difference in orientation between these films. The dipoles of the RTP films may have switched easier and aligned better with the [111] polarization direction of the rhombohedral phase in the measuring direction of the films. Another advantage of the automatically spun films was the capability of rapid thermally processing for less than 1 minute per layer. As discussed previously, the manually spun films were electrically unstable and did not yield well-developed hysteresis loops under these heating conditions. The possibility of processing for only 15 to 30 seconds per layer with RTP is promising for IC device production.

Film thickness, measured by the ellipsometer, is also listed in Tables III.2 and III.3. The thickness of the automatically spun films, roughly 5000 angstroms, was somewhat higher than the manually spun films, approximately 4000 angstroms, even though all of the films were 5 layers thick. Thickness differences likely occurred because the solution for manual spinning was dispensed sparingly by hand, and the fluid pumps of the automatic spin coater could only release larger amounts of solution onto the substrate. In addition, there was a slightly longer pause between the fluid dispense and spin stages in automatic spinning as the computer processed information for the next stage.

Figure III.11 displays the P vs. E hysteresis loops of the automatically and manually spun thin films. RTP yielded films with slimmer, better-saturated hysteresis loops. The maximum voltage applied to the films was approximately  $\pm 25$  V; however, the film spun manually with CFP for 1 minute per layer could only withstand  $\pm 15$  V without electrically shorting. More asymmetry was also observed in the hysteresis loops of the RTP films compared to the CFP films. This observation is not yet understood; however, possible factors inducing this asymmetry include interaction between the PLZT and bottom Pt electrode, the presence of a barrier or porous layer at this interface, differences in behavior between the Cu and Pt electrode interfaces and differences in the crystallinity or stress caused by rapid heating effects.

### **III.4. Summary**

An automatic spin coat reactor/analyser was used to produce PLZT thin films from acetate precursors on Pt-coated Si wafers. The automatic spin coater is computer controlled and fully automated for hands-off processing which provides a cleaner environment and more flexibility in processing parameters. The spin coating process is integrated with rapid thermal processing, atmosphere control and in-situ ellipsometry in this reactor allowing several processing steps to be completed in one chamber. It is believed that this unit, utilizing an integrated RTP process, is the first of this type of multi-process reactor that promises optimum fabrication of ferroelectric thin films for IC devices.

Thin films produced by the automatic spin coater were found to be quite uniform in thickness. A PLZT film on 3" diameter Pt-coated Si was 4292 angstroms with a maximum thickness variation of only 7%; furthermore, most of this variation occurred on the outer portion of the film. Thin films crystallized by RTP were found to have preferred orientations different from those of thin films processed by CFP. Rapid thermal processing enhanced the [110] and [111] orientations, while conventional furnace pyrolysis generally procured the [100] orientation. In this respect, RTP may have allowed the rhombohedral PLZT 2/55/45 films to more easily align in the polarization direction.

The morphology of the films was greatly affected by firing schedule. Films fired shorter per layer with longer post-anneals had much finer grain structures than the films fired 3 minutes per layer. Additionally, the rapid thermally processed films consisted of smaller grains than their conventional furnace pyrolyzed counterparts.

The electrical properties of the films produced by RTP were improved over CFP films. Dielectric constants were higher, coercive fields were lower and the hysteresis loops were better saturated. Further investigation is still necessary, however, because of the somewhat high dissipation factors and asymmetry of the hysteresis loops. Much work is yet to be accomplished in optimizing the processing conditions for these films; however, the automatic spin coater has the potential to improve the properties and processing uniformity of PLZT ferroelectric thin films.

### **III.5. References**

1. Y. Xu and J. D. MacKenzie, *Integrated Ferroelectrics*, **1**, 17 (1992).
2. J. Chen, K. R. Udayakumar, K. G. Brooks and L. E. Cross, *J. Appl. Phys.*, **71**,

- 4465 (1992).
3. F. Roozeboom and N. Parekh, *J. Vac. Sci. Technol. B*, **8**, 1249 (1990).
  4. M. Sayer, *Proc. 3rd International Symposium on Integrated Ferroelectrics*, 1 (1991).
  5. L. Shi, S. B. Krupanidhi and G. H. Haertling, *Integrated Ferroelectrics*, **1**, 111 (1992).
  6. B. A. Tuttle, R. W. Schwartz, D. H. Doughty, J. A. Voigt and A. H. Carim, *Mat. Res. Soc. Symp. Proc.*, Vol. **200**: "Ferroelectric Thin Films," (eds. E. R. Myers and A. I. Kingon), 159 (1990).
  7. R. A. Lipelis and D. J. Coleman, *Ultrastructure Proc. of Adv. Ceram.*, (eds. J. D. MacKenzie and D. R. Ulrich), John Wiley & Sons, New York, 919, 1987.
  8. R. W. Vest and J. Xu, *Ferroelectrics*, **93**, 21 (1989).
  9. A. H. Carim, B. A. Tuttle, D. H. Doughty and S. L. Martinez, *J. Am. Ceram. Soc.*, **74**, 1455 (1991).
  10. G. H. Haertling, *Ferroelectrics*, **116**, 51 (1991).
  11. H. Hu, L. Shi, V. Kumar and S. B. Krupanidhi, *Ceramic Transactions*, Vol. **25**: "Ferroelectric Films," (eds. A. S. Bhalla and K. M. Nair), 113 (1992).
  12. H. Hu, C. J. Peng and S. B. Krupanidhi, *Thin Solid Films*, **223**, 327 (1993).
  13. C. V. R. Vasant Kumar, R. Pascual and M. Sayer, *J. Appl. Phys.*, **71**, 864 (1992).
  14. S. B. Krupanidhi, *Proc. 3rd International Symposium on Integrated Ferroelectrics*, 23 (1991).
  15. G. H. Haertling, *Proc. IEEE 7th International Symposium on Applications of Ferroelectrics*, 292 (1990).

**Table II.1.** Electrical properties of PLZT bulk ceramics and thin films.

BULK CERAMICS								
	K <sub>pol</sub>	tan δ (pol)	K <sub>vir</sub>	tan δ (vir)	E <sub>C</sub> (dc) [kV/cm]	P <sub>R</sub> (dc) [μC/cm <sup>2</sup> ]	E <sub>C</sub> (ac) [kV/cm]	P <sub>R</sub> (ac) [μC/cm <sup>2</sup> ]
2/55/45	1328	.029	1293	.033	8	46	--	--
2/53/47	1885	.025	1391	.028	10	40	--	--
2/51/49	1630	.024	1234	.034	16	33	--	--
6/65/35	1355	.036	1774	.056	6	33	--	--
7/65/35	2712	.033	2479	.036	5	31	--	--
8/65/35	5700	.055	4692	.050	3	20	--	--
9/65/35	5147	.054	5007	.050	0	0	--	--
9.5/65/35	5658	.048	5603	.046	0	0	--	--
10/65/35	5548	.036	5538	.033	0	0	--	--

THIN FILMS								
2/55/45	997	.122	1228	.133	27	34	43	32
2/53/47	1265	.132	1619	.160	28	47	44	45
2/51/49	972	.122	1237	.146	28	38	46	37
6/65/35	1871	.142	1995	.141	14	21	28	25
7/65/35	2499	.170	2460	.145	14	18	27	21
8/65/35	3211	.194	3172	.176	11	15	22	19
9/65/35	4221	.195	4001	.172	9	11	22	17
9.5/65/35	4234	.190	4092	.164	7	8	19	18
10/65/35	4157	.193	4157	.209	7	10	18	16

**Table II.2.** Curie temperatures of PLZT x/65/35 bulk ceramics.

Composition	T <sub>c</sub> [acetate]	T <sub>c</sub> [oxide]
7/65/35	140	150
8/65/35	100	110
9/65/35	70	80
9.5/65/35	65	75
10/65/35	60	70

**Table II.3.** D-spacings (in angstroms) and  $2\Theta$  diffraction angles of the PLZT crystallographic planes in the 8/65/35 bulk ceramic and thin film shown in Figure II.1.

plane	film	bulk
(100)	4.13 (21.49°)	4.09 (21.72°)
(110)	2.91 (30.68°)	2.89 (30.91°)
(200)	2.06 (44.01°)	2.04 (44.36°)
(210)	1.84 (49.50°)	1.83 (49.85°)
(211)	1.68 (54.70°)	1.67 (55.03°)

**Table III.1.** Firing schedules for automatically (RTP) and manually (CFP) spun thin films.  
The total firing time was 15 minutes. All films consisted of 5 deposited layers.

	time per layer	post-anneal*
1)	3 minutes	None
2)	2 minutes	5 minutes
3)	1 minute	10 minutes
4)	30 seconds**	12.5 minutes
5)	15 seconds**	13.75 minutes

\* Rapid thermal or conventional furnace anneal

\*\* Only possible with RTP

**Table III.2.** Electrical properties of rapid thermally processed thin films.

temp/time (anneal) [min]	K <sub>pol</sub>	tan δ	K <sub>vir</sub>	tan δ	E <sub>C</sub> [kV/cm]	P <sub>R</sub> [μC/cm <sup>2</sup> ]	t [μm]
700/3	715	.085	811	.111	64	10	.48
700/2 (5)	952	.125	985	.150	43	12	.52
700/1 (10)	1090	.147	1190	.155	47	12	.47
700/0.5 (12.5)	1704	.217	2013	.229	41	17	.50
700/0.25 (13.75)	1628	.193	2079	.221	34	10	.49

**TABLE III.3.** Electrical properties of conventional furnace pyrolyzed thin films.

temp/time (anneal) [min]	Kpol	tan δ	Kvir	tan δ	E <sub>C</sub> [kV/cm]	P <sub>R</sub> [μC/cm <sup>2</sup> ]	t [μm]
700/3	597	.090	640	.130	104	11	.41
700/2 (5)	638	.088	814	.156	78	10	.40
700/1 (10)	740	.120	1061	.305	63	13	.41

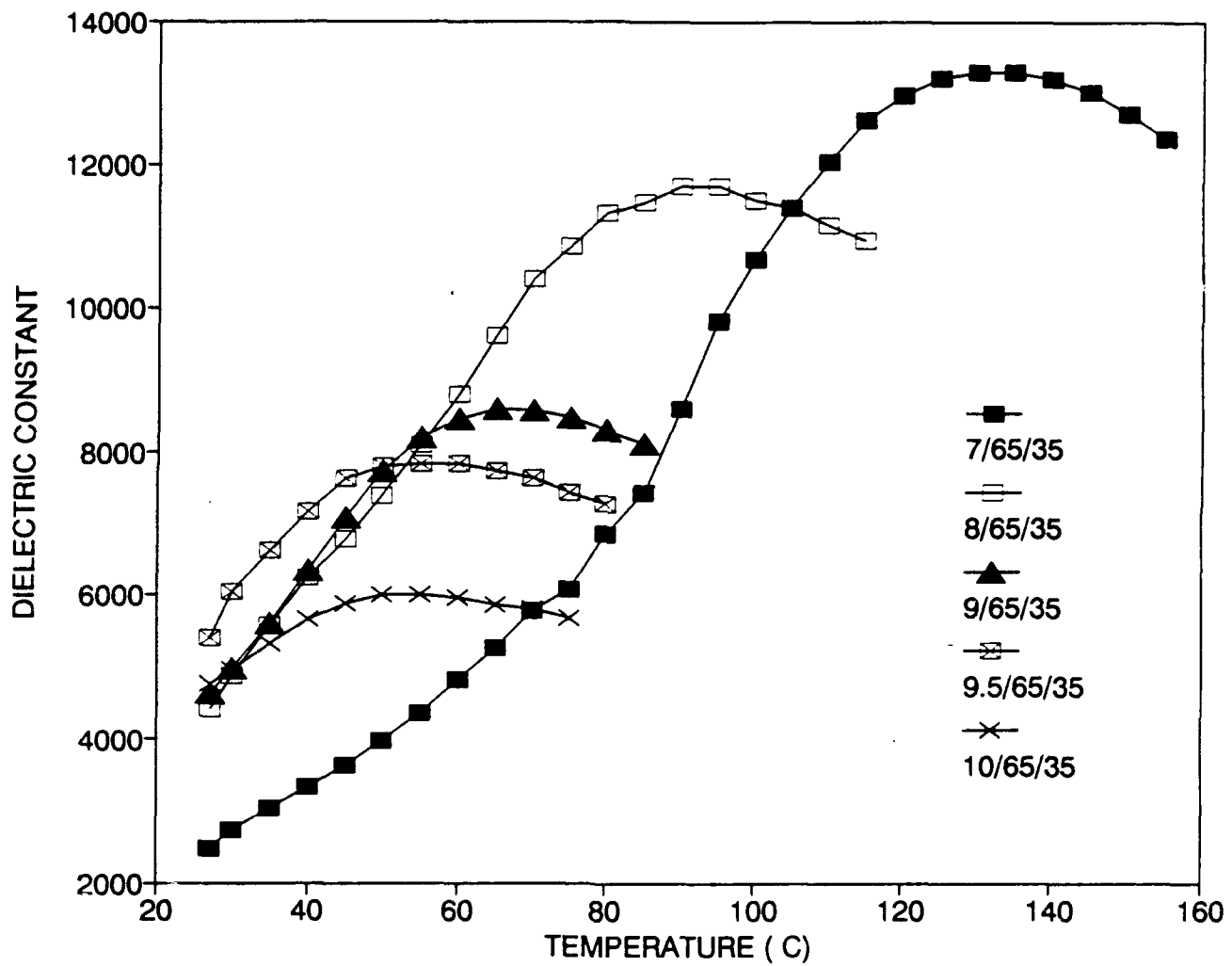
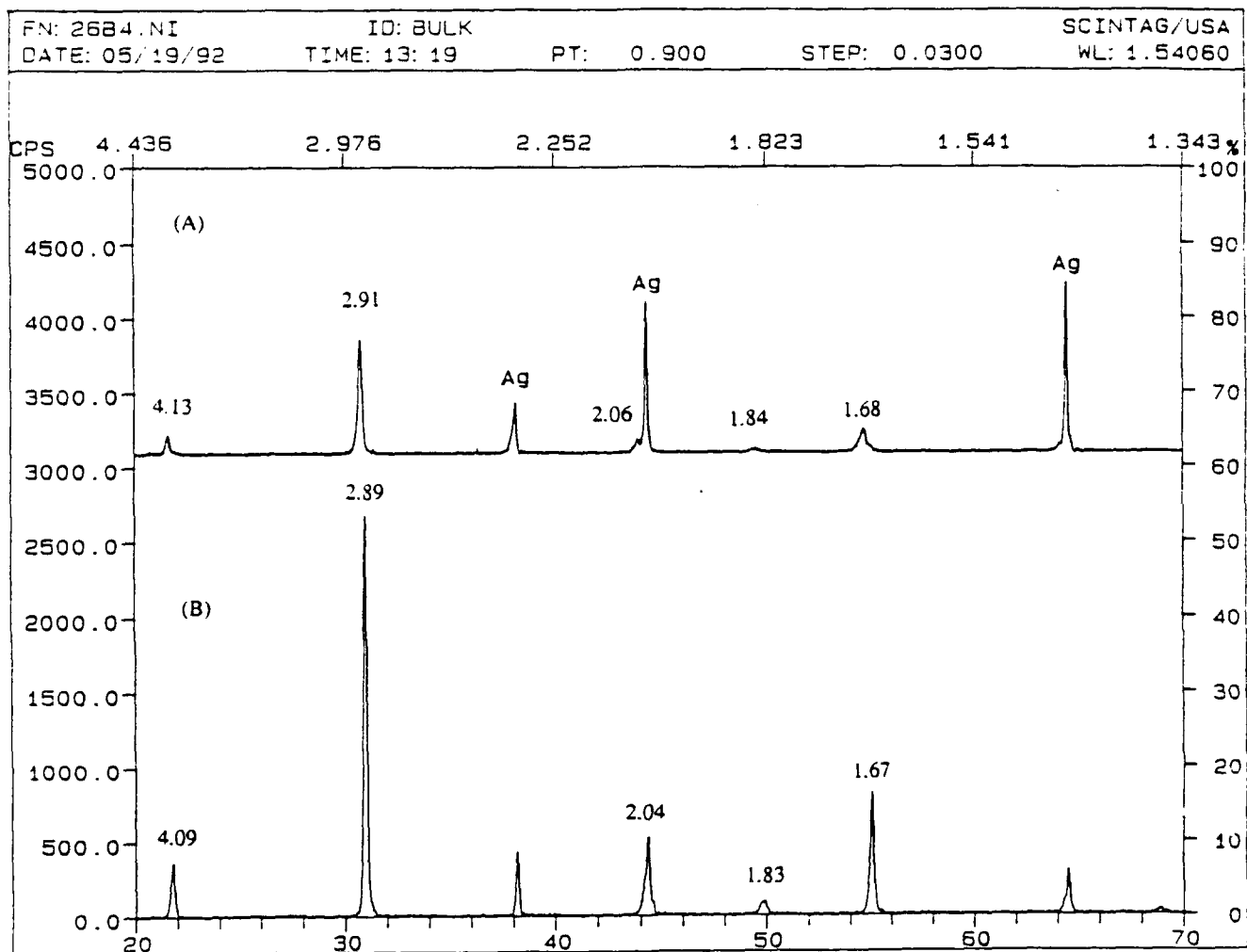
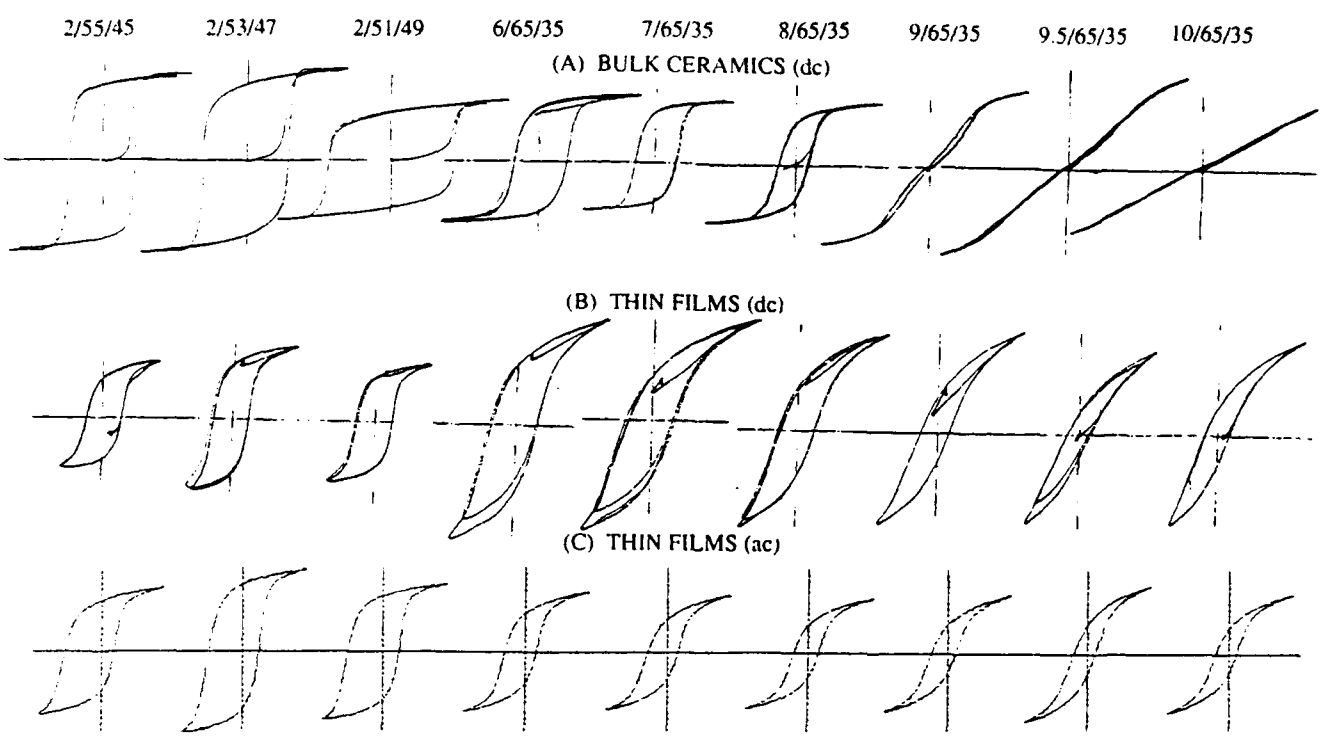


Figure II.1. Curie temperature measurements for bulk PLZT x/65/35.



**Figure II.2.** X-ray diffraction patterns of an 8/65/35 a) thin film and b) bulk ceramic. D-spacings are in angstroms.



**Figure II.3.** Hysteresis loops of several PLZT bulk and thin film materials including a) dc loops of bulk ceramics, b) dc loops of thin films and c) ac loops of thin films.

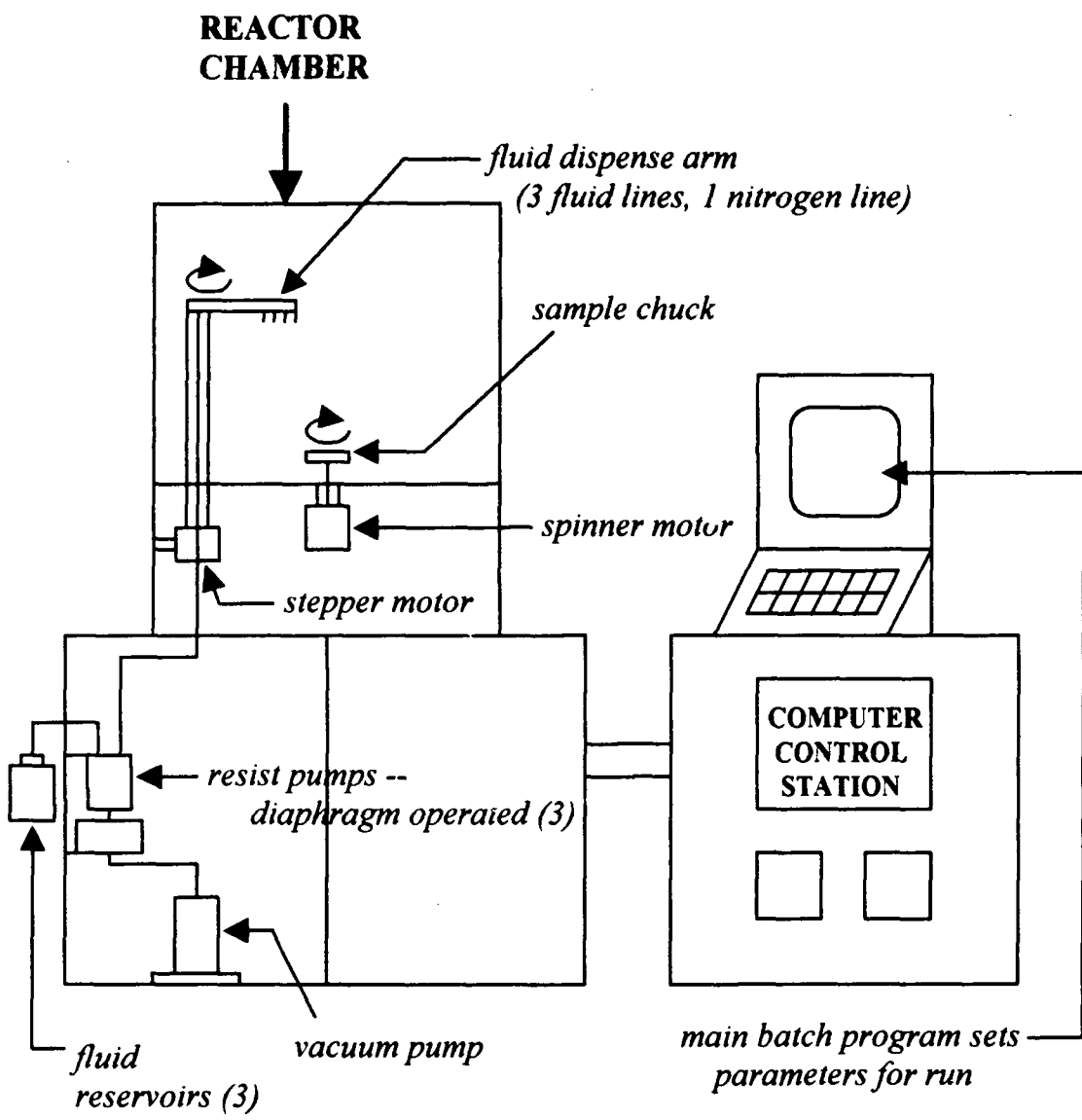


Figure III.1. Fluid dispense system of the automatic spin coat reactor/analyzer.

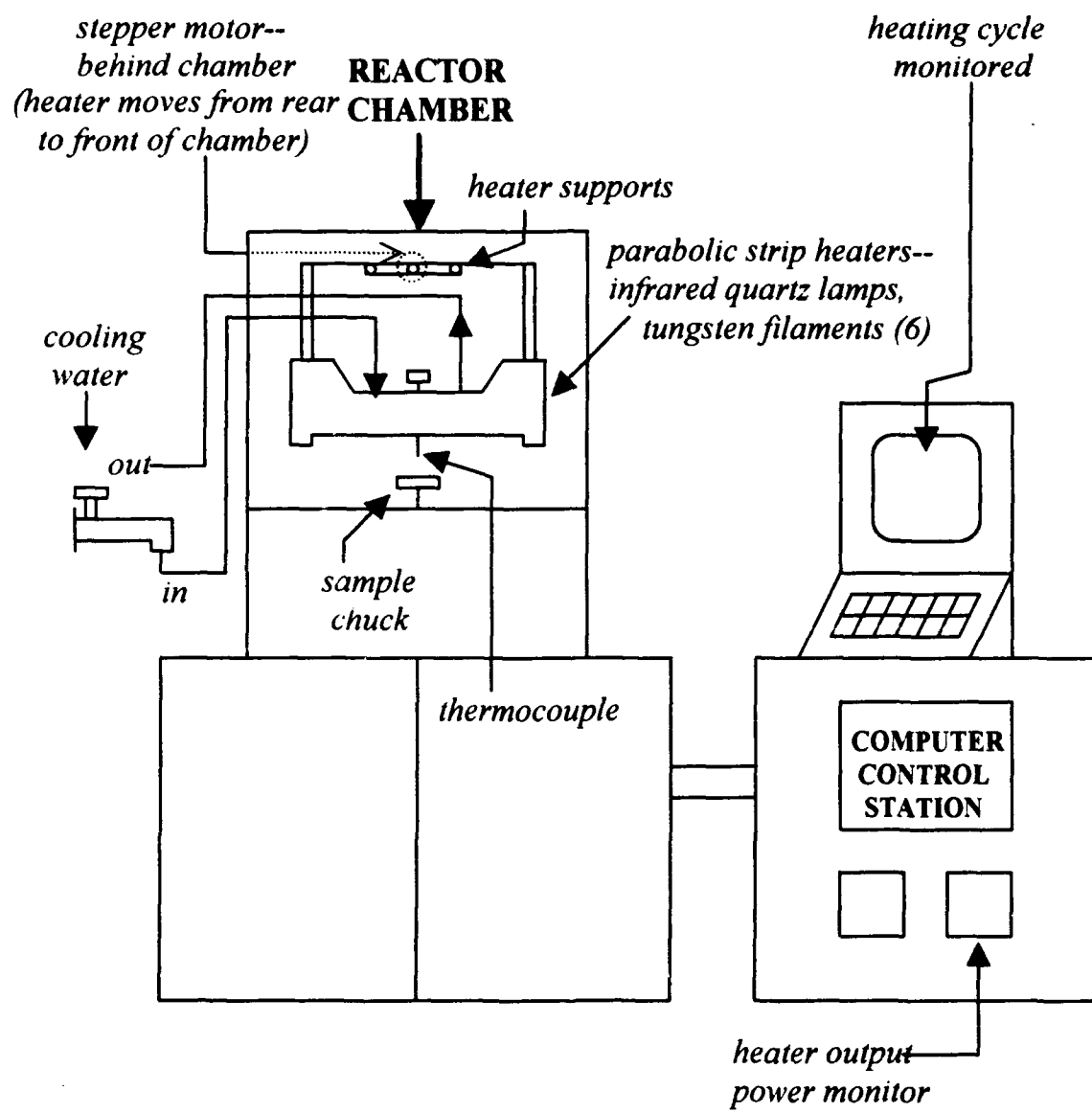
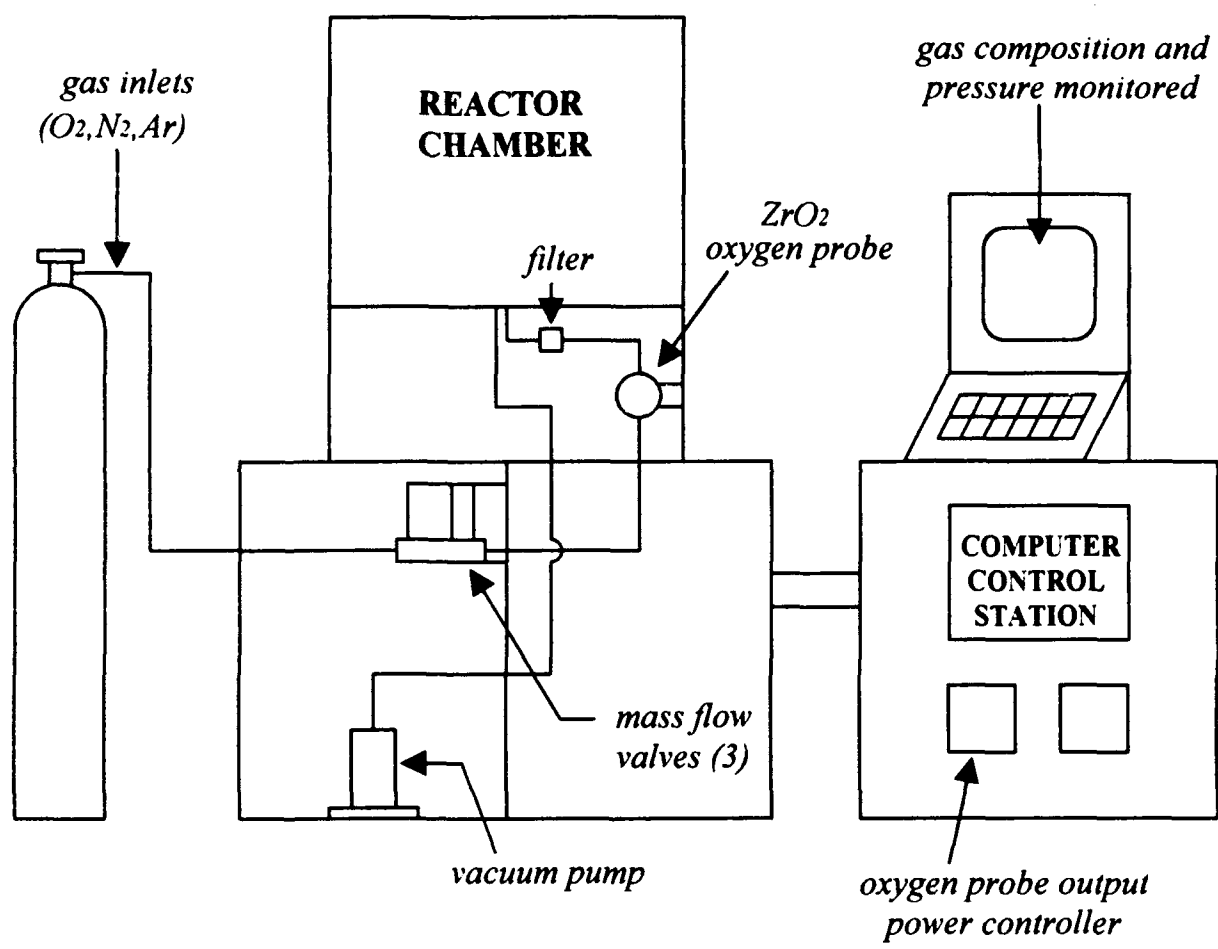
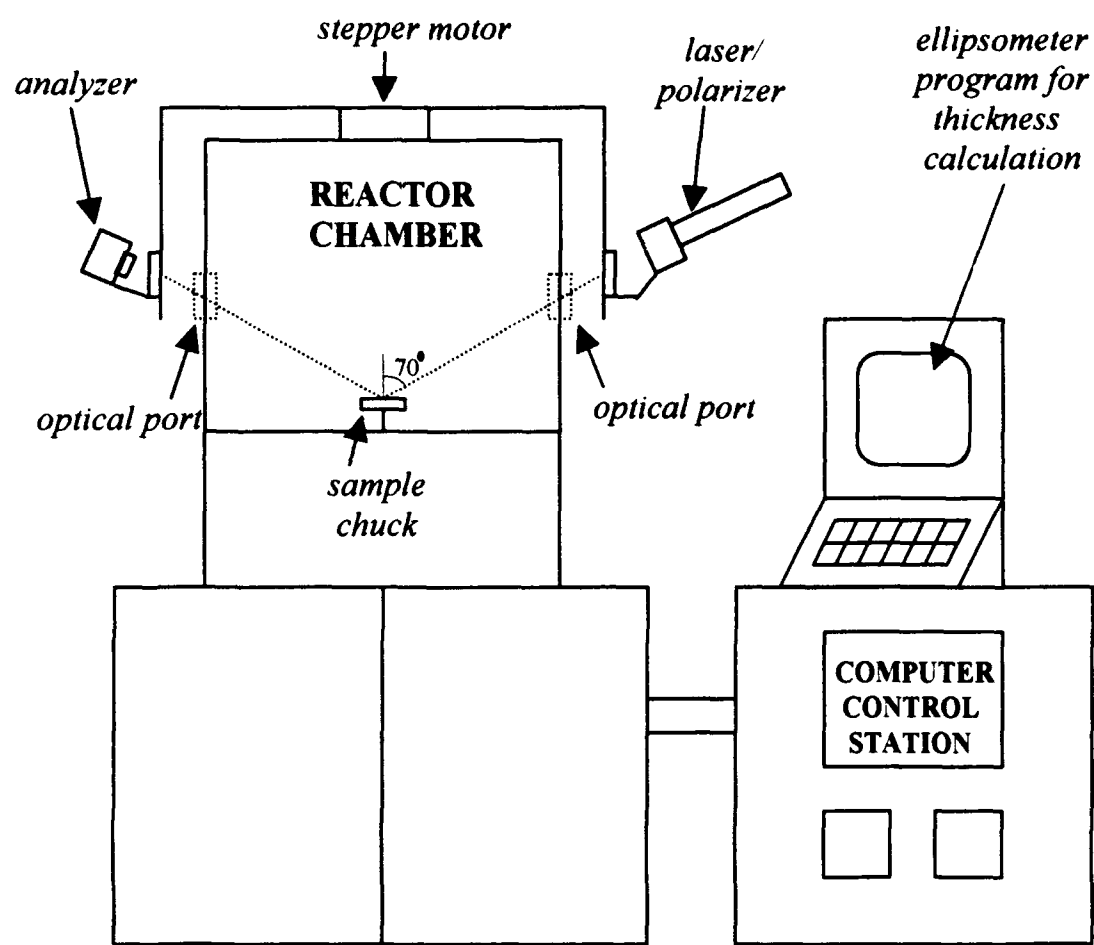


Figure III.2. Rapid thermal processing unit of the automatic spin coat reactor/analyizer.



**Figure III.3.** Atmosphere control system of the automatic spin coat reactor/analyzer.



**Figure III.4.** In-situ laser ellipsometer of the automatic spin coat reactor/analyser.

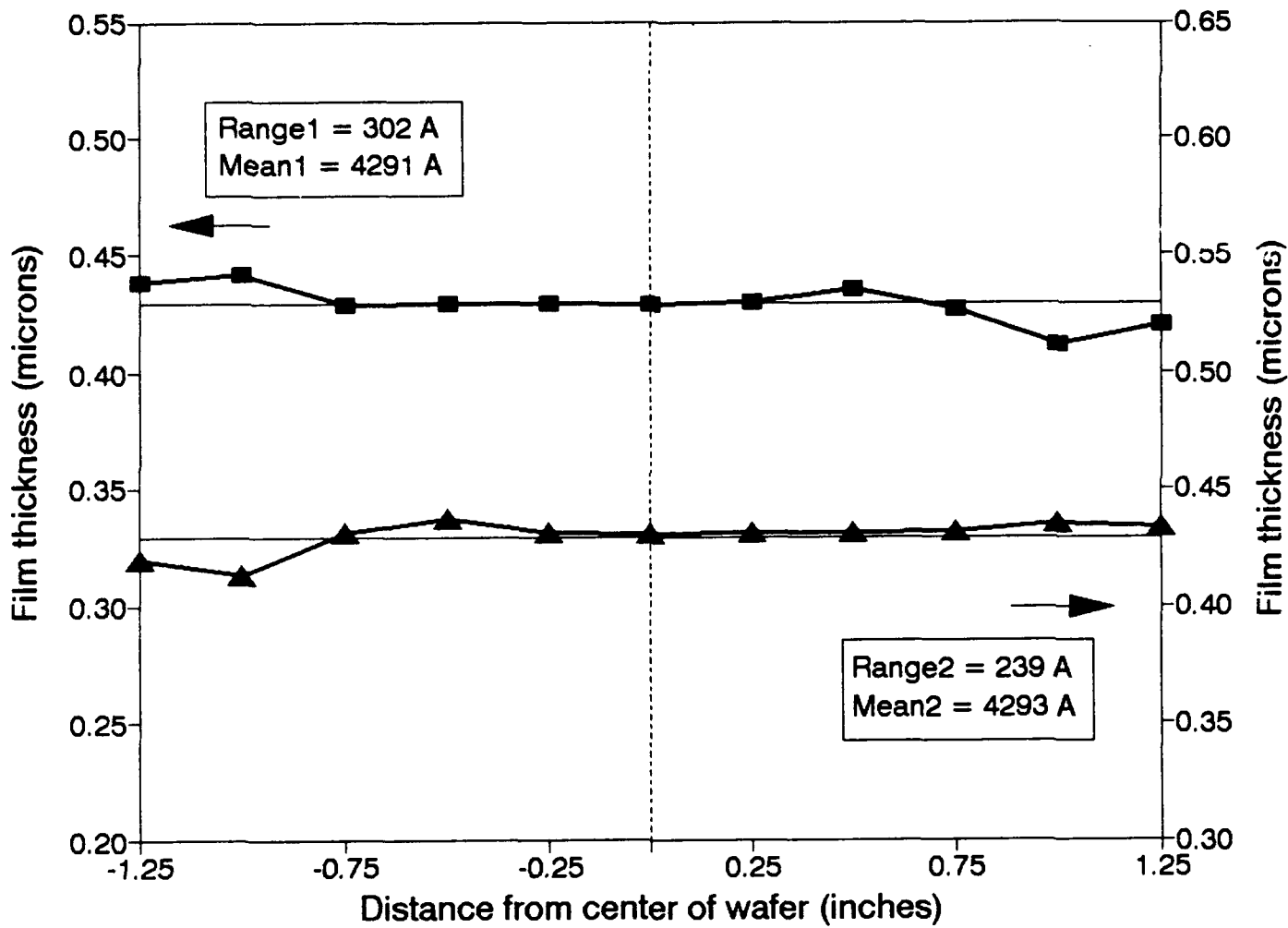


**Figure III.5.** Thickness uniformity profiles of a PLZT film on a 3" Si wafer. The film was rapid thermally processed at 700°C for 1 minute. Thickness measurements represent two scans across perpendicular diameters of the wafer, and the means and ranges are given in angstroms.

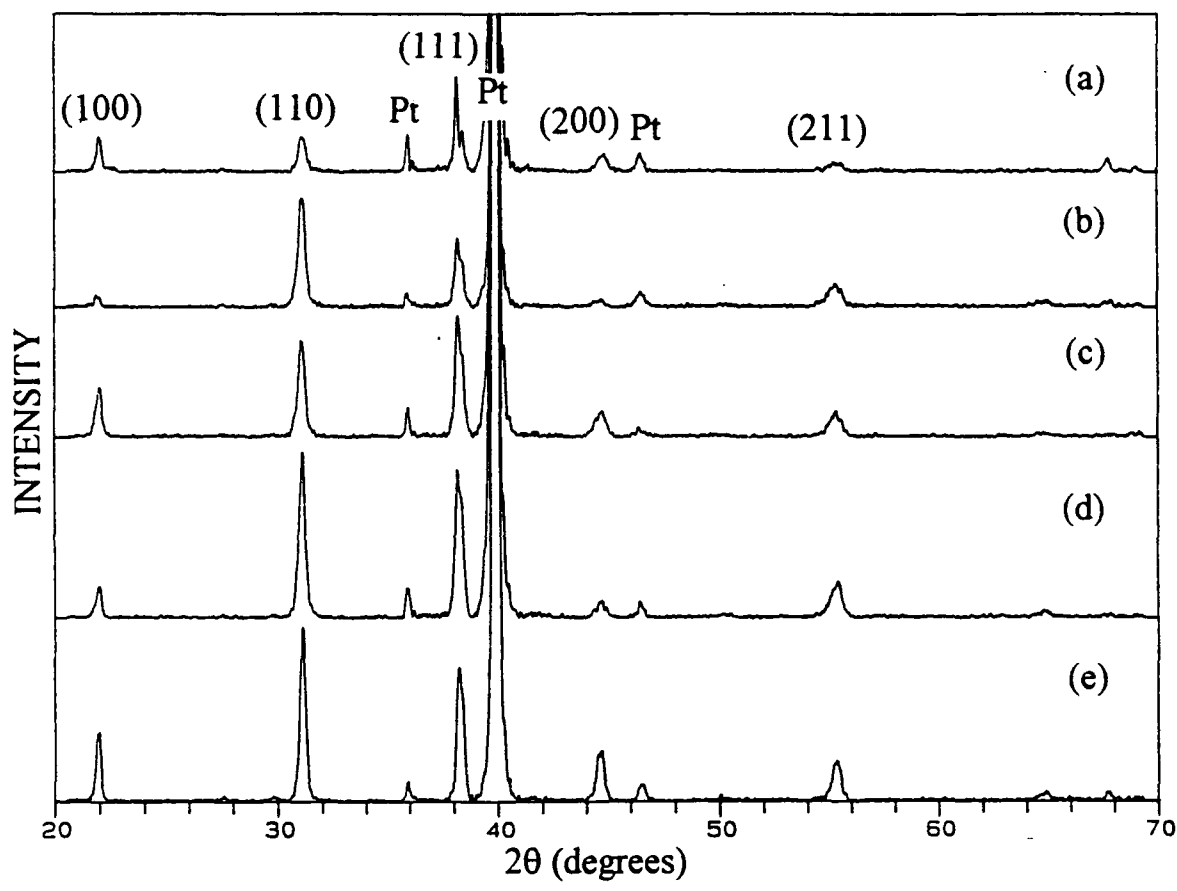


**Figure III.6.** X-ray diffraction patterns of rapid thermally processed PLZT thin films. The firing schedules for the films were (in minutes): a) 700/3, b) 700/2(5), c) 700/1(10), d) 700/0.5(12.5) and e) 700/0.25(13.75).

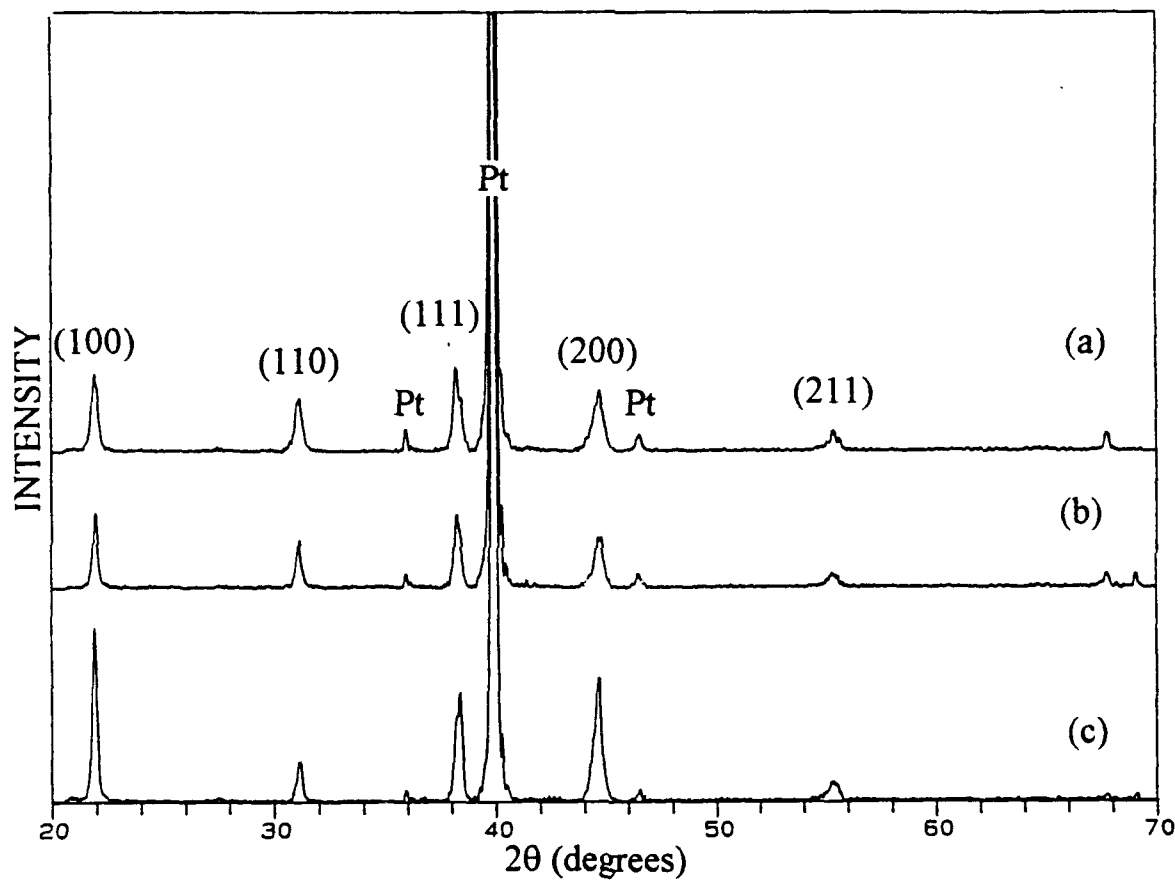


**Figure III.7.** X-ray diffraction patterns of conventional furnace pyrolyzed PLZT thin films. The firing schedules for the films were (in minutes): a) 700/3, b) 700/2(5) and c) 700/1(10).

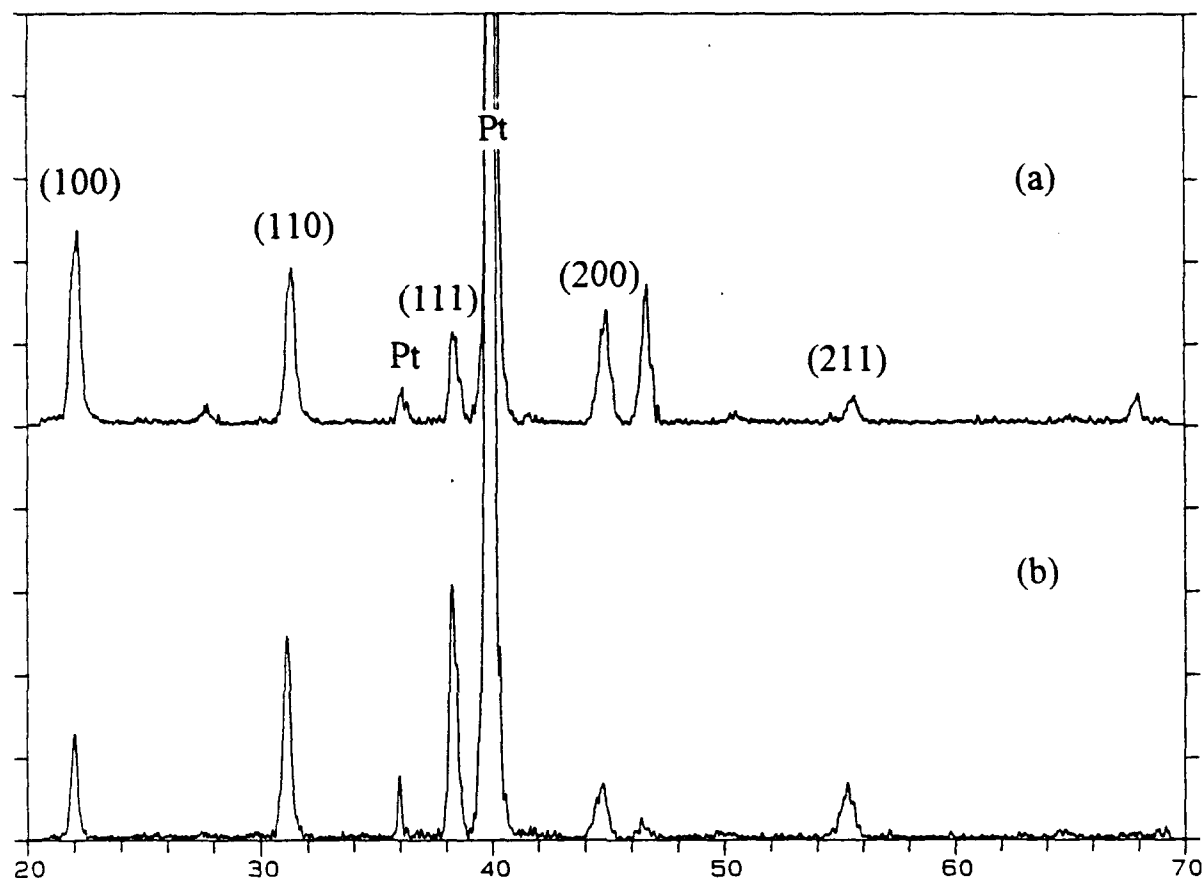


**Figure III.8.** X-ray diffraction patterns of a) a PLZT film on 3" Si rapid thermally processed at 700°C for 1 minute per layer and b) a PLZT film on 5/8" Si rapid thermally processed at 700°C for 1 minute per layer with a post-RTP at 700°C for 10 minutes.

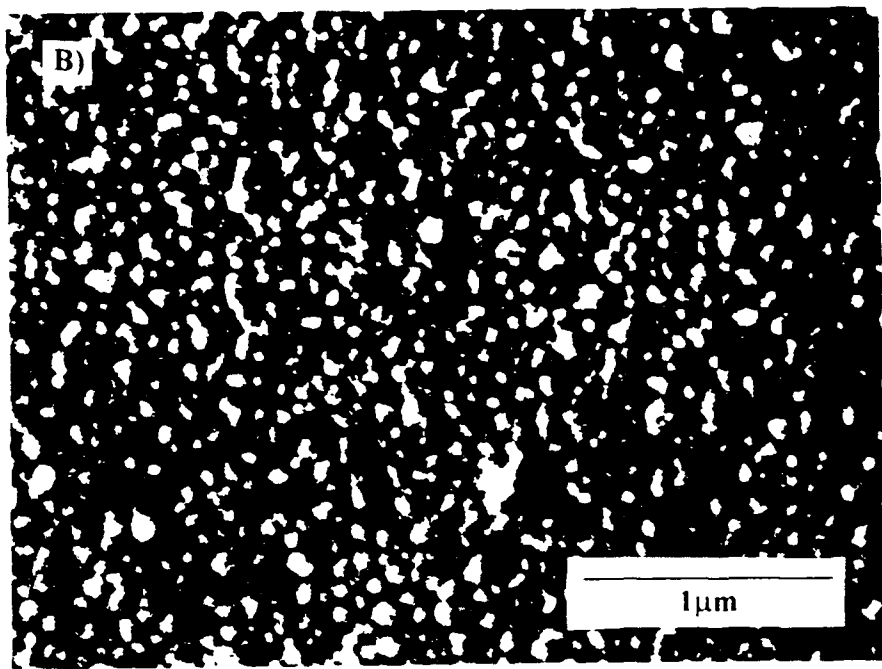
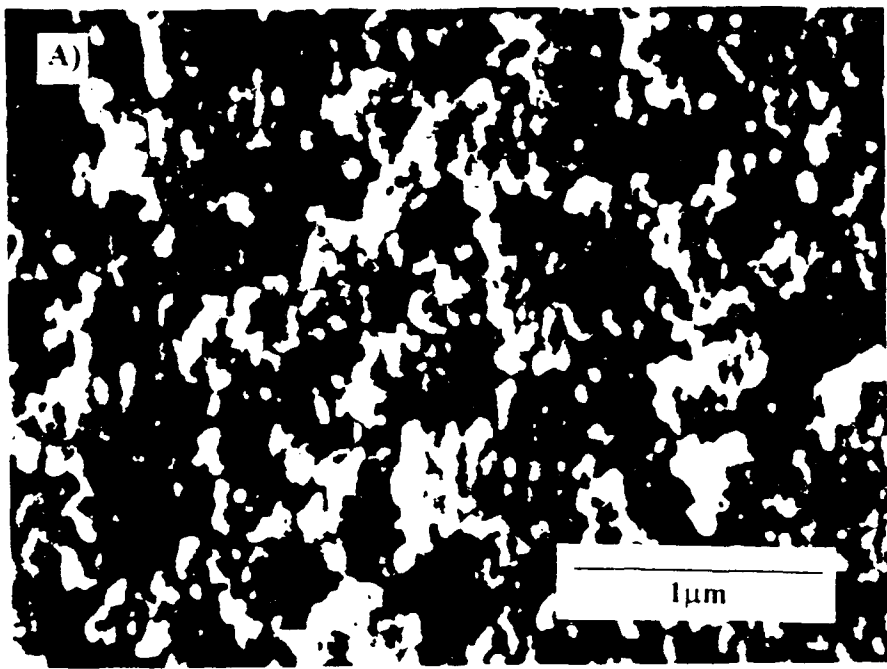


**Figure III.9.** SEM micrographs of rapid thermally processed PLZT thin films. The firing schedules for the films were (in minutes) a) 700·3 and b) 700·0 25(13·75)

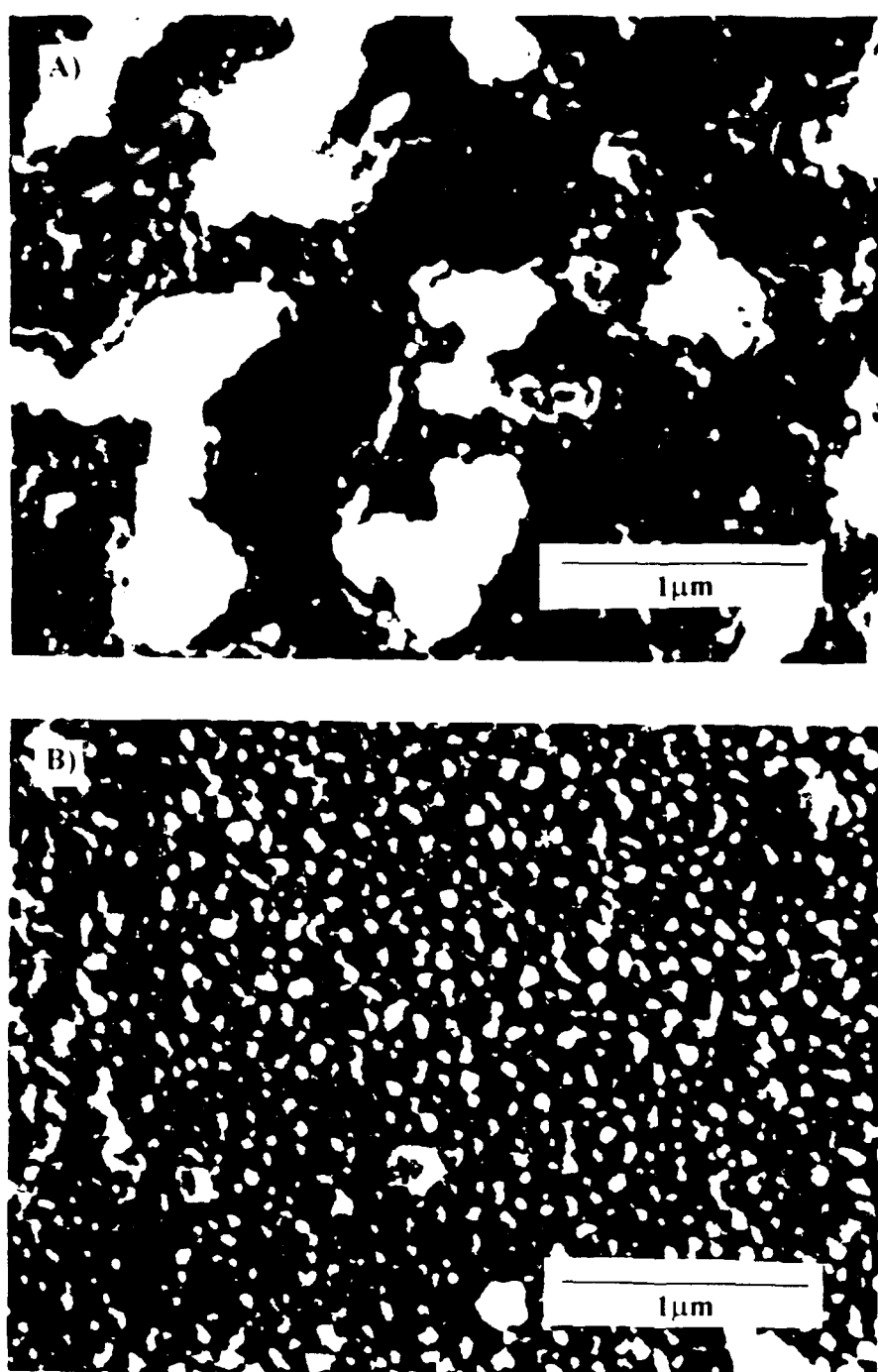


**Figure III.10.** SEM micrographs of conventional furnace pyrolyzed PLZT thin films  
The firing schedules for the films were (in minutes) a) 700 3 and b) 700 1(10)

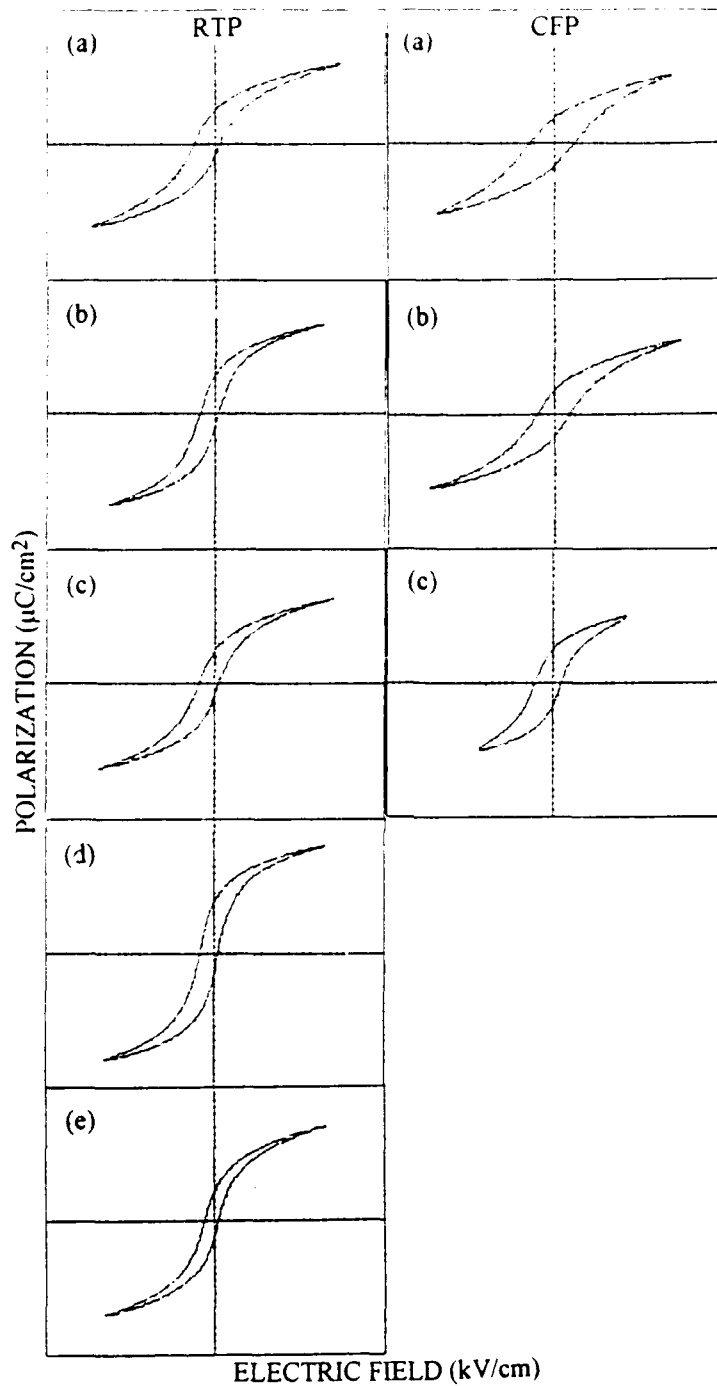


**Figure III.11.** Hysteresis loops of rapid thermally processed (RTP) and conventional furnace pyrolyzed (CFP) PLZT thin films. The firing schedules for the films were (in minutes): a) 700/3, b) 700/2(5), c) 700/1(10), d) 700/0.5(12.5) and e) 700/0.25(13.75). The scale for the y-axis (polarization) is  $15 \mu\text{C}/\text{cm}^2$  per division, and the x-axis (electric field) is  $160 \text{kV}/\text{cm}$  per division.

**Part V.**  
**Sputtered Thin Films and Electrooptics**

# **INTELLIGENT PROCESSING OF FERROELECTRIC THIN FILMS**

## **Annual Report**

### **Part V.**

#### **Sputtered Thin Films and Electrooptics**

Submitted by: Feiling Wang  
Gene Haertling

**The Gilbert C. Robinson Department of Ceramic Engineering  
Clemson University**

## **TABLE OF CONTENTS**

### **I. Introduction**

### **II. Sections**

1. F. Wang, G. H. Haertling and E. Furman, "Electrooptic Measurements of Thin Films by Means of Reflection Differential Ellipsometry."
2. F. Wang and G. H. Haertling, "Birefringent Bistability in  $(Pb,La)(Zr,Ti)O_3$  Thin Films with a Ferroelectric-Semiconductor Interface."
3. K. K. Li, F. Wang and G. H. Haertling, "Antiferroelectric Lead Zirconate Thin Films Derived from Acetate Precursor Systems."
4. F. Wang, K. K. Li, E. Furman and G. H. Haertling, "Discrete Electrooptic Response in Lead Zirconate Thin Films from a Field-Induced Phase Transition."
5. F. Wang, K. K. Li and G. H. Haertling, "Transverse Electrooptic Properties of Antiferroelectric Lead Containing Thin Films."
6. F. Wang and G. H. Haertling, "Transverse Electrooptic Properties of Magnetron Sputtered PLZT Thin Films."
7. F. Wang and G. H. Haertling, "A PLZT Optical Phase Modulator and its Applications."

## INTRODUCTION

This report summarizes the progress on the ONR project "Intelligent Processing of Ferroelectric Thin Films" in the second year of research. The main topics covered in this report include sputter-deposited ferroelectric thin films, a newly developed reflection-mode differential ellipsometry, electrooptic characterization and the applications of ferroelectric/electrooptic materials as optical modulation and storage media.

This document is organized in such a way that the detailed description of the progress in each area is contained in one or more sections. The remainder of this introduction highlights these progresses and guides reviewers to the corresponding sections.

As one of the film deposition techniques being studied in this project, deposition by magnetron sputtering using PLZT powder derived from an acetate precursor system has produced high quality PLZT thin films in terms of their dielectric and electrooptic properties (Section 6 and 2). These sputter-deposited films have enabled us to carry out a systematic investigation on their dielectric properties and electrooptic properties.

A phenomenon of birefringent bistability has been observed in ferroelectric thin films which are electrode with a metal and a semiconductor layer (Section 2). A nonvolatile electrooptic switching is realized by applying bipolar electric pulses to the MFS structure. Such birefringent bistability has great potential for performing some key functions in integrated optical or optoelectronic devices.

The exploration of the optical usefulness of antiferroelectric materials has prompted the study of deposition methods for producing optical quality antiferroelectric thin films. A suitable technique has been developed for such purpose . The deposition technique involves a dip-coating method using an acetate precursor (Section 3).

The study of the electrooptic properties of antiferroelectric thin films has gained significant momentum (Section 3-5). With a newly developed reflection-mode differential ellipsometry (Section 1), a digital electrooptic response was observed to exist in lead zirconate thin films for the first time. Under a dc bias the antiferroelectric lead zirconate thin film also exhibits a birefringent bistability.

The development and improvement of a reflection-mode differential ellipsometry has been given special attention. This measuring technique has become a powerful tool in studying the birefringent electrooptic properties of various thin film materials (Section 1). The modeling of the differential ellipsometry by taking into account the multiple reflection has resulted in a more sophisticated and reliable measuring technique (Section 2, 4). It is shown by the model that this measuring method may be utilized to separate the extraordinary index from the ordinary index in their contribution to the field-induced birefringence.

A prototype optical phase modulator has been produced from a PLZT material derived from an acetate precursor (Section 7). By choosing the dc bias, the modulator may be operated in either the linear or the quadratic region. Therefore the modulating frequency is either equal to or double the driving signal.

## **SECTION 1**

# ELECTROOPTIC MEASUREMENTS OF THIN FILMS BY MEANS OF REFLECTION DIFFERENTIAL ELLIPSOMETRY

Feiling Wang, Gene H. Haertling and Eugene Furman

Department of Ceramic Engineering

Clemson University

Clemson, SC 29634-0907

## I. Introduction

The primary role of electrooptic thin film materials in integrated optical and optoelectronic devices is to modulate guided light waves with respect to their optical phase or amplitude. Such modulations are achieved by means of the electric-field-controlled indices of refraction in the thin film materials via their transverse electrooptic properties. The characterization of the electrooptic properties of the thin film materials is, therefore, of obvious importance. In order to obtain single-mode propagation, the thickness of the electrooptic thin films, as waveguiding media, is usually less than the wavelength of the light. Accurate and reliable detection of the transverse electrooptic effects in these thin films has remained a difficult and sometimes a challenging task. In terms of the configuration of the electrodes and the light propagation, the reported detection methods may be summarized under the following three categories: 1) the transmission method for thin films grown on transparent substrates<sup>1-5</sup>; 2) the reflection-mode detection for thin films grown on opaque substrates<sup>6-9</sup> and 3) waveguide-mode method<sup>10</sup>. Under the first two categories, either intensity-sensitive or phase-sensitive detection scheme can be adopted for the electrooptic characterization.

The transmission method of category 1 is the most widely used technique where planar electrode pairs are fabricated on thin films. Despite its advantage of simplicity, a major limitation of this method is that it is only applicable to thin films deposited on transparent substrates while many integrated devices are fabricated on substrates which are opaque to the light wavelength of concern. Because of the planar structure of the electrodes in method 1, the electric-field distribution in the gap may be significantly nonuniform<sup>11</sup>; and thus the accuracy of

the measurements is unsatisfactory. Only qualitative results were obtain using method 2 with planar electrodes; again, the field nonuniformity is an obstacle. On the other hand, method 2 with parallel electrode configuration has proved both reliable and convenient. In conjunction with a phase detection scheme, method 2 has been successfully used in characterizing various electrooptic thin films deposited on opaque substrates. Also with parallel electrodes, method 3 is an alternative way of evaluating the field-induced change of indices. An advantage of method 3 is its capability of resolving the change in ordinary index from the change in the extraordinary index.

In this paper the reflection-mode phase-detection method is discussed in detail. Emphasis is placed upon the effects of multiple reflections on the accuracy of the measurements - a topic which has rarely been addressed in electrooptic measurements; but nevertheless, is important to all reflection-mode and transmission-mode methods. We intend to show how multiple reflection significantly complicates the interpretation of the measured signal thus leads to necessary corrections to the calibration method in some cases. We will also demonstrate how the interference from the multiple reflections may be utilized to separate the contribution of the extraordinary index from that of the ordinary index of the field-induced birefringence.

## II. The Principles of the Measurement

### 1. Single-Reflection Model

The principle of the reflection-mode phase-sensitive detection involves a differential-ellipsometric technique wherein the field-induced change in the ellipticity of the reflected light is measured. A parallel electrode structure is employed as shown in Figure 1. Electric signals are applied to the bottom and top electrodes during the measurement. Under an external electric field, the sandwiched thin film becomes optically uniaxial with its c axis parallel the normal of the surface as a result of the birefringent electrooptic effect. In order to detect the field-induced deformation of the index ellipsoid the probing light must be incident with a finite incident angle. The optical arrangement of the detection system is depicted in Figure 2. Two polarizers are inclined 45° with respect to the

incident plane and mutually crossed. The polarization state of the probing laser beam is modulated in a periodic manner by means of an optical phase modulator, M. The purpose of the inserted optical compensator, C, is to adjust the phase angle of the probe beam and to calibrate the detected signal.

In order to discuss the mechanism of the detection technique in a progressive way we first make a single reflection approximation by neglecting the multiple reflection of the thin film structure. At first we calculate the change of the indices along the two principal axes for the probing light propagating along the diffraction direction defined by  $\theta_1$ . We designate the light component polarized in the incident plane (defined by the incident beam the normal of the film surface) as the p-polarization and the component polarized perpendicularly to the incident plane as the s-polarization. In the following calculation, whenever p or s appears as a subscript the referred quantity is associated with p- or s-polarization respectively. In an uniaxial material the index of refraction,  $n_p(\theta_1)$ , for the p-polarization light propagating along  $\theta_1$  is given by<sup>12</sup>

$$\frac{1}{n_p^2(\theta_1)} = \frac{\cos^2 \theta_1}{n_o^2} + \frac{\sin^2 \theta_1}{n_e^2} . \quad (1)$$

For small field-induced changes in  $n_e$  and  $n_o$  we have

$$\begin{aligned} \Delta n_p(\theta_1) &= \sin^2 \theta_1 \Delta n_e + \cos^2 \theta_1 \Delta n_o ; \\ \Delta n_s &= \Delta n_o \end{aligned} \quad (2)$$

Therefore, after a single reflection, the field-induced phase shift of the p-component with respect to the s-component is given by

$$\Delta\Gamma = \frac{4\pi d}{\lambda} \frac{\sin^2 \theta_1}{\cos \theta_1} (\Delta n_e - \Delta n_o) , \quad (3)$$

where d is the thickness of the electrooptic thin film and  $\lambda$  is the wavelength of the light beam. Because  $n_e \approx n_o$ , the difference in the diffraction angles between the

two polarized component has been neglected in the above equation. In terms of the incident angle  $\theta_0$ , Equation (3) can be rewritten as

$$\Delta\Gamma = \frac{4\pi d}{\lambda} \frac{\sin^2 \theta_0}{n_o \sqrt{n_o^2 - \sin^2 \theta_0}} (\Delta n_s - \Delta n_o). \quad (4)$$

The above phase shift,  $\Delta\Gamma$ , is to be measured by using a phase-detection scheme described below.

Assuming the phase modulation provided by the optical phase modulator is given by a periodic function  $R(t)$ , the complex amplitudes for the two components of the incident beam may be written as

$$E_s = 1 \\ E_p = e^{-j[R(t)+\Gamma_c]}, \quad (5)$$

where  $\Delta\Gamma_c$  is the phase shift of the inserted optical compensator. After a single reflection the p-component picks up a phase shift  $\Gamma_p$ ; and the s-component picks up a phase shift  $\Gamma_s$ . The amplitudes of the reflected light then become

$$E_s = R_s e^{-j\Gamma_s} \\ E_p = R_p e^{-j[R(t)+\Gamma_c+\Gamma_p]}, \quad (6)$$

where  $R_s$  and  $R_p$  are the reflection coefficients of the thin film sample for s-component and p-component, respectively. Passing the second polarizer, the amplitude of the light that arrives at the photodetector is given by

$$E_A = \frac{1}{\sqrt{2}} \left\{ R_p e^{-j[R(t)+\Gamma_c+\Gamma_p]} - R_s e^{-j\Gamma_s} \right\}. \quad (7)$$

The detected intensity of the reflected light beam, therefore, takes the following form

$$I = -R_p R_s \cos [R(t) + \Gamma_c + \Gamma_p - \Gamma_s] + \frac{1}{2}(R_p^2 + R_s^2) . \quad (8)$$

The phase shift  $\Gamma_p$  consists of a zero-field part  $\Gamma_p(0)$  and a field-induced part  $\Delta\Gamma_p$ , (the same applies to  $\Gamma_s$ ):

$$\begin{aligned} \Gamma_p &= \Gamma_p(0) + \Delta\Gamma_p \\ \Gamma_s &= \Gamma_s(0) + \Delta\Gamma_s \end{aligned} \quad (9)$$

If one adjusts the optical compensator so that  $\Gamma_c + \Gamma_p(0) + \Gamma_s(0) = 0$ , the intensity of the detected light may be rewritten as

$$I = -R_p R_s \cos(M \cos \Omega t + \Delta\Gamma_p - \Delta\Gamma_s) + \frac{1}{2}(R_p^2 + R_s^2) \quad (10)$$

In the above expression the modulation function  $R(t)$  has been replaced by a sinusoid function of amplitude  $M$  and frequency  $\Omega$ , as provided by many commercially available phase modulating devices.

By setting the reference signal of the lock-in amplifier as  $\cos \Omega t$ , the output signal of the lock-in amplifier,  $S$ , is proportional to the Fourier amplitude of the light intensity associated with  $\cos \Omega t$ , which is given by

$$S = C \int_0^T I \cos \Omega t dt = CJ_1(M) \sin(\Delta\Gamma_p - \Delta\Gamma_s) . \quad (11)$$

Under single reflection approximation, the difference in the field-induced phase shifts for the two polarization components,  $\Delta\Gamma_p - \Delta\Gamma_s$ , is given by Equation (3). In most practical cases where the phase shift  $\Delta\Gamma$  is very small, the output of the lock-in amplifier may be rewritten as

$$S = C(\Delta n_s - \Delta n_o) . \quad (12)$$

The proportional constant  $C$  in the above equation can be calibrated using the inserted optical compensator.

A single-reflection model may be adequate for samples where the reflection coefficient of the top electrode is small. In general the reflection coefficients are functions of the incident angle and different from p-polarization to s-polarization. Another special case when the single-reflection model may be adequate is that the probe beam is incident at the Brewster angle for the p-component. Significant usage of Brewster angle in the detection technique will be discussed in the following sections.

## 2. Multiple-Reflection Model

As has been mentioned previously, the single-reflection model is only a simplification of the real world situation where multiple reflection of the light beam occurs in the parallel thin film structure. In the presence of multiple reflections the amplitude for both p- and s-component arriving at the photodetector is the coherent summation of each partial amplitude. In this situation, Equation (11) remains valid. However, the measured phase difference,  $\Delta\Gamma = \Delta\Gamma_p - \Delta\Gamma_s$ , is no longer, in general, proportional to the field-induced birefringence  $\Delta n = \Delta n_s - \Delta n_o$ , as given by Equation (4).

Now our task is to find the relationship between the detected phase difference  $\Delta\Gamma$  and the field-induced change of indices,  $\Delta n_s$  and  $\Delta n_o$ , by taking into account the multiple reflections. To simplify the calculation we omit the top electrode so that the multiple reflection occurs between the bottom film-substrate boundary and the top ambient-film boundary. This simplification resembles the real cases when the thickness of the top electrode is much smaller than the wavelength of the light or when the index of the top electrode is similar to that of the electrooptic thin film.

Assuming the reflection coefficient of the ambient-film boundary is  $r$ ; and the reflection coefficient of the film-substrate boundary is  $\rho$ , the summation of an infinite series of the partial amplitudes gives the following complex amplitudes for the summed s- and p-components:

$$E_s = \frac{r_s + \rho_s e^{j\delta_s}}{1 + r_s \rho_s e^{j\delta_s}} \equiv R_s e^{-j\Gamma_s}, \quad (13)$$

$$E_p = \frac{r_p + \rho_p e^{j\delta_p}}{1 + r_p \rho_p e^{j\delta_p}} e^{-j[R(t) + \Gamma_c]} \equiv R_p e^{-j\Gamma_p} e^{-j[R(t) + \Gamma_c]}$$

where  $\delta_s$  and  $\delta_p$  are the constant phase angle between the adjacent partial waves for s- and p components respectively. These two quantities can be expressed in terms of the incident angle, film thickness and indices of refraction:

$$\begin{aligned} \delta_s &= 4\pi n_s \frac{d}{\lambda} \cos\theta_1 + \phi_s \\ \delta_p &= 4\pi n_p \frac{d}{\lambda} \cos\theta_1 + \phi_p \end{aligned}, \quad (14)$$

where  $\phi_s$  and  $\phi_p$  are the phase shifts due to the bottom reflection for s- and p-components, respectively. It can be shown that the relationship between the summed phase angle  $\Gamma_s(\Gamma_p)$  and  $\delta_s(\delta_p)$  in Equation (13) is given by the following relation:

$$\Gamma = \frac{\rho(1-r^2) \sin \delta}{r(1+\rho^2) + \rho(1+r^2) \cos \delta}. \quad (15)$$

Since the above equation applies to both polarizations the subscripts associated with all the quantities have been omitted. The differentiation of Equation (15) with respect to  $\delta$  gives the change rate of the measured phase shift  $\Delta\Gamma_s(\Delta\Gamma_p)$  caused by a small change in  $\delta_s(\delta_p)$ . The latter is directly related to the field-induced indices

change through Equation (14). For both polarizations, the change rate is found to be given by:

$$w \equiv \frac{d\Gamma}{d\delta} = \frac{r\rho(1-r^2)(1+\rho^2)\cos\delta + \rho^2(1-r^2)}{\rho^2(1-r^2)^2 \sin^2\delta + [r(1+\rho^2) + \rho(1+r^2)\cos\delta]^2}. \quad (16)$$

Again, all the subscripts are omitted in the above equation. Finally, the detected field-induced phase shift  $\Delta\Gamma = \Delta\Gamma_p - \Delta\Gamma_s$ , may be expressed in terms of the field-induced indices change by combining Equations (16), (14), (2) and (3):

$$\Delta\Gamma = \frac{4\pi d}{\lambda \cos\theta_i} [w_p \sin^2\theta_i \Delta n_e - (w_s - w_p \cos^2\theta_i) \Delta n_o]. \quad (17)$$

With given optical properties of the thin film and the substrate, both  $w_s$  and  $w_p$  can be expressed as functions of the incident angle through Equation (16). It can be seen that unless  $w_s$  and  $w_p$  happen to have the same value at certain incident angles the measured phase shift  $\Delta\Gamma$  is not proportional to the field-induced birefringence  $\Delta n = \Delta n_e - \Delta n_o$ .

The evaluation of  $w_s$  and  $w_p$  involves the calculation of the reflection coefficients  $r$  and  $\rho$  when the incident angle and the indices of the thin film, as well as that of the substrate, are known. In general, both  $w_s$  and  $w_p$  are complicated functions of the incident angle and indices of the materials and possess different functional forms<sup>13</sup>. Their values may be calculated with the help of a computer. As an example,  $w_s$  and  $w_p$  are computed for the case of a typical perovskite thin film grown on a platinum bottom electrode. The thickness of the thin film is taken to be equal to unity wavelength and the index of refraction to be 2.5. The calculated  $w_s$  and  $w_p$  are plotted in Figure 3 as functions of the incident angle. It is obvious that the contribution of the extraordinary index and the ordinary index to the measured phase shift vary with the incident angle according to their respective functional forms. In other words, the field-induced index changes may get amplified or reduced as a result of the multiple reflection. In this

example, except in the neighborhood of incident angle of  $52^\circ$ , where  $w_s = w_p$ , the detected signal given by Equation (17) is not proportional to the field-induced birefringence  $\Delta n = \Delta n_e - \Delta n_o$ .

Comparing Equation (17) and (3) we find that  $w_p$  may be simply termed as the amplification of the extraordinary index change  $\Delta n_e$ ; however, the amplification of the ordinary index change takes a little more complicated form. It is easy to see that wherever  $w_s = w_p$ , the amplifications for both index changes are the same so that the detected phase shift is proportional to the field-induced birefringence of the film. An incident angle that deserves special attention is the Brewster angle for the p-component, at which  $r_p$  vanishes. It is easy to verify from Equation (16) that at the Brewster angle  $w_p = 1$ . Because the Brewster angle is easy to determine, it is sometimes a preferred incident angle for measurements.

Although the difference in the functional forms between  $w_s(\theta_0)$  and  $w_p(\theta_0)$  greatly complicates the interpretation of the detected phase shift, it provides a means of determining both  $\Delta n_e$  and  $\Delta n_o$  from the experiment. The scheme of doing this is to measure the field-induced phase shift of the electrooptic thin film at two different incident angles,  $\theta'_0$  and  $\theta''_0$ . From the model the values of  $w_p$  and  $w_s$  at these two incident angles can be calculated. Theoretically, the field-induced index changes,  $\Delta n_e$  and  $\Delta n_o$ , can be solved from the following set of equations:

$$\begin{aligned}\Delta\Gamma' &= \frac{4\pi d}{\lambda \cos\theta'_1} [w'_p \sin^2 \theta'_1 \Delta n_e - (w'_s - w'_p \cos^2 \theta'_1) \Delta n_o] \\ \Delta\Gamma'' &= \frac{4\pi d}{\lambda \cos\theta''_1} [w''_p \sin^2 \theta''_1 \Delta n_e - (w''_s - w''_p \cos^2 \theta''_1) \Delta n_o]\end{aligned}, \quad (18)$$

where  $\theta'_1$  and  $\theta''_1$  are the diffraction angles associated with the chosen incident angles,  $\theta'_0$  and  $\theta''_0$ , respectively. The reliability of this method in determining the  $\Delta n_e$  and  $\Delta n_o$  depends on how realistic the calculated  $w_p(\theta_0)$  and  $w_s(\theta_0)$  are from the model.

Now let us examine how well the present multiple reflection model predicts the profile of the detected field-induced shift as a function of the incident angle. To compare with experimental results, we choose input parameters associated with a lead lanthanum zirconate titanate (PLZT)<sup>14</sup> thin film, 680 nm thick, grown on a platinum coated substrate. Figure 4 represents the angular dependence of  $w_s$  and  $w_p$  calculated from the model. To calculate the profile of the field-induced shift we assume that  $\Delta n_o / \Delta n_s = -4$  in evaluating Equation (17). The resultant phase retardation as a function of the incident angle is shown by the 'corrected' curve in Figure 5. The phase retardation as a function of the incident angle calculated from the single reflection model, i.e., Equation (3), is shown by the 'uncorrected' curve in the same figure. Because of the interference from the multiple reflection, the 'corrected' curve has dramatic feature differences from the 'uncorrected' curve. In general, because of the change in the phase relation between the adjacent reflected waves, the detected phase shift oscillates with the change of the incident angle or the thickness of the film.

The field-induced phase retardation as a function of the incident angle was measured from a thin film sample whose parameters were those been used in the above model calculation. The measurements were done by successively measuring the phase-retardation vs. applied loops from a 8/65/35 PLZT thin film sample at different incident angles while keeping the same cycling voltage. The detected phase shift at the applied voltage of 10 volts are plotted in Figure 6 as a function of the incident angle. As shown in the figure, the measured phase retardation shows a strong dependence on the incident angle. As predicted by the model, a peak of phase retardation occurs in the measured curve; however, the peak position is shifted to a larger angle by approximately 10 degrees from the model prediction. The discrepancy in the peak position is likely due to the omission of the electrode layer in the modeling. The measured sample contains an indium-tin oxide layer of 360 nm thick as the top electrode. Despite the discrepancy in the peak position, the model successfully explains the occurrence of the phase-shift peak in its incident-angle dependence.

The above experiment shows the importance of modeling multiple reflections in the reflection-mode differential ellipsometry for electrooptic measurements. The present model, because of the simplification involving

neglecting the top electrode in calculating  $w_s$  and  $w_p$ , seems to provide semi-quantitative description to the experiment where multiple reflection plays an important role.

### III. Detection Techniques and Applications

A typical optical arrangement of the reflection-mode differential ellipsometer is shown in Figure 2. The light source is a He-Ne laser. The phase modulation of the laser beam is generated by a photo-elastic modulator which provides variable modulating amplitude at a frequency of 50 kHz, suitable for the lock-in amplification. As has been discussed in the previous section, it is preferred to adjust the optical compensator under zero applied field so that

$$\Gamma_c + \Gamma_p(0) + \Gamma_s(0) = 0 . \quad (19)$$

From Equation (10) we see that under the above condition, the waveform of the light intensity is predominantly  $2\Omega$  in frequency. Therefore the above condition, i.e. Equation (20), may be reached by observing the waveform of the light on a oscilloscope while adjusting the optical compensator. When an external electric field is applied to sample, an modulating component at frequency  $\Omega$  is created in the light intensity due to the field-induced phase shift. In order to pick out this phase shift, the reference signal of the lock-in amplifier must be set as  $\cos\Omega t$ . To obtain the best sensitivity of detection, the modulating amplitude  $M$  in Equation (11) should be adjusted to  $\pi/2$ .

To obtain the phase shift vs. applied voltage loops, a low frequency cyclic voltage may be applied to the sample between the top and the bottom electrodes. The frequency of the applied voltage must be much lower than the modulation frequency of the light provided by the optical phase modulator (50kHz) in order for the lock-in amplifier to reach an steady output at any instantaneous voltage. During our experiments the cycling frequency of the applied voltage is usually around 0.5 Hz.

The reflection-mode differential ellipsometer presented in this paper has been used to characterize various electrooptic thin films. Figure 7 shows the transverse electrooptic property of a 8/65/35 PLZT thin film sputter-deposited on a Pt/Ti-coated silicon substrate, measured by using this technique. The thickness of the PLZT film is 680 nm. The top electrode is a 360 nm thick indium-tin oxide layer deposited by sputter deposition. The birefringence vs. electric field loop was obtained with an incident angle of 67° for the probing laser beam. The Brewster angle of the p-polarized light for this PLZT sample is approximately 68°. Being very close to the Brewster angle, the amplification for the p-component,  $w_p$ , is nearly one. Coincidentally, the amplification for the s-component,  $w_s$ , evaluated from the multiple-reflection model, is also very close to one at this incident angle. Therefore no correction is necessary in converting the measured phase shift to the field-induced birefringence.

Another example is the detection of the transverse electrooptic effect of antiferroelectric lead zirconate thin films on Pt/Ti-coated silicon substrate. The films were deposited by using a dip-coating process. The thickness of the film is approximately 1 μm. Because the lead zirconate thin film possesses a similar index of refraction as the PLZT film in the previous example, the same incident angle (near the Brewster angle) was used during the measurement. A typical birefringence vs. electric field loop is presented in Figure 8. Unlike the previous example, the amplification of the s-component,  $w_s$ , for this sample is 0.18, evaluated by using the multiple reflection model. In other words, according to the model prediction, the detected field-induced phase shift is mainly attributed to the field-induced change in the extraordinary index. In labeling the Y-axis of Figure 8 as the field-induced birefringence, therefore, some approximation is involved. The digital type of electrooptic response shown in Figure 8, as a result of the field-induced antiferroelectric-ferroelectric transition<sup>8</sup>, can only be observed in a reflection-mode electrooptic measurement where parallel electrodes create a very uniform electric field inside the thin film materials.

Because parallel electrodes are used in the reflection-mode differential ellipsometry, one can measure the field-induced birefringence and the electric polarization from the same sample. This enables us to directly measure the relationship between the field-induced birefringence and the electric polarization

of thin film materials. Figure 9 shows the field-induced birefringence vs. polarization loop of a 8/65/35 PLZT thin film, obtained by simultaneously detecting the field-induced birefringence and the polarization of the thin film during a voltage cycle. This type of loop cannot be obtained in a transmission-mode electrooptic measurement because of the geometry of planar electrodes.

## VI. Conclusions

The principles of a reflection-mode differential ellipsometry for the electrooptic measurement of thin film materials is presented. The scheme of the measurement involves a phase-sensitive detection of the field-induced phase shift in a probing light beam reflected from the thin film samples. Neglecting the multiple reflections, the detected phase shift is proportional to the field-induced birefringence of the electrooptic thin film.

The occurrence of multiple reflection in the layered structure causes the "amplification" or "reduction" of the field-induced index changes in the measured signal due to the interference of the partial waves. A simplified multiple reflection model, which neglects the top electrode in considering the interference, is proposed to simulate the experimental situation. It is found from the model that the ordinary-index change and the extraordinary-index change contribute to the measured phase shift in their respective manners. Therefore the measured field-induced phase shift is not in general proportion to the field-induced birefringence. The corrections to the measured indices changes calculated from the model prove to be semi-quantitatively consistent with the experiments.

The model demonstrates the usefulness of the multiple reflection in separating the extraordinary index change from the ordinary index change. Such separation may be achieved by measuring the field-induced change at different incident angles, where the respective contributions from the extraordinary index change and the ordinary index change are different.

The experiments demonstrate that the reflection-mode differential ellipsometry is an effective and convenient way of measuring the transverse

electrooptic properties of thin films grown on opaque substrates. This measuring technique also provides a means of directly measuring the relationship between the field-induced birefringence and the polarization of thin film materials.

## References

1. C. E. Land, J. Am. Ceram. Soc. 72, 2059(1989)
2. Gene H. Haertling, Ferroelectrics, 75, 25(1987)
3. H. Adachi et al, J. Appl. Phys. 42, 867(1983)
4. K. Carl et al, Proc. of the IEEE, 61, 967(1973)
5. F. Wang et al, Proc. of the 4th International SAMPE Electronic Conf., Albuquerque, New Mexico, June 12-14, 1990
6. M. Ishida et al, Appl. Phys. Lett., 31, 433(1977)
7. D. Dimos, et al, "Electrooptic Effects and Photosensitivities of PZT Thin Films," Ferroelectric Films
8. F. Wang, et al, Optics Lett., in press
9. F. Wang et al, Appl. Phys. Lett., in press
10. B. G. Potter, Jr. et al, Appl. Phys. Lett. (to be published)
11. G. W. Farnell, et al, IEEE Trans. Sonics. Ultrasonics, SU-17, 188(1970)
12. Yariv et at, in Optical Waves in Crystals.
13. M. Born and E. Wolf, in Principlew of Optics, 4th Edition (Pergamon Press, 1970)
14. G. H. Haertling and C. E. Land, J. Am. Ceram. Soc. 54, 1(1971)

## Figure Captions

Figure 1. Parallel electrode structure of thin film samples. The propagation of the probe light in the reflection-mode detection is shown by the lines with arrows.

Figure 2. Schematic diagram of the reflection-mode differential ellipsometer.

Figure 3. The calculated amplifications,  $w_p$  and  $w_s$ , for p- and s-component as functions of the incident angle. The film thickness for the model calculation is equal to unity wavelength.

Figure 4. The calculated amplifications,  $w_p$  and  $w_s$ , for a PLZT thin film, 680 nm thick, on a platinum electrode.

Figure 5. Model prediction of the detected phase shift as a function of the incident angle. The "corrected" curve is calculated from the multiple-reflection model; the "uncorrected" curve is calculated from the single-reflection model.

Figure 6. Measured field-induced phase retardation as a function of the incident angle.

Figure 7. Field-induced birefringence vs. electric field loop for a 8/65/35 PLZT thin film sputter-deposited on a platinum-coated substrate.

Figure 8. Field-induced birefringence vs. applied voltage loop for an antiferroelectric lead zirconate thin film grown on a platinum-coated substrate.

Figure 9. Field-induced birefringence vs. polarization loop measured from an 8/65/35 PLZT thin film grown on a platinum-coated substrate.

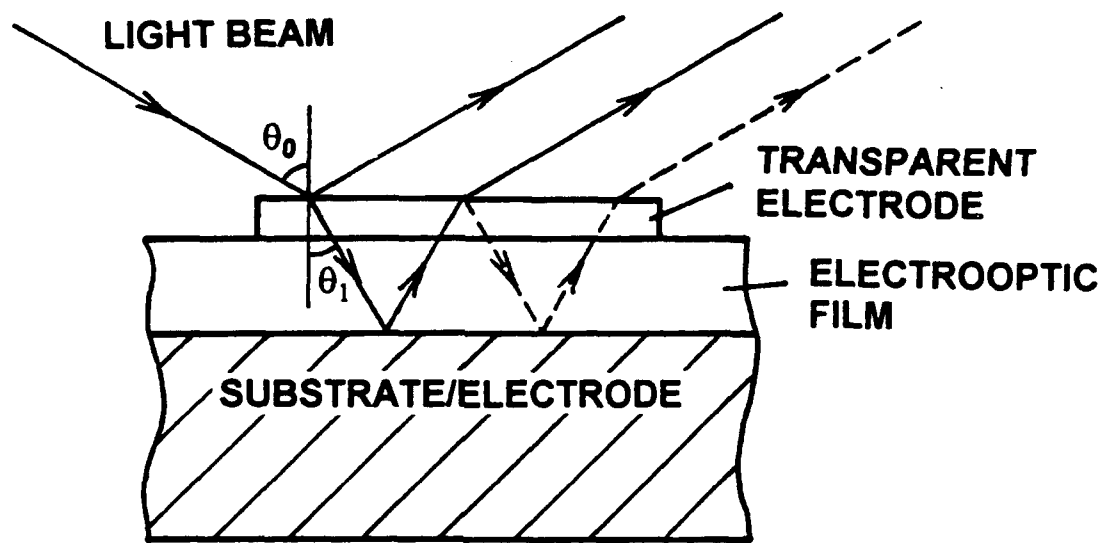


Figure 1. Parallel electrode structure of thin film samples. The propagation of the probe light in the reflection-mode detection is shown by the lines with arrows.

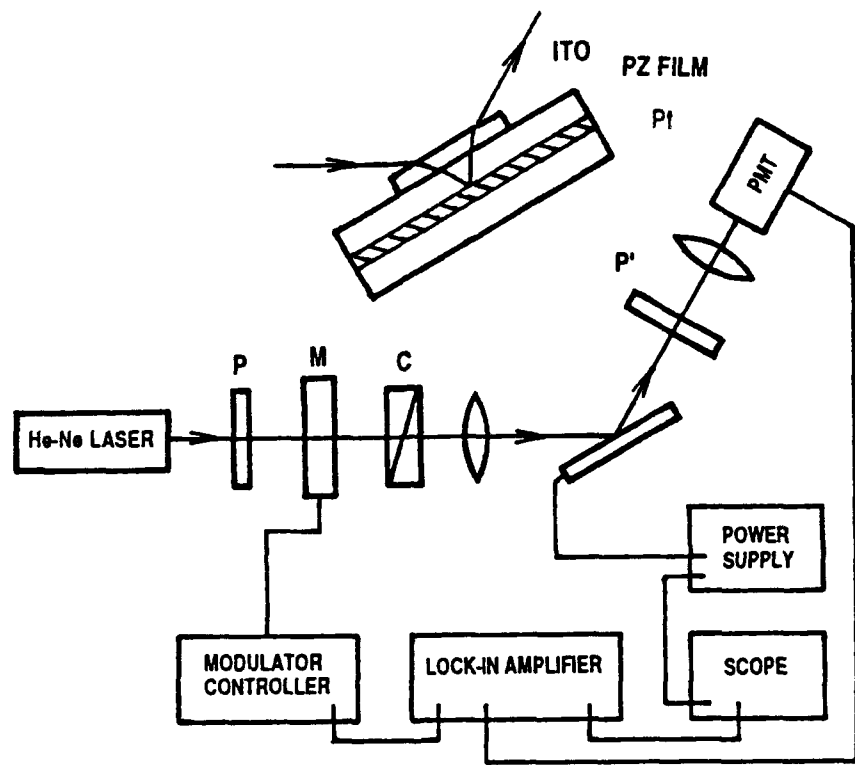


Figure 2. Schematic diagram of the reflection-mode differential ellipsometer.

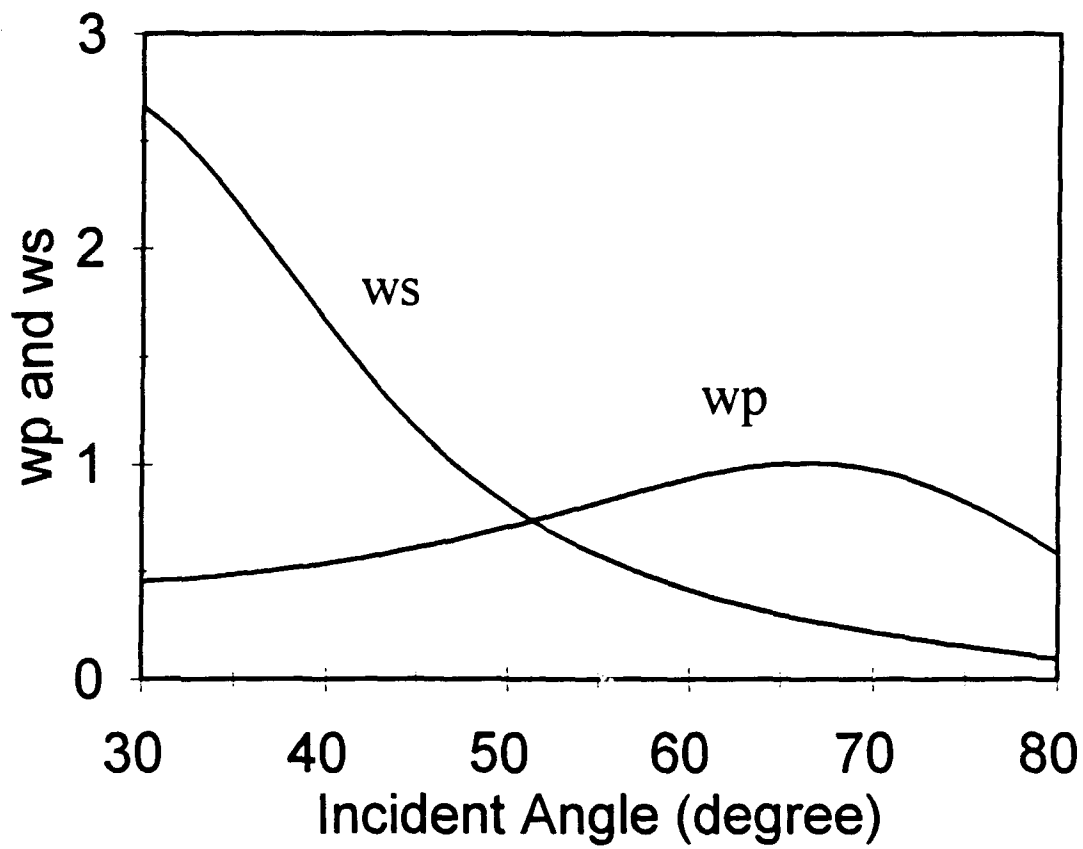


Figure 3. The calculated amplifications,  $w_p$  and  $w_s$ , for p- and s-component as functions of the incident angle. The film thickness for the model calculation is equal to unity wavelength.

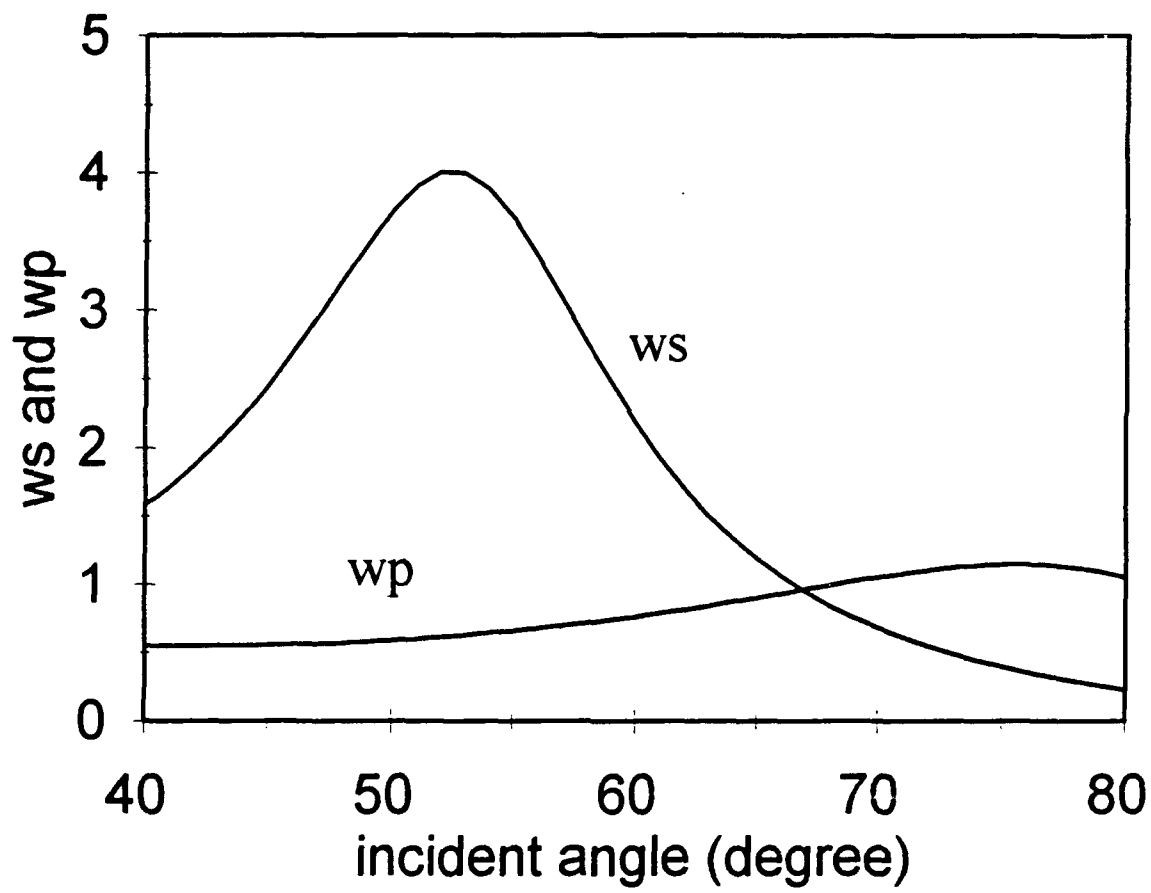


Figure 4. The calculated amplifications,  $w_p$ , and  $w_s$ , for a PLZT thin film, 680 nm thick, on a platinum electrode.

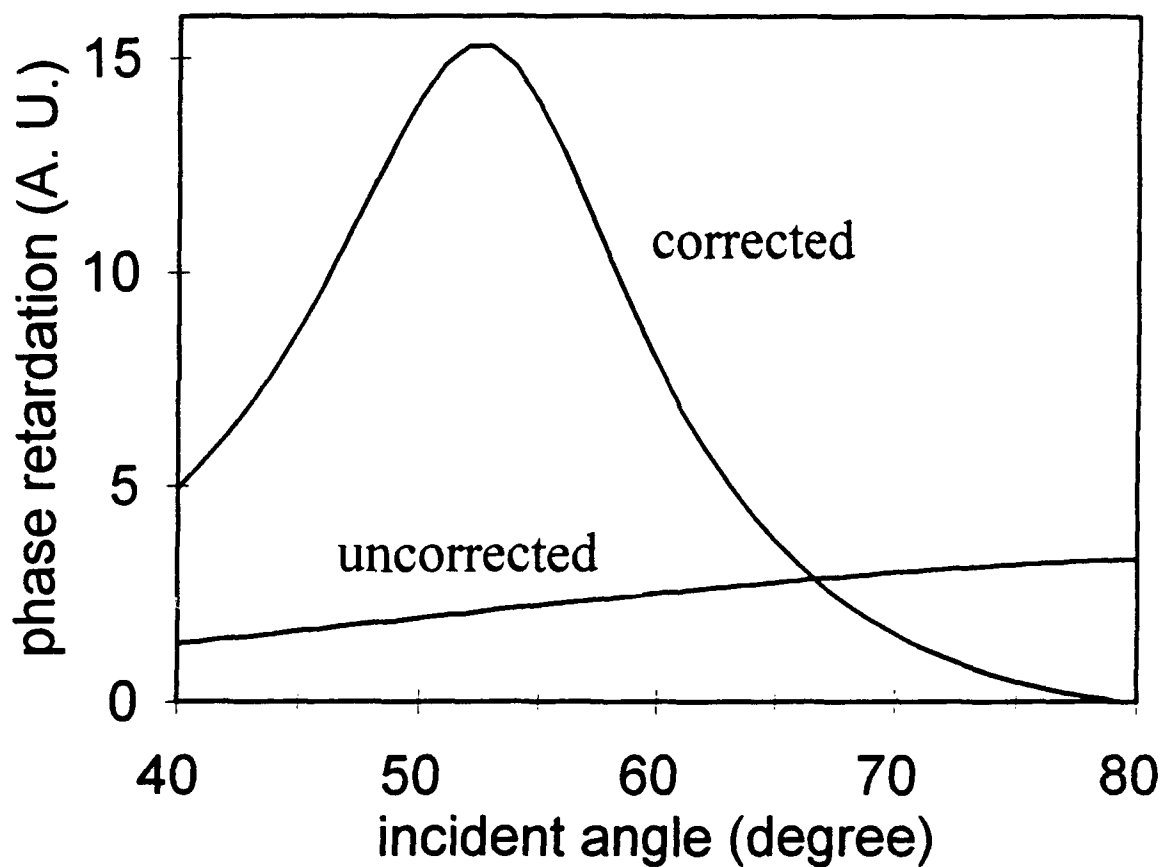


Figure 5. Model prediction of the detected phase shift as a function of the incident angle. The "corrected" curve is calculated from the multiple-reflection model; the "uncorrected" curve is calculated from the single-reflection model.

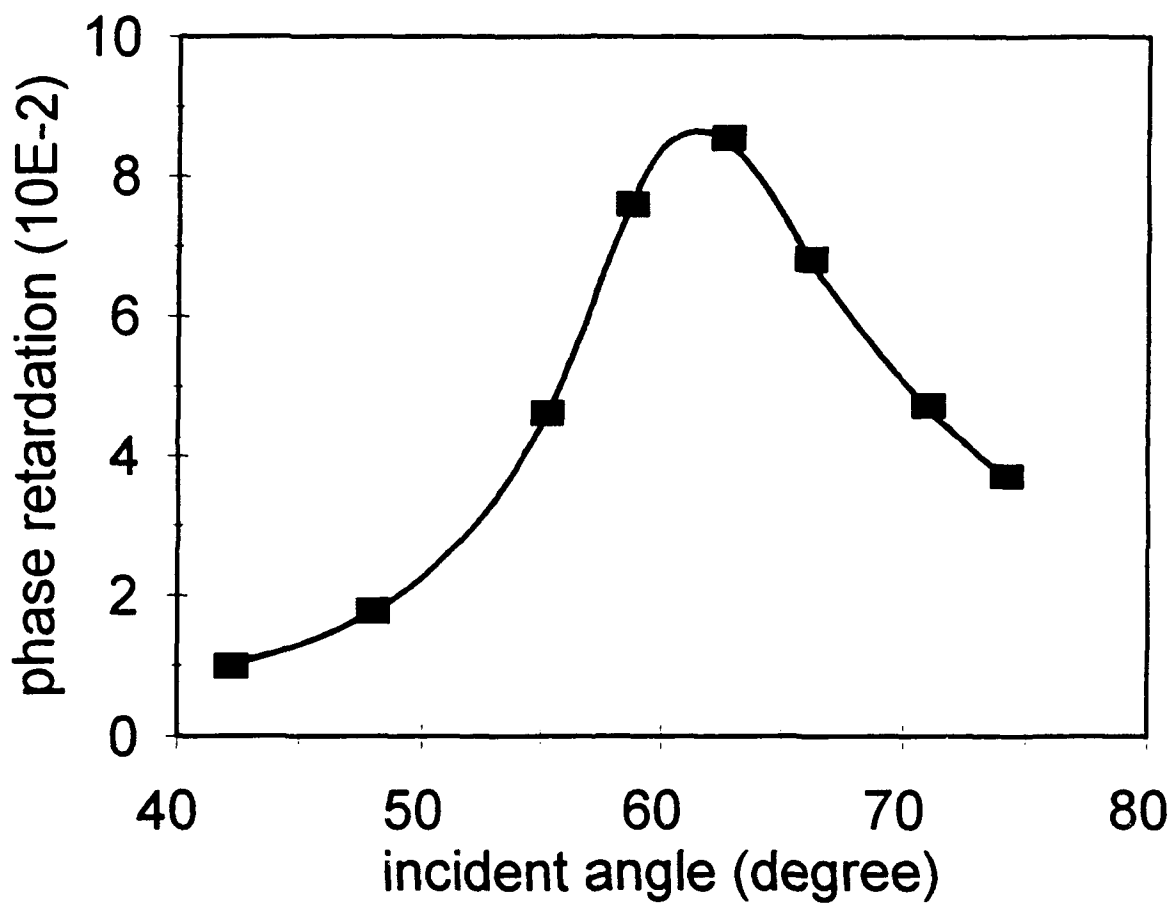


Figure 6. Measured field-induced phase retardation as a function of the incident angle.

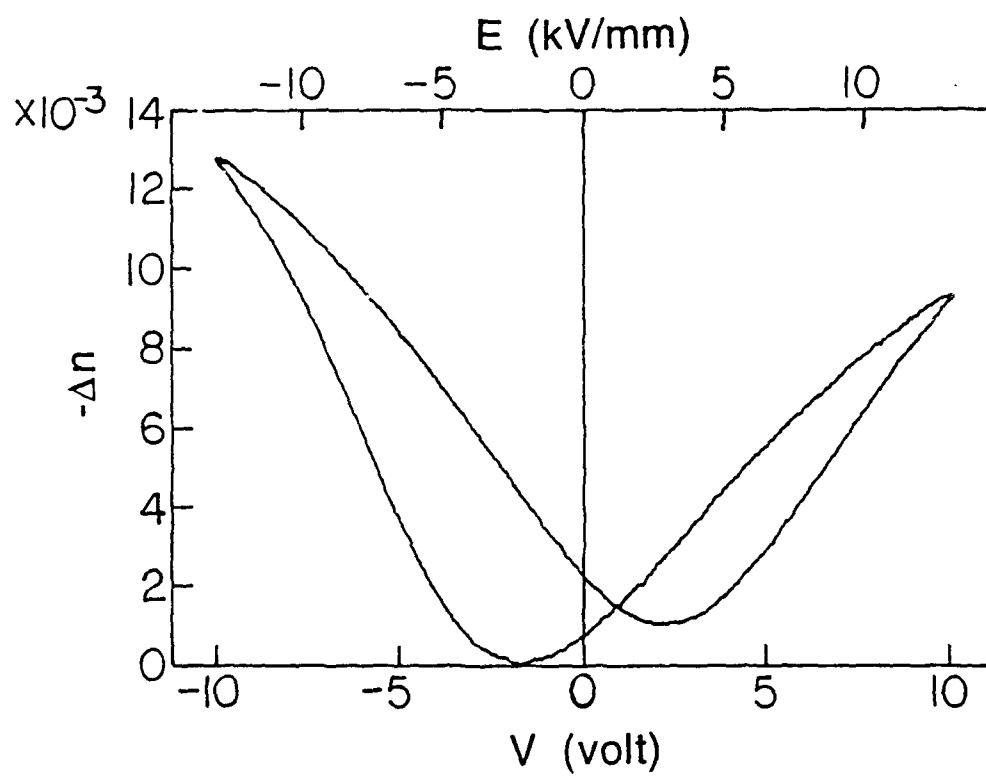


Figure 7. Field-induced birefringence vs. electric field loop for a 8/65/35 PLZT thin film sputter-deposited on a platinum-coated substrate.

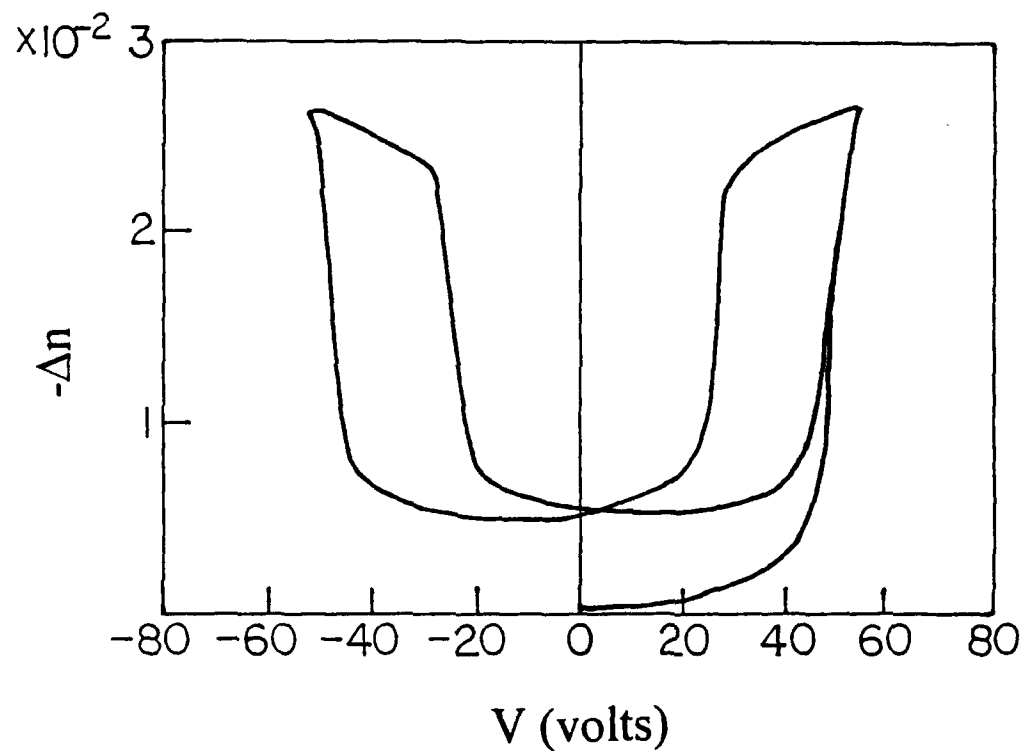


Figure 8. Field-induced birefringence vs. applied voltage loop for an antiferroelectric lead zirconate thin film grown on a platinum-coated substrate.

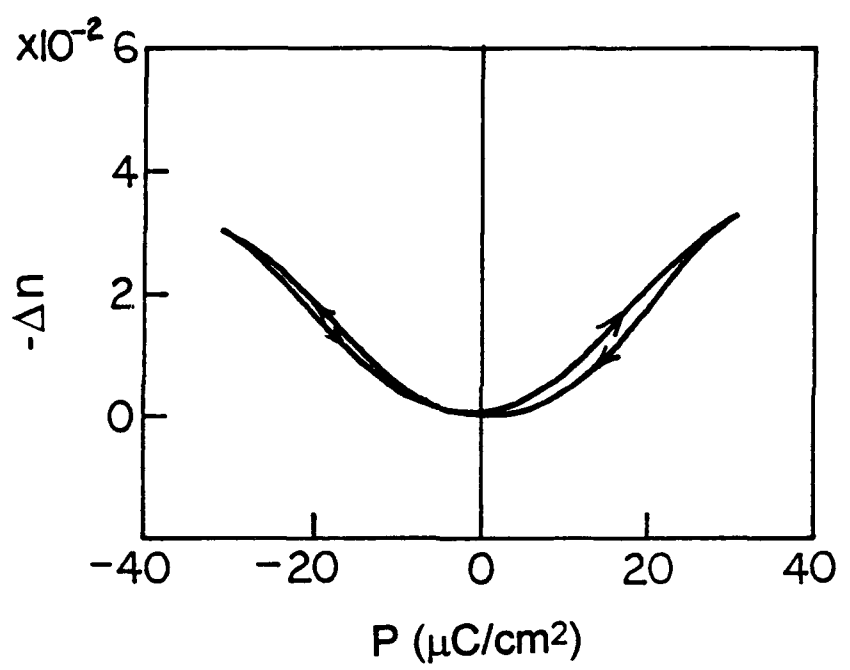


Figure 9. Field-induced birefringence vs. polarization loop measured from an 8/65/35 PLZT thin film grown on a platinum-coated substrate.

## **SECTION 2**

**Birefringent Bistability in  $(Pb,La)(Zr,Ti)O_3$  Thin Films  
with a Ferroelectric-Semiconductor Interface**

Feiling Wang and Gene H. Haertling

Department of Ceramic Engineering

Clemson University

Clemson, South Carolina 29634-0907

We report a birefringent bistability exhibited in ferroelectric thin films with a ferroelectric-semiconductor interface. Such birefringent bistability is observed in  $(Pb,La)(Zr,Ti)O_3$  (PLZT) thin films which are sandwiched between a platinum and a semiconducting indium-tin oxide (ITO) electrode. The magnitude of the birefringence between the two remanent states is approximately  $0.9 \times 10^{-3}$ . The Pt/PLZT/ITO structure features a nonvolatile electrooptic memory operation, i.e., the switching between the two remanent birefringent states with bipolar electric pulses.

Ferroelectric polarization reversal, which has facilitated a nonvolatile memory mechanism for electric signals<sup>1-2</sup>, has not proved to be able to perform a nonvolatile electrooptic memory function for optical signals due to the fact that the two remanent polarization states in normal ferroelectric materials are optically indistinguishable. The symmetry in the optical properties under polarization reversal may be broken if one of the polarization directions is made more favorable than the other under the influence of certain electrode combinations. The asymmetric polarization in ferroelectric thin films on semiconductor substrates has been observed<sup>3</sup>, however, its implications for the electrooptic properties of the thin films have not been studied. The purpose of this letter is to report the phenomenon of a birefringent bistability associated with the polarization reversal in ferroelectric (Pb,La)(Zr,Ti)O<sub>3</sub> (PLZT)<sup>4</sup> thin films which are electroded with a metal and a semiconducting layers.

The birefringent bistability in PLZT thin films was observed to exist in a thin film metal/ferroelectric/semiconductor (MFS) structure shown in Figure 1. Polycrystalline PLZT thin films of composition 8/65/35(La/Zr/Ti) were deposited on Pt-coated silicon substrates by means of magnetron sputtering. The thickness of the PLZT films was approximately 750 nm. Indium-tin oxide (ITO) films of about 350 nm in thickness were then deposited on the PLZT films also by sputtering. A post-deposition annealing process was used to obtain a perovskite crystalline structure of the PLZT material.

With DC voltage or electric pulses applied to the platinum and the ITO layers, a sandwiched PLZT film becomes birefringent with its c axis along the normal of the film surface as a result of the transverse electrooptic effect. A

phase-detection scheme in the reflection mode, with the experimental setup shown in Figure 2, was used to measure the field-induced birefringence,  $\Delta n = n_e - n_o$ , in the PLZT thin film. The modulation of the incident light was provided by a photoelastic modulator. At a finite incident angle, the reflected light polarized in the incident plane acquires a phase retardation with respect to the component polarized perpendicularly to the incident plane due to the birefringence of the PLZT thin films. Such phase retardation is associated with a modulating component of the light received by the photo-detector. With a proper setting of the reference signal, the output of the lock-in amplifier is proportional to the birefringence,  $\Delta n$ , of the PLZT thin films.

The birefringence in the PLZT films as a function of the slowly varying DC voltage exhibited severe asymmetry as revealed by a typical loop shown in the insert of Figure 3. The voltage shown in the figure is measured with respect to the platinum electrode. An important feature of Figure 3 is that there are two distinguishable remanent birefringent states dependent on the polarity of the voltage from which the zero voltage is reached. The occurrence of the two distinguishable remanent birefringent states is not a result of accidental poling of the material during the initial application of an electric field, since all samples reproduced the same features as in Figure 3 regardless of the polarity of the initial electric field. To further verify the inherent nature of these two distinguishable birefringent states, a series of plots were successively taken from a small to a large field scan range. As shown in Figure 3, with the increase-of the scan range, the two remanent birefringent states approach their saturation values,  $\Delta n_A$  and  $\Delta n_B$ , respectively.

The inter-switching of the two remanent birefringent states with electric signals was achieved by applying bipolar electric pulses to the MFS devices. With the detection system shown in Figure 2, the output voltage of the lock-in amplifier (proportional to the birefringence of the thin film) was recorded versus time when bipolar electric pulses were fed to the device. Figure 4 represents the birefringent signal forms of the PLZT film responding to bipolar electric pulses of 0.1 ms in pulse width and peak voltage ranging from 5 volts to 30 volts. The interval between the pulses was 5 seconds. The dashed line schematically denotes the polarities and positions of the bipolar pulses.

It is shown in Figure 4 that bipolar electric pulses switch the PLZT thin film between two distinguishable birefringent states, which correspond to the two remanent states for each DC cycle in Figure 3. The magnitude of the birefringence between the two remanent states (birefringent spacing) substantially increases with increasing peak voltage of the pulse until saturation behavior takes place. The saturated birefringent spacing is approximately  $0.9 \times 10^{-3}$ . Such saturation is consistent with the DC response of the devices shown in Figure 3. The nonvolatile nature of the birefringent switching is obvious in that after a positive pulse, the thin film remains in a low birefringent state until the following negative pulse switches the material to a high birefringent state. Because of the detection method, the response speed of the measuring system was determined by the integration time of the lock-in amplifier. The transient behavior of the switching, therefore, cannot be directly observed with this measurement.

Figure 5 shows the birefringent spacing of the device as a function of the pulse width while keeping the peak voltage constant. Although the intrinsic

switching speed of the PLZT thin film is essentially determined by the domain switching process, the response time of the device, however, may be predominated by the RC constant of the device, which was approximately 2.5 microseconds. It is shown in Figure 5 that when the pulse width becomes comparable to the RC constant of the device the birefringent spacing between the two states is significantly reduced, indicating an incomplete switching of the ferroelectric domains. When the pulse width becomes much larger than the RC constant the birefringent spacing is no longer dependent on the pulse width.

The occurrence of the birefringent bistability in the device may be explained by the polarity sensitive polarization of the PLZT thin films with an ferroelectric-semiconductor interface. It was recognized that electrodes in contact with a ferroelectric material play important role in sustaining polarizations in the ferroelectric material<sup>5</sup>. In particular, the compensation of surface charges by electrodes is sometimes crucial in determining the remanent polarization in thin film ferroelectrics. Experimental evidence has shown that the birefringent bistability in the MFS structure was a result of the unequal remanent polarizations of opposite polarities caused by the PLZT/ITO interface. Being an n-type semiconductor<sup>6</sup>, an ITO film is expected to form a p-n junction with the PLZT thin film that usually exhibits p-type conduction properties<sup>7</sup>. Under short-circuit condition, the band bending in the p-n junction creates a built-in bias (inside the PLZT film) that enhances the polarization in the direction of the ITO layer and suppresses the polarization in the direction of the Pt electrode. As a result, the PLZT thin films possess a higher remanent polarization when the zero voltage is reached from a negative polarity than a opposite polarity. A higher remanent polarization in turn produced a higher

remanent birefringence in the PLZT thin films. It should be pointed out that the mechanism of the birefringent bistability is yet to be fully understood.

The birefringent bistability in the MFS structure is a potential mechanism for realizing a nonvolatile programmable spatial light modulator. It is also suitable for integrated devices in waveguide architectures. The Pt/PLZT/ITO device presented here is actually a complete electrically addressable nonvolatile electrooptic memory unit.

The authors would like to thank E. Furman for many helpful discussions. This study was sponsored by the Office of Naval Research under contract No. N00014-91-J508.

### **References**

1. J. T. Evans and R. Womack, IEEE J. Solid-State Circuit, **23**, 1171(1988)
2. G. H. Haertling, J. Vac. Sci. Technol., **A9**, 414(1991)
3. Y. Xu, C. Chen, R. Xu, and J. D. Mackenzie, J. Appl. Phys., **67**, 2985(1990)
4. G. H. Haertling and C.E. Land, J. Am. Ceram. Soc., **54**, 1(1971)
5. D. Wurfel and I. P. Batra, Phys. Rev., **B8**, 5126(1973)
6. K. S. Bree Harsha, K. J. Bachmann, P. H. Schmidt, E. G. Spencer, and F. A. Thiel, Appl. Phys. Lett., **30**, 645(1977)
7. Z. Wu and M. Sayer, Proc. of the 1990 IEEE 7th International Symposium on the Applications of Ferroelectrics (IEEE Service Center, Piscataway, NJ), p.677

### **Figure Captions**

Figure 1. Structure of the Pt/PLZT/ITO thin film device. The propagation of the light beam in the phase-detection measurement is shown by the line with arrows.

Figure 2. Schematic diagram for the phase-detection scheme in the reflection mode.

Figure 3. Measured birefringence  $\Delta n$  in the PLZT thin film as a function of the slowly varying DC voltage, taken successively from a small to a large DC field scan range. A single cycle is shown in the insert. The horizontal and the vertical scales of the insert are  $5 \times 10^{-3}$  per division and 5 volts per division, respectively.

Figure 4. Inter-switching between the two remanent birefringent states with bipolar electric pulses. The peak voltage of the switching pulses are marked on each curve. The dashed line schematically denotes the positions and the polarities of the bipolar pulses. The vertical scale for the birefringence is  $10^{-3}$  per division.

Figure 5. Birefringent spacing between the two remanent states as a function of the pulse width with a fixed peak voltage of 15 volts.

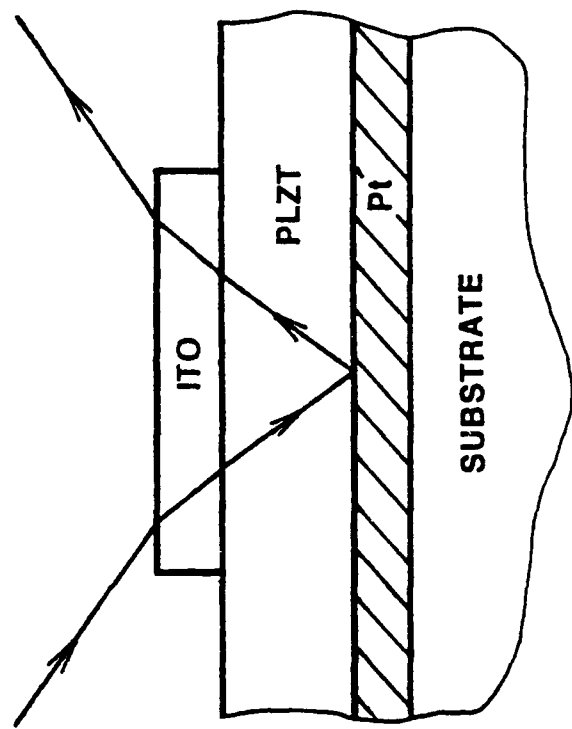


Figure 1. Structure of the Pt/PLZT/ITO thin film device. The propagation of the light beam in the phase-detection measurement is shown by the line with arrows.

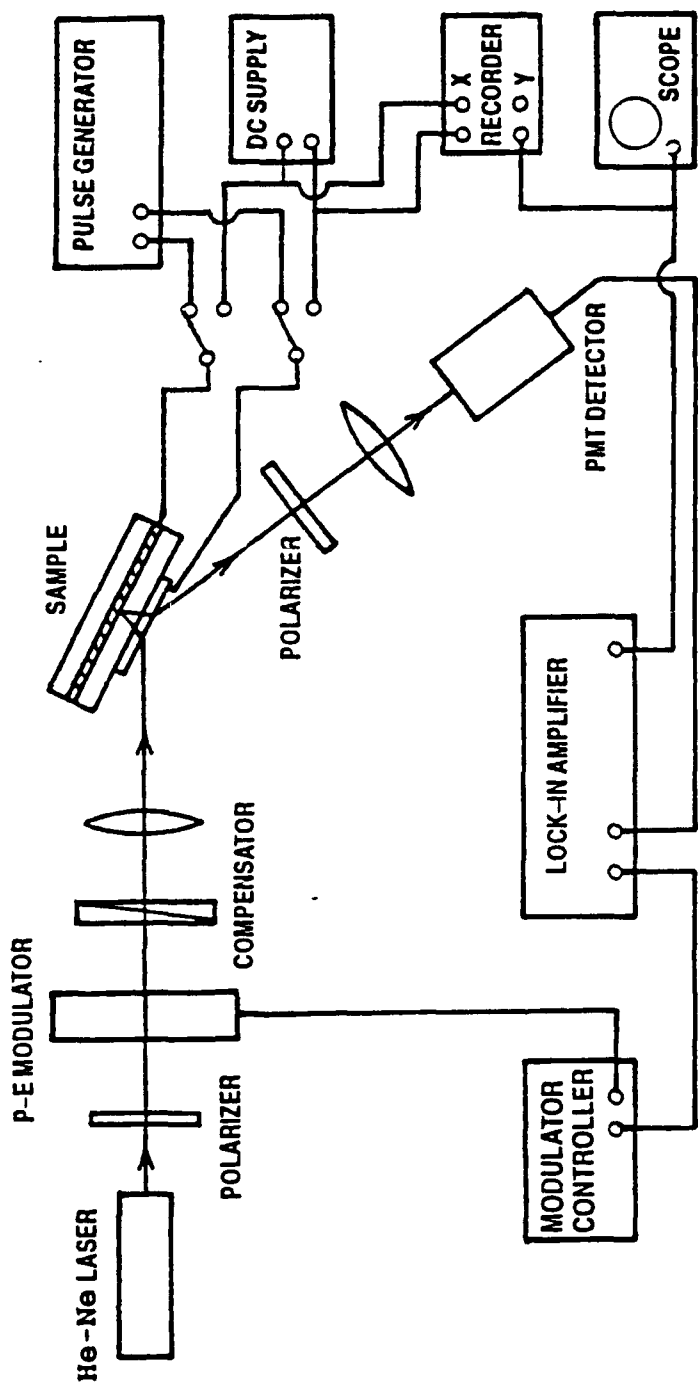


Figure 2. Schematic diagram for the phase-detection scheme in the reflection mode.

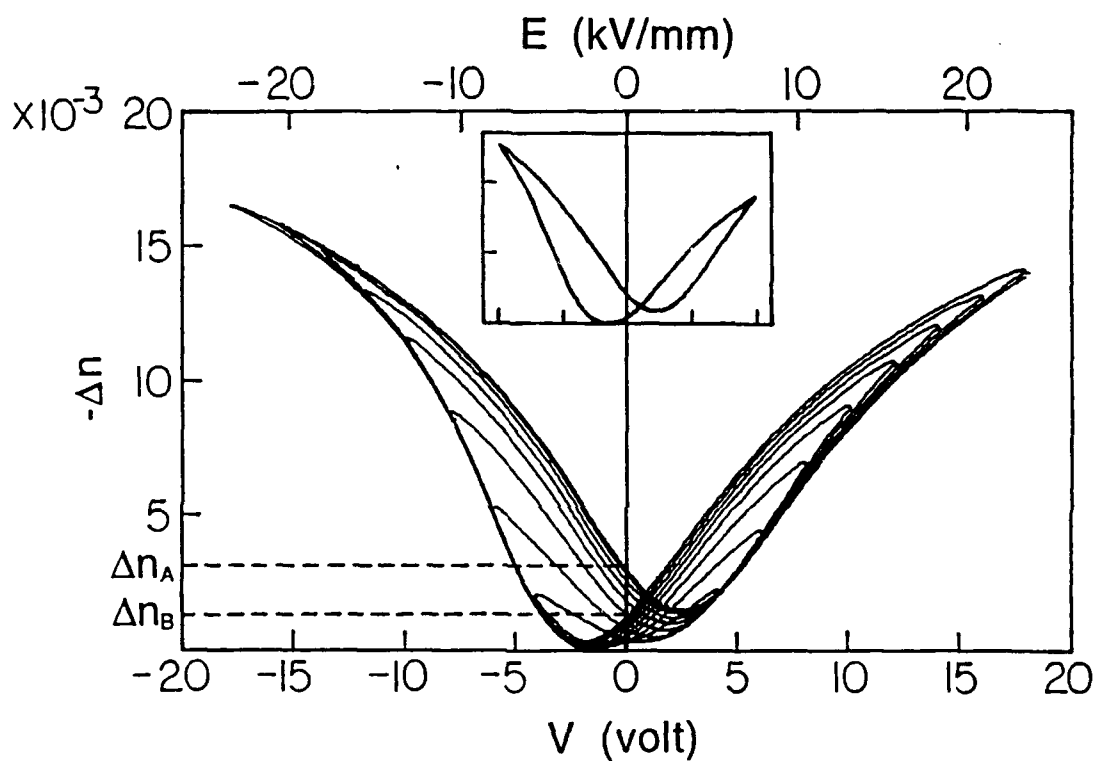


Figure 3. Measured birefringence  $\Delta n$  in the PLZT thin film as a function of the slowly varying DC voltage, taken successively from a small to a large DC field scan range. A single cycle is shown in the insert. The horizontal and the vertical scales of the insert are  $5 \times 10^{-3}$  per division and 5 volts per division, respectively.

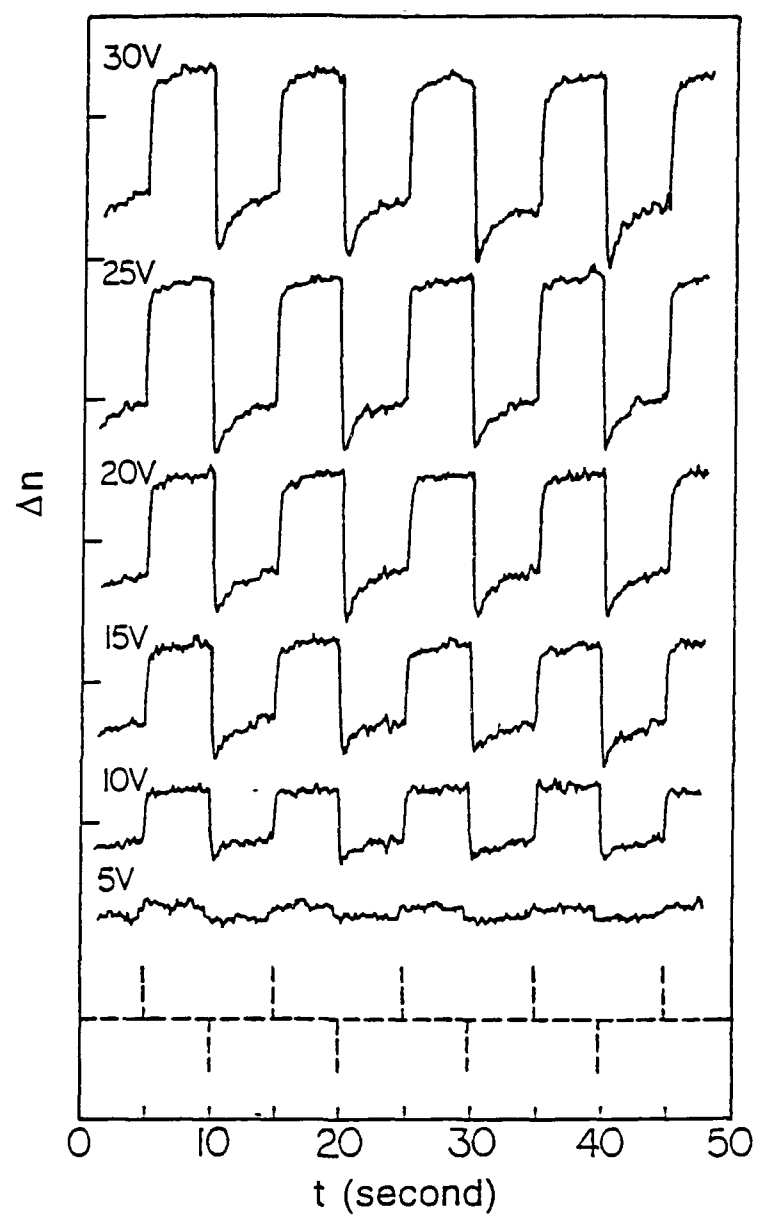


Figure 4. Inter-switching between the two remanent birefringent states with bipolar electric pulses. The peak voltage of the switching pulses are marked on each curve. The dashed line schematically denotes the positions and the polarities of the bipolar pulses. The vertical scale for the birefringence is  $10^{-3}$  per division.

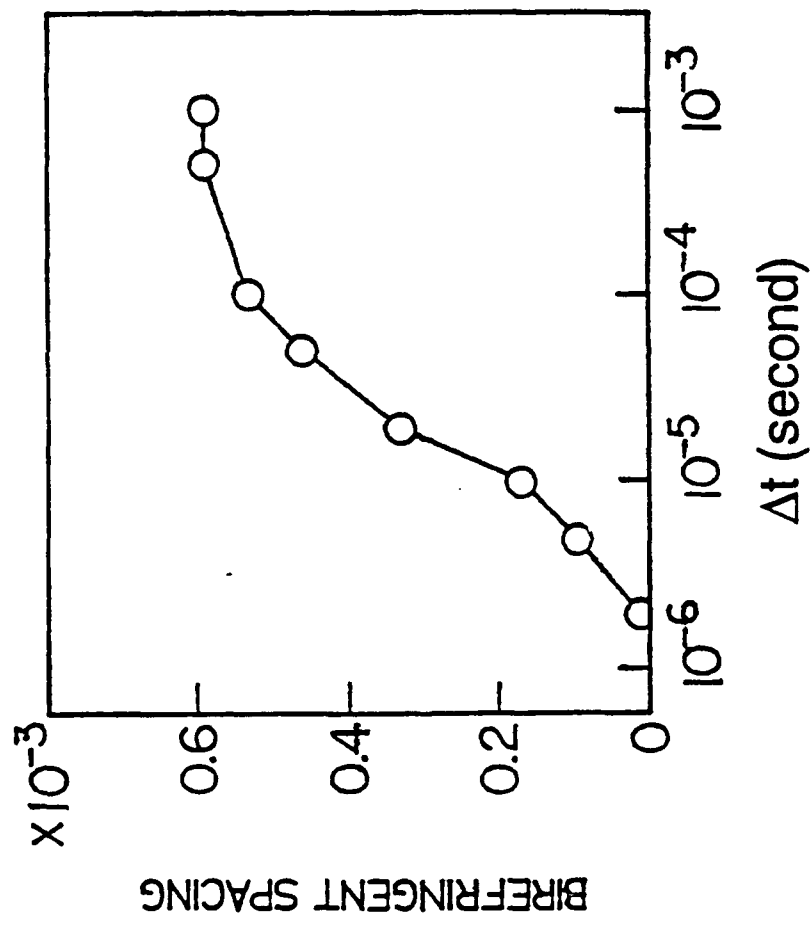


Figure 5. Birefringent spacing between the two remanent states as a function of the pulse width with a fixed peak voltage of 15 volts.

## **SECTION 3**

## **Antiferroelectric Lead Zirconate Thin Films**

### **Derived from Acetate Precursors**

Kewen K. Li, Feiling Wang and Gene H. Haertling

Department of Ceramic Engineering

Clemson University, Clemson, SC 29634-0907

Antiferroelectric lead zirconate ( $PbZrO_3$ ) films derived from acetate precursors have been fabricated on Pt/Ti-coated silicon wafers and fused silica at 700°C with an automatic dip coating process. Films formed directly on the metallized silicon wafer showed the coexistence of perovskite and pyrochlore phases. A pre-coated titania layer of about 100Å facilitated the formation of the desired perovskite phase. Films deposited on fused silica exhibited interactions between lead and silica which inhibited the crystallization of the films. In this case, a pre-coated titania layer in the range of 500-750Å acted as a diffusion barrier layer, allowing the formation of the perovskite phase. Antiferroelectricity in the films was confirmed by x-ray superstructure, dielectric double hysteresis loops and dc bias behavior at room temperature. The corresponding transverse electrooptic properties were also measured for films deposited on fused silica.

## 1. Introduction

Lead zirconate (PZ) is a typical antiferroelectric (AFE) material at room temperature [1,2], from which the ferroelectric (FE) state can be induced when subjected to a sufficiently large electric field. However, this transition field usually exceeds the material breakdown strength, and consequently, the field-enforced AFE→FE transition is usually carried out at a few degrees centigrade below its Curie point (~230°C) [2]. Owing to the antiparallel arrangement of the spontaneous polarization directions, its unit cell is a superstructure of orthorhombic symmetry consisting of eight perovskite units [3,4]. Although lead zirconate has been well studied in the bulk form, its thin film properties have rarely been reported.

Preparation of the PZ films was first motivated by a mixed-phase problem encountered in the solution-derived FE lead zirconate titanate (PZT) or La-modified PZT (PLZT) thin films. The coexistence of the perovskite and the pyrochlore phases was commonly observed in these films [5-8] fabricated from different precursor systems, and the amount of the pyrochlore phase increased as the film composition approached the Zr-rich side [5,8]. Thus, PZ was expected to be the most difficult composition in the PZT family to obtain with the desired perovskite phase. Moreover, studying the formation of the PZ films benefits the overall knowledge about microstructure evolution mechanisms as well as providing a proper processing technique which could be applied to other PZT or PLZT compositions.

Remedies to the mixed-phase problem in the PLZT films have been proposed by forming a buffer layer of either lead titanate (PT) [9] or La-modified lead titanates (PLTs) [8] prior to the PLZT film deposition. These PT-based compositions were found to crystallize readily into the perovskite structure at lower temperatures, and PLZT films isostructurally grown on these buffer layers showed enhanced perovskite phase formation. Similar conclusions were noted for sol-gel LiNbO<sub>3</sub> films [10] in which the perovskite phase was formed at a much lower temperature when deposited on top of an existing perovskite layer.

AFE materials possess unique dielectric, piezoelectric [11,12] and electrooptic properties [13] which make them suitable for devices such as micro-displacement transducers. Since PZ is the base composition for some AFE compounds [14]; for example, Sn-modified PZT, preparation of the PZ films provided a starting point for other PZ-based AFE films. Further incentive to prepare PZ films on transparent substrates resulted from the theoretical interest in studying the electrooptic behavior associated with the field-induced AFE→FE phase transition [13].

The purpose of this paper is to overview the processing aspects of the PZ films prepared from the acetate precursor system and to study their microstructure evolution. Preliminary results on the electric/dielectric and electrooptic properties of the AFE PZ films are also discussed.

## **2. Experimental Procedure**

The specific precursors used in the preparation of the PZ films and the TiO<sub>2</sub> pre-coats were previously reported in a paper describing the acetate solution system for PLZTs [15]. For the PZ composition, lead subacetate powder, Pb(OOCCH<sub>3</sub>)<sub>2</sub>•2Pb(OH)<sub>2</sub>, and aqueous zirconium acetate solution (ZAA) were used. The oxide contents of the precursors were assayed beforehand. Lead subacetate was first dissolved into the ZAA and continuously stirred for 20 min. Methanol was then added into the mixture as a solvent and stirred for another 10 min. The final coating solutions contained 6 to 8.5wt.% oxide.

The TiO<sub>2</sub> pre-coats were derived from titanium diisopropoxide biacetylacetone (TIAA), 75wt.% in isopropanol. It was mixed with methanol at a weight ratio of 1 to 5 to form the coating solution containing about 3wt.% TiO<sub>2</sub>.

Films were deposited on Pt/Ti-coated Si wafers and optically polished fused SiO<sub>2</sub> for measuring their dielectric and electrooptic properties, respectively; however, Ag foils were also occasionally used as substrates. All films were formed by an automatic dip coating process which involved a multiple dipping and firing approach [16]. Substrates were withdrawn from the solutions at a speed of 18.7cm/min. The coating cycle was repeated 15 to 30 times which gave a final film thickness ranging from 0.6 to 1μm. Each coating layer was fired at 700°C for 2 minutes.

Pulverized solid samples obtained by drying the coating solution at 60°C were subjected to thermogravimetry analysis (TGA) and differential thermal analysis (DTA) in air. The dried samples were also heated in a furnace at various temperatures for 1 hour for x-ray diffraction (XRD) and other analyses.

Dielectric measurements were made at 1kHz. Hysteresis loops were measured with a modified Sawyer-Tower circuit. The transverse electrooptic properties were measured by means of a phase-detection technique in the transmission mode [17]. Evaporated Cu was used as the electrodes.

### **3. Results and Discussions**

#### *3.1 Thermal Decomposition and Crystallization Behavior*

XRD patterns of the pyrolyzed powder are shown in Fig. 1 as a function of the firing temperatures. Powders heated below 400°C (not shown) had a very broad amorphous peak centered around ~30° 2θ (CuKα). Metallic Pb appeared at 400°C, and was subsequently oxidized at higher temperatures. A small amount of the perovskite PZ phase started to form at 600°C and became the only phase at 700°C. Formation of metallic Pb and PbO<sub>x</sub> during the thermal decomposition process was not uncommon for it has also been reported in sol-gel systems for PZT [18] and PZ [19]. The pyrochlore phase, however, was not appreciable in these XRD results.

Fig. 2 shows the TGA and DTA results of dried solid samples heated from room temperature to 800°C at a rate of 10°C/min. The sample lost about 30% of its weight during pyrolysis, and this corresponded to approximate 2 moles each of OAc<sup>-</sup> and OH<sup>-</sup>(or H<sub>2</sub>O) per mole of PZ. By comparing the results with Fig. 1 and other infrared spectra data, the dried solid first underwent dehydroxylation(or dehydration) at temperatures below 200°C. The endothermic peaks between 250 and 400°C were attributed to the decomposition of the acetate group and possibly the melting of Pb. The broad exothermic peak between 400 and 600°C accompanied by about 5% weight loss was the oxidation of residual carbonaceous material and Pb. The small exothermic peak at about 660°C corresponded to the crystallization of the perovskite PZ. From these results it was decided to set the processing temperature for the PZ films at 700°C.

### 3.2 Film Microstructure and Phase Formation

3.2.1 *Pt/Ti-coated Si substrates.* Fig. 3 shows a scanning electron microscope (SEM) photograph of a 10-layer PZ film deposited on the Pt/Ti-coated Si substrate and treated afterwards with a dilute HF-HCl etching solution. The presence of two distinct phases in the film, also detected by XRD, was a phenomenon similar to that found in PLZT films [5-8]. The pyrochlore phase region appeared darker than the perovskite one owing to their differences in Pb content.

From Fig. 1 and 2, the appearance of metallic Pb during the decomposition process and the large temperature difference between the

formation of Pb (~375°C) and the crystallization of the perovskite phase (~660°C) suggests that: (1) the loss of Pb and (2) segregation of the Pb species during the firing process might be responsible for the observed microstructure. The absence of the pyrochlore phase in powdered samples indicated that the loss of Pb was more significant in thin films. These arguments are also supported by the fact that a faster heating rate, which would shorten the time to reach the crystallization temperature, improves the film microstructure [5].

Using PT or PLT buffer layers proved to be as effective in modifying the microstructure of the PZ film as those of the PLZT films. However, a TiO<sub>2</sub> layer was also found to be capable of improving the perovskite phase formation. Results from XRD and TGA/DTA experiments on composition PT indicated that Pb had a much greater tendency to combine with Ti; i.e. no Pb was detected by XRD and perovskite PT could be formed at ~470°C which was almost 200°C lower than that of PZ. A relatively thin TiO<sub>2</sub> layer, dip-coated onto the Pt/Ti-coated Si substrate and fired at 700°C for 30sec, was estimated [16] to be in the range of 100Å and possessed a rutile structure. The etched microstructure of a PZ film processed at the same conditions as in Fig. 3 but with a pre-coated TiO<sub>2</sub> layer is shown in Fig. 4. The pyrochlore phase was not discernible in this picture and the film morphology has been improved dramatically with the TiO<sub>2</sub> pre-coat. The reasons for the improved microstructure of the PZ films deposited with a TiO<sub>2</sub> pre-coat are presently under study.

For Pt/Ti-coated Si substrates, growing films on PT or PLT layers was more easily controlled than on a TiO<sub>2</sub> layer. However, TiO<sub>2</sub> has proved to be very useful for films deposited on fused SiO<sub>2</sub> substrates. On both types of sublayers, however, the PZ films were found to retain a small amount of the pyrochlore phase when examined by XRD, therefore, excess Pb (as much as 20at.%) has been added in the preparation of subsequent films in order to compensate for the loss of Pb.

*3.2.2 Fused silica substrates.* PZ films deposited directly onto fused SiO<sub>2</sub> substrates and fired at 600-700°C were colorless and showed no crystallinity under XRD. Large cracks were present throughout the films and also the substrate surfaces, suggesting a film-substrate interaction. Films could be crystallized into the perovskite structure with the PT or PLT buffer layers but regions of imperfections still could be found. This indicated that in these Pb-containing layers, Pb was responsible for the film-substrate interactions. This effect was not unexpected since it was well known that PbO reacts easily with SiO<sub>2</sub> to form low melting silicates. The TiO<sub>2</sub> sublayer was found to be the better choice in this case, yet it required a layer thickness of 500-750Å to inhibit such interactions. Similar uses of TiO<sub>2</sub> layers have been reported for PLZT films deposited on glass substrates [20] and in CMOS devices integrated with PLZT ferroelectrics [21].

The crystallized PZ films were transparent, light yellow in color and suitable for transmission electrooptic properties measurements. Fig. 5

shows the morphology of a  $1\mu\text{m}$  PZ film deposited on a fused  $\text{SiO}_2$  substrate pre-coated with a  $\text{TiO}_2$  layer. As can be seen in Fig. 6 its XRD pattern that this film was highly crystallized into a single perovskite phase. The superstructure orthorhombic {110} peak at about  $16.9^\circ 2\theta$  confirmed the multiple cell structure of this film.

**3.2.3 Microcracks.** All PZ films deposited on the above two types of substrates had a certain degree of microcracks as can be seen in Fig. 3 to 5. While this phenomenon was not observed in other FE PLZT films deposited on the same substrates under similar processing conditions, their formation was attributed particularly to the extra volume shinkage which occurred at the phase transition from the higher temperature paraelectric state to the lower temperature AFE state [14] during the film cooling stage. On the other hand, microcracks were not seen in PZ films deposited on substrates such as Ag, which possessed a higher thermal expansion coefficient ( $22 \times 10^{-6}\text{C}^{-1}$ ) than those of the Pt-coated Si ( $2.6 \times 10^{-6}\text{C}^{-1}$ ) and fused  $\text{SiO}_2$  ( $0.5 \times 10^{-6}\text{C}^{-1}$ ). Since the general PLZT films were in a compressive state when deposited on Ag foils [22], it suggested that the microcracks could be avoided by a residual compressive stress. These microcracks, however, did not prevent the measurements of the electrical and optical properties, yet they affected somewhat the optical quality of the films on fused  $\text{SiO}_2$ .

### *3.3 Dielectric and Electrooptic Properties*

All the PZ films had a dielectric constant at 1kHz in the range of 200 to 250. Dissipation factors were 0.02 to 0.03 and dc resistivities were greater than  $10^{10}\Omega\text{-cm}$ . A typical polarization versus electric field (P-E) double hysteresis loop measured at room temperature was shown in Fig. 7 for a  $0.8\mu\text{m}$  PZ film deposited on a Pt/Ti-coated Si substrate with a  $\text{TiO}_2$  sublayer. The  $\text{AFE}\rightarrow\text{FE}$  transition field was about  $40\text{kV/mm}$  and the reverse  $\text{FE}\rightarrow\text{AFE}$  was about  $20\text{kV/mm}$ . The FE phase saturated at about  $60\text{kV/mm}$  with a polarization between  $0.3$  to  $0.4\mu\text{C/mm}^2$ .

The success in observing the double hysteresis loop of PZ film at room temperature was attributed to the superior dielectric strength usually found for thin film materials. For example, the  $\text{AFE}\rightarrow\text{FE}$  transition field found for these PZ films was an order of magnitude greater than the reported values for bulk materials [2]. Such a large field would certainly cause breakdown in bulk PZ.

Inasmuch as the slope of the P-E hysteresis loop indicates the permittivity of the sample, this parameter would be expected to increase sharply as the sample passed through the  $\text{AFE}\rightarrow\text{FE}$  and  $\text{FE}\rightarrow\text{AFE}$  phase transitions. Fig. 8 shows the variation of the permittivity of a virgin PZ film recorded as a function of a slowly varying dc bias applied first in the positive direction. The permittivity sharply increased by 40 to 60% of its original value at the  $\text{AFE}\rightarrow\text{FE}$  transition field and dropped as the loop

saturated. The increase in permittivity at the FE $\rightarrow$ AFE transition was slightly smaller than at the AFE $\rightarrow$ FE transition.

Weak ferroelectricity was usually observed in these PZ films and was best illustrated in Fig. 8. As the varying dc field just completed one half cycle and switched to the negative direction, the permittivity started to increase slightly and then dropped before the AFE $\rightarrow$ FE transition. A possible ferroelectric interface between the Ti-containing layer and the PZ film might explain this phenomenon, however, earlier results on pure PZ films also showed some ferroelectric behavior at low fields. This effect will require further detailed study.

Fig. 9 demonstrates the dc bias-induced hysteresis behavior obtained in the antiferroelectric films. As expected, this film behaved like a linear capacitor when the alternating field ( $\pm 24.6\text{kV/mm}$ ) was below the AFE $\rightarrow$ FE transition field ( $\sim 32.3\text{kV/mm}$ ). When biased with a dc voltage at 16V (24.6kV/mm), the P-E hysteresis loop behaved like a normal ferroelectric material with two polarization states. This was originated from the hysteresis in the AFE $\leftrightarrow$ FE phase transitions.

The films deposited on fused  $\text{SiO}_2$  substrate were electroded with an interdigital pattern having a gap width of  $10\ \mu\text{m}$ . The birefringence curve shown in Fig. 10 again showed the ferroelectric behavior at small fields. The AFE $\rightarrow$ FE transition was accompanied by a steep increase in the birefringence. A detailed description of this transverse electrooptic behavior has been given elsewhere [13].

#### **4. Summary**

AFE PbZrO<sub>3</sub> films derived from acetate precursors were deposited on several substrates by an automatic dip coating process. The phase inhomogeneity observed in these films was attributed to the volatility of the Pb species formed during the precursor decomposition process. A thin TiO<sub>2</sub> layer was able to facilitate the formation of the perovskite PbZrO<sub>3</sub> and also inhibit the interactions between Pb and SiO<sub>2</sub> at the processing temperature. X-ray diffraction revealed the superstructure characteristic of the antiferroelectric phase in these films. The antiferroelectric properties, along with the dc bias behavior, were measured for PbZrO<sub>3</sub> films at room temperature.

## References

1. E. Sawaguchi, G. Shirane and Y. Takagi, *J. Phys. Soc. Japan* **6** (1951) 333.
2. G. Shirane, E. Sawaguchi and Y. Takagi, *Phys. Rev.* **84** (1951) 476.
3. E. Sawaguchi, H. Maniwa and H. Hoshina, *Phys. Rev.* **83** (1951) 1078.
4. H. Fujishita, Y. Shiozaki, N. Achiwa and E. Sawaguchi, *J. Phys. Soc. Japan* **51** (1982) 3583.
5. L.N. Chapin and S.A. Myers, *Mater. Res. Soc. Symp. Proc.* **200** (1990) 153.
6. C.-C. Hsueh and M.L. Mecartney, *ibid*, p. 219.
7. A.H. Carim, B.A. Tuttle, D.H. Doughty and S.L. Martinez, *J. Am. Ceram. Soc.* **74** (1991) 1455.
8. K.D. Preston and G.H. Haertling, *Integrated Ferroelectrics* **1** (1992) 89.
9. S.L. Swartz, S.J. Bright, P.J. Melling and T.R. Shrout, *Ferroelectrics* **108** (1990) 71.
10. S. Hirano and K. Kato, *J. Non-Cryst. Solids* **100** (1988) 538.
11. B. Jaffe, *Proc. Inst. Radio Engrs.* **49** (1961) 1264.
12. K. Uchino and S. Nomura, *Ferroelectrics* **50** (1983) 191.
13. F. Wang, K.K. Li and G.H. Haertling, *Opt. Lett.* **17** (1992) 1122.
14. D. Berlincourt, H.H.A. Krueger and B. Jaffe, *J. Phys. Chem. Solids* **25** (1964) 659.
15. G. H. Haertling, *Ferroelectrics* **116**, 51 (1991).

16. K.K. Li, G.H. Haertling and W.-Y. Howng, *Integrated Ferroelectrics*. **3** (1992) to be published.
17. F. Wang, C.B. Juang, C. Bustamante and A.Y. Wu, in Proc. of the 4th Intern. SAMPE Electronic Conf., Albuquerque, New Mexico, June, 1990 (Soc. Advancement of Mater. & Process Engr., Covina, Calif.) p.712.
18. Y. Takahashi, Y. Matsuoka, K. Yamaguchi, M. Matsuki and K. Kobayashi, *J. Mater. Sci.* **25** (1990) 3960.
19. K.D. Budd, S.K. Dey and D.A. Payne, *Brit. Ceram. Proc.* **36** (1985) 107.
20. Y. Takahashi and K. Yamaguchi, *J. Mater. Sci.* **25** (1990) 3950.
21. B.A. Tuttle, private communication.
22. K.K. Li, G.H. Haertling and W.-Y. Hwong, presented at the Am. Ceram. Soc. 94th Ann. Meeting, Minneapolis, MN, April 1992. (Abstr.45-E-92)

## Figure Captions

- Fig. 1. XRD patterns of dried powder pyrolyzed at different temperatures. (#: Pb, o: oxidized Pb, \*: perovskite  $\text{PbZrO}_3$ .)
- Fig. 2. TGA and DTA curves of dried  $\text{PbZrO}_3$  powder heated in air at a rate of  $10^\circ\text{C}/\text{min}$ .
- Fig. 3. SEM photograph of a 10-layer  $\text{PbZrO}_3$  film deposited on a Pt/Ti-coated Si substrate.
- Fig. 4. SEM photograph of a 10-layer  $\text{PbZrO}_3$  film formed on a Pt/Ti-coated Si substrate with a thin  $\text{TiO}_2$  pre-coat.
- Fig. 5. A  $1\mu\text{m}$   $\text{PbZrO}_3$  film formed on fused  $\text{SiO}_2$  pre-coated with a  $\text{TiO}_2$  layer.
- Fig. 6. XRD pattern of the  $\text{PbZrO}_3$  film shown in Fig. 5 and its superstructure peak characterizing the antiferroelectricity.
- Fig. 7. A typical dielectric double hysteresis loop of  $\text{PbZrO}_3$  film deposited on Pt/Ti-coated Si substrate with a  $\text{TiO}_2$  layer.
- Fig. 8. Variation of the  $\text{PbZrO}_3$  film permittivity as a function of the dc bias.
- Fig. 9. P-E hysteresis loop of a  $\text{PbZrO}_3$  film with and without a dc bias when the alternating field is lower than the AFE $\rightarrow$ FE transition field.
- Fig. 10. Birefringence shift,  $\Delta n$ , versus electric field, E, plot of an antiferroelectric  $\text{PbZrO}_3$  film on fused  $\text{SiO}_2$ .

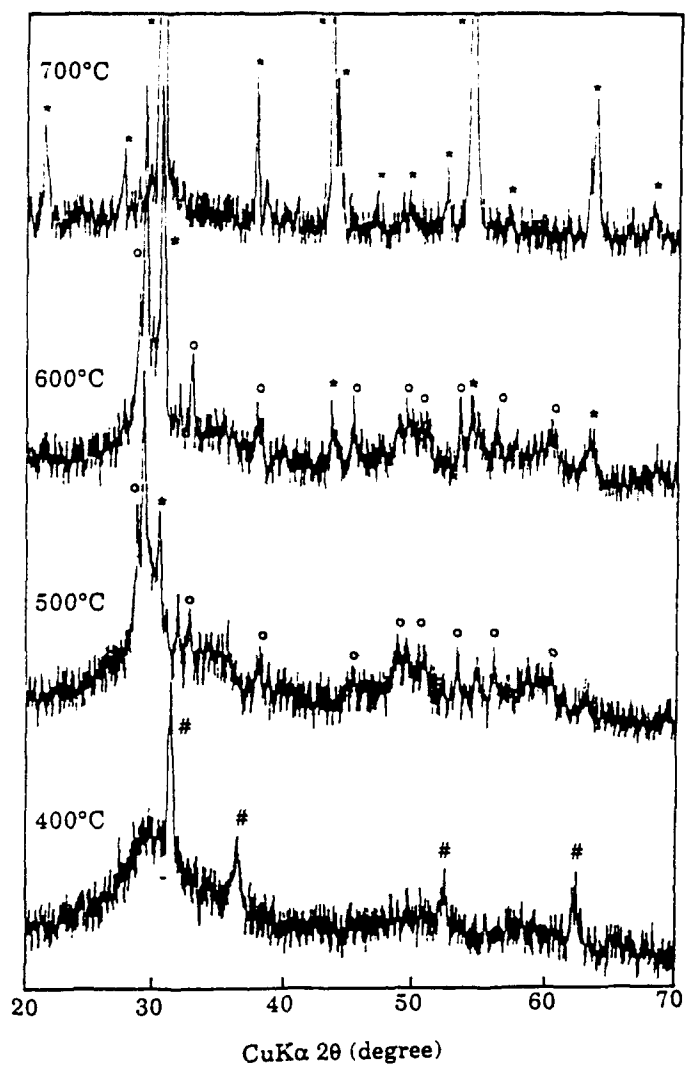


Fig. 1. XRD patterns of dried powder pyrolyzed at different temperatures. (#: Pb,  $\circ$ : oxidized Pb, \*: perovskite  $\text{PbZrO}_3$ .)

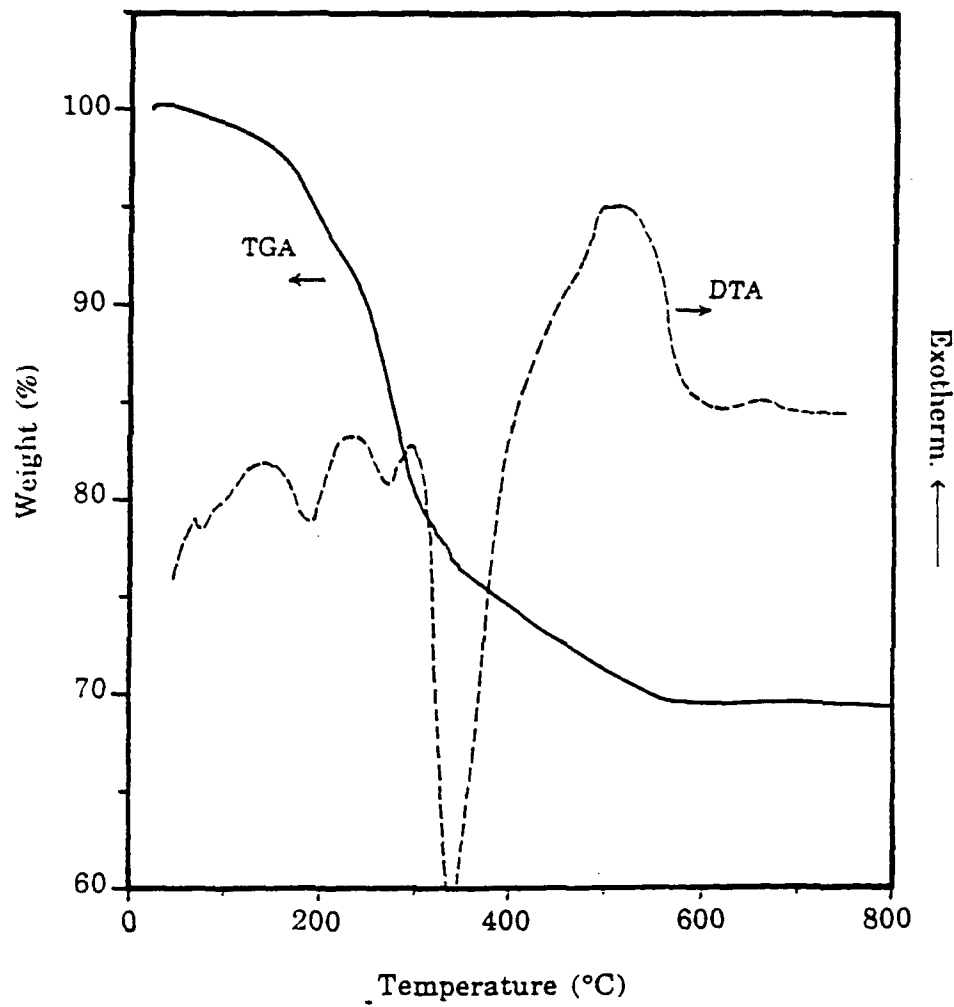


Fig. 2. TGA and DTA curves of dried  $\text{PbZrO}_3$  powder heated in air at a rate of  $10^\circ\text{C}/\text{min}$ .

Figure 3.

(K.K. Li, F. Wang and G.H. Haertling)

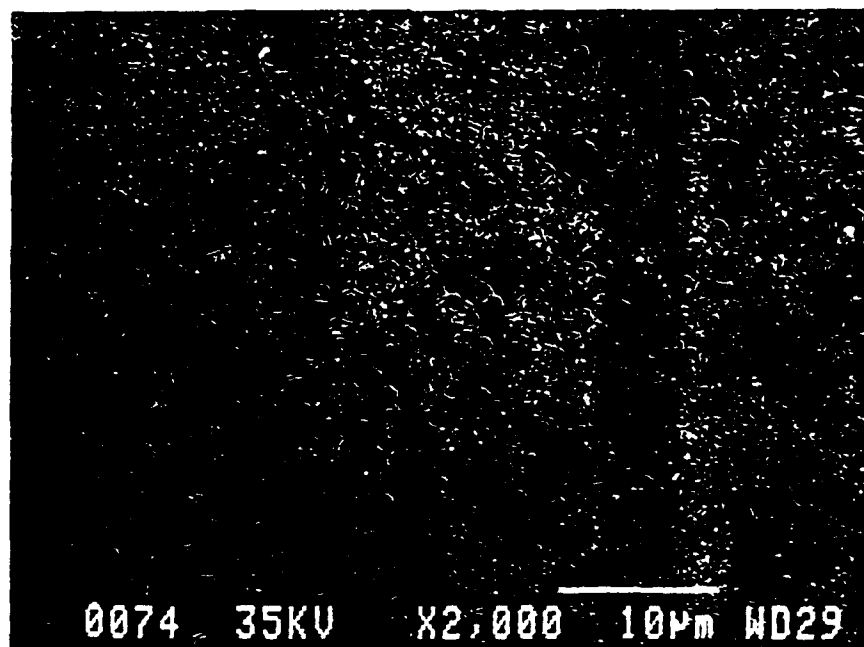


Fig. 3. SEM photograph of a 10-layer PbZrO<sub>3</sub> film deposited on a Pt/Ti-coated Si substrate.

Figure 4.

(K.K. Li, F. Wang and G.H. Haertling)

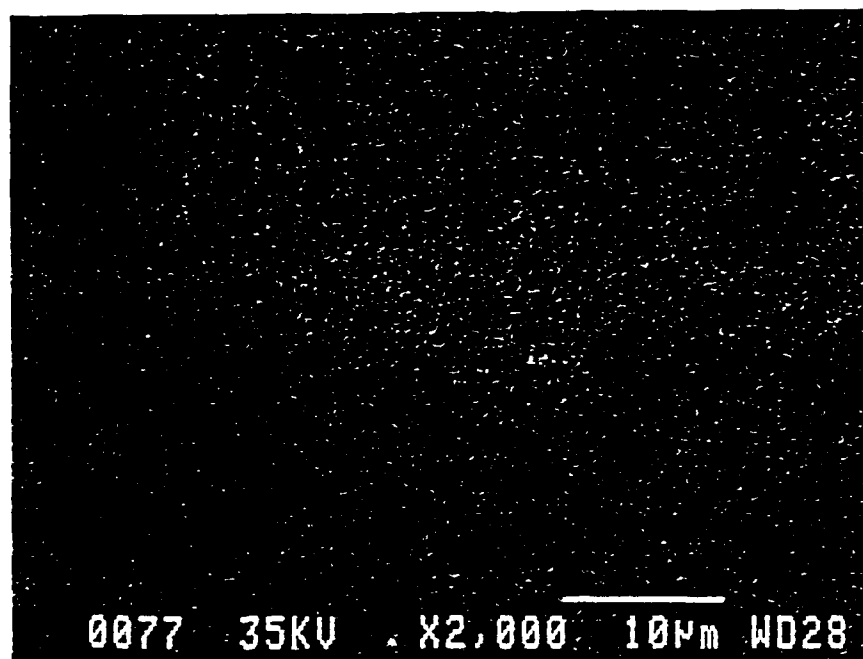


Fig. 4. SEM photograph of a 10-layer PbZrO<sub>3</sub> film formed on a Pt/Ti-coated Si substrate with a thin TiO<sub>2</sub> pre-coat.

Figure 5.

(K.K. Li, F. Wang and G.H. Haertling)

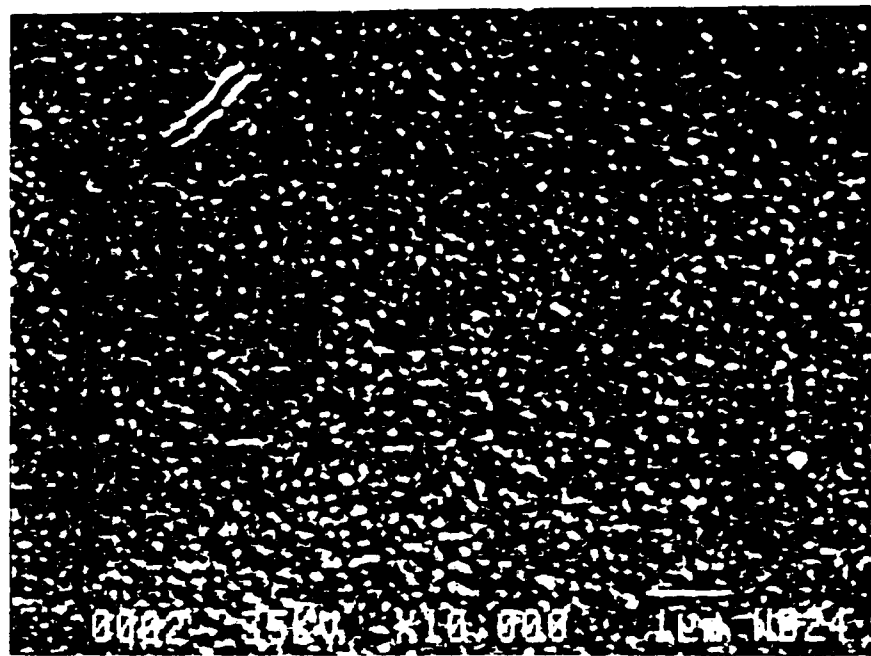


Fig. 5. A  $1\mu\text{m}$   $\text{PbZrO}_3$  film formed on fused  $\text{SiO}_2$  pre-coated with a  $\text{TiO}_2$  layer.

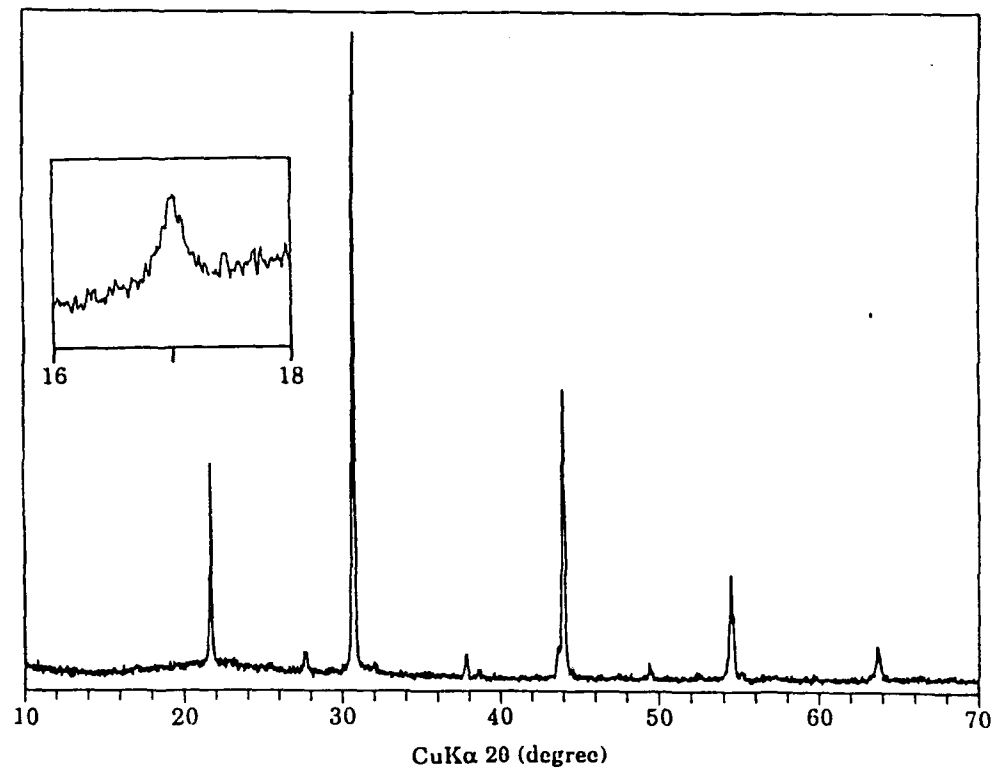


Fig. 6. XRD pattern of the  $\text{PbZrO}_3$  film shown in Fig. 5 and its superstructure peak characterizing the antiferroelectricity.

Figure 7.

(K.K. Li, F. Wang and G.H. Haertling)

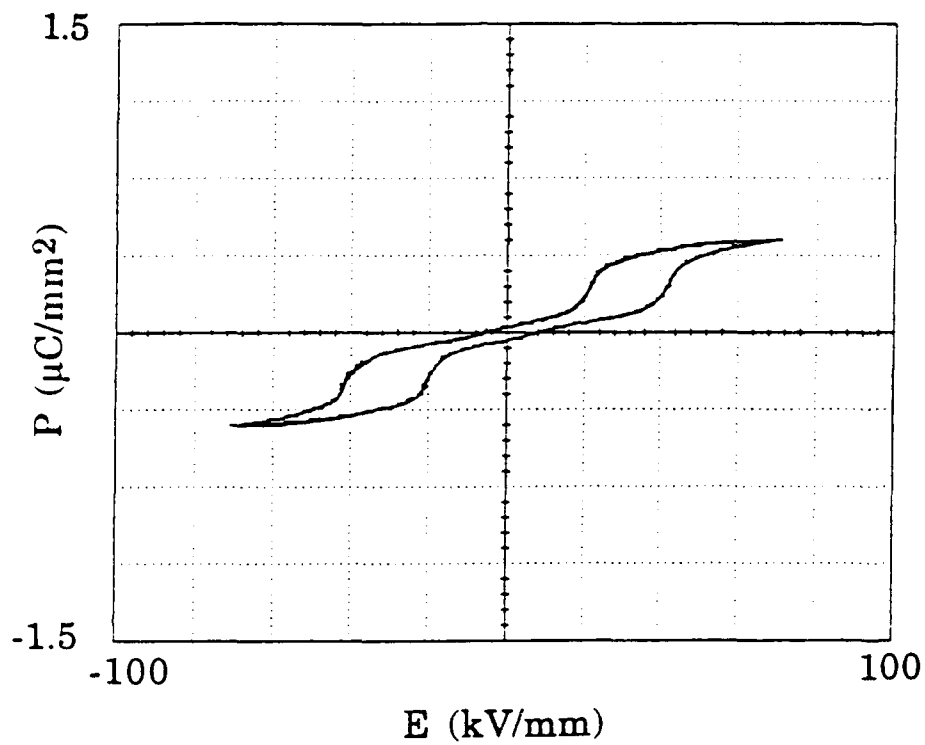


Fig. 7. A typical dielectric double hysteresis loop of  $\text{PbZrO}_3$  film deposited on Pt/Ti-coated Si substrate with a  $\text{TiO}_2$  layer.

Figure 8.

(K.K. Li, F. Wang and G.H. Haertling)

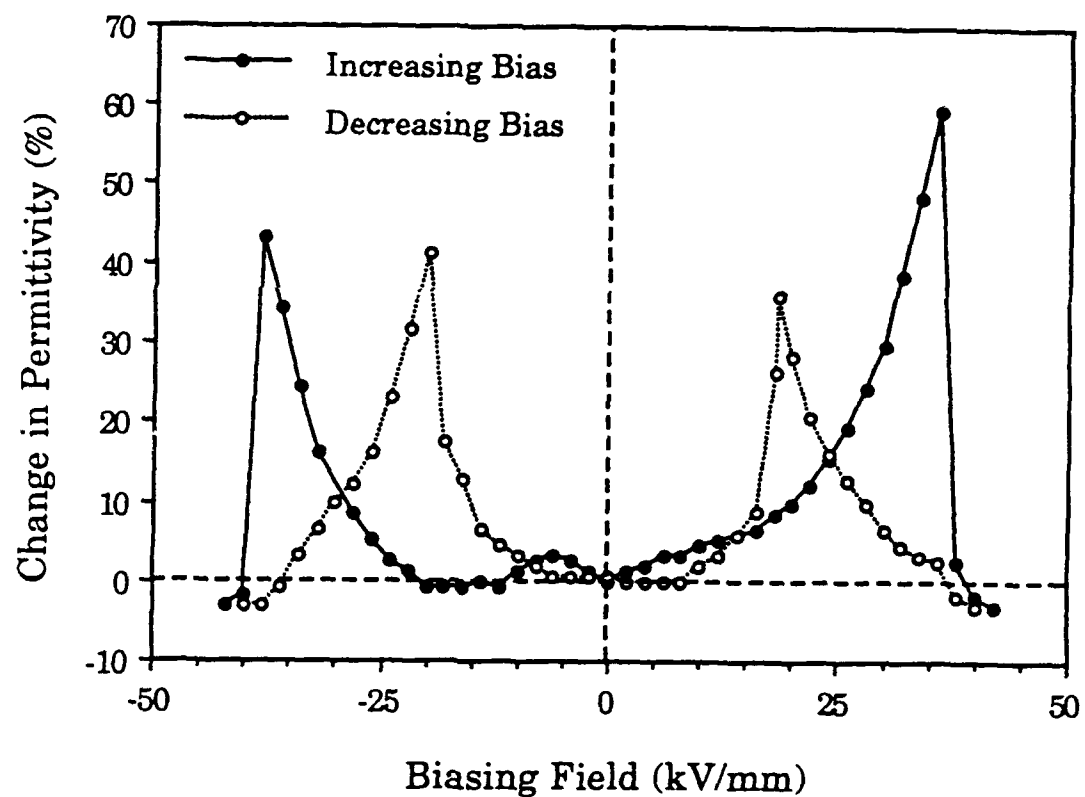


Fig. 8. Variation of the  $\text{PbZrO}_3$  film permittivity as a function of the dc bias.

Figure 9.

(K.K. Li, F. Wang and G.H. Haertling)

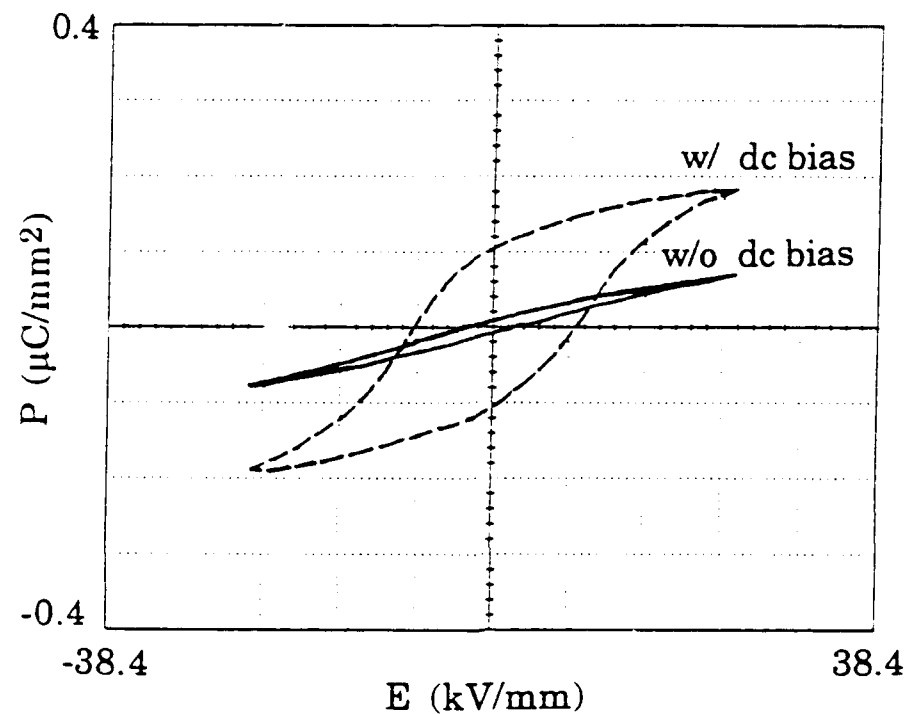


Fig. 9. P-E hysteresis loop of a  $\text{PbZrO}_3$  film with and without a dc bias when the alternating field is lower than the  $\text{AFE} \rightarrow \text{FE}$  transition field.

Figure 10.

(K.K. Li, F. Wang and G.H. Haerling)

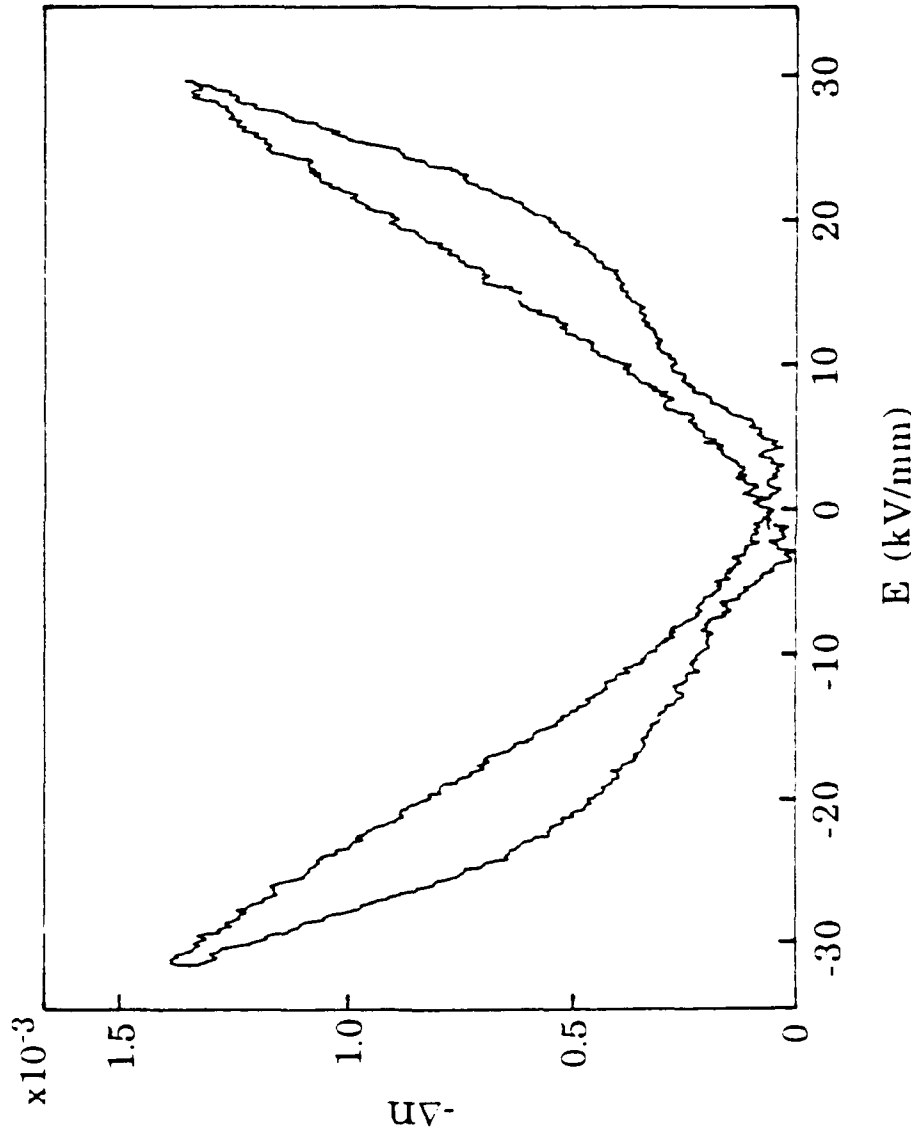


Fig. 10. Birefringence shift,  $\Delta n$ , versus electric field,  $E$ , plot of an antiferroelectric  $PbZrO_3$  film on fused  $SiO_2$ .

## **SECTION 4**

**Discrete Electrooptic Response in Lead Zirconate Thin Films  
due to Field-Induced Phase Transition**

Feiling Wang, Kewen K. Li, Eugene Furman and Gene H Haertling

Department of Ceramic Engineering

Clemson University

Clemson, South Carolina 29634

A discrete transverse electrooptic response associated with a field-induced antiferroelectric-ferroelectric phase transition has been observed to exist in lead zirconate thin films grown on Pt/Ti-coated silicon substrates. The magnitude of the birefringence jump from the antiferroelectric to the ferroelectric state is approximately  $2.5 \times 10^{-2}$ . Quantitative correlation between the field-induced birefringence and the polarization was also experimentally studied. The discrete birefringent change in the thin films may be a desirable property for applications in optical switches or other integrated optical devices.

The field-induced antiferroelectric (AFE)-ferroelectric (FE) phase transition has been utilized to produce discrete strain for applications in actuators and shape memory<sup>1,2</sup>. To exploit optical usefulness of antiferroelectric materials, questions can be asked as to whether a field-induced AFE-FE phase transition is accompanied by a discrete change in optical properties of the materials. In a recent paper, the transverse electrooptic effect in antiferroelectric lead zirconate (PZ) thin films was reported<sup>3</sup>. It was found that the field-induced birefringence in the lead zirconate films exhibited a characteristic response different from that of ferroelectric materials; this response was attributed to the field-induced AFE-FE structural transition. However, because of the field nonuniformity created by the planar electrodes, the measured birefringence did not clearly show the discrete change under field-induced AFE-FE phase transition predicted by a phenomenological model. The electrooptic measurement in the transmission mode also made it infeasible to experimentally study the correlation between the birefringence of the thin film materials and their polarization because 1) the electrooptic properties and the dielectric properties had to be measured from thin films deposited on two different type of substrates and 2) the direction of the external electric field was different for the two type of measurements due to the requirements of the measuring methods.

With a newly developed measuring method using phase-detection scheme in the reflection mode, it has become possible to measure the electrooptic effect of thin films deposited on opaque substrates. Both dielectric and electrooptic properties of the thin films, therefore, can be measured from the same sample with the same configuration of electrodes. The purpose of this letter is to report the first observation of the discrete birefringent change in PZ thin films under field-induced AFE-FE phase transitions and the direct measurement of the correlation between the field-induced birefringence and the polarization of the materials.

Polycrystalline lead zirconate films were deposited on Pt/Ti-coated silicon wafers by using a automated dip-coating technique from an acetate precursor<sup>4,5</sup>. Indium-tin oxide (ITO) layers were deposited onto the films as top electrodes by means of magnetron sputtering for both dielectric and electrooptic measurements. The dielectric properties of the films were measured by

means of a Sawyer-Tower circuit. When a voltage is applied to the ITO and the Pt electrodes, a sandwiched PZ thin film becomes birefringent with its c axis along the normal of the film surface as a result of the transverse electrooptic effect. A reflection mode phase-detection technique, a modification of the transmission mode phase-detection technique<sup>6</sup>, was used to measure the field-induced birefringence,  $\Delta n = n_e - n_o$ , in the PZ thin films. The arrangement of the optics and the electrodes is illustrated in Figure 1. A He-Ne laser of 632.8 nm wavelength was utilized as the light source. The polarizers, P and P', are inclined 45 degrees with respect to the incident plane and mutually crossed. The polarization state of the light beam was modulated in a periodic manner by means of a photoelastic modulator, M. At a finite incident angle, the reflected light polarized in the incident plane acquires a phase retardation with respect to the component polarized perpendicularly to the incident plane due to the birefringence of the PZ thin film. Under a properly chosen reference signal in the lock-in amplifier at the modulation frequency (synchronized with the photoelastic modulator), the output signal of the lock-in amplifier is proportional to the phase retardation generated by the thin film. The proportional constant was calibrated by using the adjustable optical compensator, C.

A typical response of the birefringence in the PZ films versus low frequency (approximately 0.2 Hz) voltage is shown in Figure 2(a). The voltage was measured with respect to the bottom electrode, i.e. platinum coating. The thickness of the PZ film was approximately 1  $\mu\text{m}$ . A clear transition is manifested with an abrupt increase of the birefringence as the increasing external field reaches approximately 40 kV/mm (40 volts). The enhanced birefringence is sustained until the field is reduced below approximately 30 kV/mm (30 volts). In order to relate the observed electrooptic response of the PZ thin film with its dielectric properties, a polarization versus voltage loop, shown in Figure 2(b), was taken from the same sample. Figure 2(b) exhibits a typical double hysteresis loop for antiferroelectric materials under a field-induced AFE-FE structural transition. Comparing Figure 2(a) and 2(b), it is clear that the transition behavior in the electrooptic response occurs precisely at the electric field where the field-induced AFE-FE transition occurs. Such electrooptic response is consistent with an earlier prediction<sup>3</sup>. The reason

for the discrete change in the birefringence to be observed in this measurement was that the electric field in the thin film material during the reflection mode phase-detection measurement was uniform. The magnitude of the birefringent difference between the AFE state ( $\Delta n_A$ ) and the FE state ( $\Delta n_F$ ) is approximately  $\Delta n_A - \Delta n_F = 2.5 \times 10^{-2}$ , which is very similar to that of perovskite thin film in ferroelectric phase, i.e., 8/65/35 PLZT, under polarization saturation.

Although the main features of the electrooptic response shown in Figure 2 are consistent with the theoretical prediction, the quantitative correlation between the birefringence  $\Delta n$  and the polarization of the thin film materials possesses a more complicated behavior. In Figure 3, the field-induced birefringence is plotted as a function of the polarization by detecting both quantities simultaneously in a low frequency voltage cycle. Portion A of the curve corresponds to the AFE state of the material; portion F and F' correspond to the field-induced FE state while portion B and B' of the curve correspond to the phase transition, which occupies a very small portion of the time duration in the voltage cycle. In the field-induced FE state the birefringence exhibits a different polarization dependence from that in the AFE state. Detailed measurements showed that within the AFE region the birefringence of the thin films can be described by a quadratic function of the polarization as expected by using a phenomenological model similar to that for ferroelectric materials. In the field-induced FE region, however, the birefringence exhibits a saturation behavior that is not fully understood at present. The splitting of the curve in the phase transition region indicates that a single order parameter, namely polarization, is not sufficient in determining the birefringence of the material during the phase transition. The asymmetry shown in both Figure 2 and 3 may be attributed to a ferroelectric-semiconductor contact behavior in the presence of ITO electrodes<sup>7</sup>.

The quadratic electrooptic R coefficient for the PZ thin film in the AFE phase is evaluated from the experimental data to be approximately  $3 \times 10^{-19} (\text{m/V})^2$ , which is two orders of magnitude smaller than that of a typical ferroelectric perovskite thin film material. Because the low-frequency linear susceptibility of the PZ films is an order of magnitude smaller than that of ferroelectric perovskite materials, the quadratic polarization-optical g coefficient defined by

$$\Delta n = -\frac{1}{2} n^3 g P^2 \quad , \quad (1)$$

where  $P$  is the polarization of the material, yields  $g = 0.05 \text{ m}^4 \text{C}^{-2}$ , that is very close to the typical value for perovskite materials in ferroelectric phase<sup>8</sup>. This result seems to extend the validity of Miller's rule<sup>9</sup> into antiferroelectric materials. An explanation of the constancy of the polarization-optical  $g$  coefficient is that the field-induced birefringence in a perovskite material is determined by the (low frequency) local bias field that is dominated by the linear susceptibility of the materials at the low frequency, provided that the nonlinear polarizability at optical frequencies is similar for all perovskite materials including antiferroelectric materials. The nonlinear polarizability of the materials at optical frequencies is known to be dominated by the electronic polarization determined by a structure common to all perovskites, namely, oxygen-octahedra<sup>10,11</sup>.

The observed discrete change of the field-induced birefringence at the AFE-FE phase transition field may be utilized in optical switches or spatial light modulators. With a bias field, the thin film materials exhibit a birefringent bistability as shown by a biased  $\Delta n$  versus voltage loop in Figure 4. Such bistability may be used to realize programmable spatial light modulator, where the on/off status of a pixel can be inter-switched by bipolar electric pulses.

This study was sponsored by the Office of Naval Research under contract No. N00014-19-J-508.

## **Figure Captions**

**Figure 1.** Measuring system for the field-induced birefringence of the PZ films. Also shown is the arrangement of the electrodes.

**Figure 2.** (a): Field-induced birefringence as a function of the applied low-frequency voltage; (b): Polarization as a function of the applied low-frequency voltage. The horizontal scale is 20 volts per division. The vertical scales are  $0.7 \times 10^{-2}$  and  $20 \mu\text{C}/\text{cm}^2$  for (a) and (b), respectively.

**Figure 3.** Birefringence as a function of the polarization. The horizontal and vertical scales are  $10 \mu\text{C}/\text{cm}^2$  per division and  $0.7 \times 10^{-2}$ , respectively.

**Figure 4.** Birefringence versus applied voltage curve under bias = -20 volts. The horizontal and vertical scales are 10 volts per division and  $0.7 \times 10^{-2}$  per division respectively.

## References

1. K. Uchino, Japan. J. Appl. Phys. **24**, Suppl. 24-2, 460(1985)
2. W. Pan, C. Q. Dam, Q. Zhang and L. E. Cross, J. Appl. Phys. **66**, 6014(1989)
3. F. Wang, K. K. Li and G. H. Haertling, Optics Lett. **17**, 1122(1992)
4. K. K. Li, F. Wang and G. H. Haertling, "Antiferroelectric lead zirconate thin films derived from an acetate precursor system," J. Mater. Sci. (to be published)
5. G. H. Haertling, Ferroelectrics, **116**, 51(1991)
6. F. Wang, "Electrooptic Properties of (Pb,La)(Zr,Ti)O<sub>3</sub> Thin Film and Related Materials," Ph.D. Dissertation, University of New Mexico (1991), p.12
7. F. Wang and G. H. Haertling, "Birefringent bistability in (Pb,La)(Zr,Ti)O<sub>3</sub> thin films with a ferroelectric-semiconductor interface," Appl. Phys. Lett. (to be published)
8. P. D. Thacher, J. Appl. Phys. **41**, 4790 (1970)
9. R. C. Miller, Appl. Phys. Lett. **5**, 17 (1964)
10. M. DiDomenico, Jr. and S. H. Wemple, J. Appl. Phys. **40**, 720 (1969)
11. F. Wang and A. Y. Wu, Phys. Rev. **B46**, 3709 (1992)

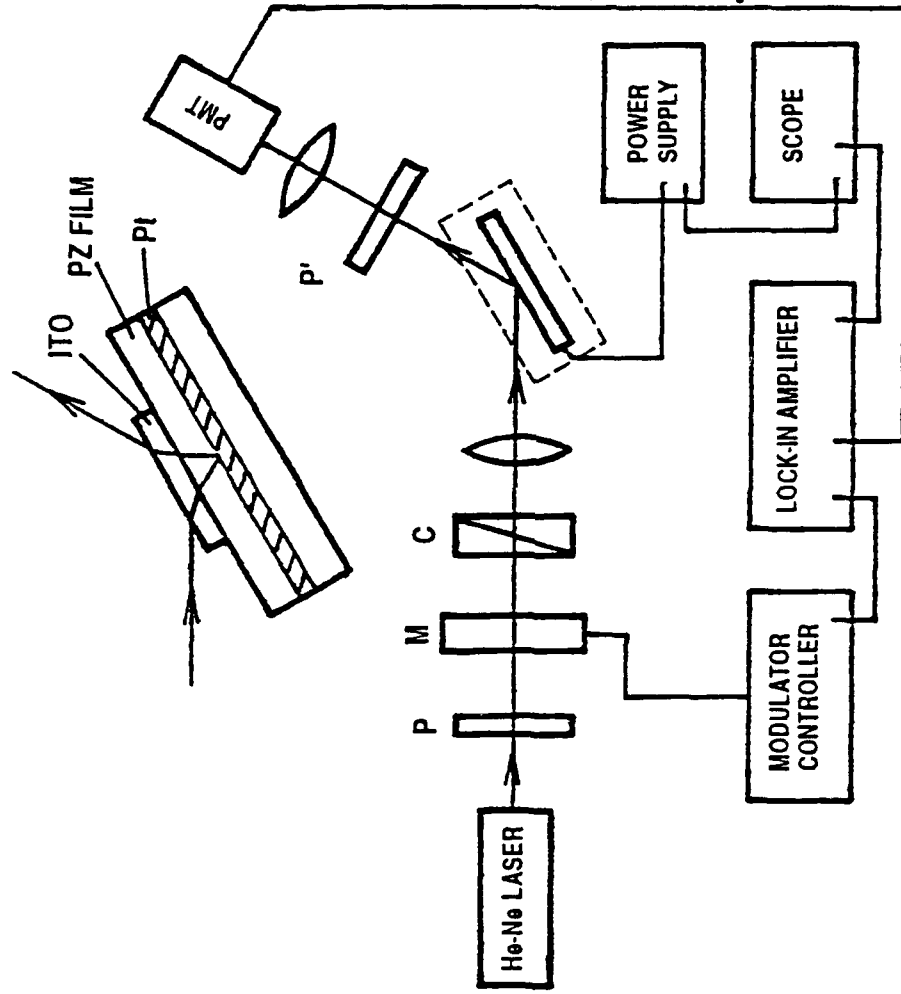


**Figure 1.** Measuring system for the field-induced birefringence of the PZ films. Also shown is the arrangement of the electrodes.

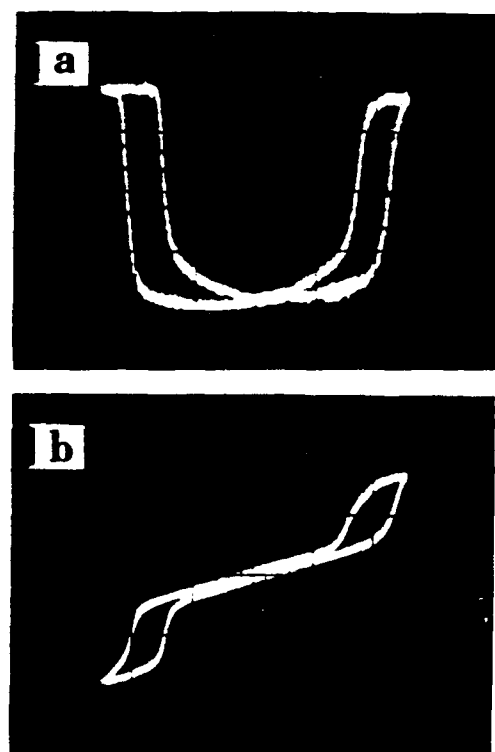


**Figure 2.** (a): Field-induced birefringence as a function of the applied low-frequency voltage; (b): Polarization as a function of the applied low-frequency voltage. The horizontal scale is 20 volts per division. The vertical scales are  $0.7 \times 10^{-2}$  and  $20 \mu\text{C}/\text{cm}^2$  for (a) and (b), respectively.

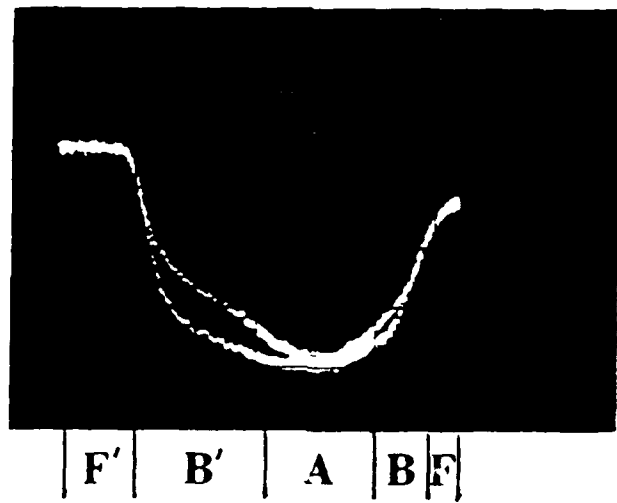


**Figure 3.** Birefringence as a function of the polarization. The horizontal and vertical scales are  $10 \mu\text{C}/\text{cm}^2$  per division and  $0.7 \times 10^{-2}$ , respectively.

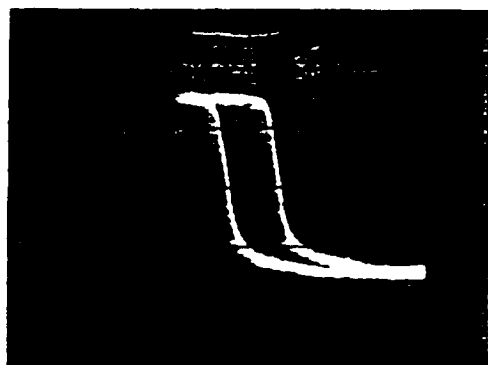


**Figure 4.** Birefringence versus applied voltage curve under bias = -20 volts. The horizontal and vertical scales are 10 volts per division and  $0.7 \times 10^{-2}$  per division respectively.

## **SECTION 5**

# TRANSVERSE ELECTROOPTIC PROPERTIES OF ANTIFERROELECTRIC LEAD CONTAINING THIN FILMS

Feiling Wang, Kewer K. Li and Gene H. Haertling  
Department of Ceramic Engineering  
Clemson University  
Clemson, South Carolina 29634-0907

The transverse electrooptic effect was observed in solution coated lead zirconate thin films. The electric-field-induced birefringent shift exhibited a characteristic response which differed from the normal butterfly-like loops for ferroelectric materials. The observed unique response in lead zirconate thin films was related to their antiferroelectric nature and the electric-field-induced antiferroelectric-ferroelectric phase transition. The possible applications of the materials for optical memory are discussed.

## Introduction

Ferroelectric (FE) thin films, owing to their high dielectric constant and two electrically switchable remanent states, have attracted great interest for the development of nonvolatile memory devices and other applications<sup>1,2</sup>. A variety of ferroelectric materials are also known to possess transverse electrooptic properties, i.e. the electric-field-controlled birefringence; however, ferroelectric switching (polarization reversal with an electric field) has not proved equally useful in integrated optical and/or optoelectronic devices. To facilitate an optical memory function in optoelectronic devices, it is desirable for the waveguide materials to possess two electrically switchable birefringent states. However, the two remanent polarization states are not distinguishable for the index ellipsoid in ferroelectric materials. Therefore, it is not feasible to realize optical memory in ferroelectric materials by switching between the two remanent polarization states.

Recently the transverse electrooptic effects in antiferroelectric (AFE) lead zirconate ( $PbZrO_3$ ) thin films were observed<sup>3</sup>. The electric-field-induced birefringent shift in the lead zirconate thin films showed a characteristic response not exhibited in ferroelectric materials. The unique electrooptic response in the antiferroelectric thin films was found to stem from the electric-field-induced antiferroelectric-ferroelectric phase transition. Besides its importance as a fundamental material property, the transverse electrooptic effect in the antiferroelectric thin films may also furnish a mechanism for optical memory in optoelectronic devices. In this report the latest measurements of the transverse electrooptic properties in antiferroelectric lead zirconate thin films are presented.

## Experimental Method

Lead zirconate thin films were deposited onto fused silica and Pt/Ti coated silicon substrates by a solution coating technique from an acetate precursor<sup>4,5</sup>. The antiferroelectric crystal structure of the resultant thin films was confirmed by the appearance of the X-ray diffraction peak at  $2\theta = 16.9^\circ$ , characterizing the antiferroelectric double cell structure. For the measurement of the dielectric properties of the materials, copper dots were evaporated onto the thin films deposited on the Pt/Ti-coated silicon substrate. For the detection of the transverse electrooptic properties, copper interdigitated electrodes with gap widths ranging from 5 to 40  $\mu m$  were deposited on top of the thin films grown on the fused silica substrates.

The electric-field-induced birefringent shift of the thin film was measured by means of a phase-detection technique<sup>6</sup>, using a He-Ne laser of wavelength of 632.8 nm as the light source. The phase modulation of the incident light was provided by means of a modulator. The measurements were performed with a transmission mode. In the phase detection scheme, the amplitude of the output signal (from a lock-in amplifier) at the modulating frequency was directly proportional to the phase retardation of the sample, provided that the total phase retardation of the sample was sufficiently small. A slow varying dc voltage was applied to the interdigitated electrodes during the measurement. An optical compensator was used to calibrate the measuring system.

## Results and Discussion

A typical electrooptic response of the lead zirconate thin film is shown in Figure 1 where the birefringent shift of the thin film is plotted as a function of the slow varying dc electric field. The thickness of the film was 1  $\mu m$ . Interdigital electrodes with a gap width of 10  $\mu m$  was used in the measurement. As shown in the figure, the electrooptic response of the antiferroelectric thin film exhibits a number of features different from that of ferroelectric materials. For the purpose of comparison, a typical birefringence versus E-field curve for a ferroelectric thin film, i.e. PLZT<sup>7</sup> of composition 2/55/45, is shown in Figure 2. The birefringence versus E-field curve for the lead zirconate thin film is characterized by (1) enhanced hysteretic

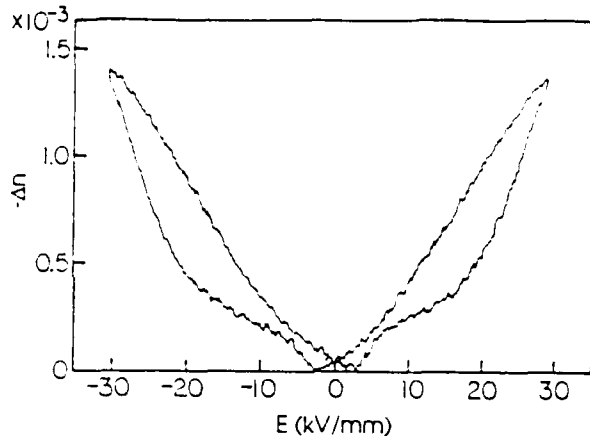


Figure 1 Measured birefringent shift as a function of the external dc electric field for a lead zirconate thin film deposited on a fused silica substrate.

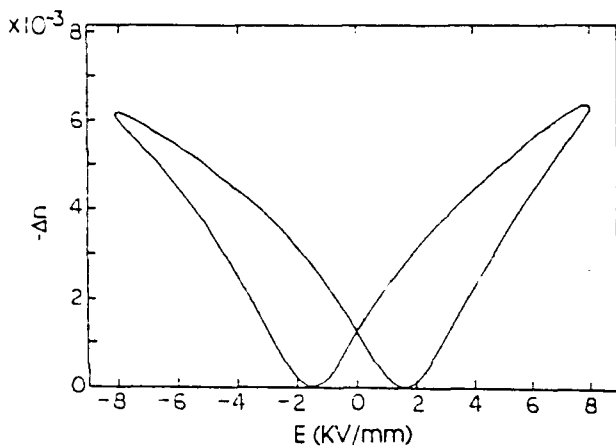


Figure 2 Measured birefringent shift as a function of the external dc electric field for a ferroelectric PLZT thin film deposited on a sapphire substrate.

behavior in the region of field strength above 10 kV/mm, (2) diminished hysteretic behavior in the region of field strength below 5 kV/mm and (3) rapid increase of the slope when the increasing electric field exceeds 20 kV/mm. It was found that the characteristic response of the lead zirconate thin films was attributed to the electric-field-induced AFE-FE structural transition<sup>3</sup>.

With the help of a phenomenological model, the correlation between the field-induced birefringent shift of a material and electric polarization P(E) can be described by the following relation:

$$\Delta n \propto [E + \beta P(E)]^2, \quad (1)$$

where  $\beta$  is a constant dependent on the crystal structure of the material ( $4\pi/3$  for cubic structure). The main features for the electrooptic response of the lead zirconate thin films shown in Figure 1 are consistent with those predicted from the dielectric properties (double hysteresis loop) by using relation (1).

To better understand the nature of the antiferroelectric lead zirconate thin films, a static bias electric field was applied to the thin film material in both the dielectric and electrooptic measurements. Thin films deposited on the Pt/Ti coated silicon substrates were used for the measurement of the dielectric behavior. With the increase of the dc bias, the polarization versus E field curve of the lead zirconate thin film gradually evolves from a double hysteresis loop to a single hysteresis loop. As shown in Figure 3, under an appropriate bias field, the shape of the biased single hysteresis loop very much resembles the normal hysteresis loop for ferroelectric materials. Unlike the ferroelectric materials, however, the two remanent states in the biased single hysteresis loop (denoted by  $P_A$  and  $P_B$  in Fig.3) possess polarizations of different magnitude, which produce two distinguished birefringent states in the thin films. These two birefringent states are clearly represented in the biased birefringence versus E-field curve, as shown in Fig.4, measured from a lead zirconate thin film grown on a fused silica substrate. A static bias field of approximately 17 kV/mm was applied during the measurement. It is obvious that the two distinguished remanent birefringent states  $\Delta n_A$  and  $\Delta n_B$  are associated with the two remanent polarization states  $P_A$  and  $P_B$  in the biased single hysteresis loop shown in Figure 3. It should be noted, however, that to avoid the breakdown of the electrodes through the air, the bias electric field and the scan range are lower in the measurement of the electrooptic properties than in the measurement of the dielectric property. In addition, because these two measurements involve thin films deposited on two different types of substrates with different directions of applied electric field, quantitative correlation between these two measurements is not possible.

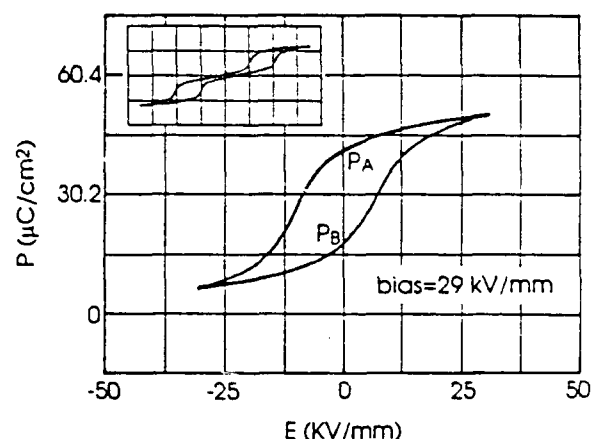


Figure 3 Dielectric properties of a lead zirconate thin film grown on a Pt/Ti-coated silicon substrate, taken under a static bias field of 29 kV/mm. The insert is a hysteresis loop of the same sample taken with zero bias field. The horizontal and vertical scales for the insert plot are 25 kV/mm per division and 30.2  $\mu\text{C}/\text{cm}^2$  per division, respectively.

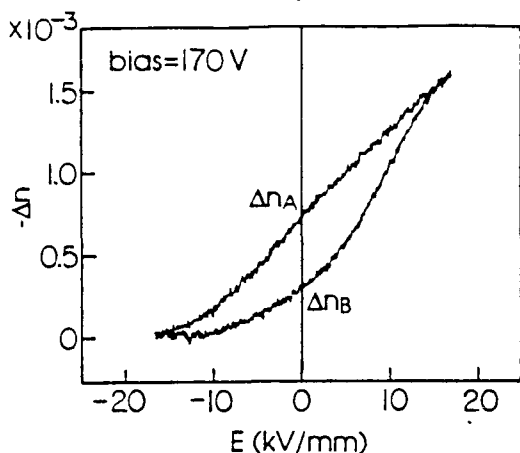


Figure 4 Birefringent shift as a function of the slow varying external field measured with a dc bias field of 17 kV/mm for a lead zirconate thin film on a fused silica substrate.

It was found that the lead zirconate thin films acquired a permanent birefringence once an initial electric field of sufficient magnitude was applied. Shown in Figure 5 is the birefringent shift of a lead zirconate thin film as a function of the slow varying external electric field recorded during the first few cycles of the field scan. In the first half cycle of the field scan, the birefringence of the material drastically increased when the increasing electric field exceeded approximately 16 kV/mm. When the external electric field was reduced to zero, the material retained a significant remanent birefringent shift. During the next few scan cycles, this remanent birefringence kept increasing yet the increment was smaller and smaller after each cycle. A stable remanent birefringence (permanent birefringence) was finally reached as shown previously in the birefringence versus E-field curve of Figure 1. The stable remanent birefringent state, under zero external electric field, was chosen as the zero-

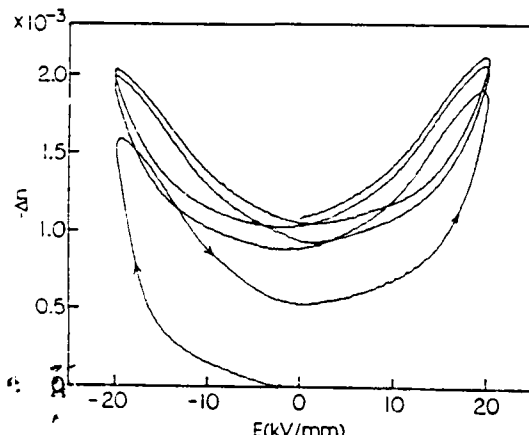


Figure 5 The evolution of the electrooptic response of a lead zirconate thin film on a fused silica substrate during the first few cycles of the electric field scan.

birefringence point in plotting both Figure 1 and Figure 4. After testing a few lead zirconate thin film samples, it was found that this initiating process of the material was reproducible.

The observed permanent birefringence in the antiferroelectric thin films mentioned above may be related to other types of memory behavior previously observed in antiferroelectric lead zirconate materials<sup>8</sup>. A possible explanation for this birefringence memory is that when the AFE-FE phase transition occurred under a sufficiently high electric field the ferroelectric domains are forced to align along the direction of the E-field; although the structure of antiparallel dipoles was restored after the withdrawal of the external E-field, the antiferroelectric dipoles remained preferentially aligned in the direction along which the E-field was previously applied. Such an explanation for the birefringence memory is supported by an optical study of the lead zirconate crystal which showed that the index of refraction is the smallest for the light polarized along the *a* axis of the antiferroelectric unit cell<sup>9</sup>. This mechanism of birefringence memory is distinguished from that of ferroelectric materials where birefringence memory is mainly caused by the remanent polarization.

The characteristic electrooptic response of the lead zirconate thin films may furnish a means of realizing optical memory in optoelectronic devices. Two different mechanisms may be utilized in optical memory devices. In the first type of memory, the information may be stored in a virgin material by applying a sufficiently high electric field. After the withdrawal of the electric field, as shown in Figure 5, the thin film material becomes permanently oriented and possesses a permanent birefringence of approximately  $1.3 \times 10^{-3}$ . The second type of memory is associated with the two distinguished birefringent states of the thin film materials in the presence of a bias electric field as shown in Figure 4. Because these two birefringent states,  $\Delta n_A$  and  $\Delta n_B$ , are produced by the two remanent states of polarization,  $P_A$  and  $P_B$ , of the material, they are stable under the bias field. The merit of the second type of memory is that the two birefringent states are electrically switchable. For example, a TIR switch<sup>10</sup> made of the antiferroelectric thin film would allow the inter-switching of the light between the two waveguide channels by electric pulses of opposite polarities, operated under a static bias field. Such a switch is not possible with ferroelectric materials in which the two remanent polarization states are optically equivalent.

### Conclusions

The transverse electrooptic property of the solution coated lead zirconate thin film exhibits a characteristic response which is attributed to the electric-field-induced antiferroelectric-ferroelectric phase transition. Under an appropriate static bias electric field, the material possess two distinguishable birefringent states

associated with the two remanent polarization states of the material. The thin films were also found to acquire a permanent birefringence once a sufficiently high electric field was applied to the virgin materials.

Two types of mechanisms are proposed for utilizing the antiferroelectric thin films for optical memory in optoelectronic devices. The first type of memory makes use of the permanent orientation of the material induced by an initial electric field. The second type of memory involves the inter-switching between the two distinguishable birefringent states of the material under a bias field with electric pulses.

#### Acknowledgment

This study was partially sponsored by the Office of Naval Research under contract No. N00014-91-J-508.

#### References

- [1] G.H. Haertling, "Ferroelectric Thin Film for Electronic Applications," *J. Vac. Sci. Technol. A*, 9, 414(1991)
- [2] D. Bonsurant and F. Gnadinger, "Ferroelectrics for Nonvolatile RAMs," *IEEE Spectrum*, July 1989, p.30
- [3] F. Wang, K.K. Li, and G.H. Haertling, "Transverse Electro-Optic Effect of Antiferroelectric Lead Zirconate Thin Films," *Optics Lett.* 17, 1122(1992)
- [4] K.K. Li, F. Wang, and G.H. Haertling, "Antiferroelectric Lead Zirconate Thin Films Derived from an Acetate Precursor System," *J. Mater. Sci.* (to be published)
- [5] G.H. Haertling, "PLZT Thin Film Prepared from Acetate Precursors," *Ferroelectrics*, 116, 51(1991)
- [6] F. Wang, C.B. Juang, C. Bustamante, and A.Y. Wu, "Electro-optic Properties of  $(\text{Pb}, \text{La})(\text{Zr}, \text{Ti})\text{O}_3$ ,  $\text{BaTiO}_3$ ,  $(\text{Sb}, \text{Ba})\text{Nb}_2\text{O}_6$  and  $\text{BaNaNb}_5\text{O}_{15}$  Thin Films," in *Proc. of 4th International SAMPE Electronic Conference*, p.712
- [7] G. H. Haertling and C.E. Land, "Hot-pressed  $(\text{Pb}, \text{La})(\text{Zr}, \text{Ti})\text{O}_3$  Ferroelectric Ceramic for Electronic Applications," *J. Am. Ceram. Soc.* 54, 1(1971)
- [8] K. Uchino, "Digital Displacement Transducer Using Antiferroelectrics," *Japan. J. Appl. Phys.* 24, suppl., 24(1985)
- [9] F. Jona, G. Shirane, and R. Pepinsky, "Optical Study of  $\text{PbZrO}_3$  and  $\text{NaNbO}_3$  Single Crystals," *Phys. Rev.* 97, 1585(1955)
- [10] H. Higashino, T. Kawaguchi, H. Adachi, T. Makino and O. Yamazaki, "High Speed Optical TIR Switches Using PLZT Thin Film Waveguides on Sapphire," *Jap. J. Appl. Phys.* 24, suppl., 284(1985)

## **SECTION 6**

## TRANSVERSE ELECTROOPTIC PROPERTIES OF MAGNETRON SPUTTERED PLZT THIN FILMS

F. WANG and G.H. HAERTLING  
Department of Ceramic Engineering,  
Clemson University,  
Clemson, SC 29634 , USA

**ABSTRACT.** Ferroelectric thin films of  $(\text{Pb},\text{La})(\text{Zr},\text{Ti})\text{O}_3$  ceramics were deposited on various substrates by magnetron sputtering. With the use of a phase-detection technique, the transverse electrooptic properties of the films were characterized. It was found that the electrooptic response of the films is strongly dependent on the grain orientation of the thin film materials.

### 1. Introduction

Lead lanthanum zirconate titanate (PLZT) thin films have been deposited onto various substrates by means of solution coating techniques using acetate precursors [1-3]. In search of the optimum coating technique for producing high quality PLZT thin films for various applications, PLZT powders derived from the acetate precursors have been used as target materials in a radio-frequency (RF) magnetron sputter deposition technique designed to complement the *solution coating methods*.

Recently, increasing attention has been paid to the choice of substrates in obtaining thin films of desired properties [2]. It was reported that the thermal expansion mismatch between a ferroelectric thin film and its substrate significantly influences the orientational preference of ferroelectric domains, thus their dielectric properties. This paper is mainly concerned with the observed divergence of the transverse electrooptic properties in PLZT thin films deposited on various substrates by the RF magnetron sputtering.

### 2. Experimental Method

A high vacuum RF magnetron sputter unit was used to deposit PLZT thin films. The target material was a PLZT powder of composition 2/55/45 (La/Zr/Ti) produced by a coprecipitation method from a water soluble acetate precursor [1]. A post-deposition annealing process was utilized to obtain perovskite PLZT films. Typical deposition and annealing parameters are listed below:

RF power:	70 watt	Annealing temperature:	650°C
Total pressure:	10 micron	Annealing time:	40 min.
Oxygen percentage:	40%		
Substrate temperature:	350°C		
Deposition rate:	250 nm/hour		

375

Thin films were deposited onto three types of substrates, i.e. Pt/Ti-coated silicon, randomly oriented sapphire and fused silica substrates.

The transverse electrooptic properties of the PLZT thin films on sapphire and fused silica substrates were measured by a phase-detection technique [4] in a transmission mode using a He-Ne laser as the light source. Planar copper electrodes with a gap width of 50  $\mu\text{m}$  were fabricated on top of the thin film by a photolithography process.

### 3. Results and Discussion

#### 3.1 GRAIN ORIENTATION

With the identical deposition and annealing processes mentioned previously, the thin films deposited on the three types of substrates exhibited significant differences in grain orientation as revealed by x-ray diffraction patterns.

By comparing to the diffraction pattern of the powder, it was found that peak heights for (100) and (110) orientations in thin films on Pt/Ti-coated silicon were reversed, as shown in Figure 1(a). In contrast to the films on Pt/Ti-coated silicon, films on sapphire substrates, shown in Figure 1(b), exhibit a strengthening of the (110) peak, indicating a preferred (110) grain orientation. The most drastic preferential orientation of crystal grains was observed in the thin films deposited on fused silica substrate with (100) being the dominant orientation, as shown in Figure 1(c). Summarized in Table 1 are the types of preferential grain orientation for 2/55/45 PLZT thin films deposited on the three different substrate along with their thermal expansion coefficients.

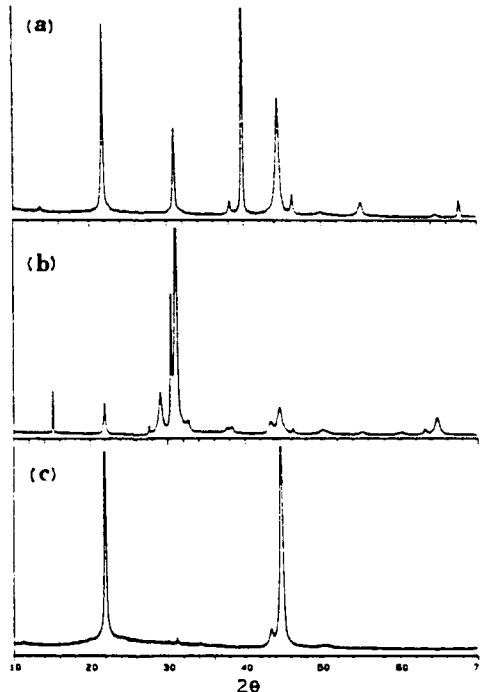


Figure 1. X-ray diffraction patterns for 2/55/45 PLZT thin films deposited on (a) Pt/Ti-coated silicon, (b) sapphire and (c) fused silica substrates.

TABLE 1. Orientation of 2/55/45 PLZT thin films

Substrate	thermal expansion coef. (ppm/ $^{\circ}$ C)	film orientation
fused silica	0.5	dominant (100)
silicon	2.5	preferred (100)
sapphire	8.0	preferred (110)

Noticing that the thermal expansion coefficient of PLZT materials (approximately 5 ppm/ $^{\circ}$ C) is intermediate between those of silicon and sapphire, the results strongly suggest that there is a correlation between the grain orientation and the thermal expansion property of the substrates in sputter deposited thin films. As shown in Table 1, thin films deposited on substrates with smaller thermal expansion coefficients exhibited dominant or preferred (100) orientation while thin films deposited on substrate with larger expansion coefficient exhibits preferred (110) grain orientation. It is not clear at present whether the preferred grain orientations are formed during the low temperature deposition or during the annealing procedure.

### 3.2. ELECTROOPTIC PROPERTIES

The field-induced birefringence of soft ferroelectric materials generally exhibit butterfly loops. In order to quantitatively describe this hysteretic electrooptic effect, three quantities are proposed to characterize a butterfly loop in the following discussion. These quantities are: the optical coercive field  $E_{OC}$  where two birefringence minima occur, the birefringence at the crossover point of a loop  $\Delta n_c$  (measured from the bottom of a curve) and the birefringence at the tip of a loop  $\Delta n_t$ . The value of  $\Delta n_t$  is meaningful only when the corresponding electric field at the tip  $E_t$  is given.

A series of butterfly loops for the electrooptic effect of a sputtered 2/55/45 PLZT film on a sapphire substrate is shown in Figure 2, created by a series field scans from a small range to a large range. Compared to the films on sapphire substrate, the 2/55/45 PLZT thin films deposited on the fused silica substrate exhibit much poorer electrooptic response as shown in Figure 3. The  $\Delta n_t$  for the film on fused silica is approximately one fourth of that for the film on sapphire substrate, taken under the same  $E_t$ . Table 2 lists the three characteristic quantities for films on both sapphire and fused silica substrates.

TABLE 2. Electrooptic properties of 2/55/45 PLZT thin films

Substrate	Thickness (nm)	$E_{OC}$ (kV/mm)	$\Delta n_t \cdot 10^{-3}$	$\Delta n_c \cdot 10^{-3}$
f. silica	620	2.0	1.5	0.2
sapphire	620	1.6	6.2	1.3

$\Delta n_t$  values were taken at  $E_t=8$  kV/mm for both samples.

Being a rhombohedral material, the polar direction of a 2/55/45 PLZT crystal grain is along a three-fold direction of a oxygen-octahedra, i.e. a (111) crystal direction. When the external electric field is parallel to the substrate surface in the phase-detection measurement in the transmission mode, there is virtually no chance for the external field to encounter the (111) crystal direction of the grains in films on fused silica with (100) dominant orientation. Films of this type of orientation, therefore, are unfavorable for utilizing the transverse electrooptic effect of the films in the transmission mode.

In contrast to the films on fused silica, sputtered films on sapphire substrate possess (110) preferred grain orientation, which enhances the possibility for the external electric field to encounter the (111) crystal direction. This preferred grain orientation, therefore,

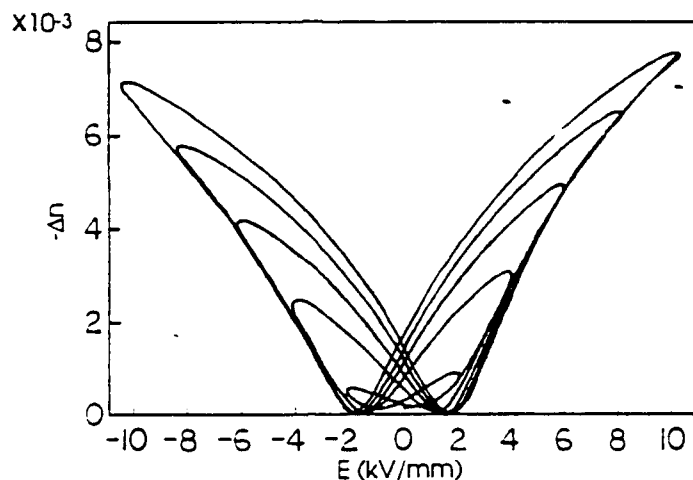


Figure 2. The evolution of the electrooptic response from a small to a large field scan range for a 2/55/45 PLZT film of thickness of 0.62  $\mu\text{m}$  on a sapphire substrate.

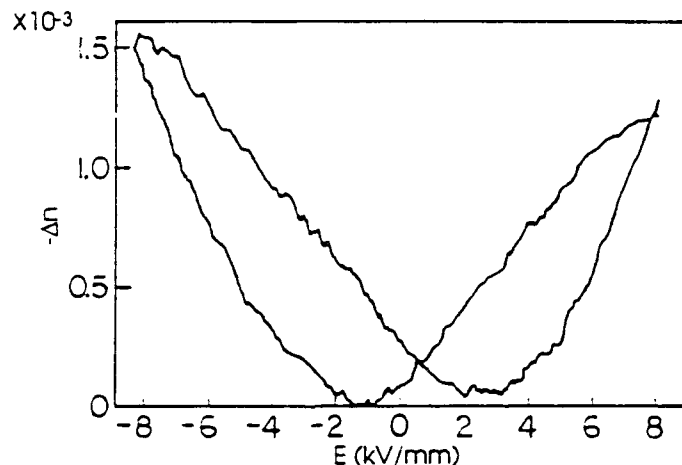


Figure 3. The electrooptic response of a 2/55/45 PLZT film of 0.62  $\mu\text{m}$  thickness on a fused silica substrate.

favors the polarization, which in turn produces a large field-induced birefringence in the materials. As shown in Table 2, films deposited on sapphire substrates with preferred (110) grain orientation indeed exhibited superior electrooptic response.

#### 4. Conclusions

PLZT thin films of composition 2/55/45 were deposited on various substrate with a RF magnetron sputtering technique using powders derived from an acetate precursor.

The electrooptic characterization shows that the films on sapphire with preferred (110) orientation exhibits superior electrooptic response over the films on fused silica with dominant (100) grain orientation. The difference is attributed to the fact that (110) orientation favors the polarization in rhombohedral thin film materials when the external electric field is along a planar direction.

#### 5. Acknowledgements

This research was supported by the Office of Naval Research under contract No. N00014-91-J-508.

#### 6. References

1. G.H. Haertling, Ferroelectrics **116** (1991) 51.
2. K.D. Preston and G.H. Haertling, Appl. Phys. Lett. **60** (1992) 2831.
3. K.K. Li, G.H. Haertling and W.Y. Howng, Integrated Ferroelectrics vol.3, No.1 (in print, 1992)
4. F. Wang, C.B. Juang, C. Bustamante, and A.Y. Wu, in Proc. of 4th International SAMPE Electronic Conference, Albuquerque, New Mexico, June 12-14, 1990, p.712.

## **SECTION 7**

# A PLZT OPTICAL PHASE MODULATOR AND ITS APPLICATIONS

Feiling Wang and Gene H Haertling  
Department of Ceramic Engineering  
Clemson University  
Clemson, South Carolina 29634-0907

An electrooptic phase modulator was designed and fabricated by using the quadratic electrooptic effect of PLZT ceramic of composition 10/65/35. The modulator can be operated at either the fundamental or double frequency of the AC signal driver. The modulator proved effective as a phase modulation device in a phase-detection measurement of small birefringent shift of thin film materials. The principles for such usage are discussed.

## Introduction

Relaxor ceramic materials in the  $(\text{Pb},\text{La})(\text{Zr}, \text{Ti})\text{O}_3$  (PLZT) system are known to possess strong quadratic or slim-looped transverse electrooptic effects<sup>1</sup>. The applications of the materials in optical area have been found in light shutters, spatial light modulators, second harmonic generation as well as waveguide devices such as total internal reflection switches<sup>2,3</sup>. Although single crystal materials that possess linear electrooptic effects such as  $\text{LiNbO}_3$  and KDP have traditionally been the primary material group for optical phase modulation, polycrystalline PLZT ceramics which possess quadratic electrooptic effects can also be used as optical phase modulation media. In this report, an optical phase modulator made from a hot-pressed PLZT ceramic is presented. The application of the modulator in a phase-detection technique for the measurements of small optical phase retardation in thin film materials is discussed.

## Design and Operation

A bulk 10/65/35 PLZT wafer was chosen as the modulating medium. The material was made with a hot pressing process using stoichiometric powder derived from a water-soluble precursor. The material was transparent and showed typical dielectric properties for the material in this composition, i.e. high dielectric constant and very slim hysteresis loop. The electrooptic characterization showed that the dependence of the birefringence shift on the external electric field was primarily quadratic, as presented in Figure 1. The thickness of the PLZT wafer was 0.5 mm (20 mil) with both sides being optically polished. To accommodate the ac driving signal, copper planar electrodes were fabricated on one side of the material by a photolithography technique. The electrode gap width was 50  $\mu\text{m}$ , which allowed a light beam to pass the device without a special focusing effort. An ac electric signal of adjustable amplitude was fed to the electrode pair to drive the modulator. In addition, an adjustable dc bias was also applied to the modulator.

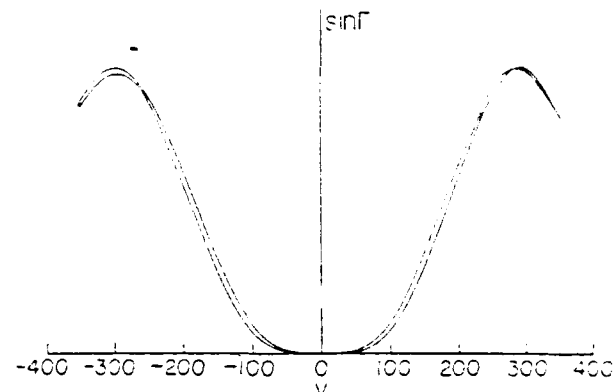


Figure 1 The electrooptic response of a 10/65/35 PLZT ceramic, measured by means of a phase-detection scheme. The Y axis is proportional to  $\sin\Gamma$  with  $\Gamma$  being the optical phase shift due to the birefringence of the material.

Under sufficiently small external field, the field-induced birefringent shift of the material can be expressed as a quadratic function of the applied field:

$$\Delta n = \text{constant} (E_b + E \sin\Omega t)^2, \quad (1)$$

where  $E_b$  is the field strength of the dc bias,  $\Omega$  is the frequency of the ac driving electric field. It is obvious that under a non-zero bias field, the phase shift generated by the modulator contains both  $\Omega$  and  $2\Omega$  components. By adjusting the bias field  $E_b$ , the relative amplitude of  $\Omega$  and  $2\Omega$  components can be altered. The function of the bias field in changing the primary modulating frequency is illustrated in Figure 2 where function  $\Gamma(t)$  is the phase retardation produced by the modulator.

To visualize the phase modulating function of the modulator and the interchange of the modulating frequency with the bias electric field, the modulator was sandwiched between two crossed polarizers with the modulation axis, the direction of the applied electric field, being oriented at 45 degree angle with respect to the polarization direction of the polarizer. With such a arrangement the polarization state of the originally linearly polarized light beam was periodically changed due to the phase shift  $\Gamma(t)$  imposed by the modulator. The intensity of the light output  $I(t)$  is given by:

$$I(t) = B \sin^2[\Gamma(t)/2] = B \sin^2[A(E_b + E \sin\Omega t)^2], \quad (2)$$

where A and B are two system constants. The waveform of the light intensity given by Equation (2) is graphically analyzed in Figure 2. As shown by the figure, the modulation is purely  $2\Omega$  in frequency at zero bias and gradually becomes dominated by the  $\Omega$  component with the increase of the bias electric field.

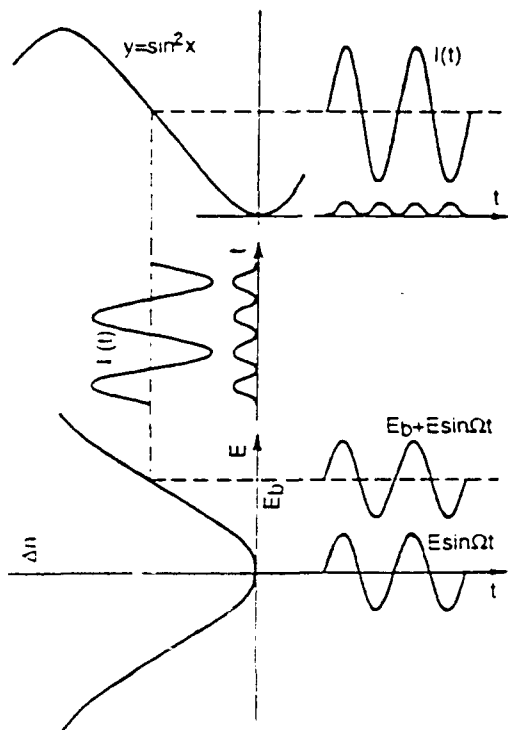


Figure 2 A graphic analysis of the operation modes of the PLZT phase modulator with and without dc bias field.

According to Equation (1), the modulation always contains a  $2\Omega$  component although its relative magnitude becomes very small compared to the  $\Omega$  component when a sufficient bias field is applied. A pure  $\Omega$  modulation mode can actually be achieved by using the saturation behavior in the electrooptic response of the material. The saturation behavior of the electrooptic response in PLZT materials have been observed<sup>4,5</sup>. In the presence of such saturation, the quadratic relation for the field-induced birefringence is no longer adequate; higher order terms or entirely new functional dependence needs to be used. In the electrooptic response curve that shows saturation behavior, there must be a point where the second derivative of the curve is zero. If a bias electric field is applied to this point, the modulation will be purely  $\Omega$  in frequency.

In practice, only a fairly low bias field is needed in order for the modulation at  $2\Omega$  frequency to become insignificant compared to the  $\Omega$  component. Figure 3 shows the waveforms of the light output, recorded by an

oscilloscope, from the second polarizer with the PLZT modulator driven by a 1kHz ac signal operating under various dc bias voltage. The square waves in the pictures are the trigger signal synchronized with the ac driving voltage. As expected, the modulation was purely  $2\Omega$  in frequency under zero bias and eventually became dominated by  $\Omega$  frequency components under a bias voltage of 150 volts. Components of both frequencies are clearly represented under an intermediate bias, as shown by Figure 3(b). The relative amplitude of modulation at both frequencies as functions of the dc bias was measured by a lock-in amplifier synchronized with the driving function generator. As shown in Figure 4, with the increase of the dc bias voltage, the amplitude of the  $2\Omega$  component decreased while the  $\Omega$  component increased. Under a bias voltage of approximately 120 volts the  $2\Omega$  component becomes zero while the  $\Omega$  component approaches a maximum. Under this bias voltage, the PLZT modulator provides

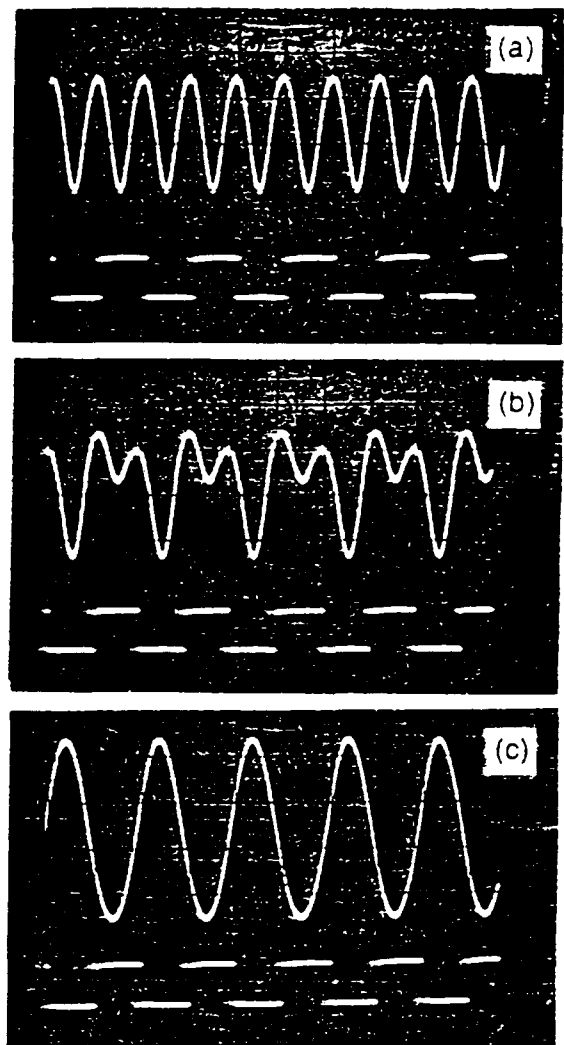


Figure 3 The waveforms of the output light modulated by the PLZT phase modulator operated under (a) bias=0V, (b) bias=20V and (c) bias=150V.

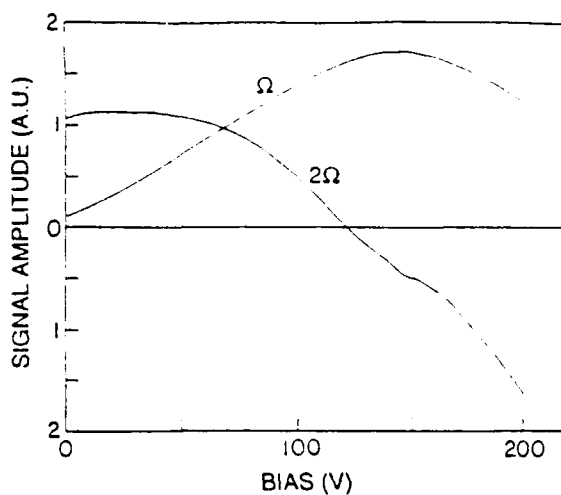


Figure 4 The  $\Omega$  and  $2\Omega$  frequency components in the light modulated by the PLZT phase modulator plotted as functions of the bias voltage.

the same modulation as that from a traditional modulator utilizing the linear electrooptic effect of single crystals, except that there is a constant phase shift. The constant phase shift can be compensated with an optical compensator in applications where it is not desirable. Much lower ac driving voltages are needed to achieve the same phase modulation depth for the PLZT modulator than for traditional modulators because of the strong quadratic electrooptic effect in the PLZT ceramic.

#### Applications

The PLZT phase modulator has been successfully used as a phase modulation device in a phase-detection scheme for the measurement of small birefringences of thin film materials. The optical arrangement for such application is shown in Figure 5. The PLZT compensator together with an optical compensator and the sample to be measured are sandwiched between two crossed polarizers. The modulating axis of the modulator is oriented 45 degrees with respect to the polarizer but parallel (or perpendicular) to the principle

optical axes of the sample determined by the direction of the external electric field. The purpose of the compensator is to compensate the constant phase shift generated by the modulator and to calibrate the system.

With the PLZT phase modulator being driven by an ac signal of frequency  $\Omega$  under zero bias, the total phase retardation for the light polarized along the modulating axis consists of contributions from all three components, namely, modulator, compensator and sample:

$$\Gamma = \Gamma_{\text{mod.}} + \Gamma_{\text{comp.}} + \Gamma_{\text{samp.}} \quad (3)$$

As been previously pointed out, the electrooptic effect of PLZT materials exhibits high order field dependence and saturation behavior in some circumstances. The phase modulation produced by the PLZT modulator, therefore, should be expressed by the following Fourier series:

$$\Gamma_{\text{mod.}}(t) = \text{constant} + \sum_{m=1}^{\infty} C_m \sin 2m\Omega t, \quad (4)$$

where coefficient  $C_1$  is proportional to the quadratic electrooptic coefficient of the PLZT modulating medium;  $C_2$  is proportional to the quartic electrooptic coefficient, etc. Although in most instances only  $C_1$  needs to be considered, the whole summation in Equation (4) is retained for the strictness of the following discussion.

By adjusting the compensator, the constant in Equation (4) can be eliminated; therefore we have

$$\Gamma(t) = \sum_{m=1}^{\infty} C_m \sin 2m\Omega t + \Gamma_{\text{samp.}} \quad (5)$$

The light intensity detected by the photomultiplier tube (PMT) is therefore given by

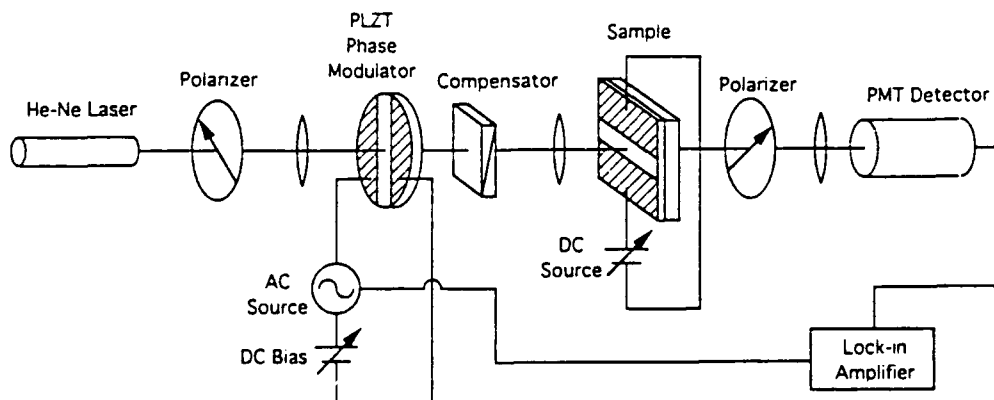


Figure 5 The optical arrangement in a phase-detection scheme using the PLZT modulator as a phase modulating device.

$$I(t) = I_0 \sin^2(\Gamma/2)$$

$$= (I_0/2)[1 + \cos(\sum_{m=1}^{\infty} C_m \sin 2m\Omega t + \Gamma_{\text{samp}})]. \quad (6)$$

If the reference signal of the lock-in amplifier is chosen as  $\sin 2\Omega t$ , the output signal of the lock-in amplifier, S, is proportional to the amplitude of the  $\sin 2\Omega t$  term in the Fourier expansion of Equation (6), that is

$$S = D \int_0^t I(t) \sin 2\Omega t dt$$

$$= D \int_0^t \cos(\sum_{m=1}^{\infty} C_m \sin 2m\Omega t + \Gamma_{\text{samp}}) \sin 2\Omega t dt \quad (7)$$

where D is a system constant. It can be shown that the above integration is approximately given by

$$S = D J_1(C_1) \sin \Gamma_{\text{samp}}. \quad (8)$$

where  $J_1$  is the Bessel function of the first order. With a fixed driving signal amplitude,  $C_1$  is a constant; the output signal from the lock-in amplifier therefore is proportional to the phase retardation generated by the sample, namely,  $\Gamma_{\text{samp}}$ . Moreover, in detecting the electrooptic effect of thin film materials, the phase retardation of the sample is usually very small so that the output from the lock-in amplifier becomes directly proportional  $\Gamma_{\text{samp}}$ , while the proportional constant can be determined by the compensator.

With the PLZT phase modulator, the above scheme has proven an effective way of detecting very small phase retardations produced by electrooptic effects in thin film materials. As an example, Figure 6 shows the birefringence versus E-field curve of a 2/55/45 thin

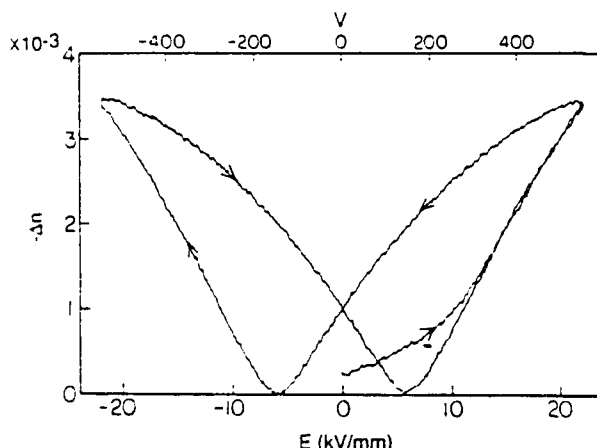


Figure 6 The birefringence versus E-field curve for a 2/55/45 PLZT thin film of 0.5  $\mu\text{m}$  thickness sputter-deposited on a fused silica substrate, measured with the phase-detection scheme using the PLZT phase modulator.

film of 0.5  $\mu\text{m}$  thick grown on a fused silica substrate, measured with the above phase-detection system under zero-bias mode.

When an appropriate bias field is applied, the modulation becomes predominated by the  $\Omega$  component. With the reference signal of the lock-in amplifier set at  $\sin \Omega t$ , the above measuring system functions similarly as in the zero-bias mode.

### Conclusions

An optical phase modulator was made by using the quadratic electrooptic effect of a hot-pressed PLZT ceramic. The device can be operated in a zero-bias mode which provides a modulation at double the frequency of the driving signal. When an appropriate bias is applied, the modulator provides a modulation dominated by the component at the frequency of the driving signal. Application of the PLZT modulator has been found in the phase-detection scheme for the measurement of very small birefringence in thin film materials.

### References

- [1] G.H. Haertling and C.E. Land, "Hot-pressed (Pb,La)(Zr,Ti)O<sub>3</sub> Ferroelectric Ceramic for Electronic Applications," *J. Am. Ceram. Soc.* 54, 1(1971)
- [2] G.H. Haertling, "PLZT Electrooptic Materials and Applications-A Review," *Ferroelectrics*, 75, 25(1987)
- [3] H. Higashino, T. Kawaguchi, H. Adachi, T. Makino and O. Yamazaki, "High Speed Optical TIR Switches Using PLZT Thin Film Waveguides in Sapphire," *Japan. J. Appl. Phys.* 24 suppl., 284(1985)
- [4] F. Wang and A.Y. Wu, "Electro-optical and Nonlinear Optical Properties of Thin Film Materials Containing Oxygen-Octahedra under High DC Electric Field," *Proc. 7th Intern. Symposium on the Application of Ferroelectrics*, pp.131-134, Urbana, IL, June 6-8, 1990.
- [5] G.H. Haertling, unpublished results.

**Part VI.**

**Publications**

# AUTOMATED SYSTEM FOR PROCESSING OF PLZT POWDERS DERIVED FROM ACETATE PRECURSORS

J R Barrett and E C Skaar  
Department of Ceramic Engineering, Clemson University  
Clemson, S C 29634-0907

## Abstract

An IBM-PC based system to produce and control the production of PLZT powders from acetate precursors is described. Problems with the development of appropriate sensing systems and algorithms are discussed. A proposed prototype system is presented.

## Introduction

The increasing need for better manufacturing methods for new (and old) materials has been the purpose for this study. In advanced materials systems, it is often necessary to very closely monitor a process, which can be very expensive if the procedure is too complicated or too abstract to be overseen by conventional sensors and computer equipment. The development of advanced sensors can enable the reduction of labor-intensive procedures.<sup>1</sup> The use of advanced sensors in conjunction with high-level control methods, such as artificial intelligence, can result in a cheaper, yet higher quality product in processes that may involve complicated processing steps. This study examines the use of software and hardware combined in an automated process to produce PLZT powders from water soluble acetate precursors.

## Intelligent Processing of Materials

The purpose of the method of Intelligent Processing of Materials (IPM) is to reduce the period between materials development and the production of those materials while at the same time increasing the quality of the product. The quality that is achieved through the IPM process is built-in during production and not the result of an inspection after manufacture.<sup>1</sup> IPM is desirable because it can improve the quality, reliability, and the yield of processed materials.<sup>2</sup> IPM combines the expertise of the process engineer and the knowledge of the materials scientist through the use of an expert system.<sup>2</sup> The expert system is a computer's software that is an application of artificial intelligence which utilizes efficient and effective data handling and retrieval to analyze and predict processing even.<sup>3</sup> The system is designed in such a way that corrections and/or compensations may be made instantaneously in a process so that the result is a high-quality product. This system monitors all processing steps from raw material characteristics to the final product during the manufacturing so that changes can be made in each step and in future steps to achieve the highest quality product. Process models and real-time sensors are heavily relied upon in the IPM strategy so that higher levels of control and awareness than in conventional processes can be attained. In-situ sensors can monitor complex characteristics such as microstructure in real time and combine this data with conventionally sensed data, such as temperature or viscosity, and the resulting combination is used by the expert system to make process judgements.<sup>1</sup> It is through these judgements that the process is improved continually to compensate for process and raw material variability.

To implement IPM in the production of powders from PLZT acetate solutions, a production process that is compatible with the requirements of an automated process is needed. The production

process must be completely defined. The entire process for this system includes the making of PLZT acetate solutions, the precipitation of a solid, the separation of the solid from the liquid, and the processing of the solid into a powder. As the process is defined, process variables are defined and assessed. These variables must be isolated and treated in a manner that is consistent with the IPM process. It is also important that the equipment that makes up the system be compatible so that it can be linked efficiently and effectively. The hardware, such as mixing equipment, valves, and sensors must be linked to the software (computer) that runs the system. The hardware and software are the two major components of any IPM system, and each has its own purpose.

## Sensors

One of the common measurements in a coprecipitation process is the pH of the solution. However, pH measurements have been found to be impractical and not suited for automated processes for this particular material system. The presence of acetic acid, either from addition or from the bulk raw materials, and the high methanol concentration of the water soluble solutions prohibits an accurate and reliable measurement of pH because the glass bulb of the pH probe is strongly attacked under these conditions.<sup>4</sup> The pH measurement is based on the Nernst equation, which assumes that the hydrogen ion activity is equal to the hydrogen ion concentration. However, the Nernst equation is not valid for low hydrogen ion concentrations, and that is the condition that exists with this system. In addition, the ammonium hydroxide used as a precipitating agent destroys the hydrated layer that is used to generate the potential difference for a pH reading. The potential difference is the signal that is converted to a pH value. It is possible to take pH measurements in this system in a laboratory environment, but it is not possible to implement this sensing method in an automated process because of the constant maintenance that is required to keep the pH electrode in operating condition. A long stabilization time for a pH reading also contributed to the decision that pH is not suitable for this IPM procedure.

A method of sensing material properties that has been found to be useful for automated processes is the measurement of resistivity/conductivity. A two-conductor probe was constructed and tested for reading stabilization (response) time and stability of the reading over extended time periods with no probe maintenance. The first attempts to use the probe were made using direct current as the electrical source. It was found that DC measurements would not stabilize or would stabilize only after a long period of time. Because the solutions are polar in nature, it is believed that a polarization of the solution was taking place, causing the readings to drift. As a result, alternating current was used as the electrical source. Using the same probe, as shown in Figure 1, the AC measurement resulted in a quick reading response time, in the range of two to five seconds. The stabilization of the reading was also satisfactory, as the readings stabilized almost immediately. The probe was left in a variety of raw material, solvent, and batch solutions for periods of hours to days, and the readings were extremely stable.

The voltage measurement of the solution,  $V_2$ , was used to

find the resistance of the solution after the current,  $I$ , was found using Ohm's Law for the known resistor in the probe system and measuring the voltage across it,  $V_1$ . The change in resistance of the solution as the constituents were added to make a 9/65.35 PLZT acetate solution batch for coprecipitation was plotted against the weight of the total batch, as shown in Figure 2. An order of addition of constituents was chosen to best suit the homogeneity of the batch.

Generally, the resistance of the total batch solution increased as each constituent was added. This result is encouraging evidence that an AC resistance probe can be used in an IPM process for PLZT acetate solutions when an expert system has "learned" the characteristics of the batching process with respect to change in solution resistance vs weight of addition. The constituent that shows a possible exception for the upward trend is lead subacetate, for which the resistance decreased after a point. However, the neural network that runs the system can be "trained" to compensate for this result. Naturally, the weight of the batch must be monitored and the process model for this procedure must be available to the network, so that the computer can tailor the batching additions and other parameters to fit the model. At this point in the development of the system, it is believed that the lead subacetate data may actually not be much cause for concern. Because of the difficulty in keeping the material dissolved during this particular test and other conditions, such as the high evaporation rate in this open-air test, there is reason to believe that a test of a larger batch size in a closed container should solve the problem.

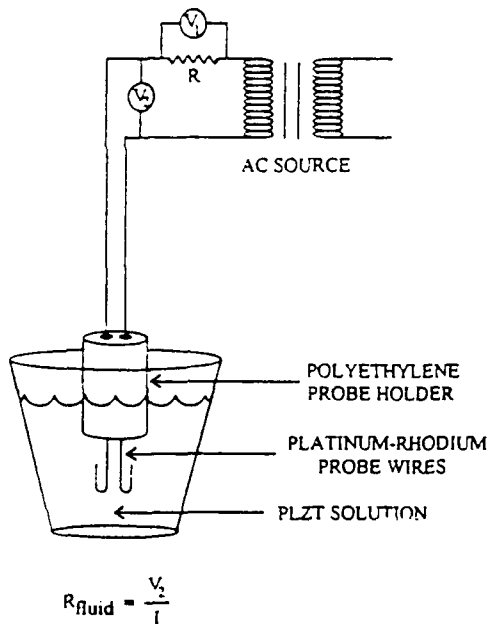


Figure 1. Method of measuring resistance of PLZT acetate solution using alternating current.

#### Algorithm Development

The control algorithm for this process is a two part algorithm. The first part is a normal weighing or batching algorithm. It contains a database of recipes for the solutions required to make powders of various compositions. As long as the process does not vary, and all the settings remain constant, the process is capable of running with this section of the algorithm alone. The second part of the algorithm (currently under development) is designed to sense problems and make corrections to the process.

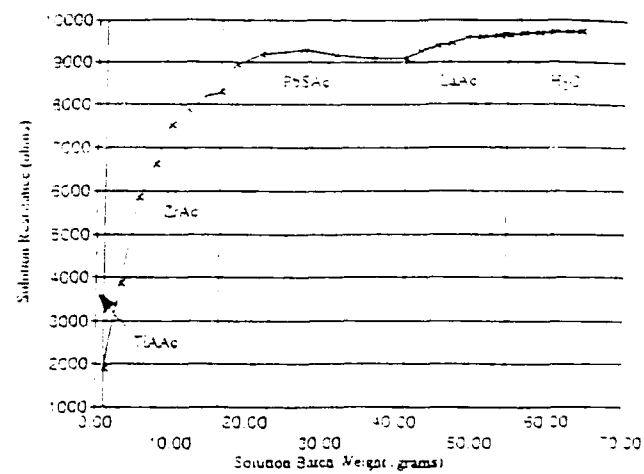


Figure 2. Solution resistance (AC measurement) for the total PLZT acetate batch as constituents were added

This second section is an artificially intelligent program based on a neural network. It is designed to sense "out of control" conditions and make appropriate corrections to the weighing or batching algorithm.

Neural networks excel at pattern recognition, diagnosis, and decision making.<sup>5</sup> The idea behind this section of the algorithm is to recognize an assignable problem as it develops, and compensate. In a sense, the computer is programmed to utilize statistical process control.

For example, suppose the metering mechanism for one of the constituents became partially clogged. The result would be a variance from normal with respect to the weight and the resistance measurements for the batch. The pattern of these measurements would change. The neural network would be taught to recognize this pattern, and effect the appropriate compensation. Other types of assignable problems would also present their unique patterns which the neural network would be taught to recognize.

The unique beauty of using neural network technology for this application is that the teaching of the network is not a function of programming, but rather simulation. For the network to function, it has to be taught the patterns that specific problems create. We accomplish this by actually simulating the problem in the process. The network is programmed to learn and recognize the resulting sensor patterns. Once the network recognizes the pattern, it is programmed to compensate for the deficiency. A properly designed network, therefore, does not depend upon an exhaustive database of every problem. Rather, as experience is gained with a process, the problems and solutions can be taught to the network. The algorithm improves with operating experience and thus the process can proceed toward optimization.

#### Automated Batching System

The entire automated process for the production of PLZT acetate powders that is being developed has many parts that need to be both optimized and automated. The section of the process that has received the greatest attention to this point in the development of the total process is the automated batching system. Figure 3 shows this system, which utilizes manually filled reservoirs containing the liquified constituents of the PLZT acetate system which supply smaller, computer-controlled reservoirs that are used to dispense batch amounts. A switch system that consists of two stainless steel screws and a low current is used as a liquid-contact switch such that when the valve from the larger, manually controlled reservoirs is opened, the fluid will flow until the liquid

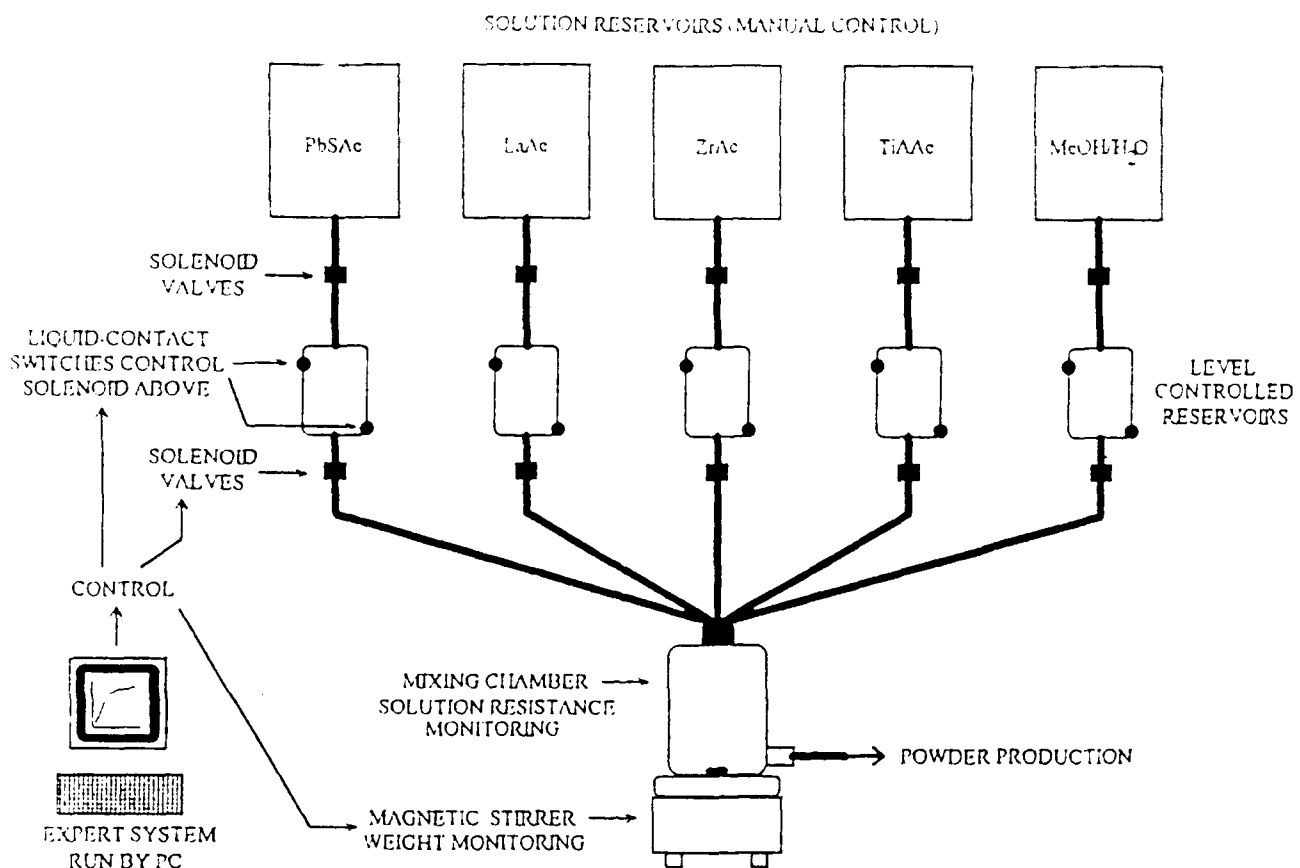


Figure 3. Automated solution batching system controlled by IBM PC.

completes the circuit between the two contacts. The contacts are positioned at the top and at the bottom of the reservoir. The flow of fluid in the system is controlled by sets of solenoid valves that are run by the computer. Once the circuit is completed, as the fluid fills the reservoir, the switch will be activated and the solenoid valve will be closed by the computer to stop the fluid flow. Then, the valves of the smaller dispensing reservoirs are opened for a time period that has been previously determined, based on material characteristics, to a larger mixing reservoir. The longer the time that the valve is opened, the more fluid is added to the batch.

The weight of the constituent is checked and recorded by the computer to check the accuracy of the system. The AC resistance probe will also be used here to detect any changes and be a part of the control in the batching procedures. The system is designed to be able to compensate for clogging of the valves and changes in viscosity by taking in data on the raw materials and the trends in the process. The expert system can then execute an order to make a change in the process parameters if it is necessary to keep the process at the correct level, such as leaving the valve open a longer or shorter period of time. The next step is the mixing of the constituents. After mixing, a valve is opened and the constituents will flow into the precipitation reactor for the coprecipitation process.

The automated batching system will be run by the expert system in a manner in which it will be possible to enter the desired composition of the PLZT acetate solution to be made, and then the process will be changed to yield the correct amounts of each constituent needed.

#### Summary

The requirements for the use of better manufacturing methods in the production of materials that normally require labor-intensive procedures have been the reason for this study. The reduction of labor hours and the substantial improvement in quality of the materials that is possible are the integral in the theory of Intelligent Processing of Materials. An expert system can be used to develop algorithms to control the system if sensors and sensing methods can be improved or developed to suit the needs of such a data intensive system. The next step in the automation of this process is the linking of the system to the other components that are needed in the process, a coprecipitation step and a calcination/powder production step.

#### Acknowledgement

This work was supported by the Office of Naval Research under contract number N00014-91-J-1508.

#### References

- [1] H. T. Yoiken, "Intelligent Processing of Materials," Materials Research Society Bulletin, April 1988, p. 17.
- [2] B. G. Kushner and P. A. Parrish, "The Intelligent Processing of Advanced Materials," Intelligent Processing of Materials and Advanced Sensors, 1987, pp. 173-184.

- [3] P. A. Parnish, 'Design and Manufacturing of Advanced Materials and Structures,' Intelligent Processing of Materials, 1990, pp. 3-15
- [4] Private Communication, Fisher Scientific, Pittsburgh, February 1992
- [5] NeuroWindows, Ward Systems Group, July 1991, pp. 1-3

# PLZT POWDERS FROM ACETATE PRECURSORS VIA COPRECIPITATION

C. Lin, B. I. Lee, and G. H. Haertling  
Department of Ceramic Engineering  
Clemson University, Clemson, S.C. 29634

**Abstract:** Various chemical coprecipitation techniques used for the production of PLZT 2/55/45 (La/Zr/Ti) powders were investigated. The coprecipitation condition corresponding to 0.5 M oxalic acid at a titration rate of 24 cc/min and at a temperature of 21°C yielded the largest surface area calcined powders, hence this condition was selected as the optimum in regard to sinterability of the powders. The characteristics of the PLZT 2/55/45 powders under the best precipitation condition were observed and evaluated. It was found by means of FTIR and XRD that the perovskite phase formation occurred at 550°C.

## Introduction

There has been great interest in lead-based perovskite ferroelectric compounds within the  $(\text{Pb}_{1-x}\text{La}_x)(\text{Zr}_y\text{Ti}_{1-y})_{1-x/4}\text{O}_3$  system owing to their distinct electrooptic properties and their utilization for transparent ferroelectric ceramics<sup>1,2</sup>. The purpose of the present work was to observe the characteristics of PLZT 2/55/45 powders obtained from some specific precipitation conditions. Before selecting the final precipitation condition, some important factors relating to the precipitation process were selected i.e., (1) type, (2) concentration, (3) rate of titration and (4) temperature of precursors. These coprecipitation conditions were then screened in regard to the specific surface area of powders obtained from these conditions. Finally, the condition for the formation of PLZT phase was investigated by heat treatment.

## Experimental Procedure

### Selection of Experimental Conditions

The system of the experimental design<sup>3</sup> is given as in Table 1.

Table 1. PLZT Coprecipitation Conditions

Type	C	K	T	R
1	0.35M	ox	21°C	12 cc/min
2	0.35M	amc	50°C	24 cc/min
3	0.50M	ox	21°C	24 cc/min
4	0.50M	amc	50°C	12 cc/min
5	0.65M	ox	50°C	12 cc/min
6	0.65M	amc	21°C	24 cc/min
7	0.80M	ox	50°C	24 cc/min
8	0.80M	amc	21°C	12 cc/min

C. Concentration (unit: Molarity).

T. Temperature of precursors

R. Rate of titration of precipitating agent.

K. Kind of precipitating agents

(for brevity: ox: oxalic acid solution, amc:  $(\text{NH}_4)_2\text{CO}_3(\text{aq})$ )

## Powder Preparation

The starting precursor chemicals used in this study were lanthanum acetate (LaAc), zirconium acetate (ZrAc), lead subacetate (PbsubAc) and Titanium acetylacetone (Tiacac). The oxide content (wt%) of each precursor and the stoichiometric batch proportions are given in Table 2.

The flowchart representation for the overall preparation process is shown in Figure 1.

Table 2. Precursor and Batch Weight Proportions for PLZT 2/55/45

Oxide	PbO	La <sub>2</sub> O <sub>3</sub>	ZrO <sub>2</sub>	TiO <sub>2</sub>
mole ratio	0.96	0.01	0.547	0.448
Precursor				
oxide wt %	7.6	5.76	22.61	16.96
Precursor	PbsubAc	LaAc	ZrAc	Tiacac
Batch				
0.0307 mole				
Batch weight	8.537g	1.474g	9.144g	6.742g

## Powder Production

**Type 1 Coprecipitation Process** The conditions for this process were C=0.35M, K=ox., T=21°C, and R=12 cc/min. A clear solution of 9.305 g ZrAc, 1.474 g LaAc, 6.970 g Tiacac and 8.536 g PbsubAc was prepared in 75 ml of methanol. The solution was titrated at the rate of 12 ml/min with 100 ml 0.35M oxalic acid solution under constant stirring and a constant temperature of T=21°C by means of a water bath. The precipitate suspension was stirred for 5 additional minutes after the titration was completed. Then, the entire precipitate suspension was poured into a stainless pan and was dried in an oven at 70°C. The dried powder was calcined for 7 hours in air at 550°C. The specific surface area of the powders obtained above was measured using the BET multi-point method (Model: Micromeritics, Gemini 2360).

**Types 2-8 Coprecipitation Processes** The conditions were the same as Type 1 except concentration, kind, temperature and rate were changed according to Table 1.

**Direct Pyrolyzation Process** The conditions were the same as that of Type 1 except no precipitating agent was involved.

**Spray Pyrolysis Process** The conditions were the same as Type 3. After titration, drying was performed by spraying the colloidal precipitate suspension into a tube furnace at 450°C. The powders were collected at the exit of the furnace.

## Characterization of PLZT 2/55/45 Powders

Five samples obtained from the optimum coprecipitation condition Type 3 were processed separately with five different heat treatment conditions: (1) 220°C/2 hrs, (2) 400°C/4 hrs, (3) 500°C/7 hrs, (4) 550°C/4 hrs and (5) 550°C/7 hrs. The properties of the PLZT powders were measured using FTIR (Perkin-Elmer 1600 on KBr pellet absorbance mode), X-ray diffraction (Scintag XDS 2000, Cu K $\alpha$ -radiation) and electron microscopy SEM (JEOL, JSM-848).

### Results and Discussion

#### Selection of the best coprecipitation condition

The Type 3 coprecipitation condition was evaluated as the best condition in regard to the results of the specific surface area as shown in Table 3.

In Table 3, it was noted that the low surface area of uncalcined powders in Types 2, 4, and 6 resulted from aggregation of powders during degassing (200°C/2 hrs) in the BET test, while the low surface areas of uncalcined powders in Types 7 and 8 were mainly due to supersaturation. Also, as shown in Table 4, it indicates that a higher titration rate (comparison between Types 1 and 3 in oxalates) enhances larger number of nuclei of a new phase as well as more rapid precipitation<sup>4</sup>. This results in finer particles with higher surface area in both uncalcined and calcined powders. The effect of temperature as shown in Table 5

indicates that low temperature was favorable for forming powders with higher surface area. This was interpreted that high temperature affects nucleation and hence larger particles due to growth. The effect of kind of precipitant as shown in Table 6 indicates that oxalic acid was a better precipitant.

As shown in Figure 1, the various processes involve liquid state mixing at the molecular level. The mixed solutions of Pb, La, Zr, and Ti precursors was coprecipitated as the oxalates or carbonates. The selection of the best coprecipitation condition was based on the largest specific surface area of the resulting PLZT 2/55/45 powder. It was found that the conditions of Type 3 coprecipitation (i.e., 0.5M oxalic acid titrated at 24 cc/min at 21°C) were optimum for producing submicron PLZT 2/55/45 powders.

The FTIR spectra of powders prepared under different calcining conditions are shown in Figure 2. The spectra show reduction in the absorbance peaks at ~1700 cm<sup>-1</sup>, which is due to C-O vibration, as the calcination temperature and/or time increased. On the other hand, the peak at ~575 cm<sup>-1</sup> is due to metal-oxygen bond, more specifically ZrO<sub>6</sub>TiO<sub>6</sub> octahedra vibrational mode. The increase in the peak size as the degree of calcination increased indicates the formation of crystalline PLZT powder. The small peaks at ~1600 - 1700 cm<sup>-1</sup> are believed to be originated from the impurities in KBr and at ~1490 cm<sup>-1</sup> from acetate. The spectra show that calcination at 550°C for 4 hrs is nearly sufficient to calcine PLZT powder for the given coprecipitated powders. There are always absorbance peaks around 2920 cm<sup>-1</sup> which correspond to the residual carboxylic acid functional groups, i.e., oxalic acid.

The X-ray diffraction pattern shown in Figure 3 indicates that the Type 3 coprecipitated PLZT powder is a mixed phase which is composed of a perovskite PLZT phase and lesser pyrochlore phase ( $2\theta=27.93^\circ$  only) with an approximate mean particle size<sup>5, 6</sup> of 18 nm. This approximation is a calculated value based on the Scherrer relationship of the X-ray diffraction broadening. Improved results for achieving the perovskite phase were obtained by spray pyrolysis as shown in Figure 4. The reason is that spray pyrolysis provides a looser agglomeration of the uncalled powders which is favorable to forming a better diffusivity environment for the gaseous products during thermal decomposition.

SEM micrographs in Figures 5-6 show the morphologies of the submicron particles.

Table 3: Effect of Surface Area on PLZT Powders		
Type	Uncalcned	Calcned (550°C/7 hrs)
1	47.5 m <sup>2</sup> /g	4.97 m <sup>2</sup> /g
2	1.58	4.24
3	79.54	5.21
4	1.49	3.50
5	31.11	4.98
6	1.55	2.98
7	2.75	2.80
8	2.72	1.72
MCD	1.52	3.04

Table 4: Mean Effect of Titration Rate on Surface Area of PLZT Powders via Oxalate precipitation

Date	Uncalcned	Calcned (550°C/7 hrs)
12 hr/min	49.13 m <sup>2</sup> /g	4.82 m <sup>2</sup> /g
24 hr/min	41.20	3.48

Table 5: Mean Effect of Temperature on Surface Area of PLZT Powders via Oxalate precipitation

Temperature	Uncalcned	Calcned (550°C/7 hrs)
200°C	43.93 m <sup>2</sup> /g	4.74 m <sup>2</sup> /g
250°C	71.40	3.64

Table 6: Mean Effect of Kind of Precipitant on Surface Area of PLZT Powders

Kind	Uncalcned	Calcned (550°C/7 hrs)
oxal.	45.16 m <sup>2</sup> /g	9.11 m <sup>2</sup> /g
aceto.	1.75	1.11

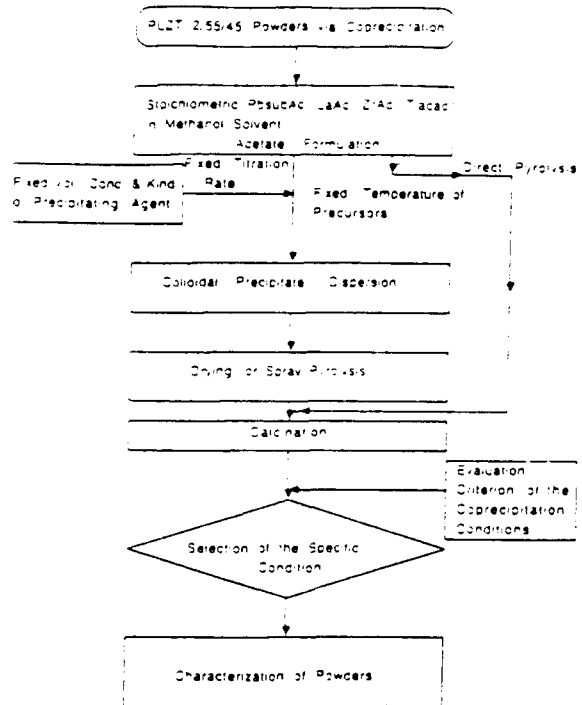


Figure 1. Flowchart of Coprecipitation Processes for PLZT 2/55/45 Powders.

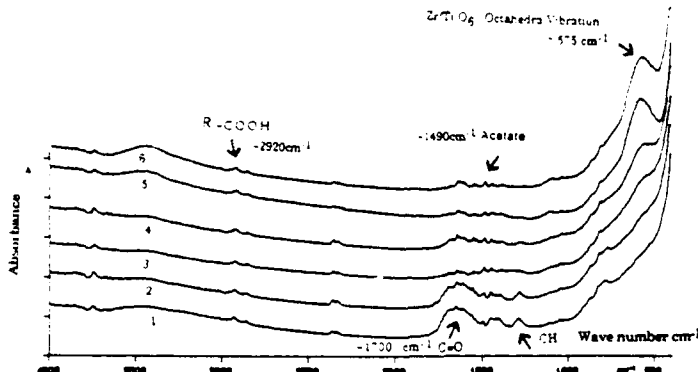


Figure 2. FTIR spectra of PLZT powders: (1) no calcination, (2) 220°C/2 hrs, (3) 400°C/4 hrs, (4) 500°C/7 hrs, (5) 550°C/4 hrs and (6) 550°C/7 hrs.

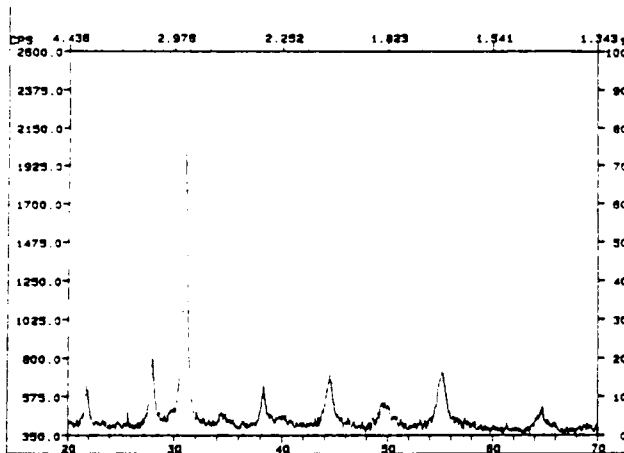


Figure 3. X-ray diffraction pattern of Type 3 calcined (550°C/7 hrs) PLZT powder.

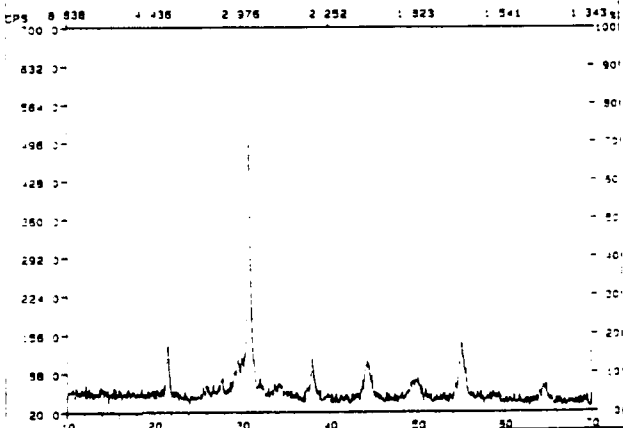


Figure 4. X-ray diffraction pattern of Type 3 calcined (550°C/7 hrs) PLZT powder using spray pyrolysis instead of drying.

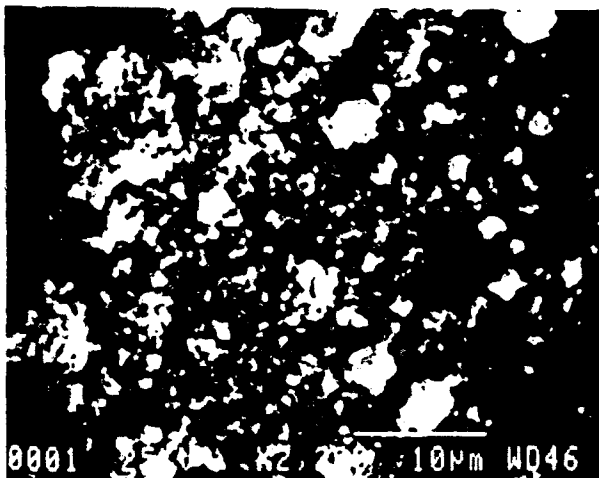


Figure 5. SEM micrograph of Type 3 uncalcined PLZT powder.

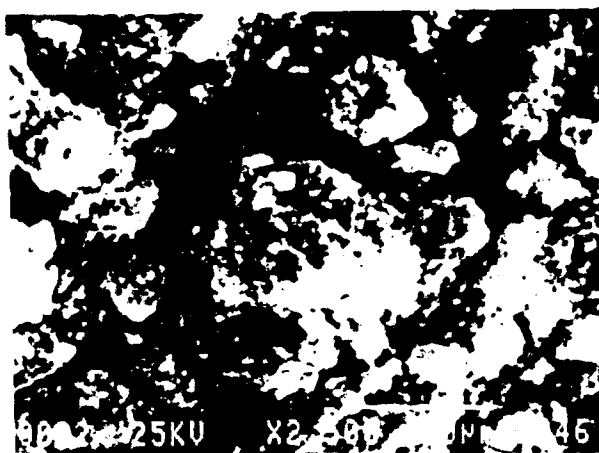


Figure 6. SEM micrograph of Type 3 calcined (550°C/7 hrs) PLZT powder.

### Conclusions

There were totally eight coprecipitation processes evaluated in the production of PLZT powders. The oxalates yielded powders with larger specific surface areas (mean value  $9.11 \text{ m}^2/\text{g}$  after calcination) than that of the ammonium carbonates (mean value  $3.11 \text{ m}^2/\text{g}$ ).

Under the oxalate conditions, the calcined powders prepared at a lower temperature of precursors yielded higher specific surface area than those at a higher temperature. For the lower temperature cases, the faster titration rate produced calcined powders with higher surface areas than that at the slower rate. Single phase perovskite PLZT powders were produced by using a spray pyrolysis technique for preparing the calcined powders.

### Acknowledgement

The project is sponsored by the Office of Naval Research under contract No. N00014-91-J-1508

### References

- [1] C. E. Land, P. D. Thatcher, and G. H. Haertling, Electrooptic Ceramics, Appl. Solid State Sci. Vol. 4, R. Wolfe, Ed. Academic Press, New York, 1974.
- [2] A. E. Krumins and V. Y. Fritsberg, "Semiconductor Properties and General Applications of Optical Ceramics," Ferroelctrics, vol. 35 pp. 149-154, 1981.
- [3] G. Taguchi, System of Experimental Design, Unipub/Kraus International Publications, New York, 1988.
- [4] M. L. Salutsky and W. R. Grace, Precipitates, Treatise on Analytical Chemistry, Part I, Vol. 1, pp 737-764, I. M. Kolthoff, Ed. The Interscience Encyclopedia, New York, 1959.
- [5] C. R. Veale, Fine Powders, Applied Science Publishers Ltd. London, 1972.
- [6] H. P. Klum and L. P. Alexander, X-ray Diffraction Procedures, Wiley, New York, 1954.

## BULK VS. THIN FILM PLZT FERROELECTRICS

D E Dausch and G H Haertling

Department of Ceramic Engineering, Clemson University  
Clemson, SC 29634-0907

**Abstract.** Lead lanthanum zirconate titanate (PLZT) ferroelectrics were produced in bulk ceramic and thin film form in order to compare their electrical and physical properties. Both bulk and thin film samples of selected compositions were produced from the same acetate precursor solutions. Properties examined were dielectric permittivity, dissipation factor, remanent polarization, coercive field, Curie temperature and crystallinity. Bulk ceramics were hot pressed from chemically coprecipitated powders, and chemically derived thin films were fabricated by spin coating. Typical conditions for hot pressing were 1200°C for 4 hours at 14 MPa (2000 psi), whereas the thin films were sintered at 700°C for 4 minutes per layer. The similarities and differences between the materials are described.

### Introduction

Ferroelectric thin films have been the subject of years of ongoing research in the study and optimization of their processing and properties. The importance of ferroelectric thin films is evident in their many applications ranging from nonvolatile memories to electrooptic devices.<sup>1</sup> These thin film applications stem from the many ferroelectric bulk ceramic components successfully developed over the years. In some instances, however, thin films possess advantages over bulk ceramics which make them more desirable for many devices and broaden the range of applications for ferroelectric materials. Lower operating voltage, higher speed, easier integration with silicon technology and lower cost are among the advantages favoring thin film ferroelectrics.

In order to more fully understand and optimize thin film ferroelectric behavior, a comparison is necessary to bulk ferroelectric phenomena. Direct correlation between the bulk and thin film materials is difficult since the precursors and processing techniques of each are typically so dissimilar; however, a study is presented here that diminishes this disparity. This research focuses on the fabrication and characterization of PLZT bulk ceramics and thin films produced from the same acetate precursor solutions. It is believed that this process allows for a close comparison of PLZT bulk and thin film ferroelectrics by minimizing or eliminating differences in the processing of these materials induced by batching variations, precursor impurities and differences in mixing, reactivity and chemical composition of the precursor materials. A study of several PLZT compositions is presented to explore similarities and differences in the behavior of hot pressed bulk ceramics produced from chemically coprecipitated powders and spin coated thin films produced by a metallorganic decomposition (MOD) process.

### Experimental Procedure

#### Processing

PLZT hot pressed ceramics and spin coated thin films were fabricated using a process similar to previously reported processes using a water soluble acetate precursor system.<sup>2</sup> The acetate precursors were chosen primarily for their chemical stability, insensitivity to moisture and low cost. The starting precursors included lead subacetate (PbAc) powder, lanthanum acetate (LaAc), zirconium acetate (ZrAc) and titanium acetylacetonate (TiAAc) solutions. For processing simplicity and accuracy, PbAc

was mixed into solution by the addition of acetic acid and methanol, so that all of the acetate precursors were in liquid form. This ensured that the beginning acetate formulation was readily and completely mixed into solution. This step becomes important since only a small portion of the total acetate formulation is used for spin coating. Incomplete mixing would produce compositional fluctuations between bulk and thin film solutions. It should be noted that all of the precursors were assayed before experimentation, and the same stock solution of each precursor was used throughout these experiments. These precautions were taken to reduce the possibility of batching variations between bulk and thin film materials so that similarities and differences in their properties were not a result of these variations.

After initial acetate formulation, the solution was separated into bulk and thin film portions. The bulk portion was coprecipitated in a high speed blender with oxalic acid and methanol and then vacuum dried at 70°C to produce a solid, friable cake. The cake was crushed, calcined at 500°C for 4 hours and milled in trichloroethylene for 6 hours to produce a PLZT oxide powder. Typically, 100g of powder was produced for hot pressing. Hot pressing conditions were 1200°C for 4 hours at 14 MPa. To prepare samples for electrical measurement, the hot pressed parts were sliced on a diamond saw and lapped to 0.5 mm (20 mil) thickness. Electroless nickel electrodes were plated onto the samples.

For thin film production, a small portion (usually 5g) of the acetate solution was decanted and diluted with methanol at a 2:1 ratio by weight. The solution was spun onto silver foil substrates using a photoresist spinner at 2000 rpm for 15 seconds, allowed to dry for 15 seconds and pyrolyzed at 700°C for 4 minutes. Repeating this process for 10 layers produced a PLZT thin film approximately 0.9 μm thick. For measurement of electrical properties, copper electrodes were applied to the surface of the films via vacuum evaporation. This process allowed for the fabrication of both bulk and thin film materials from the same batch.

#### Measurements

Bulk and thin film samples were analyzed using several electrical and physical measurement techniques. The dielectric properties (virgin and poled capacitance and dissipation factor) were measured on bulk and thin film samples using a Leader LCR meter at a measuring frequency of 1 kHz. Polarization (P) vs. electric field (E) hysteresis loops were also measured for both materials. The bulk samples were measured using a Sawyer-Tower circuit with a dc applied voltage of ±1400 V. The hysteresis loops were plotted with a Goerz Metrawatt X-Y plotter. Hysteresis loops of the thin film samples were customarily measured using a 60 Hz Sawyer-Tower circuit and an oscilloscope readout; however, in order to more accurately compare measurement of bulk and film hysteresis loops, the thin films were also measured using a low voltage (±30-50 V) dc looper.

The Curie temperature of bulk samples was determined for several PLZT compositions. Bulk samples were placed in a stirred oil bath and heated while taking capacitance and loss tangent measurements at 5°C increments. The Curie temperature was indicated by a maximum in the measured capacitance. X-ray diffraction analysis was also performed on bulk and thin film samples using a Scintag XDS 2000 diffractometer with Cu K-alpha radiation.

## Results and Discussion

Several compositions were chosen for study near phase boundaries in the PLZT system. The morphotropic phase boundary compositions consisted of 2/55/45, 2/53/47 and 2/51/49 which regularly exhibit ferroelectric memory behavior. Compositions approaching and entering the paraelectric phase region with 65/35 Zr/Ti ratios included those with 6, 7, 8, 9, 9.5 and 10% La. These materials typically are memory materials at 6% La and range toward slim-loop ferroelectric materials in the 9 to 10% La range. Hot pressed bulk ceramics and spin coated thin films on Ag foil substrates were fabricated, and a comparison of properties was established.

### Dielectric Properties

Dielectric and ferroelectric properties are listed for bulk and thin film samples in Table I including virgin and poled dielectric constants for each. As expected, thin film dielectric constants were generally lower than their bulk counterparts. These effects have previously been reported to be due to several effects caused by the obvious differences between bulk and thin film configurations including small grain size of the thin films, mechanical clamping effects and voltage sensitivity of the dielectric measurement due to the high electric field applied to a <1  $\mu\text{m}$  thin film.<sup>2</sup> The difference in dielectric properties found in the present results, however, was not as significant as that reported earlier.

In comparing bulk 2% La samples to thin films, some similarities and differences were noted. Unsurprisingly, both bulk and thin film data showed maxima in  $K_{vir}$  and  $K_{pol}$  at the 2/53/47 composition indicating the existence of the morphotropic phase boundary near this composition, although the position of the boundary for the thin films seemed to be slightly different than that of the bulk samples.  $K_{pol}$  and  $K_{vir}$  for 2/51/49 thin films was essentially equal to that of 2/55/45 films, while bulk 2/51/49 had a much greater poled dielectric constant than bulk 2/55/45. This

result suggested that thin films and bulk ceramics did not behave equivalently near the morphotropic phase boundary since the dielectric constant was expected to peak at this boundary. A comparable result occurred for x/65/35 compositions when the paraelectric phase boundary was encountered. The dielectric constant was expected to reach a maximum at this phase boundary which was previously reported at the 9/65/35 composition for mixed oxide processes.<sup>3</sup> Though both bulk and thin film samples seemed to have maximum dielectric constants at the 9.5/65/35 compositions, the 9/65/35 thin films were closer to 9.5/65/35 than the bulk. Note the occurrence of the high  $K_{pol}$  for the 8.65/35 bulk sample despite the lower  $K_{vir}$  shown by this sample. The bulk ceramics demonstrated a larger difference in dielectric constants between the 9 and 9.5/65/35 compositions. Additionally, the thin film 6/65/35 composition revealed a higher dielectric constant than the bulk 6/65/35. These results would suggest that bulk and thin film samples showed dissimilar behavior also near the paraelectric phase boundary.

As mentioned above, the expected maximum dielectric constant for x/65/35 bulk ceramics produced via mixed oxide processes was 9/65/35; however, the results in Table I for the chemical process generally indicate a maximum at the 9.5/65/35 composition. Furthermore, the dielectric constants for all of these compositions were higher than values reported for mixed oxide processes.<sup>3</sup> These results could possibly be explained by realizing the type of process used in this study for fabricating bulk ceramics and thin films: i.e. thoroughly mixed acetate precursor solutions to produce chemically derived powders and thin films. This process may provide improved mixing of components which could slightly alter stoichiometry in the bulk and thin film samples-- especially Zr/Ti ratio and dispersion of the La dopant in PLZT. This could have produced higher dielectric constants and shifted the maximum in dielectric constants of these materials to 9.5% La. In order to explore this supposition, Curie temperatures of bulk x/65/35 samples were measured and are shown in Table 2 and Figure 1.

### BULK CERAMICS

	$K_{pol}$	$\tan \delta$ (pol)	$K_{vir}$	$\tan \delta$ (vir)	$E_C$ (dc) [kV/cm]	$P_R$ (dc) [uC/cm <sup>2</sup> ]	$E_C$ (ac) [kV/cm]	$P_R$ (ac) [uC/cm <sup>2</sup> ]
2/55/45	1328	.029	1293	.033	8	46	--	--
2/53/47	1885	.025	1391	.028	10	40	--	--
2/51/49	1630	.024	1234	.034	16	33	--	--
6/65/35	1355	.036	1774	.056	6	33	--	--
7/65/35	2712	.033	2479	.036	5	31	--	--
8/65/35	5700	.055	4692	.050	3	20	--	--
9/65/35	5147	.054	5007	.050	0	0	--	--
9.5/65/35	5658	.048	5603	.046	0	0	--	--
10/65/35	5548	.036	5538	.033	0	0	--	--

### THIN FILMS

2/55/45	997	.122	1228	.133	27	34	43	32
2/53/47	1265	.132	1619	.160	28	47	44	45
2/51/49	972	.122	1237	.146	28	38	46	37
6/65/35	1871	.142	1995	.141	14	21	28	25
7/65/35	2499	.170	2460	.145	14	18	27	21
8/65/35	3211	.194	3172	.176	11	15	22	19
9/65/35	4221	.195	4001	.172	9	11	22	17
9.5/65/35	4234	.190	4092	.164	7	8	19	18
10/65/35	4157	.193	4157	.209	7	10	18	16

Table I. Electrical properties of PLZT bulk ceramics and thin films.

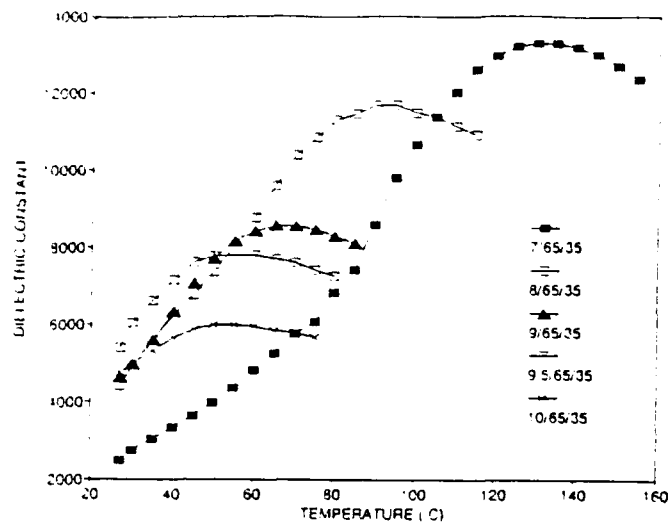


Figure 1 Curie temperature measurements of bulk x/65/35

Table 2. Curie temperatures of PLZT x/65/35 bulk ceramics.

Composition	T <sub>c</sub>
7/65/35	140
8/65/35	100
9/65/35	70
9.5/65/35	65
10/65/35	60

The Curie temperatures measured were consistently 100°C lower than previously reported for bulk samples produced by a mixed oxide process.<sup>3</sup> This result further emphasizes the possibility that the stoichiometries of the chemically prepared materials presented here were slightly different than the mixed oxide materials.

#### Crystallinity

X-ray diffraction patterns of thin film 8/65/35 and bulk 8/65/35 samples are shown in Figures 2a and 2b, respectively, and d-spacings are labeled for the PLZT peaks. Due to their greater intensities, the three Ag substrate peaks labeled on the thin film pattern masked three PLZT film peaks expected at the same angles. The thin film sample produced lower intensity PLZT peaks than the corresponding bulk sample. This could be a result of the thin film having either a lower degree of crystallinity than the bulk sample or simply a smaller quantity of material being analyzed by the

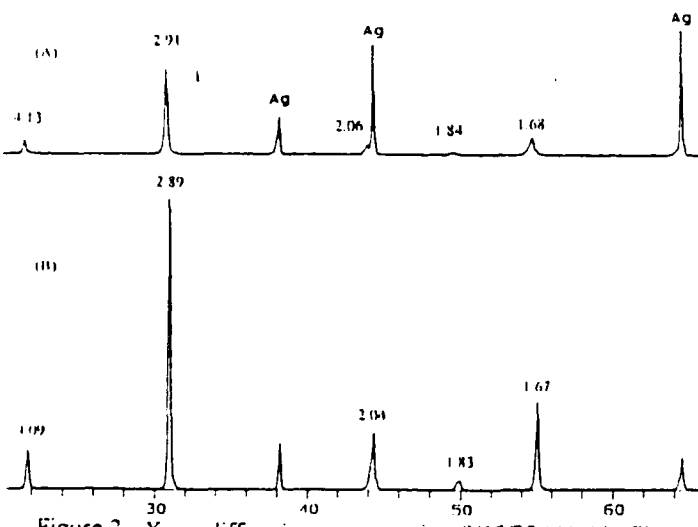


Figure 2 X-ray diffraction patterns of an 8/65/35 (A) thin film and (B) bulk ceramic. D-spacings are in angstroms.

diffractometer. In analyzing the lattice spacings of the materials, it was found that the thin film d-spacings were slightly larger than the bulk material. Watanabe et al.<sup>4</sup> proposed that mechanical stress present in PZT thin films caused by lattice or thermal expansion mismatch between the film and the substrate can cause differences in lattice constant between bulk and thin film materials. This may be the cause of the difference in d-spacing observed here. The increase in d-spacing for the thin films is quite small—approximately 0.6 to 1% between the bulk and thin film samples. An absence of larger differences in d-spacings could be attributed to the Ag substrates used which are quite ductile and may allow the films to be relatively stress free compared to films fabricated on more rigid substrates (i.e. Si, sapphire, MgO).

#### Ferroelectric Properties

The ferroelectric properties calculated in Table I were taken from the P vs. E hysteresis loops shown in Figure 3. As stated above in the discussion of dielectric properties, both bulk and thin film materials indicated a transition across the morphotropic phase boundary. This transition was also evident in the hysteresis loops of the materials. In the bulk materials, the transition was obvious with a widening of the hysteresis loop signaling the emergence of the tetragonal phase in the 2/51/49 material. This phenomenon, however, did not occur in the thin film samples. The tetragonal phase was evident in the dc hysteresis loops of the thin films by a slightly more square hysteresis loop for 2/51/49 than for the rhombohedral 2/55/45 film. The phase transition was apparent in both ac and dc hysteresis loops of the films by a rise in remanent polarization in the 2/53/47 film. Previous work mentioned that thin films have a lower P<sub>R</sub> and higher E<sub>C</sub> than bulk materials for reasons similar to differences in dielectric properties mentioned above (grain size, clumping, voltage sensitivity).<sup>2</sup> Although the thin films presented here with 2% La had a higher E<sub>C</sub>, the P<sub>R</sub> of these films was not necessarily lower than for bulk materials. In fact, 2/53/47 and 2/51/49 films had a higher P<sub>R</sub> than bulk samples of the same composition. Again, as with dielectric properties, the ferroelectric properties of the thin films seemed to be different across the phase boundary than the bulk ceramics. This was also the case for x/65/35 materials.

In PLZT bulk x/65/35 samples, the hysteresis loops obtained were similar to those expected for these compositions. The remanent polarizations and coercive fields calculated were lower than reported mixed oxide values<sup>3</sup>, and this can possibly be attributed to the difference in processing between the coprecipitation and mixed oxide processes as discussed above. As anticipated, the 6, 7 and 8% La materials were memory materials, and the 9, 9.5 and 10% La materials were slim-loop materials. For the memory materials, E<sub>C</sub> was higher and P<sub>R</sub> was lower for thin films than for bulk materials which was similar to previously reported results.<sup>2</sup> Although both bulk and thin film memory materials experienced narrowing of their hysteresis loops with increasing %La, the bulk materials transformed to slim-loop materials at 9% La, while the thin films maintained ferroelectric memory hysteresis loops beyond 9% La. Research by Gu et al.<sup>5</sup> on quenched PLZT 9.5/65/35 ceramics showed that internal stresses induced in quenched samples can enhance polar region ordering and produce a more ferroelectric-like response. This produced higher remanent polarizations in quenched samples than in annealed samples. These findings could explain the memory behavior observed in the 9, 9.5 and 10/65/35 thin films in this study. Residual stresses in the thin films which could have produced the differences in d-spacings discussed above may have caused these films to retain ferroelectric memory hysteresis loops that were not observed in the bulk materials of the same compositions. Nevertheless, thin film behavior again differed from bulk ceramic behavior near the paraelectric phase boundary.

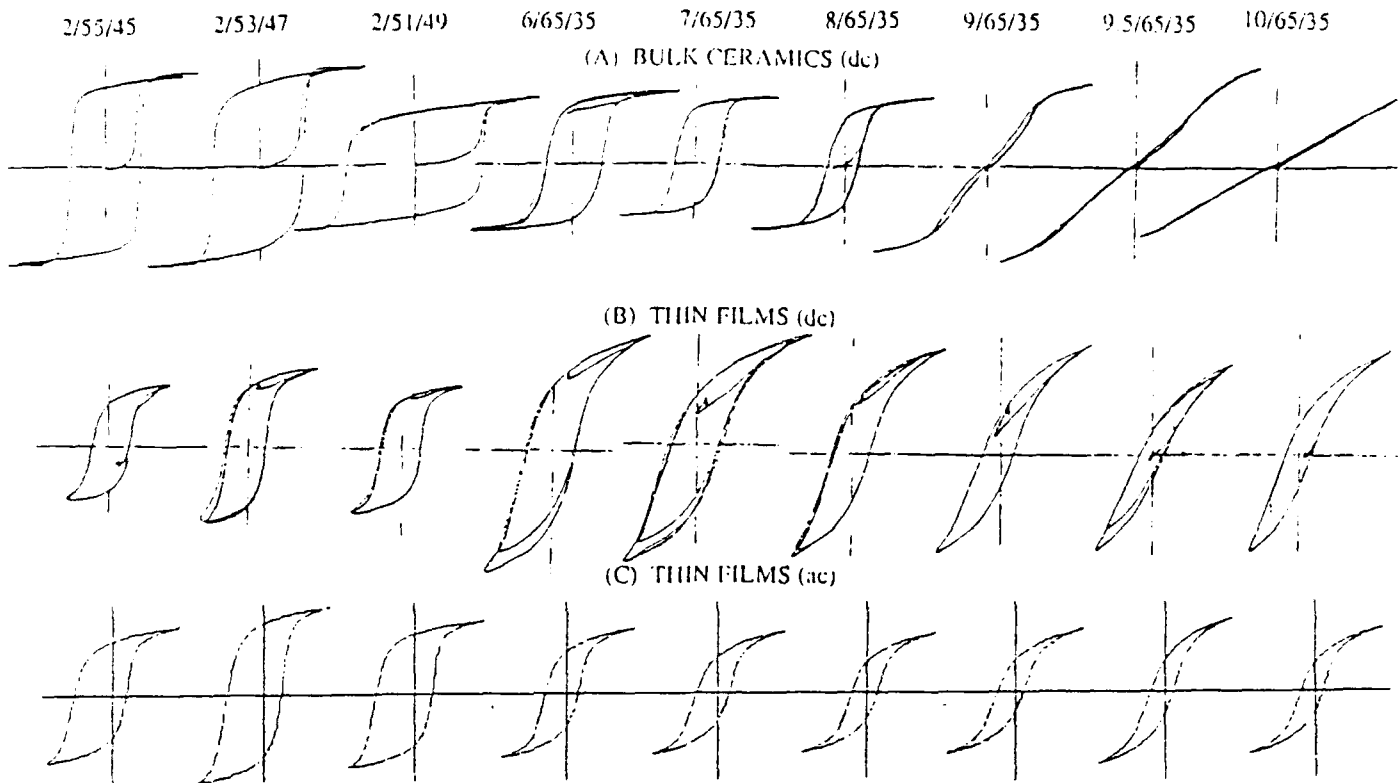


Figure 3. Hysteresis loops of several PLZT bulk and thin film materials including (A) dc loops of bulk ceramics, (B) dc loops of thin films and (C) ac loops of thin films.

#### Summary and Conclusions

PLZT bulk ceramics and thin films were fabricated from the same acetate precursor solutions in order to minimize batching variations and accurately compare properties between bulk and thin film samples of the same compositions. It was found that materials near the morphotropic phase boundary with 2% La differed in behavior. Maximum dielectric constants were found at 2/53/47 for both materials; however, the bulk 2/51/49 had a proportionally higher dielectric constant than the thin film when compared to their respective 2/55/45 samples. The hysteresis loops of the bulk samples indicated a transition to a tetragonal phase with a widening of hysteresis loops (increased  $E_C$ , decreased  $P_R$ ). Thin films also indicated a transition but with a maximum in  $P_R$  for the 2/53/47 composition.

Bulk  $x/65/35$  materials behaved as expected with the exception of slightly lower Curie temperatures, coercive fields and remanent polarizations and slightly higher dielectric constants than previously reported. The 6, 7 and 8/65/35 materials produced memory hysteresis loops, and the 9, 9.5 and 10/65/35 materials produced slim hysteresis loops. The thin film memory loops were somewhat thinner than the bulk memory loops, and continual narrowing of the loops occurred toward the paraelectric phase boundary; however, slim-loop ferroelectrics were never completely achieved in the thin film materials. X-ray diffraction analysis showed that thin film lattice spacings were only slightly greater than the corresponding bulk spacings as indicated by diffraction peaks slightly shifted in diffraction angle between the two materials.

This comparison of bulk and thin film ferroelectrics is believed to be an accurate comparison of properties caused only by the inherent differences in configuration between bulk ceramics and thin films. It is believed that the current process used to fabricate these materials is one in which complete mixing of precursors and accurate batching of materials provided a minimization of batching differences that could cause serious variations in composition and

properties of bulk and thin film PLZT ferroelectrics. Hence, this process provided a valid comparison between these materials.

#### Acknowledgement

This work was supported by ONR under contract #N00014-91-J-1508

#### References

- [1] L.M. Sheppard, "Advances in Processing of Ferroelectric Thin Films," *Am.Cer.Soc.Bull.*, vol. 71(1), pp. 85-95, 1992.
- [2] G.H. Haertling, "An Acetate Process for Bulk and Thin Film PLZT," in *IEEE 7th International Symposium on Applications of Ferroelectrics*, pp. 292-5, 1990.
- [3] G.H. Haertling, "Electrooptic Ceramics and Devices," in *Engineered Materials Handbook*, vol. 4 (Ceramics and Glasses), ASM International, pp. 1124-30, 1991.
- [4] H. Watanabe, T. Mihara and C.A. Paz De Araujo, "Device Effects of Various Zr/Ti Ratios of PZT Thin Films Prepared by Sol-Gel Method," in *Proceedings of the 3rd International Symposium on Integrated Ferroelectrics*, pp. 139-50, 1991.
- [5] W.Y. Gu, E. Furman, A. Bhalla and L.E. Cross, "Effects of Thermal Treatment on the Electrical Properties in Relaxor PLZT Ceramics," *Ferroelectrics*, vol. 89, pp. 221-30, 1989.

# A PLZT OPTICAL PHASE MODULATOR AND ITS APPLICATIONS

Feiling Wang and Gene H. Haertling  
Department of Ceramic Engineering  
Clemson University  
Clemson, South Carolina 29634-0907

An electrooptic phase modulator was designed and fabricated by using the quadratic electrooptic effect of PLZT ceramic of composition 10/65/35. The modulator can be operated at either the fundamental or double frequency of the AC signal driver. The modulator proved effective as a phase modulation device in a phase-detection measurement of small birefringent shift of thin film materials. The principles for such usage are discussed.

## Introduction

Relaxor ceramic materials in the  $(\text{Pb}, \text{La})_x \text{Zr}_x \text{TiO}_3$  (PLZT) system are known to possess strong quadratic or slim-looped transverse electrooptic effects<sup>1</sup>. The applications of the materials in optical area have been found in light shutters, spatial light modulators, second harmonic generation as well as waveguide devices such as total internal reflection switches<sup>2,3</sup>. Although single crystal materials that possess linear electrooptic effects such as  $\text{LiNbO}_3$  and KDP have traditionally been the primary material group for optical phase modulation, polycrystalline PLZT ceramics which possess quadratic electrooptic effects can also be used as optical phase modulation media. In this report, an optical phase modulator made from a hot-pressed PLZT ceramic is presented. The application of the modulator in a phase-detection technique for the measurements of small optical phase retardation in thin film materials is discussed.

## Design and Operation

A bulk 10/65/35 PLZT wafer was chosen as the modulating medium. The material was made with a hot pressing process using stoichiometric powder derived from a water-soluble precursor. The material was transparent and showed typical dielectric properties for the material in this composition, i.e. high dielectric constant and very slim hysteresis loop. The electrooptic characterization showed that the dependence of the birefringence shift on the external electric field was primarily quadratic, as presented in Figure 1. The thickness of the PLZT wafer was 0.5 mm (20 mil) with both sides being optically polished. To accommodate the ac driving signal, copper planar electrodes were fabricated on one side of the material by a photolithography technique. The electrode gap width was 50  $\mu\text{m}$ , which allowed a light beam to pass the device without a special focusing effort. An ac electric signal of adjustable amplitude was fed to the electrode pair to drive the modulator. In addition, an adjustable dc bias was also applied to the modulator.

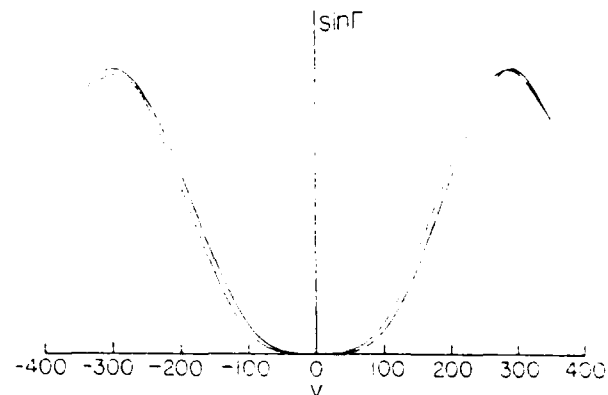


Figure 1 The electrooptic response of a 10/65/35 PLZT ceramic, measured by means of a phase-detection scheme. The Y axis is proportional to  $\sin\Gamma$  with  $\Gamma$  being the optical phase shift due to the birefringence of the material.

Under sufficiently small external field, the field-induced birefringent shift of the material can be expressed as a quadratic function of the applied field:

$$\Delta n = \text{constant} (E_b + E \sin\Omega t)^2, \quad (1)$$

where  $E_b$  is the field strength of the dc bias,  $\Omega$  is the frequency of the ac driving electric field. It is obvious that under a non-zero bias field, the phase shift generated by the modulator contains both  $\Omega$  and  $2\Omega$  components. By adjusting the bias field  $E_b$ , the relative amplitude of  $\Omega$  and  $2\Omega$  components can be altered. The function of the bias field in changing the primary modulating frequency is illustrated in Figure 2 where function  $\Gamma(t)$  is the phase retardation produced by the modulator.

To visualize the phase modulating function of the modulator and the interchange of the modulating frequency with the bias electric field, the modulator was sandwiched between two crossed polarizers with the modulation axis, the direction of the applied electric field, being oriented at 45 degree angle with respect to the polarization direction of the polarizer. With such a arrangement the polarization state of the originally linearly polarized light beam was periodically changed due to the phase shift  $\Gamma(t)$  imposed by the modulator. The intensity of the light output  $I(t)$  is given by:

$$I(t) = B \sin^2[\Gamma(t)/2] = B \sin^2[A(E_b + E \sin\Omega t)^2], \quad (2)$$

where A and B are two system constants. The waveform of the light intensity given by Equation (2) is graphically analyzed in Figure 2. As shown by the figure, the modulation is purely  $2\Omega$  in frequency at zero bias and gradually becomes dominated by the  $\Omega$  component with the increase of the bias electric field.

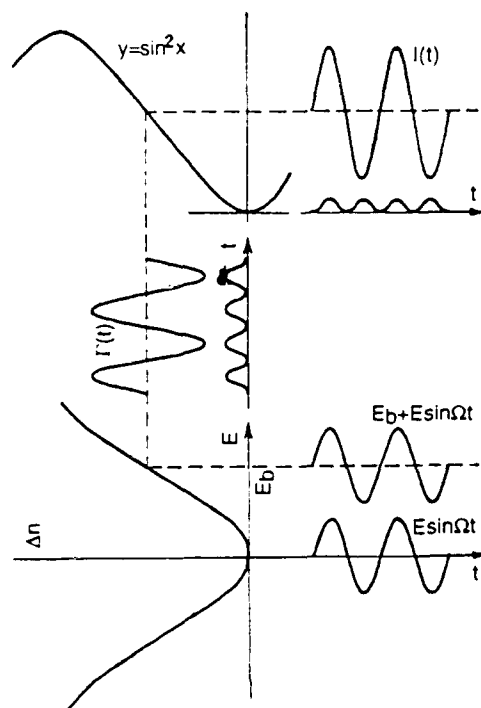


Figure 2 A graphic analysis of the operation modes of the PLZT phase modulator with and without dc bias field.

According to Equation (1), the modulation always contains a  $2\Omega$  component although its relative magnitude becomes very small compared to the  $\Omega$  component when a sufficient bias field is applied. A pure  $\Omega$  modulation mode can actually be achieved by using the saturation behavior in the electrooptic response of the material. The saturation behavior of the electrooptic response in PLZT materials have been observed<sup>4,5</sup>. In the presence of such saturation, the quadratic relation for the field-induced birefringence is no longer adequate; higher order terms or entirely new functional dependence needs to be used. In the electrooptic response curve that shows saturation behavior, there must be a point where the second derivative of the curve is zero. If a bias electric field is applied to this point, the modulation will be purely  $\Omega$  in frequency.

In practice, only a fairly low bias field is needed in order for the modulation at  $2\Omega$  frequency to become insignificant compared to the  $\Omega$  component. Figure 3 shows the waveforms of the light output, recorded by an

oscilloscope, from the second polarizer with the PLZT modulator driven by a 1kHz ac signal operating under various dc bias voltage. The square waves in the pictures are the trigger signal synchronized with the ac driving voltage. As expected, the modulation was purely  $2\Omega$  in frequency under zero bias and eventually became dominated by  $\Omega$  frequency components under a bias voltage of 150 volts. Components of both frequencies are clearly represented under an intermediate bias, as shown by Figure 3(b). The relative amplitude of modulation at both frequencies as functions of the dc bias was measured by a lock-in amplifier synchronized with the driving function generator. As shown in Figure 4, with the increase of the dc bias voltage, the amplitude of the  $2\Omega$  component decreased while the  $\Omega$  component increased. Under a bias voltage of approximately 120 volts the  $2\Omega$  component becomes zero while the  $\Omega$  component approaches a maximum. Under this bias voltage, the PLZT modulator provides

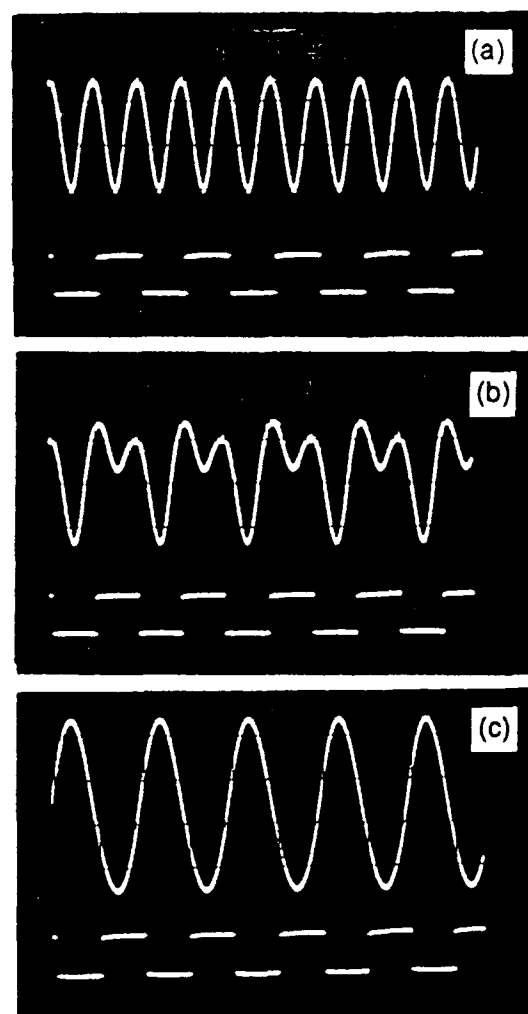


Figure 3 The waveforms of the output light modulated by the PLZT phase modulator operated under (a) bias=0V, (b) bias=20V and (c) bias=150V.

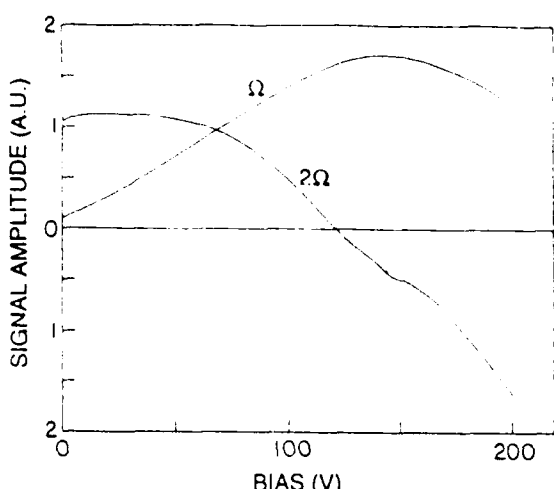


Figure 4 The  $\Omega$  and  $2\Omega$  frequency components in the light modulated by the PLZT phase modulator plotted as functions of the bias voltage.

the same modulation as that from a traditional modulator utilizing the linear electrooptic effect of single crystals, except that there is a constant phase shift. The constant phase shift can be compensated with an optical compensator in applications where it is not desirable. Much lower ac driving voltages are needed to achieve the same phase modulation depth for the PLZT modulator than for traditional modulators because of the strong quadratic electrooptic effect in the PLZT ceramic.

#### Applications

The PLZT phase modulator has been successfully used as a phase modulation device in a phase-detection scheme for the measurement of small birefringences of thin film materials. The optical arrangement for such application is shown in Figure 5. The PLZT compensator together with an optical compensator and the sample to be measured are sandwiched between two crossed polarizers. The modulating axis of the modulator is oriented 45 degrees with respect to the polarizer but parallel (or perpendicular) to the principle

optical axes of the sample determined by the direction of the external electric field. The purpose of the compensator is to compensate the constant phase shift generated by the modulator and to calibrate the system.

With the PLZT phase modulator being driven by an ac signal of frequency  $\Omega$  under zero bias, the total phase retardation for the light polarized along the modulating axis consists of contributions from all three components, namely, modulator, compensator and sample:

$$\Gamma = \Gamma_{\text{mod.}} + \Gamma_{\text{comp.}} + \Gamma_{\text{samp.}} \quad (3)$$

As been previously pointed out, the electrooptic effect of PLZT materials exhibits high order field dependence and saturation behavior in some circumstances. The phase modulation produced by the PLZT modulator, therefore, should be expressed by the following Fourier series:

$$\Gamma_{\text{mod.}}(t) = \text{constant} + \sum_{m=1}^{\infty} C_m \sin 2m\Omega t, \quad (4)$$

where coefficient  $C_1$  is proportional to the quadratic electrooptic coefficient of the PLZT modulating medium;  $C_2$  is proportional to the quartic electrooptic coefficient, etc. Although in most instances only  $C_1$  needs to be considered, the whole summation in Equation (4) is retained for the strictness of the following discussion.

By adjusting the compensator, the constant in Equation (4) can be eliminated; therefore we have

$$\Gamma(t) = \sum_{m=1}^{\infty} C_m \sin 2m\Omega t + \Gamma_{\text{samp.}} \quad (5)$$

The light intensity detected by the photomultiplier tube (PMT) is therefore given by

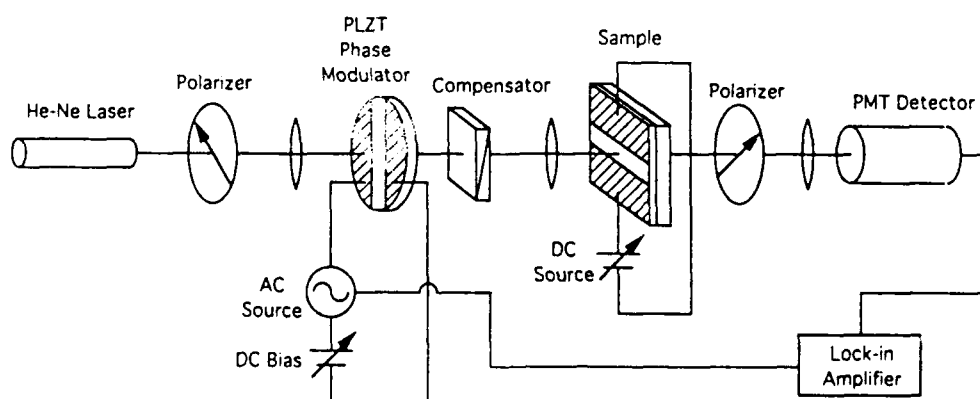


Figure 5 The optical arrangement in a phase-detection scheme using the PLZT modulator as a phase modulating device.

$$I(t) = I_0 \sin^2(\Gamma/2)$$

$$= (I_0/2)[1 + \cos(\sum_{m=1}^{\infty} C_m \sin 2m\Omega t + \Gamma_{\text{samp}})]. \quad (6)$$

If the reference signal of the lock-in amplifier is chosen as  $\sin 2\Omega t$ , the output signal of the lock-in amplifier, S, is proportional to the amplitude of the  $\sin 2\Omega t$  term in the Fourier expansion of Equation (6), that is

$$S = D \int_0^t I(t) \sin 2\Omega t dt$$

$$= D \int_0^t \cos(\sum_{m=1}^{\infty} C_m \sin 2m\Omega t + \Gamma_{\text{samp}}) \sin 2\Omega t dt \quad (7)$$

where D is a system constant. It can be shown that the above integration is approximately given by

$$S = D J_1(C_1) \sin \Gamma_{\text{samp}}. \quad (8)$$

where  $J_1$  is the Bessel function of the first order. With a fixed driving signal amplitude,  $C_1$  is a constant; the output signal from the lock-in amplifier therefore is proportional to the phase retardation generated by the sample, namely,  $\Gamma_{\text{samp}}$ . Moreover, in detecting the electrooptic effect of thin film materials, the phase retardation of the sample is usually very small so that the output from the lock-in amplifier becomes directly proportional  $\Gamma_{\text{samp}}$ , while the proportional constant can be determined by the compensator.

With the PLZT phase modulator, the above scheme has proven an effective way of detecting very small phase retardations produced by electrooptic effects in thin film materials. As an example, Figure 6 shows the birefringence versus E-field curve of a 2/55/45 thin

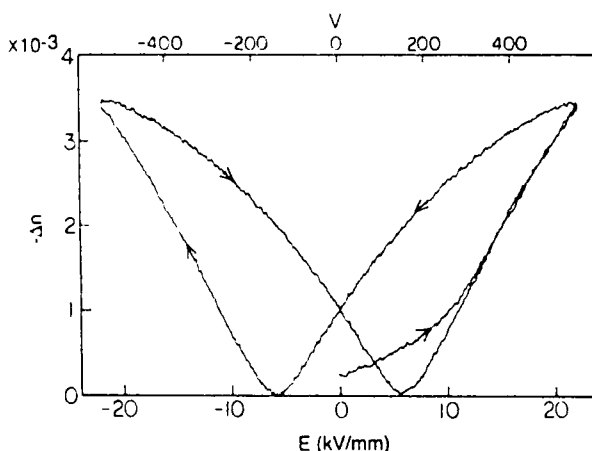


Figure 6 The birefringence versus E-field curve for a 2/55/45 PLZT thin film of 0.5  $\mu\text{m}$  thickness sputter-deposited on a fused silica substrate, measured with the phase-detection scheme using the PLZT phase modulator.

film of 0.5  $\mu\text{m}$  thick grown on a fused silica substrate, measured with the above phase-detection system under zero-bias mode.

When an appropriate bias field is applied, the modulation becomes predominated by the  $\Omega$  component. With the reference signal of the lock-in amplifier set at  $\sin \Omega t$ , the above measuring system functions similarly as in the zero-bias mode.

### Conclusions

An optical phase modulator was made by using the quadratic electrooptic effect of a hot-pressed PLZT ceramic. The device can be operated in a zero-bias mode which provides a modulation at double the frequency of the driving signal. When an appropriate bias is applied, the modulator provides a modulation dominated by the component at the frequency of the driving signal. Application of the PLZT modulator has been found in the phase-detection scheme for the measurement of very small birefringence in thin film materials.

### References

- [1] G.H. Haertling and C.E. Land, "Hot-pressed (Pb,La)(Zr,Ti)O<sub>3</sub> Ferroelectric Ceramic for Electronic Applications," *J. Am. Ceram. Soc.* 54, 1(1971)
- [2] G.H. Haertling, "PLZT Electrooptic Materials and Applications-A Review," *Ferroelectrics*, 75, 25(1987)
- [3] H. Higashino, T. Kawaguchi, H. Adachi, T. Makino and O. Yamazaki, "High Speed Optical TIR Switches Using PLZT Thin Film Waveguides in Sapphire," *Japan. J. Appl. Phys.* 24 suppl., 284(1985)
- [4] F. Wang and A.Y. Wu, "Electro-optical and Nonlinear Optical Properties of Thin Film Materials Containing Oxygen-Octahedra under High DC Electric Field," *Proc. 7th Intern. Symposium on the Application of Ferroelectrics*, pp.131-134, Urbana, IL, June 6-8, 1990.
- [5] G.H. Haertling, unpublished results.

# TRANSVERSE ELECTROOPTIC PROPERTIES OF ANTIFERROELECTRIC LEAD CONTAINING THIN FILMS

Feiling Wang, Kewen K. Li and Gene H. Haertling  
Department of Ceramic Engineering  
Clemson University  
Clemson, South Carolina 29634-0907

The transverse electrooptic effect was observed in solution coated lead zirconate thin films. The electric-field-induced birefringent shift exhibited a characteristic response which differed from the normal butterfly-like loops for ferroelectric materials. The observed unique response in lead zirconate thin films was related to their antiferroelectric nature and the electric-field-induced antiferroelectric-ferroelectric phase transition. The possible applications of the materials for optical memory are discussed.

## Introduction

Ferroelectric (FE) thin films, owing to their high dielectric constant and two electrically switchable remanent states, have attracted great interest for the development of nonvolatile memory devices and other applications<sup>1,2</sup>. A variety of ferroelectric materials are also known to possess transverse electrooptic properties, i.e. the electric-field-controlled birefringence; however, ferroelectric switching (polarization reversal with an electric field) has not proved equally useful in integrated optical and/or optoelectronic devices. To facilitate an optical memory function in optoelectronic devices, it is desirable for the waveguide materials to possess two electrically switchable birefringent states. However, the two remanent polarization states are not distinguishable for the index ellipsoid in ferroelectric materials. Therefore, it is not feasible to realize optical memory in ferroelectric materials by switching between the two remanent polarization states.

Recently the transverse electrooptic effects in antiferroelectric (AFE) lead zirconate ( $PbZrO_3$ ) thin films were observed<sup>3</sup>. The electric-field-induced birefringent shift in the lead zirconate thin films showed a characteristic response not exhibited in ferroelectric materials. The unique electrooptic response in the antiferroelectric thin films was found to stem from the electric-field-induced antiferroelectric-ferroelectric phase transition. Besides its importance as a fundamental material property, the transverse electrooptic effect in the antiferroelectric thin films may also furnish a mechanism for optical memory in optoelectronic devices. In this report the latest measurements of the transverse electrooptic properties in antiferroelectric lead zirconate thin films are presented.

## Experimental Method

Lead zirconate thin films were deposited onto fused silica and Pt/Ti coated silicon substrates by a solution coating technique from an acetate precursor<sup>4,5</sup>. The antiferroelectric crystal structure of the resultant thin films was confirmed by the appearance of the X-ray diffraction peak at  $2\theta = 16.9^\circ$ , characterizing the antiferroelectric double cell structure. For the measurement of the dielectric properties of the materials, copper dots were evaporated onto the thin films deposited on the Pt/Ti-coated silicon substrate. For the detection of the transverse electrooptic properties, copper interdigitated electrodes with gap widths ranging from 5 to 40  $\mu m$  were deposited on top of the thin films grown on the fused silica substrates.

The electric-field-induced birefringent shift of the thin film was measured by means of a phase-detection technique<sup>6</sup>, using a He-Ne laser of wavelength of 632.8 nm as the light source. The phase modulation of the incident light was provided by means of a modulator. The measurements were performed with a transmission mode. In the phase detection scheme, the amplitude of the output signal (from a lock-in amplifier) at the modulating frequency was directly proportional to the phase retardation of the sample, provided that the total phase retardation of the sample was sufficiently small. A slow varying dc voltage was applied to the interdigitated electrodes during the measurement. An optical compensator was used to calibrate the measuring system.

## Results and Discussion

A typical electrooptic response of the lead zirconate thin film is shown in Figure 1 where the birefringent shift of the thin film is plotted as a function of the slow varying dc electric field. The thickness of the film was 1  $\mu m$ . Interdigital electrodes with a gap width of 10  $\mu m$  was used in the measurement. As shown in the figure, the electrooptic response of the antiferroelectric thin film exhibits a number of features different from that of ferroelectric materials. For the purpose of comparison, a typical birefringence versus E-field curve for a ferroelectric thin film, i.e. PLZT<sup>7</sup> of composition 2/55/45, is shown in Figure 2. The birefringence versus E-field curve for the lead zirconate thin film is characterized by (1) enhanced hysteretic

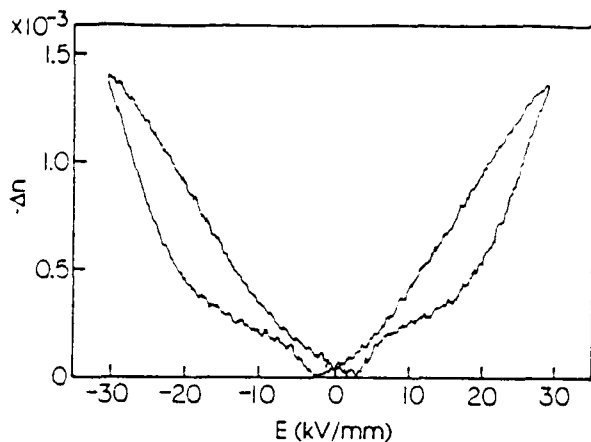


Figure 1 Measured birefringent shift as a function of the external dc electric field for a lead zirconate thin film deposited on a fused silica substrate.

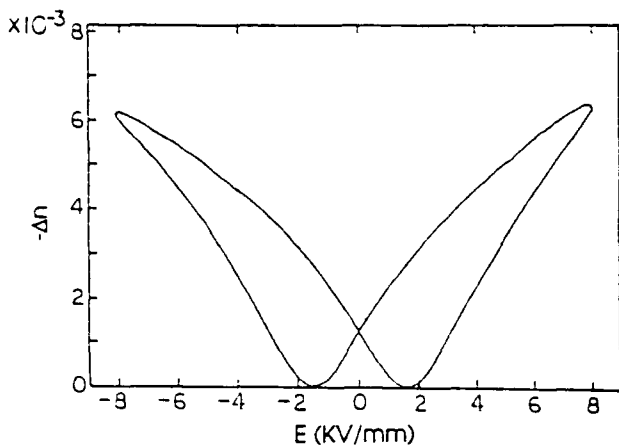


Figure 2 Measured birefringent shift as a function of the external dc electric field for a ferroelectric PLZT thin film deposited on a sapphire substrate.

behavior in the region of field strength above 10 kV/mm, (2) diminished hysteretic behavior in the region of field strength below 5 kV/mm and (3) rapid increase of the slope when the increasing electric field exceeds 20 kV/mm. It was found that the characteristic response of the lead zirconate thin films was attributed to the electric-field-induced AFE-FE structural transition<sup>3</sup>.

With the help of a phenomenological model, the correlation between the field-induced birefringent shift of a material and electric polarization  $P(E)$  can be described by the following relation:

$$\Delta n \propto [E + \beta P(E)]^2, \quad (1)$$

where  $\beta$  is a constant dependent on the crystal structure of the material ( $4\pi/3$  for cubic structure). The main features for the electrooptic response of the lead zirconate thin films shown in Figure 1 are consistent with those predicted from the dielectric properties (double hysteresis loop) by using relation (1).

To better understand the nature of the antiferroelectric lead zirconate thin films, a static bias electric field was applied to the thin film material in both the dielectric and electrooptic measurements. Thin films deposited on the Pt/Ti coated silicon substrates were used for the measurement of the dielectric behavior. With the increase of the dc bias, the polarization versus  $E$  field curve of the lead zirconate thin film gradually evolves from a double hysteresis loop to a single hysteresis loop. As shown in Figure 3, under an appropriate bias field, the shape of the biased single hysteresis loop very much resembles the normal hysteresis loop for ferroelectric materials. Unlike the ferroelectric materials, however, the two remanent states in the biased single hysteresis loop (denoted by  $P_A$  and  $P_B$  in Fig.3) possess polarizations of different magnitude, which produce two distinguished birefringent states in the thin films. These two birefringent states are clearly represented in the biased birefringence versus  $E$ -field curve, as shown in Fig.4, measured from a lead zirconate thin film grown on a fused silica substrate. A static bias field of approximately 17 kV/mm was applied during the measurement. It is obvious that the two distinguished remanent birefringent states  $\Delta n_A$  and  $\Delta n_B$  are associated with the two remanent polarization states  $P_A$  and  $P_B$  in the biased single hysteresis loop shown in Figure 3. It should be noted, however, that to avoid the breakdown of the electrodes through the air, the bias electric field and the scan range are lower in the measurement of the electrooptic properties than in the measurement of the dielectric property. In addition, because these two measurements involve thin films deposited on two different types of substrates with different directions of applied electric field, quantitative correlation between these two measurements is not possible.

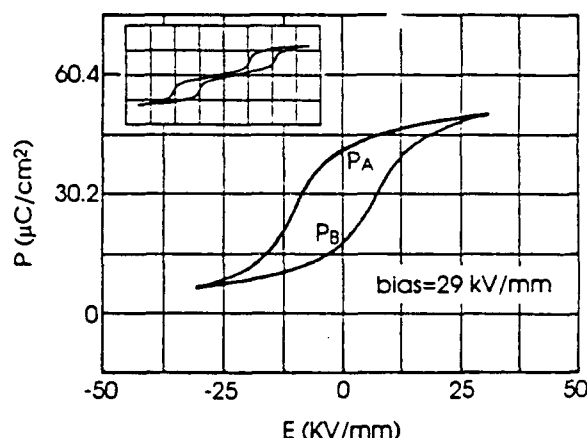


Figure 3 Dielectric properties of a lead zirconate thin film grown on a Pt/Ti-coated silicon substrate, taken under a static bias field of 29 kV/mm. The insert is a hysteresis loop of the same sample taken with zero bias field. The horizontal and vertical scales for the insert plot are 25 kV/mm per division and 30.2  $\mu\text{C}/\text{cm}^2$  per division, respectively.

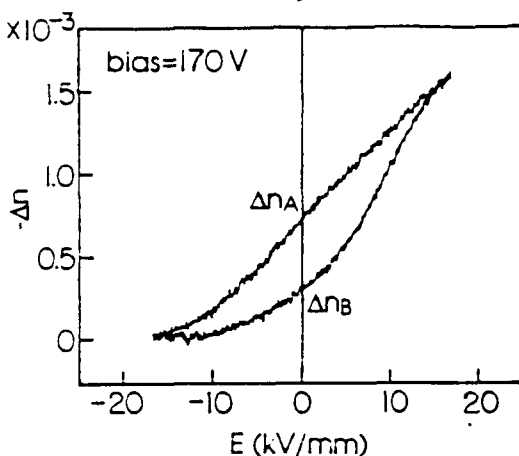


Figure 4 Birefringent shift as a function of the slow varying external field measured with a dc bias field of 17 kV/mm for a lead zirconate thin film on a fused silica substrate.

It was found that the lead zirconate thin films acquired a permanent birefringence once an initial electric field of sufficient magnitude was applied. Shown in Figure 5 is the birefringent shift of a lead zirconate thin film as a function of the slow varying external electric field recorded during the first few cycles of the field scan. In the first half cycle of the field scan, the birefringence of the material drastically increased when the increasing electric field exceeded approximately 16 kV/mm. When the external electric field was reduced to zero, the material retained a significant remanent birefringent shift. During the next few scan cycles, this remanent birefringence kept increasing yet the increment was smaller and smaller after each cycle. A stable remanent birefringence (permanent birefringence) was finally reached as shown previously in the birefringence versus E-field curve of Figure 1. The stable remanent birefringent state, under zero external electric field, was chosen as the zero-

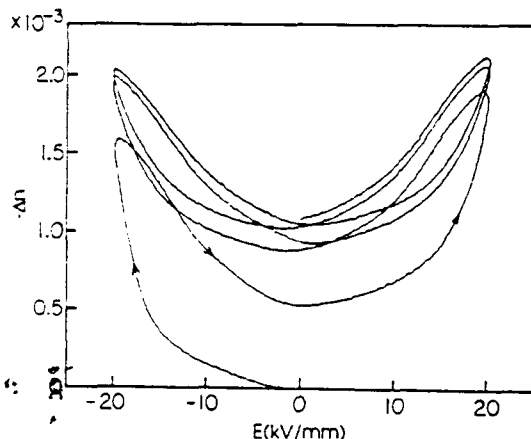


Figure 5 The evolution of the electrooptic response of a lead zirconate thin film on a fused silica substrate during the first few cycles of the electric field scan.

birefringence point in plotting both Figure 1 and Figure 4. After testing a few lead zirconate thin film samples, it was found that this initiating process of the material was reproducible.

The observed permanent birefringence in the antiferroelectric thin films mentioned above may be related to other types of memory behavior previously observed in antiferroelectric lead zirconate materials<sup>8</sup>. A possible explanation for this birefringence memory is that when the AFE-FE phase transition occurred under a sufficiently high electric field the ferroelectric domains are forced to align along the direction of the E-field; although the structure of antiparallel dipoles was restored after the withdrawal of the external E-field, the antiferroelectric dipoles remained preferentially aligned in the direction along which the E-field was previously applied. Such an explanation for the birefringence memory is supported by an optical study of the lead zirconate crystal which showed that the index of refraction is the smallest for the light polarized along the  $a$  axis of the antiferroelectric unit cell<sup>9</sup>. This mechanism of birefringence memory is distinguished from that of ferroelectric materials where birefringence memory is mainly caused by the remanent polarization.

The characteristic electrooptic response of the lead zirconate thin films may furnish a means of realizing optical memory in optoelectronic devices. Two different mechanisms may be utilized in optical memory devices. In the first type of memory, the information may be stored in a virgin material by applying a sufficiently high electric field. After the withdrawal of the electric field, as shown in Figure 5, the thin film material becomes permanently oriented and possesses a permanent birefringence of approximately  $1.3 \times 10^{-3}$ . The second type of memory is associated with the two distinguished birefringent states of the thin film materials in the presence of a bias electric field as shown in Figure 4. Because these two birefringent states,  $\Delta n_A$  and  $\Delta n_B$ , are produced by the two remanent states of polarization,  $P_A$  and  $P_B$ , of the material, they are stable under the bias field. The merit of the second type of memory is that the two birefringent states are electrically switchable. For example, a TIR switch<sup>10</sup> made of the antiferroelectric thin film would allow the inter-switching of the light between the two waveguide channels by electric pulses of opposite polarities, operated under a static bias field. Such a switch is not possible with ferroelectric materials in which the two remanent polarization states are optically equivalent.

### Conclusions

The transverse electrooptic property of the solution coated lead zirconate thin film exhibits a characteristic response which is attributed to the electric-field-induced antiferroelectric-ferroelectric phase transition. Under an appropriate static bias electric field, the material possess two distinguishable birefringent states

associated with the two remanent polarization states of the material. The thin films were also found to acquire a permanent birefringence once a sufficiently high electric field was applied to the virgin materials.

Two types of mechanisms are proposed for utilizing the antiferroelectric thin films for optical memory in optoelectronic devices. The first type of memory makes use of the permanent orientation of the material induced by an initial electric field. The second type of memory involves the inter-switching between the two distinguishable birefringent states of the material under a bias field with electric pulses.

#### Acknowledgment

This study was partially sponsored by the Office of Naval Research under contract No. N00014-91-J-508.

#### References

- [1] G.H. Haertling, "Ferroelectric Thin Film for Electronic Applications," *J. Vac. Sci. Technol. A*, 9, 414(1991)
- [2] D. Bonsurant and F. Gnadinger, "Ferroelectrics for Nonvolatile RAMs," *IEEE Spectrum*, July 1989, p.30
- [3] F. Wang, K.K. Li, and G.H. Haertling, "Transverse Electro-Optic Effect of Antiferroelectric Lead Zirconate Thin Films," *Optics Lett.* 17, 1122(1992)
- [4] K.K. Li, F. Wang, and G.H. Haertling, "Antiferroelectric Lead Zirconate Thin Films Derived from an Acetate Precursor System," *J. Mater. Sci.* (to be published)
- [5] G.H. Haertling, "PLZT Thin Film Prepared from Acetate Precursors," *Ferroelectrics*, 116, 51(1991)
- [6] F. Wang, C.B. Juang, C. Bustamante, and A.Y. Wu, "Electro-optic Properties of  $(\text{Pb}, \text{La})(\text{Zr}, \text{Ti})\text{O}_3$ ,  $\text{BaTiO}_3$ ,  $(\text{Sb}, \text{Ba})\text{Nb}_2\text{O}_6$  and  $\text{BaNaNb}_5\text{O}_{15}$  Thin Films," in *Proc. of 4th International SAMPE Electronic Conference*, p.712
- [7] G. H. Haertling and C.E. Land, "Hot-pressed  $(\text{Pb}, \text{La})(\text{Zr}, \text{Ti})\text{O}_3$  Ferroelectric Ceramic for Electronic Applications," *J. Am. Ceram. Soc.* 54, 1(1971)
- [8] K. Uchino, "Digital Displacement Transducer Using Antiferroelectrics," *Japan. J. Appl. Phys.* 24, suppl., 24(1985)
- [9] F. Jona, G. Shirane, and R. Pepinsky, "Optical Study of  $\text{PbZrO}_3$  and  $\text{NaNbO}_3$  Single Crystals," *Phys. Rev.* 97, 1585(1955)
- [10] H. Higashino, T. Kawaguchi, H. Adachi, T. Makino and O. Yamazaki, "High Speed Optical TIR Switches Using PLZT Thin Film Waveguides on Sapphire," *Jpn. J. Appl. Phys.* 24, suppl., 284(1985)

## TRANSVERSE ELECTROOPTIC PROPERTIES OF MAGNETRON SPUTTERED PLZT THIN FILMS

F. WANG and G.H. HAERTLING  
Department of Ceramic Engineering,  
Clemson University,  
Clemson, SC 29634 , USA

**ABSTRACT.** Ferroelectric thin films of  $(\text{Pb},\text{La})(\text{Zr},\text{Ti})\text{O}_3$  ceramics were deposited on various substrates by magnetron sputtering. With the use of a phase-detection technique, the transverse electrooptic properties of the films were characterized. It was found that the electrooptic response of the films is strongly dependent on the grain orientation of the thin film materials.

### 1. Introduction

Lead lanthanum zirconate titanate (PLZT) thin films have been deposited onto various substrates by means of solution coating techniques using acetate precursors [1-3]. In search of the optimum coating technique for producing high quality PLZT thin films for various applications, PLZT powders derived from the acetate precursors have been used as target materials in a radio-frequency (RF) magnetron sputter deposition technique designed to complement the solution coating methods.

Recently, increasing attention has been paid to the choice of substrates in obtaining thin films of desired properties [2]. It was reported that the thermal expansion mismatch between a ferroelectric thin film and its substrate significantly influences the orientational preference of ferroelectric domains, thus their dielectric properties. This paper is mainly concerned with the observed divergence of the transverse electrooptic properties in PLZT thin films deposited on various substrates by the RF magnetron sputtering.

### 2. Experimental Method

A high vacuum RF magnetron sputter unit was used to deposit PLZT thin films. The target material was a PLZT powder of composition 2/55/45 (La/Zr/Ti) produced by a coprecipitation method from a water soluble acetate precursor [1]. A post-deposition annealing process was utilized to obtain perovskite PLZT films. Typical deposition and annealing parameters are listed below:

RF power:	70 watt	Annealing temperature:	650°C
Total pressure:	10 micron	Annealing time:	40 min.
Oxygen percentage:	40%		
Substrate temperature:	350°C		
Deposition rate:	250 nm/hour		

375

Thin films were deposited onto three types of substrates, i.e. Pt/Ti-coated silicon, randomly oriented sapphire and fused silica substrates.

The transverse electrooptic properties of the PLZT thin films on sapphire and fused silica substrates were measured by a phase-detection technique [4] in a transmission mode using a He-Ne laser as the light source. Planar copper electrodes with a gap width of 50 nm were fabricated on top of the thin film by a photolithography process.

### 3. Results and Discussion

#### 3.1 GRAIN ORIENTATION

With the identical deposition and annealing processes mentioned previously, the thin films deposited on the three types of substrates exhibited significant differences in grain orientation as revealed by x-ray diffraction patterns.

By comparing to the diffraction pattern of the powder, it was found that peak heights for (100) and (110) orientations in thin films on Pt/Ti-coated silicon were reversed, as shown in Figure 1(a). In contrast to the films on Pt/Ti-coated silicon, films on sapphire substrates, shown in Figure 1(b), exhibit a strengthening of the (110) peak, indicating a preferred (110) grain orientation. The most drastic preferential orientation of crystal grains was observed in the thin films deposited on fused silica substrate with (100) being the dominant orientation, as shown in Figure 1(c). Summarized in Table 1 are the types of preferential grain orientation for 2/55/45 PLZT thin films deposited on the three different substrate along with their thermal expansion coefficients.

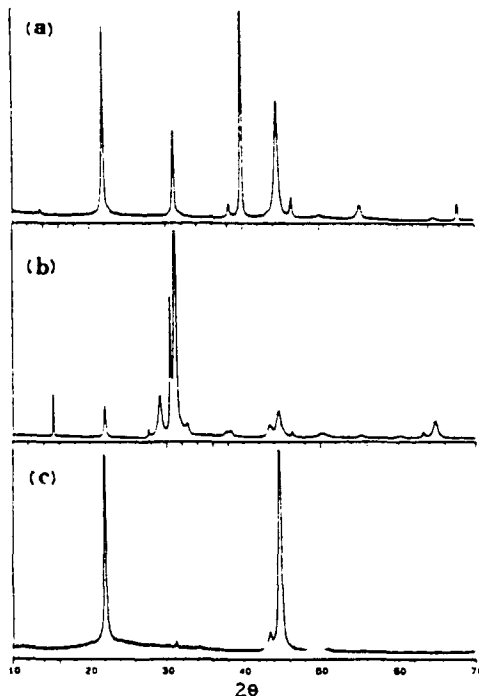


Figure 1. X-ray diffraction patterns for 2/55/45 PLZT thin films deposited on (a) Pt/Ti-coated silicon, (b) sapphire and (c) fused silica substrates.

TABLE 1. Orientation of 2/55/45 PLZT thin films

Substrate	thermal expansion coef. (ppm/ $^{\circ}$ C)	film orientation
fused silica	0.5	dominant (100)
silicon	2.5	preferred (100)
sapphire	8.0	preferred (110)

Noticing that the thermal expansion coefficient of PLZT materials (approximately 5 ppm/ $^{\circ}$ C) is intermediate between those of silicon and sapphire, the results strongly suggest that there is a correlation between the grain orientation and the thermal expansion property of the substrates in sputter deposited thin films. As shown in Table 1, thin films deposited on substrates with smaller thermal expansion coefficients exhibited dominant or preferred (100) orientation while thin films deposited on substrate with larger expansion coefficient exhibits preferred (110) grain orientation. It is not clear at present whether the preferred grain orientations are formed during the low temperature deposition or during the annealing procedure.

### 3.2. ELECTROOPTIC PROPERTIES

The field-induced birefringence of soft ferroelectric materials generally exhibit butterfly loops. In order to quantitatively describe this hysteretic electrooptic effect, three quantities are proposed to characterize a butterfly loop in the following discussion. These quantities are: the optical coercive field  $E_{OC}$  where two birefringence minima occur, the birefringence at the crossover point of a loop  $\Delta n_C$  (measured from the bottom of a curve) and the birefringence at the tip of a loop  $\Delta n_t$ . The value of  $\Delta n_t$  is meaningful only when the corresponding electric field at the tip  $E_t$  is given.

A series of butterfly loops for the electrooptic effect of a sputtered 2/55/45 PLZT film on a sapphire substrate is shown in Figure 2, created by a series field scans from a small range to a large range. Compared to the films on sapphire substrate, the 2/55/45 PLZT thin films deposited on the fused silica substrate exhibit much poorer electrooptic response as shown in Figure 3. The  $\Delta n_t$  for the film on fused silica is approximately one fourth of that for the film on sapphire substrate, taken under the same  $E_t$ . Table 2 lists the three characteristic quantities for films on both sapphire and fused silica substrates.

TABLE 2. Electrooptic properties of 2/55/45 PLZT thin films

Substrate	Thickness (nm)	$E_{OC}$ (kV/mm)	$\Delta n_t \cdot 10^{-3}$	$\Delta n_C \cdot 10^{-3}$
f. silica	620	2.0	1.5	0.2
sapphire	620	1.6	6.2	1.3

$\Delta n_t$  values were taken at  $E_t=8$  kV/mm for both samples.

Being a rhombohedral material, the polar direction of a 2/55/45 PLZT crystal grain is along a three-fold direction of a oxygen-octahedra, i.e. a (111) crystal direction. When the external electric field is parallel to the substrate surface in the phase-detection measurement in the transmission mode, there is virtually no chance for the external field to encounter the (111) crystal direction of the grains in films on fused silica with (100) dominant orientation. Films of this type of orientation, therefore, are unfavorable for utilizing the transverse electrooptic effect of the films in the transmission mode.

In contrast to the films on fused silica, sputtered films on sapphire substrate possess (110) preferred grain orientation, which enhances the possibility for the external electric field to encounter the (111) crystal direction. This preferred grain orientation, therefore,

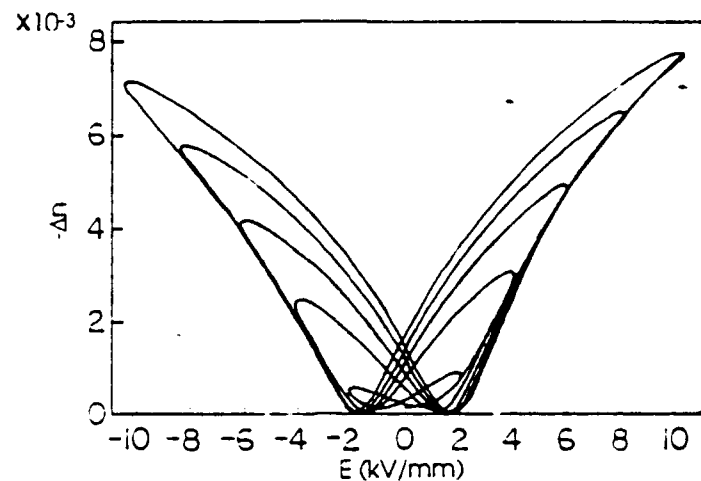


Figure 2. The evolution of the electrooptic response from a small to a large field scan range for a 2/55/45 PLZT film of thickness of  $0.62 \mu\text{m}$  on a sapphire substrate.

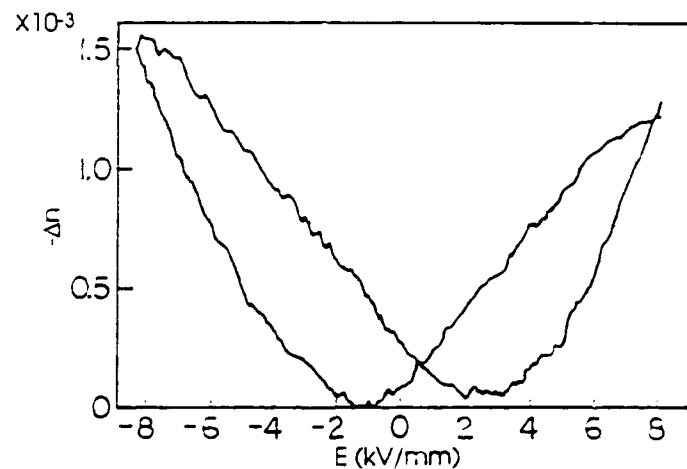


Figure 3. The electrooptic response of a 2/55/45 PLZT film of  $0.62 \mu\text{m}$  thickness on a fused silica substrate.

favors the polarization, which in turn produces a large field-induced birefringence in the materials. As shown in Table 2, films deposited on sapphire substrates with preferred (110) grain orientation indeed exhibited superior electrooptic response.

#### 4. Conclusions

PLZT thin films of composition 2/55/45 were deposited on various substrate with a RF magnetron sputtering technique using powders derived from an acetate precursor.

The electrooptic characterization shows that the films on sapphire with preferred (110) orientation exhibits superior electrooptic response over the films on fused silica with dominant (100) grain orientation. The difference is attributed to the fact that (110) orientation favors the polarization in rhombohedral thin film materials when the external electric field is along a planar direction.

#### 5. Acknowledgements

This research was supported by the Office of Naval Research under contract No. N00014-91-J-508.

#### 6. References

1. G.H. Haertling, Ferroelectrics 116 (1991) 51.
2. K.D. Preston and G.H. Haertling, Appl. Phys. Lett. 60 (1992) 2831.
3. K.K. Li, G.H. Haertling and W.Y. Howng, Integrated Ferroelectrics vol.3, No.1 (in print, 1992)
4. F. Wang, C.B. Juang, C. Bustamante, and A.Y. Wu, in Proc. of 4th International SAMPE Electronic Conference, Albuquerque, New Mexico, June 12-14, 1990, p.712.

## DIELECTRIC AND ELECTROOPTIC PROPERTIES OF ACETATE DERIVED PLZT X/65/35 THIN FILMS

GENE H. HAERTLING

Clemson University, Clemson, South Carolina, U.S.A.

Abstract PLZT solutions were prepared from the as-received acetate precursors by means of a simple mixing procedure which produced a stock solution of approximately 10% oxide solids. Films were fabricated via dip coating and heat treating at 700°C for two minutes per layer. As many as 150 layers were deposited with an automatic dip coating system. All of the resulting films were optically transparent and well crystallized in the perovskite phase. The films were evaluated with respect to dielectric and electrooptic properties. Shutter contrast ratios as high as 1000 to 1 were measured.

### INTRODUCTION

Thin films of ferroelectric (FE) compositions in the PLZT system are promising candidates for future devices involving memory and non-memory dielectrics, piezoelectric resonators, pyroelectric detectors and electrooptic modulators. A number of these applications necessitate films with thicknesses greater than those presently being designed for low voltage (1-3V) random access memories; i.e., 0.1-0.4 microns. A typical example of such an application is that of a transverse-mode spatial light modulator (SLM) which generally requires a film of several microns thick in order to generate the necessary optical retardation for sufficient optical contrast. Although much of the needed retardation can be produced via the direct electrooptic effect by simply increasing the electric field, there is an limit to this process since saturation of polarization or dielectric breakdown eventually occur. Consequently, for a given material composition, further gains in total retardation must be achieved by increasing the optical path length; i.e., the film thickness.

This investigation reports on work involved in the study of thicker films (0.5-6.5  $\mu\text{m}$ ) of PLZT compositions composed of varying concentrations of La (0-12 atom percent) at a constant Zr/Ti ratio of 65/35.

### EXPERIMENTAL

The precursor materials used in the fabrication of the PLZT films consisted of lead subacetate ( $\text{PbsubAc}$ ) powder with a  $\text{PbO}$  concentration of 78.6 wt.%, lanthanum acetate ( $\text{LaAc}$ ) aqueous solution with an  $\text{La}_2\text{O}_3$  content of 6.7 wt.%, zirconium acetate ( $\text{ZrAc}$ ) aqueous solution containing 22.22 wt.%  $\text{ZrO}_2$  and titanium acetylacetone ( $\text{TiAAc}$ ) chelated solution consisting of 16.96 wt.%  $\text{TiO}_2$ .

## G.H. HAERTLING

The various steps involved in the processing and fabrication of the films are shown in Figure 1. Compositions of various PLZT formulations ranging in La content from 0 to 12 atom % at a constant 65/35 Zr/Ti ratio were prepared by

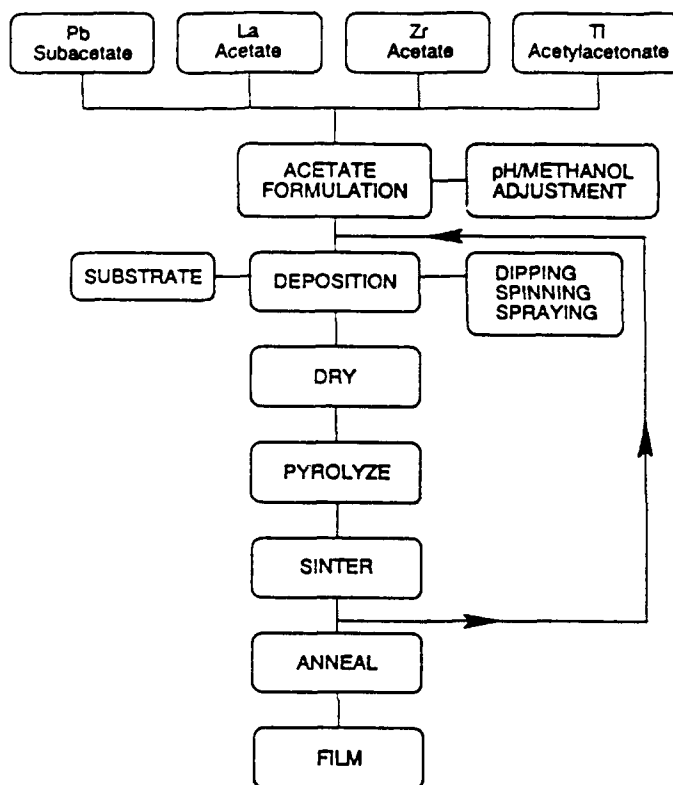


FIGURE 1. Flowsheet of the acetate process

mixing the precursor ingredients in the proper proportions as they were received from the vendors. The solutions were then deposited via a dip coating process onto substrates consisting of either electrically conductive tin oxide coated (30 nm) PLZT (0.375 mm thick), randomly oriented sapphire (1.25 cm dia x 0.5 mm thick) or Ag foil (0.127 mm thick). After drying for several seconds, the films were moved directly into the heating chamber and sintered at 700°C for two minutes per layer. An automatic, computer-controlled, dip coating apparatus was used to deposit and sinter the films.<sup>1</sup> As many as 150 layers were deposited, thus producing a total sintered thickness of 6.5 um for the thickest films. A plot of the sintered film thickness as a function of the number of layers is given in Figure 2. As can be seen, the sintered film thickness is linearly related to the number of layers throughout the major portion of the deposition process. The slope of the plot in the linear region was calculated to be 415 angstroms (0.0415 um) per layer; however, this value was less than half of the slope for the first few layers which was approximately 1000 angstroms (0.1 um) per layer. The deposition behavior exhibited in this portion of the curve is believed to be due to the influence of the substrate surface.

A final anneal of the film, when performed, was carried out at 100°C below the sintering temperature for a period of 30 minutes with a slow cool in the furnace to

## DIELECTRIC AND ELECTROOPTIC PROPERTIES OF PLZT FILMS

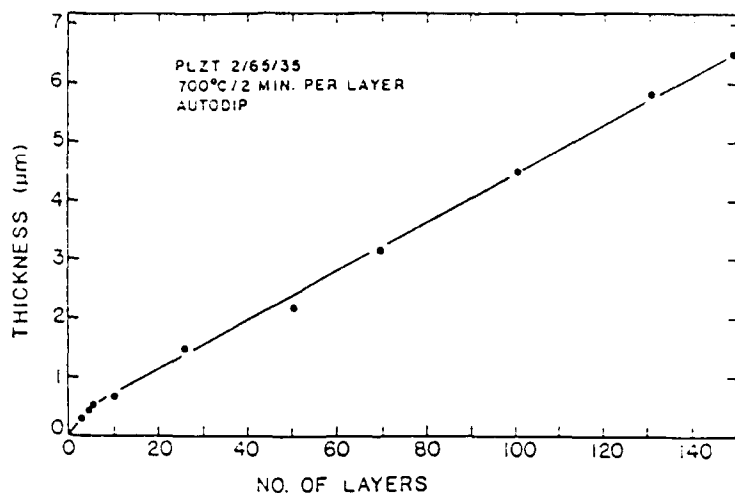


FIGURE 2. Relationship of film thickness to the number of layers.

room temperature; however, most of the films were not given an anneal in this study since the benefits of stress relief for these PLZT films on a PLZT substrate were considered to be marginal.

For the dielectric and hysteresis loop measurements, top copper electrodes, one mm. dia., were deposited on the films through a mask via vacuum evaporation. Small signal dielectric measurements were carried out on a digital LCR meter at 1 kHz. Hysteresis loops ( $P$  vs.  $E$ ) were measured on the films at frequencies of 1 kHz and near dc (1/8 Hz) at a driving voltage of <20 volts. Since PLZT substrates were inappropriate for use when determining the electrooptic characteristics of PLZT films, sapphire was chosen as an alternate substrate. Sapphire is highly transparent and readily available, however, it should be kept in mind that a thermal expansion mismatch between the film and substrate (i.e., 5.4 vs.  $9 \times 10^{-6}/^{\circ}\text{C}$ , respectively) could lead to stresses in the film which may alter their properties. While it was felt that this could be the case with the films of less than one micron thickness, such a mismatch was not considered to be a significant factor in the measurements on the thicker films.

Electrooptic measurements were made on films dip coated on sapphire and electrodeposited with thermally evaporated aluminum. Several 50 μm gaps for producing the transverse electric field were photolithographically generated in the electrodes using a commercial aluminum etch which did not attack the PLZT film. The setup for the measurements is shown in Figure 3. An incandescent white light source along with a Babinet-Soleil compensator, crossed polarizers, a variable dc power supply and a United Detector Technology, Model S370, detector were used to make the birefringence measurements.

### RESULTS AND DISCUSSION

### MATERIALS

Examples of the transparency of PLZT 2/65/35 films of various thicknesses ranging

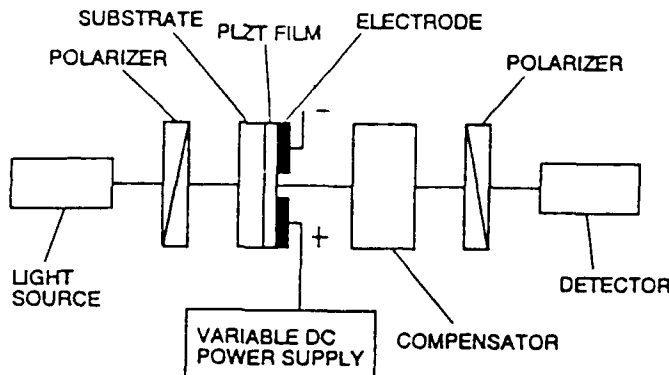


FIGURE 3. The setup for electrooptic measurements.

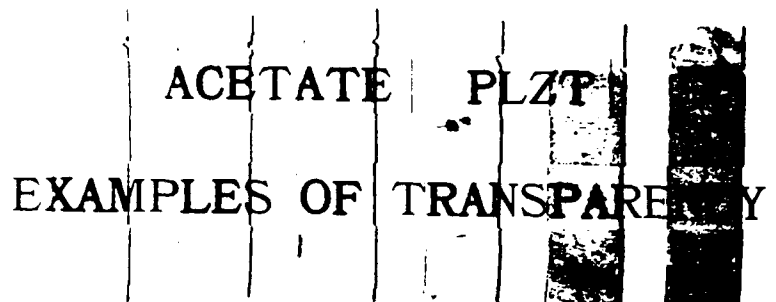


FIGURE 4. PLZT dip coated (2/65/35) on  $\text{SnO}_2/\text{PLZT}$  substrates illustrating optical transparency of the 5, 10, 25, 50, 69 and 100 layer samples (left to right).

from 0.5  $\mu\text{m}$  (5 layers) to 4.5  $\mu\text{m}$  (100 layers) are shown in Figure 4. These specimens were autodip coated on PLZT substrates with a full sintering cycle for each layer. It was observed that all of the films were optically transparent and crack free, having a smooth, highly polished appearance. The grain sizes of these films ranged from 0.5 - 2 microns.

An typical optical transmission curve for a 5.5  $\mu\text{m}$  thick PLZT film on sapphire is given in Figure 5. Overall, it may be observed that the transmittance of this film is very similar to that of the bulk material.<sup>2</sup> Additionally, it should be noted that the total transmission of the film is approximately the same as that of the bulk; i.e., 64% at 800 nm wavelength vs. approximately 67% for the bulk at the same wavelength. The onset of transparency was found to take place at approximately 360 nm, which is slightly lower than the 370 nm of the bulk.

An optical photomicrograph of a polished cross section and an SEM micrograph of a fractured surface are given in Figure 6. This figure shows the excellent thickness uniformity of the films after sintering as well as revealing the intimate growth between the many deposited layers. It also points out the fact that the thicker films are actually single, monolithic entities with bulk-like characteristics. X-ray diffraction patterns taken on several of the films indicated that the films

## DIELECTRIC AND ELECTROOPTIC PROPERTIES OF PLZT FILMS

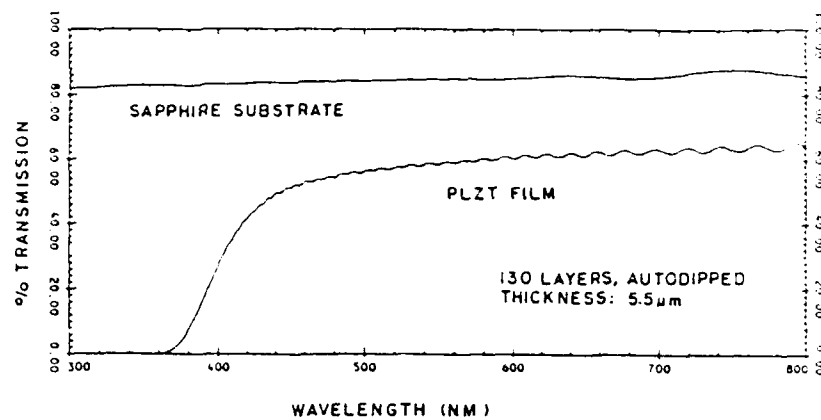


FIGURE 5. Optical transmittance of a 5.5  $\mu\text{m}$  thick PLZT film on sapphire and the sapphire substrate without the film.

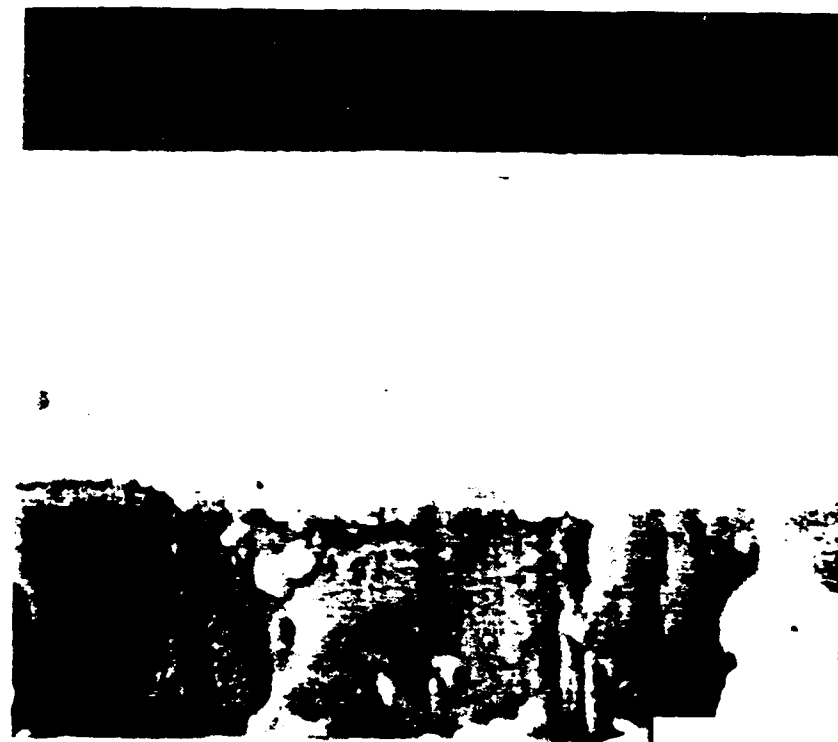


FIGURE 6. Cross section photomicrographs of 2.2  $\mu\text{m}$  (50 layers) thick PLZT 2/65/35 film on PLZT substrate at x1250 magnification (top) and 3.2  $\mu\text{m}$  (69 layers) thick PLZT film at x11,000 (bottom).

possessed well developed, perovskite structures with little evidence for preferred orientation.

# G.H. HAERTLING

## DIELECTRIC PROPERTIES

The dielectric properties of several of the PLZT films are listed in Table 1 as a function of thickness and in Table 2 as a function of composition. In Table 1, it can be noted that the small signal relative dielectric constants (avg. = 702) and dissipation factors (avg. = .108) did not change significantly with increasing film thickness, however, this was not the case with the large signal properties taken from the hysteresis loops. Remanent polarization ( $P_R$ ) increased with increasing thickness, and coercive field ( $E_c$ ) decreased with increasing thickness. These results again point out that the thicker films generally possessed properties more closely associated with bulk materials.

TABLE 1. Electrical properties of PLZT 2/65/35 films of varying thickness.

NO. LAYER	FILM THICK ( $\mu\text{m}$ )	DIELECTRIC CONSTANT	DISSIPATION FACTOR	$P_R$ ( $\mu\text{C}/\text{cm}^2$ )	$E_c$ ( $\text{kV}/\text{cm}$ )
5	.5	664	.124	26	67
10	.8	714	.135	28	45
25	1.5	776	.109	29	51
50	2.1	708	.103	33	51
69	3.2	712	.095	36	46
100	4.5	638	.081	37	43

TABLE 2. Dielectric properties of 0.6  $\mu\text{m}$  thick PLZT films dip coated on Ag foil; ( $r_c$  values were obtained on sapphire substrates).

COMP.	T <sub>c</sub>	DIELECTRIC CONSTANT	TANGENT DELTA-%	$P_R$ $\mu\text{C}/\text{cm}^2$	$E_c$ $\text{kV}/\text{cm}$	$r_c$ $\times 10^{10} \text{ m/V}$
0/65/35	235	455	.095	43	96	1.08
2/65/35	205	500	.110	41	95	—
6/65/35	145	685	.104	29	80	.79
8/65/35	125	790	.092	19	62	.53
9/65/35	120	875	.095	10	40	.44
9.5/65/35	—	860	.090	—	—	.37
10/65/35	118	845	.080	8	35	—
11/65/35	115	730	.063	5	25	—
12/65/35	—	700	.056	4	20	—

## DIELECTRIC AND ELECTROOPTIC PROPERTIES OF PLZT FILMS

Dielectric data on compositions with La concentrations ranging from 0 to 12 atom % at a constant Zr/Ti ratio of 65/35 are given in Table 2. The trends noted in these results generally follow those of the bulk materials; however, their absolute values, in some cases, were significantly different. For example, (1) the Curie temperatures ( $T_c$ ) for all of the films were lower than the bulk by 50 to 80°C; (2) the dielectric constants were also lower, but the deviation from the bulk only became significant at La contents greater than 6%; (3)  $P_{rs}$ s were higher (more remanence) than the bulk for La contents of 9% or higher and (4)  $E_c$ s were substantially higher than the bulk for all compositions. The curves showing the temperature dependence of dielectric constant and the hysteresis loops for this series of compositions are given in Figures 7 and 8, respectively.

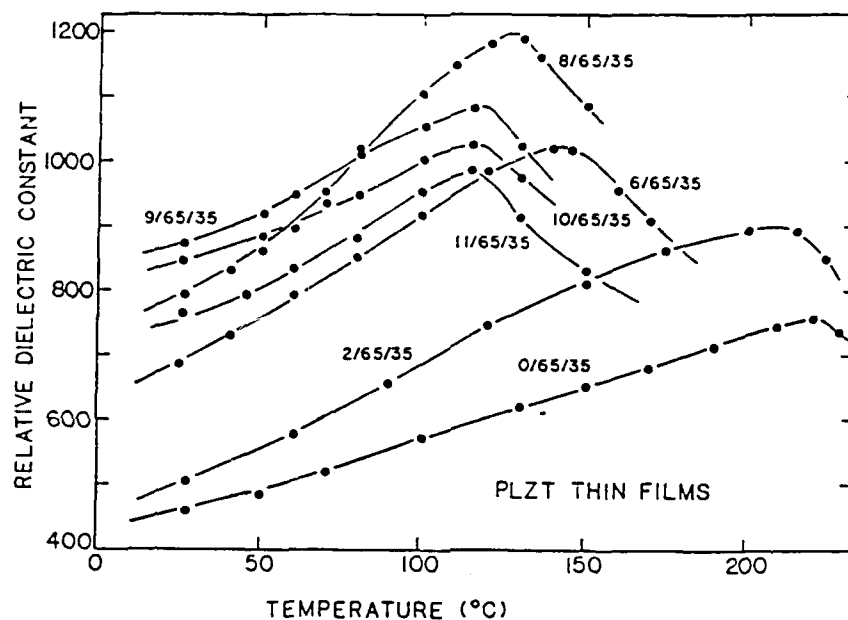


FIGURE 7. Temperature dependence of dielectric constant for various PLZT compositions

## ELECTROOPTIC PROPERTIES

Using the setup shown in Figure 3, birefringence measurements were made on several of the films (5.5  $\mu\text{m}$  thickness) deposited on sapphire. These data are given in Figure 9. It can be seen that the PLZT composition 0/65/35 at the top of the figure is ferroelectric with definite remanent birefringence and switching characteristics, whereas, all of the other compositions (6, 8 and 9% La) appear to have very little remanent birefringence. The birefringences in these latter compositions appear to be primarily of the electrically-induced, quadratic nature which is similar to that of the bulk PLZT relaxor materials but only within the range from 9 to 12% La. The reason for the lack of remanence in compositions 6/65/35 and 8/65/35 is not understood at this time; but it is believed to be due, at least in part, to stresses in the film from thermal mismatches or substrate clamping during activation when the film is constrained from moving piezoelectrically.

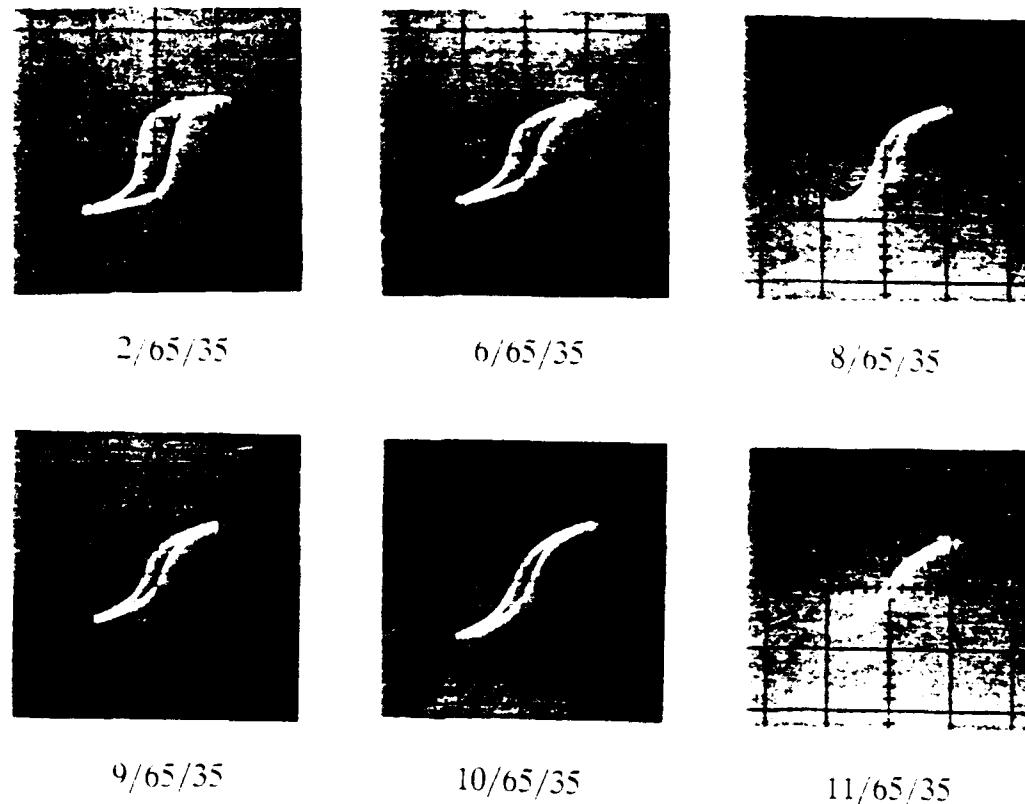


FIGURE 8. Hysteresis loops of selected films (0.6 um thick) of PLZT dip coated on Ag foil.

A closer examination of the non-remanent birefringence curves of Figure 9 reveals that at lower electric fields (<50 Kv/cm) the dependence is quadratic, however, "saturation effects" at higher fields causes the overall curve to be approximately linear. The saturation effect is, in all likelihood, the normal approach toward the half-wave retardation condition as experienced in bulk material, but spread out over much higher values of electric field. It was not possible in any of the films to actually achieve half-wave retardation, and this again, is believed to be due to the clamping effects of the substrate. Such effects were similarly noted by Wang, et.al. for compositions in the PLZT system.<sup>3</sup>

Although the required electrical fields for the films were substantially higher than the bulk materials (15 kV/cm vs. 150 kV/cm), it should also be noted that the birefringence values achieved were quite competitive with the bulk; i.e., -0.004 to -0.016 at 150 Kv/cm for a 5.5 um thick film. The electrooptic  $r_e$  coefficients, calculated as a linear coefficient across the useable range of electric fields from 0 to 150 Kv/cm, were determined for the various compositions and are given in Table 2. As seen, the values range from  $1.08 \times 10^{-10}$  m/V for 0/65/35 to  $0.37 \times 10^{-10}$  m/V for 9.5/65/35. A comparison of these values with similar ones for bulk material shows that the films at the 5 um thick level possess bulk-like electrooptic properties.

Further evidence for the bulk-like character of these films is given in Figure 10. This figure is a photograph of one of the measured films (0/65/35) with one of the gaps activated while the other gap was held in the inactive state. To date, contrast ratios of up to 1000 to 1 have been obtained.



FIGURE 10. Transverse-mode PLZT thin film device with one gap activated (right) and one gap inactive; (thickness = 5.5  $\mu\text{m}$  and gap = 40  $\mu\text{m}$ ).

#### ACKNOWLEDGEMENTS

The author wishes to gratefully acknowledge the assistance of Kewen K. Li and Kimberly D. Preston for the preparation of some of the PLZT thin and thick film samples. This work was supported by the Office of Naval Research under contract No. N0014-91-J-1508.

#### REFERENCES

1. K.K. Li, G.H. Haertling and W.Y. Howng, Integrated Ferroelectrics (to be published).
2. G.H. Haertling, Ferroelectrics, 75, 1 (1987).
3. F. Wang and A.Y. Wu, Proceedings of 1990 Intl. Sym. Appl. Ferroelectrics, Urbana, 131 (1992).

## DIELECTRIC AND ELECTROOPTIC PROPERTIES OF PLZT FILMS

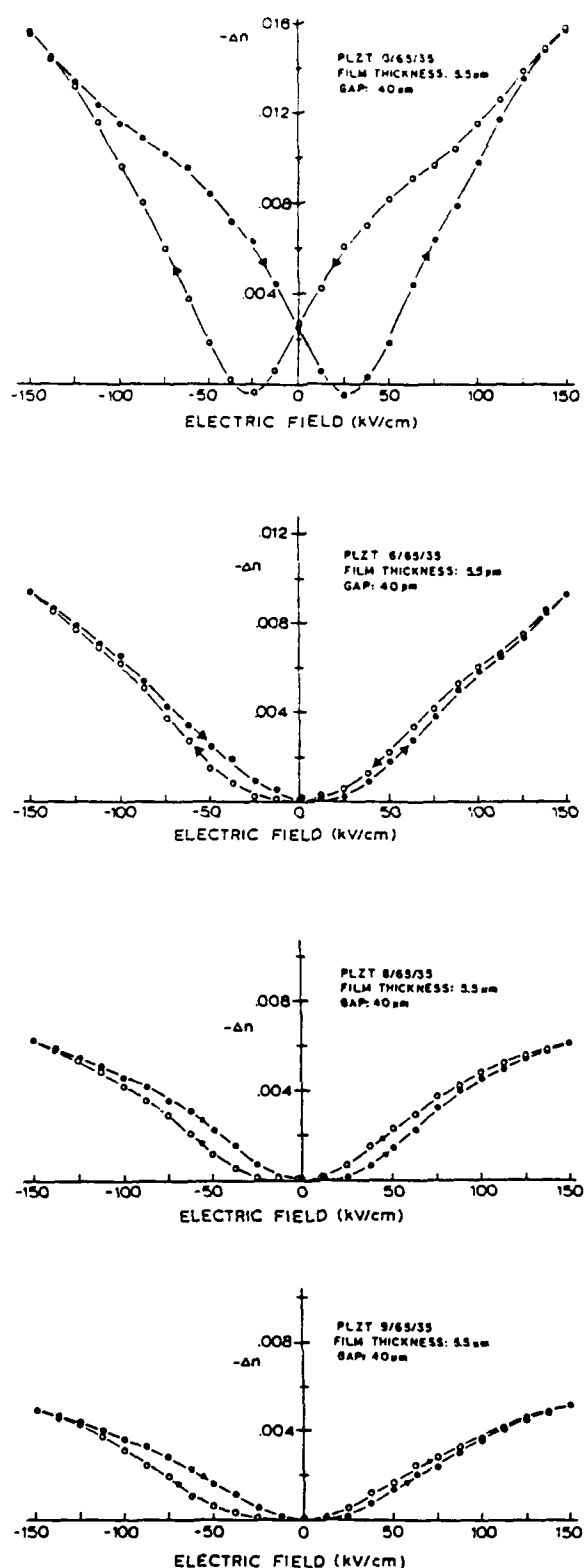


FIGURE 9. Electrooptic transverse-mode birefringence data on films of selected PLZT compositions